UNIVERSITY OF CALIFORNIA SAN DIEGO

Preparation and Deployment of the Telescopes and POLARBEAR-2b Receiver for the Simons Array Cosmic Microwave Background Polarization Experiment

A dissertation submitted in partial satisfaction of the
requirements for the degree
Doctor of Philosophy

in

Physics

by

Lindsay Ng Lowry

Committee in charge:

Professor Brian Keating, Chair
Professor Kam Arnold
Professor Samuel Buss
Professor David Meyer
Professor Shelley Wright

2021

The dissertation of Lindsay Ng Lowry is approved, and it is acceptable in quality and form for publication on microfilm and electronically.

University of California San Diego

2021

DEDICATION

To my wonderful family,

and to my wonderful TomTom.

TABLE OF CONTENTS

LIST OF FIGURES

LIST OF TABLES

ACKNOWLEDGEMENTS

It could be argued that, of all the pieces of this dissertation, the writing in this section is what I have been thinking about for the longest time. I am enormously grateful for all of the people in my life that have made the research presented in this dissertation, the dissertation itself, and my overall wonderful experience in grad school possible.

First and foremost, I must thank the entire POLARBEAR/Simons Array collaboration and the UCSD experimental cosmology group. This project is the result of so many individuals working together toward our shared goal of better understanding the universe. As the field progresses and we take on tougher technological and logistical challenges in order to measure the CMB, larger collaborations are emerging. These groups have provided a wonderfully nurturing environment in which to grow my own skills as well as to really understand how projects like ours become successful.

The POLARBEAR/Simons Array collaboration consists of many people, and to break that down a little I'd like to start by thanking my advisor, Professor Brian Keating. He welcomed me into the group in 2014, making it clear that UCSD would be a great place to continue to work on the type of experiments I had grown to love as an undergraduate student on the other side of the country, and he was right. Brian has managed to create a group at UCSD that works together and constantly supports each other, and has been leading projects that will further our understanding of cosmology. He has given me guidance and freedom in my research within the Simons Array project and beyond, and has supported me in all of my pursuits.

Secondly, I'd like to thank Professor Kam Arnold. Kam has been an advisor in every sense of the word since I started grad school, although this document will not officially reflect that. He has made time for me whenever I needed it, whether it was a technical question about cosmology or our experiment, advice about which sub-projects to pursue, or support in preparing for the next stage in my career. This was even more the case over the past year when, like most other things, work on the Simons Array and my plans for graduation became extremely uncertain.

He is also the person who helped me to become so involved in work at the Simons Array site, and has supported me in all my trips that have shaped my life as a grad student.

I'd also like to thank Professors Shelley Wright, Samuel Buss, and David Meyer for serving on my thesis committee and providing guidance with respect to my research over the past few years.

My fellow cosmology group members at UCSD have also had a hugely positive impact on my time in grad school. Grad school can often be described as isolating and competitive, and not once have I felt either of those things while working in my lab. In fact, it is the opposite. The students and post-docs who have made up our group over the past seven years are somehow always willing to take the time to help one another. Feeling comfortable asking my fellow lab-mates for help on homework problems, understanding papers, figuring out how to best evaluate data, or even just lifting the heavy receiver panels into place is something that truly got me through grad school both academically and mentally. Thank you to Darcy Barron, who overlapped with me at UCSD for only one year but who continued to be a fantastic resource and mentor in the collaboration through all my years at UCSD. Thank you to Praween Siritanasak, who I went to with almost all my questions about the lab. Praween helped me patiently with any issue that came up, always willing to provide the reassurance I craved and helping me to build confidence in the lab (and forcing me to expand my baking horizons beyond chocolate, which, I suppose, is not a bad thing). Even after he left UCSD this past year, he has taken the time to answer my questions on Slack and even stayed on the phone with me as I tried clumsily to resolve computer networking issues on multiple occasions. Thank you to Fred Matsuda and Nate Stebor, with whom I worked closely on different projects during my first few years of grad school as I was just getting introduced to the collaboration. Thank you to David Leon, who sat at the desk behind me and was always willing to discuss my questions about theory and analysis if I turned around. Thank you to Marty Navaroli, with whom I spent a few of my most entertaining days of grad school discussing physics and cosmology with elementary school students. Thank you to Tucker

Elleflot, who helped me navigate my first trip to the telescope site and who on multiple occasions took the time to explain in detail the concepts behind our readout and detector schemes to me. Thank you to Logan Howe, who joined the group with me in 2014. Having someone who would become such a good friend at the desk next to mine as I figured out how to manage classes and research made the transition so much easier. Logan is responsible for much of the success of the POLARBEAR-2b receiver (on which much of this dissertation is based), and the project would not be where it is today without his efforts. Thank you to Max Silva-Feaver, who has taught me so much about CMB readout and has done so much to create a sense of community within our lab and CASS. Thank you to Jen Ito, who has become my POLARBEAR-2b partner over the past two years as we attempt to integrate the receiver with the telescope in Chile and get our first glimpse of the sky with this instrument. The past two years have not been what we expected, and I cannot imagine how they would have gone if Jen had not been with me through all the receiver testing, packing and shipping coordination, deployment decisions, travel and safety uncertainties, and trips to the French bakery. Thank you to Joe Seibert, who worked with me on the lab's FTS, a project not discussed in this dissertation but one I am excited about, especially as Joe has recently gotten it working for its intended purpose of characterizing detectors. Thanks also to Joe for jointly advising undergraduate students with me on projects related to the FTS. Thank you to Jake Spisak, for coming up with astronomy numbers of the week with me. Thank you to Grant Teply for his help in editing this dissertation. And thank you to all my other fellow cosmology grad students and post-docs over the years – Jon Kaufman, Nick Galitzki, Alex Zahn, Megan Russell, Tran Tsan, Roman Gerasimov, Michael Randall, and Bryce Bixler – who have made my work in the lab truly enjoyable and enriching.

I'd also like to thank the undergraduate students and post-baccalaureate researchers with whom I've worked at UCSD – Christopher Aleman, Kevin D. Crowley, Chris Ellis, Eduardo Garcia, Chris Johnson, Kavon Kazemzadeh, Eddie Mendoza, Joseph Rodriguez, Ben Schocket-Greene, Walker Stevens, Calvin Tsai, Connor Vancil, Joanna Xu, and Larry Yu. These students

and researchers not only did significant portions of the lab work that has gotten the Simons Array projects I have been involved in to where they are today, but also helped me to become a better advisor and communicator. Special thanks to Christopher and Kevin, with whom I worked closely on telescope accessories for the Simons Array. Special thanks also to Calvin Tsai, who played a crucial role in preparing the POLARBEAR-2b receiver in the lab and in preparing and maintaining the Simons Array site in Chile for the receiver's arrival, and who also worked with me closely on design and procurement of telescope accessories.

Next I'd like to thank the many people who have helped support UCSD's efforts with the Simons Array – Chris Munson, Delwin Johnson, Peggy McCoy, Liz Daniels, Liz Kelly, Dana Johnson, Laura Purkey, Gwen Maley, Laura Russell, and Stuart Volkow. Additional thanks to UCSD's shipping and export control teams, who have helped me to coordinate countless shipments between UCSD and Chile.

A significant amount of my time in grad school was spent at the Simons Array site in Chile. I have spent a total of 32 weeks working in Chile over nine trips, including right now as I write these acknowledgements. None of the work I've accomplished at the site would have been possible without the support of the Simons Array team in Chile – Nolberto Oyarce, Jose Cortes, Dave Boettger, and Oriel Arriagada. This team has always helped me to achieve my ambitious goals for my site trips while making sure I am safe (and, importantly, have plenty of chocolate). Especially over the past year as we have navigated how to work on our project safely despite the pandemic, the site team has gone above and beyond to make sure our project moves forward. Thanks also to Julia Araya for helping coordinate my trips.

Thank you to the many individuals across institutions all over the world who work on the Simons Array not already mentioned. In particular thank you to those with whom I've collaborated in-person on hardware projects at UC Berkeley and at KEK, and to those with whom I've worked at the site. I have felt so lucky to be able to work on this project, made possible by the dedication and expertise of this amazing group of people.

Finally, I'd like to thank Hans Paar and Andy Friedman, two members of the UCSD cosmology group who passed away during my time as a grad student. Both Hans and Andy brought an incredibly positive energy to the group that is sadly missed. In addition to supporting me on Simons Array projects, Hans was my first-year advisor, and each time I attend a colloquium or talk outside the field of cosmology I remember his encouragement to explore and learn about different fields. I did not work closely with Andy, but I remember the enthusiasm and talent with which he would share science with our group and with the world, and his care and respect for the students he worked with.

I joined the Simons Array collaboration after sparking an interest in experimental cosmology as an undergraduate student at Johns Hopkins University. If not for the incredible team at Johns Hopkins working on the CLASS experiment who allowed me to learn from and be inspired by them, none of my work with the Simons Array would have been realized.

In addition to those already mentioned who were directly involved in my research, there are several other groups of people who have impacted my time as a grad student for the better.

Firstly, CASS. The supportive environment I mentioned inside the experimental cosmology lab extends to the entire UCSD astrophysics community. From journal clubs and seminars to B/ZASHs, from conversations about astronomy or outreach to just needing to borrow a scale, the people in CASS have removed much of the intimidation that can come with studying physics and become wonderful friends.

I am also grateful for the members of CASS and the wider UCSD physics community with whom I've worked on outreach- and diversity-related topics. The Graduate Women in Physics group has been part of my life since I started grad school. This group supplied me with a support system, a sounding board, workout buddies, and friends, and was a necessary resource that strengthened me during my time at UCSD. I am also grateful for the UCSD Cosmic Tours portable planetarium with which I've had the privilege of being involved, made possible by Professor Shelley Wright. Working with this group of people has taught me so much about

astronomy and teaching, and has allowed me to interact with the public and express my love for science in the most engaging way. Similarly, I'd like to thank Sanchit Sabhlok for helping me implement my idea of a scientist pen-pal program, another fun way in which I've been able to share science with the public. Finally, thank you to the members of the Graduate Student Diversity Initiative. My academic accomplishments highlighted in the writing of this dissertation were made possible not only because of the people I've mentioned here, but also because of the privilege I've experienced throughout my life. The difficult work this group is doing to promote diversity in physics, starting with our own department, and to encourage the physics community to think critically about how our actions can be used to create more equitable and anti-racist systems is crucial in making sure all those who want to pursue physics have the support and encouragement they need. I am thankful to have had the opportunity to work with them over the past year.

I'd also like to thank the UCSD physics department staff, who have supported me in my academic, research, and outreach endeavors throughout grad school.

Another group of people who added to my experience at UCSD is the physics incoming graduate class of 2014. I could not have asked for a better group of friends with whom to start grad school. Together we made it through our first-year classes and preparing for the qualifying exam, always looking to lift each other up rather than feeling competitive. We created lasting friendships with each other and each other's families, surrounding me with support and filling my life with much needed potlucks, game nights, tennis matches, and volleyball games. I feel so lucky to have had this group of people by my side.

Outside of physics I've also made some great friendships in San Diego that I hope will stay with me. To all my friends in San Diego, thank you for climbing with me, doing gymnastics with me, sharing your pets with me, and eating delicious food with me.

The most difficult part of my decision to come to UCSD was the fact that it would mean moving across the country, away from my friends and family who had been such essential parts

of my life before grad school. I was nervous that the distance would make it difficult to stay close to the people I loved so much. I am so happy to say that I had no reason to worry.

First, thank you so much to my friends whom I've known since elementary school, Paige Scrofani, Carrie Mildner, and Reed Zukerman. Paige, Carrie, Reed, and I have had a group text chain going since before I started grad school, and we continue to talk on it nearly every day. All of our lives and careers are very different, and each one of them has inspired me to accomplish my goals and to stand up for and take care of myself. They are often the first people I turn to if I am overwhelmed or conflicted, because I know someone will be there to listen and provide advice if I need it. I will always be jealous of the nacho nights I've missed from living far away, but I think our friendship has only grown stronger despite the distance and I love that we make the time to see each other and celebrate the accomplishments and occasions I miss every time I do make it to back New York. Thank you for always being there for me. And a special thank you to Paige for talking to me on the phone before every single one of my trips to Chile, helping me to stay calm and prepare for the travel.

Thank you also to Kielan Crow, who I've also become closer to despite living in different cities. Kielan has been fiercely supportive of everything I've done in grad school, celebrating all my accomplishments and sharing in my joy. He has also been part of countless adventures with me, somehow staying cheerful and making me feel comfortable even when I start feeling anxious. I am excited for the many more adventures and celebrations yet to come. Thank you also to Kielan's family, who have been so inspiring and kind to me.

I'd also like to thank the Ayotte/Capozza family who welcomed me when we first met and who continues to encourage me. My trips to Boston have always been welcome escapes from some of the stressors of grad school, and I am so lucky to have their love and support.

Lastly, to the amazing people to whom this dissertation is dedicated – my family and my fiancé, Tom. There will never be enough room to thoroughly express my gratitude for my family and for Tom, but I will try my best to show a glimpse of what they mean to me.

My family is the best in the world. I feel as though I've always had a happy life, something I know cannot be taken for granted, and that is entirely because of my parents, Delores and Andy. The list of things they have done and continue to do for me to make sure I have every opportunity to be happy is truly endless. Since before I can remember, my dad would help me with my schoolwork – working with me on science fair projects, quizzing me on my middle school vocabulary words, and even helping me understand complicated integration techniques. He does all this and more for me while also remaining dedicated and hard-working in his own interests and career. I would not have achieved the level of success I have today without his help. The same is true for my mom, who is the most generous, caring, and friendly person I know. The ease and confidence with which she talks to people and chooses to do the right thing, the thing that will help people, even if it is the thing that would make me hesitate and feel awkward, is incredible. Our careers are very different, but the way my mom applies herself to her work as a social worker shows in the way she treats all those around her. I have learned to be a better person because of my mom, and it has provided me with strong relationships in both my personal life and my career, including my relationship with her, that have stayed with me through grad school.

My sister, Jenna, is another amazing person who has been an incredible resource for me in grad school. She is confident, compassionate, and honest. I have enormous respect for her opinion because I know she takes the time to think about everything she does, and her advice has been vital as I've faced this last challenging year of grad school. We are similar in so many more ways than I realized when were growing up, and I know she will be able to relate to and support me in any problem I might encounter.

I am immensely lucky to be able to say that the familial support I've received extends well beyond my immediate family. My aunts and uncles have been constant sources of love in my life from the day I was born. I am so grateful for all the time they've devoted to me through all the stages of my life and career so far. We've spent every holiday season (among so many other occasions) with one another, coming from all over the world to be together in the most loving and

wonderfully chaotic environment. I can say that I have a special relationship with every one of my aunts and uncles, and I know they always want what is best for me.

Likewise, my cousins mean the world to me. They have always been and will always be some of my best friends. I grew up with constant visits to and vacations with Emily, Ryan, and Katie, who lived near me on the east coast. I cannot imagine my life without them, nor can I imagine ever feeling closer to or more comfortable with a group of people. Again, even after I moved across the country, we stayed close with texts, video calls, and visits in both directions. I can always be myself with my cousins, and knowing they are always there for me and that I am always there for them has helped me get through so many challenges. Special thanks to Katie who even sat with me on Facetime while we wrote our papers together and let me bother her with frequent updates about my dissertation progress. I'd also like to thank my cousins who live farther away, Julia, Louisa, Maya, and Carter, but who have nonetheless been so important in my life. Though we are usually only able to see each other in person over the holidays, each year it feels like nothing has changed. We've been through so much together and I will never have any doubt that we all have each other's backs. I am so happy to know that my cousins will be in my life forever. That knowledge has helped me through grad school and will continue to motivate me as I take on new challenges.

A final shoutout to everyone in my family that I've already mentioned for taking the time to get together on Zoom every week for over a year now to check in, laugh, and "give updates."

The final person to whom I owe so much of my success in grad school is my incredible fiancé, Tom. He has literally been by my side through every overwhelming and stressful experience, through every success and every failure, through every uncertainty. He has grown with me so much over the past seven years, always looking to better understand how he can best support me in my goals and help me to feel happy and calm. He has listened to me explain every situation where I felt unsure and given me confidence to confront it. He has talked to me in the middle of the night and encouraged me to breathe when I've been working at the site and feeling

anxious. He has come into lab with me on nights and weekends to pack thousands of screws or to make sure I wasn't alone when working in the machine shop. He has thought about how all the decisions he makes will impact my life and my career, always considering what is best for me. He has inspired me to go on adventures, to try new things, and to always keep learning. He has cooked for me and run errands for me and picked me up from work and the airport. He has even joined me at our telescope site in Chile, 17,000 ft above sea level. The list goes on and on. My life has been made so much better because of him, and I know just how lucky I am to have had him with me through grad school.

I would not be who or where I am today without all this help. To everyone I've mentioned and more, thank you so much.

Land Acknowledgement as written by the UCSD Intertribal Resource Center: *The UC San Diego community holds great respect for the land and the original people of the area where our campus is located. The university is built on the un-ceded territory of the Kumeyaay Nation. Today, the Kumeyaay people continue to maintain their political sovereignty and cultural traditions as vital members of the San Diego community. We acknowledge their tremendous contributions to our region and thank them for their stewardship.*

The dissertation author acknowledges ESA and the Planck Collaboration for production of Figures 1.2, 1.3, and 1.7, originally published in Planck Collaboration, 2020 [1].

Chapter 2 (Figure 2.21) and Chapter 3 include material published in J. Ito, L. N. Lowry, T. Elleflot, K. T. Crowley, L. Howe, P. Siritanasak, T. Adkins, K. Arnold, C. Baccigalupi, D. Barron, B. Bixler, Y. Chinone, J. Groh, M. Hazumi, C. A. Hill, O. Jeong, B. Keating, A. Kusaka, A. T. Lee, K. Mitchell, M. Navaroli, A. T. P. Pham, C. Raum, C. L. Reichardt, T. J. Sasse, J. Seibert, A. Suzuki, S. Takakura, G. P. Teply, C. Tsai, and B. Westbrook, "Detector and readout characterization for POLARBEAR-2b," in *Millimeter, Submillimeter, and Far-Infrared Detectors and Instrumentation for Astronomy X* (J. Zmuidzinas and J.-R. Gao, eds.), vol. 11453, pp. 286

- 301, International Society for Optics and Photonics, SPIE, 2020. The dissertation author was second author on and made essential contributions to this work.

VITA

2013	B. S. in Physics, Johns Hopkins University
2013	B. S. in Mathematics, Johns Hopkins University
2018	M. S. in Physics, University of California San Diego
2021	Ph. D. in Physics, University of California San Diego

PUBLICATIONS

Y. Segawa, H. Hirose, D. Kaneko, M. Hasegawa, S. Adachi, P. Ade, M. A. O. A. Fa?undez, Y. Akiba, K. Arnold, J. Avva, C. Baccigalupi, D. Barron, D. Beck, S. Beckman, F. Bianchini, D. Boettger, J. Borrill, J. Carron, S. Chapman, K. Cheung, Y. Chinone, K. Crowley, A. Cukierman, T. de Haan, M. Dobbs, R. Dunner, H. E. Bouhargani, T. Elleflot, J. Errard, G. Fabbian, S. Feeney, C. Feng, T. Fujino, N. Galitzki, N. Goeckner-Wald, J. Groh, G. Hall, N. Halverson, T. Hamada, M. Hazumi, C. Hill, L. Howe, Y. Inoue, J. Ito, G. Jaehnig, O. Jeong, N. Katayama, B. Keating, R. Keskitalo, S. Kikuchi, T. Kisner, N. Krachmalnicoff, A. Kusaka, A. T. Lee, D. Leon, E. Linder, L. N. Lowry, A. Mangu, F. Matsuda, Y. Minami, J. Montgomery, M. Navaroli, H. Nishino, J. Peloton, A. T. P. Pham, D. Poletti, G. Puglisi, C. Raum, C. L. Reichardt, C. Ross, M. Silva-Feaver, P. Siritanasak, R. Stompor, A. Suzuki, O. Tajima, S. Takakura, S. Takatori, D. Tanabe, G. P. Teply, C. Tsai, C. Verges, B. Westbrook, and Y. Zhou, "Method for rapid performance validation of large tes bolometer array for polarbear-2a using a coherent millimeter-wave source," *AIP Conference Proceedings*, vol. 2319, no. 1, p. 040019, 2021

D. Barron, K. Mitchell, J. Groh, K. Arnold, T. Elleflot, L. Howe, J. Ito, A. T. Lee, L. N. Lowry, A. Anderson, J. Avva, T. Adkins, C. Baccigalupi, K. Cheung, Y. Chinone, O. Jeong, N. Katayama, B. Keating, J. Montgomery, H. Nishino, C. Raum, P. Siritanasak, A. Suzuki, S. Takatori, C. Tsai, B. Westbrook, and Y. Zhou, "Integrated electrical properties of the frequency multiplexed cryogenic readout system for polarbear/simonsarray," *IEEE Transactions on Applied Superconductivity*, vol. 31, no. 5, pp. 1Ð5, 2021

J. Groh, K. Arnold, J. Avva, D. Barron, K. T. Crowley, M. Dobbs, T. de Haan, W. Holzapfel, A. Lee, L. N. Lowry, J. Montgomery, M. Silva-Feaver, A. Suzuki, and N. Whitehorn, "Anomalous frequency noise from the megahertz channelizing resonators in frequency-division multiplexed transition edge sensor readout," *IEEE Transactions on Applied Superconductivity*, vol. 31, no. 5, pp. 1Ð5, 2021

J. Ito, L. N. Lowry, T. Elleflot, K. T. Crowley, L. Howe, P. Siritanasak, T. Adkins, K. Arnold, C. Baccigalupi, D. Barron, B. Bixler, Y. Chinone, J. Groh, M. Hazumi, C. A. Hill, O. Jeong, B. Keating, A. Kusaka, A. T. Lee, K. Mitchell, M. Navaroli, A. T. P. Pham, C. Raum, C. L. Reichardt, T. J. Sasse, J. Seibert, A. Suzuki, S. Takakura, G. P. Teply, C. Tsai, and B. Westbrook,

"Detector and readout characterization for POLARBEAR-2b," in *Millimeter, Submillimeter, and Far-Infrared Detectors and Instrumentation for Astronomy X* (J. Zmuidzinas and J.-R. Gao, eds.), vol. 11453, pp. 286 - 301, International Society for Optics and Photonics, SPIE, 2020

J. Seibert, P. Ade, A. M. Ali, K. Arnold, N. F. Cothard, N. Galitzki, K. Harrington, S.-P. P. Ho, B. Keating, L. N. Lowry, M. Russell, M. Silva-Feaver, P. Siritanasak, G. P. Teply, C. Tucker, E. M. Vavagiakis, and Z. Xu, "Development of an optical detector testbed for the Simons Observatory," in *Millimeter, Submillimeter, and Far-Infrared Detectors and Instrumentation for Astronomy X* (J. Zmuidzinas and J.-R. Gao, eds.), vol. 11453,pp. 341 Ð 352, International Society for Optics and Photonics, SPIE, 2020

S. Adachi, M. A. O. Aguilar Faúndez, K. Arnold, C. Baccigalupi, D. Barron, D. Beck, F. Bianchini, S. Chapman, K. Cheung, Y. Chinone, K. Crowley, M. Dobbs, H. El Bouhargani, T. Elleflot, J. Errard, G. Fabbian, C. Feng, T. Fujino, N. Galitzki, N. Goeckner-Wald, J. Groh, G. Hall, M. Hasegawa, M. Hazumi, H. Hirose, A. H. Jaffe, O. Jeong, D. Kaneko, N. Katayama, B. Keating, S. Kikuchi, T. Kisner, A. Kusaka, A. T. Lee,D. Leon, E. Linder, L. N. Lowry, F. Matsuda, T. Matsumura, Y. Minami, M. Navaroli, H. Nishino, A. T. P.Pham, D. Poletti, C. L. Reichardt, Y. Segawa, P. Siritanasak, O. Tajima, S. Takakura, S. Takatori, D. Tanabe, G. P. Teply, C. Tsai, C. Vergès, B. Westbrook, Y. Zhou, and Polarbear Collaboration, "A Measurement of the CMB E-mode Angular Power Spectrum at Subdegree Scales from 670 Square Degrees of POLARBEAR Data," *The Astrophysical Journal*, vol. 904, p. 65, Nov. 2020

M. A. Faúndez, K. Arnold, C. Baccigalupi, D. Barron, D. Beck, S. Beckman, F. Bianchini, J. Carron, K. Cheung, Y. Chinone, H. E. Bouhargani, T. Elleflot, J. Errard, G. Fabbian, C. Feng, T. Fujino, N. Goeckner-Wald, T. Hamada, M. Hasegawa, M. Hazumi, C. A. Hill, H. Hirose, O. Jeong, N. Katayama, B. Keating, S. Kikuchi, A. Kusaka, A. T. Lee, D. Leon, E. Linder, L. N. Lowry, F. Matsuda, T. Matsumura, Y. Minami, M. Navaroli, H. Nishino, A. T. P. Pham, D. Poletti, G. Puglisi, C. L. Reichardt, Y. Segawa, B. D. Sherwin, M. Silva-Feaver, P. Siritanasak, R. Stompor, A. Suzuki, O. Tajima, S. Takatori, D. Tanabe, G. P. Teply, C. Tsai, and Polarbear Collaboration, "Measurement of the Cosmic Microwave Background Polarization Lensing Power Spectrum from Two Years of POLARBEAR Data," *The Astrophysical Journal*, vol. 893, p. 85, Apr. 2020

S. Adachi, M. A. O. Aguilar Faúndez, Y. Akiba, A. Ali, K. Arnold, C. Baccigalupi, D. Barron, D. Beck, F. Bianchini, J. Borrill, J. Carron, K. Cheung, Y. Chinone, K. Crowley, H. El Bouhargani, T. Elleflot, J. Errard, G. Fabbian, C. Feng, T. Fujino, N. Goeckner-Wald, M. Hasegawa, M. Hazumi, C. A. Hill, L. Howe, N. Katayama, B. Keating, S. Kikuchi, A. Kusaka, A. T. Lee, D. Leon, E. Linder, L. N. Lowry, F. Matsuda, T. Matsumura, Y. Minami, T. Namikawa, M. Navaroli, H. Nishino, J. Peloton, A. T. P. Pham, D. Poletti, G. Puglisi, C. L. Reichardt, Y. Segawa, B. D. Sherwin, M. Silva-Feaver, P. Siritanasak, R. Stompor, O. Tajima, S. Takatori, D. Tanabe, G. P. Teply, C. Vergès, and Polarbear Collaboration, "Internal Delensing of Cosmic Microwave Background Polarization B-Modes with the POLARBEAR Experiment," *Physical Review Letters*, vol. 124, p. 131301, Apr. 2020

D. Kaneko, S. Adachi, P. A. R. Ade, M. Aguilar Faúndez, Y. Akiba, K. Arnold, C. Baccigalupi, D. Barron,D. Beck, S. Beckman, F. Bianchini, D. Boettger, J. Borrill, J. Carron, S. Chapman, K. Cheung, Y. Chinone, K. Crowley, A. Cukierman, M. Dobbs, R. Dünner, H. El-Bouhargani, T. Elleflot, J. Errard, G. Fabbian, S. M.Feeney, C. Feng, T. Fujino, N. Galitzki, A. Gilbert, N. Goeckner-Wald, J. Groh, G. Hall, N. W. Halverson,T. Hamada, M. Hasegawa, M. Hazumi, C. A. Hill, L. Howe, Y. Inoue, G. Jaehnig, O. Jeong, N. Katayama,B. Keating, R. Keskitalo, S. Kikuchi, T. Kisner, N. Krachmalnicoff, A. Kusaka, A. T. Lee, D. Leon, E. Linder,L. N. Lowry, A. Mangu, F. Matsuda, Y. Minami, M. Navaroli, H. Nishino, J. Peloton, A. T. P. Pham,D. Poletti, G. Puglisi, C. L. Reichardt, C. Ross, Y. Segawa, M. Silva-Feaver, P. Siritanasak, N. Stebor,R. Stompor, A. Suzuki, O. Tajima, S. Takakura, S. Takatori, D. Tanabe, G. P. Teply, T. Tomaru, C. Tsai,C. Verges, B. Westbrook, and Y. Zhou, "Deployment of POLARBEAR-2A," *Journal of Low Temperature Physics*, vol. 199, pp. 1137Ð1147, Mar. 2020

Polarbear Collaboration, S. Adachi, M. A. O. Aguilar Faúndez, K. Arnold, C. Baccigalupi, D. Barron, D. Beck, S. Beckman, F. Bianchini, D. Boettger, J. Borrill, J. Carron, S. Chapman, K. Cheung, Y. Chinone, K. Crowley, A. Cukierman, M. Dobbs, H. El Bouhargani, T. Elleflot, J. Errard, G. Fabbian, C. Feng, T. Fujino, N. Galitzki, N. Goeckner-Wald, J. Groh, G. Hall, N. Halverson, T. Hamada, M. Hasegawa, M. Hazumi, C. A. Hill, L. Howe, Y. Inoue, G. Jaehnig, O. Jeong, D. Kaneko, N. Katayama, B. Keating, R. Keskitalo, S. Kikuchi, T. Kisner, N. Krachmalnicoff, A. Kusaka, A. T. Lee, D. Leon, E. Linder, L. N. Lowry, A. Mangu, F. Matsuda, Y. Minami, M. Navaroli, H. Nishino, A. T. P. Pham, D. Poletti, G. Puglisi, C. L. Reichardt, Y. Segawa, M. Silva-Feaver, P. Siritanasak, N. Stebor, R. Stompor, A. Suzuki, O. Tajima, S. Takakura, S. Takatori, D. Tanabe, G. P.Teply, C. Tsai, C. Verges, B. Westbrook, and Y. Zhou, "A Measurement of the Degree-scale CMB B-mode Angular Power Spectrum with POLARBEAR," *The Astrophysical Journal*, vol. 897, p. 55, July 2020

T. Elleflot, K. Arnold, D. Barron, K. T. Crowley, M. Dobbs, J. Groh, M. Hasegawa, M. Hazumi, C. Hill, L. Howe, J. Ito, O. Jeong, D. Kaneko, N. Katayama, B. Keating, A. Kusaka, A. T. Lee, L. N. Lowry, C. Raum, J. Seibert, M. Silva-Feaver, P. Siritanasak, A. Suzuki, S. Takakura, S. Takatori, C. Tsai, and B. Westbrook, "Effect of Stray Impedance in Frequency-Division Multiplexed Readout of TES Sensors in POLARBEAR-2b," *Journal of Low Temperature Physics*, vol. 199, pp. 840Ð848, Mar. 2020

F. Matsuda, L. Lowry, A. Suzuki, M. Aguilar Faúndez, K. Arnold, D. Barron, F. Bianchini, K. Cheung, Y. Chinone, T. Elleflot, G. Fabbian, N. Goeckner-Wald, M. Hasegawa, D. Kaneko, N. Katayama, B. Keating, A. T. Lee, M. Navaroli, H. Nishino, H. Paar, G. Puglisi, P. L. Richards, J. Seibert, P. Siritanasak, O. Tajima, S. Takatori, C. Tsai, and B. Westbrook, "The POLARBEAR Fourier transform spectrometer calibrator and spectroscopic characterization of the POLARBEAR instrument," *Review of Scientific Instruments*, vol. 90,p. 115115, Nov. 2019

T. Namikawa, Y. Chinone, H. Miyatake, M. Oguri, R. Takahashi, A. Kusaka, N. Katayama, S. Adachi, M. Aguilar, H. Aihara, A. Ali, R. Armstrong, K. Arnold, C. Baccigalupi, D. Barron, D. Beck, S. Beckman, F. Bianchini, D. Boettger, J. Borrill, K. Cheung, L. Corbett, K. T. Crowley, H. El Bouhargani, T. Elleflot, J. Errard, G. Fabbian, C. Feng, N. Galitzki, N. Goeckner-Wald, J. Groh,

T. Hamada, M. Hasegawa, M. Hazumi, C. A. Hill, L. Howe, O. Jeong, D. Kaneko, B. Keating, A. T. Lee, D. Leon, E. Linder, L. N.Lowry, A. Mangu, F. Matsuda, Y. Minami, S. Miyazaki, H. Murayama, M. Navaroli, H. Nishino, A. J. Nishizawa, A. T. P. Pham, D. Poletti, G. Puglisi, C. L. Reichardt, B. D. Sherwin, M. Silva-Feaver, P. Siritanasak, J. S. Speagle, R. Stompor, A. Suzuki, P. J. Tait, O. Tajima, M. Takada, S. Takakura, S. Takatori, D. Tanabe, M. Tanaka, G. P. Teply, C. Tsai, C. Verges, B. Westbrook, Y. Zhou, POLARBEAR COLLABORATION, and SUBARU HSC SSP Collaboration, "Evidence for the Cross-correlation between Cosmic Microwave Background Polarization Lensing from Polarbear and Cosmic Shear from Subaru Hyper Suprime-Cam," *The Astrophysical Journal*, vol. 882, p. 62, Sept. 2019

M. Aguilar Faúndez, K. Arnold, C. Baccigalupi, D. Barron, D. Beck, F. Bianchini, D. Boettger, J. Borrill, J. Carron, K. Cheung, Y. Chinone, H. El Bouhargani, T. Elleflot, J. Errard, G. Fabbian, C. Feng, N. Galitzki, N. Goeckner-Wald, M. Hasegawa, M. Hazumi, L. Howe, D. Kaneko, N. Katayama, B. Keating, N. Krachmalnicoff, A. Kusaka, A. T. Lee, D. Leon, E. Linder, L. N. Lowry, F. Matsuda, Y. Minami, M. Navaroli, H. Nishino, A. T. P. Pham, D. Poletti, G. Puglisi, C. L. Reichardt, B. D. Sherwin, M. Silva-Feaver, R. Stompor, A. Suzuki, O. Tajima, S. Takakura, S. Takatori, G. P. Teply, C. Tsai, C. Verges, and Polarbear Collaboration, "Cross-correlation of CMB Polarization Lensing with High-z Submillimeter Herschel-ATLAS Galaxies," *The Astrophysical Journal*, vol. 886, p. 38, Nov. 2019

B. Westbrook, P. A. R. Ade, M. Aguilar, Y. Akiba, K. Arnold, C. Baccigalupi, D. Barron, D. Beck, S. Beckman, A. N. Bender, F. Bianchini, D. Boettger, J. Borrill, S. Chapman, Y. Chinone, G. Coppi, K. Crowley, A. Cukierman, T. de Haan, R. Dunner, M. Dobbs, T. Elleflot, J. Errard, G. Fabbian, S. M. Feeney, C. Feng, G. Fuller, N. Galitzki, A. Gilbert, N. Goeckner-Wald, J. Groh, N. W. Halverson, T. Hamada, M. Hasegawa, M. Hazumi, C. A. Hill, W. Holzapfel, L. Howe, Y. Inoue, G. Jaehnig, A. Jaffe, O. Jeong, D. Kaneko, N. Katayama, B. Keating, R. Keskitalo, T. Kisner, N. Krachmalnicoff, A. Kusaka, M. Le Jeune, A. T. Lee, D. Leon, E. Linder, L. Lowry, A. Madurowicz, D. Mak, F. Matsuda, A. May, N. J. Miller, Y. Minami, J. Montgomery, M. Navaroli, H. Nishino, J. Peloton, A. Pham, L. Piccirillo, D. Plambeck, D. Poletti, G. Puglisi, C. Raum, G. Rebeiz, C. L.Reichardt, P. L. Richards, H. Roberts, C. Ross, K. M. Rotermund, Y. Segawa, B. Sherwin, M. Silva-Feaver, P. Siritanasak, R. Stompor, A. Suzuki, O. Tajima, S. Takakura, S. Takatori, D. Tanabe, R. Tat, G. P. Teply, A. Tikhomirov, T. Tomaru, C. Tsai, N. Whitehorn, and A. Zahn, "The POLARBEAR-2 and Simons Array Focal Plane Fabrication Status," *Journal of Low Temperature Physics*, vol. 193, pp. 758Ð770, Dec. 2018

P. Ade, J. Aguirre, Z. Ahmed, S. Aiola, A. Ali, D. Alonso, M. A. Alvarez, K. Arnold, P. Ashton, J. Austermann, H. Awan, C. Baccigalupi, T. Baildon, D. Barron, N. Battaglia, R. Battye, E. Baxter, A. Bazarko, J. A. Beall, R. Bean, D. Beck, S. Beckman, B. Beringue, F. Bianchini, S. Boada, D. Boettger, J. R. Bond, J. Borrill, M. L.Brown, S. M. Bruno, S. Bryan, E. Calabrese, V. Calafut, P. Calisse, J. Carron, A. Challinor, G. Chesmore, Y. Chinone, J. Chluba, H.-M. S. Cho, S. Choi, G. Coppi, N. F. Cothard, K. Coughlin, D. Crichton, K. D.Crowley, K. T. Crowley, A. Cukierman, J. M. DÕEwart, R. Dunner, T. de Haan, M. Devlin, S. Dicker, J. Didier, M. Dobbs, B. Dober, C. J. Duell, S. Duff, A. Duivenvoorden, J. Dunkley, J. Dusatko, J. Errard, G. Fabbian, S. Feeney, S. Ferraro, P. Fluxà, K. Freese, J. C. Frisch, A. Frolov, G. Fuller, B. Fuzia, N. Galitzki, P. A.

Gallardo, J. Tomas Galvez Ghersi, J. Gao, E. Gawiser, M. Gerbino, V. Gluscevic, N. Goeckner-Wald, J. Golec, S. Gordon, M. Gralla, D. Green, A. Grigorian, J. Groh, C. Groppi, Y. Guan, J. E. Gudmundsson, D. Han, P. Hargrave, M. Hasegawa, M. Hasselfield, M. Hattori, V. Haynes, M. Hazumi, Y. He, E. Healy, S. W. Henderson, C. Hervias-Caimapo, C. A. Hill, J. C. Hill, G. Hilton, M. Hilton, A. D. Hincks, G. Hinshaw,R. Hložek, S. Ho, S.-P. P. Ho, L. Howe, Z. Huang, J. Hubmayr, K. Huffenberger, J. P. Hughes, A. Ijjas, M. Ikape, K. Irwin, A. H. Jaffe, B. Jain, O. Jeong, D. Kaneko, E. D. Karpel, N. Katayama, B. Keating, S. S. Kernasovskiy, R. Keskitalo, T. Kisner, K. Kiuchi, J. Klein, K. Knowles, B. Koopman, A. Kosowsky, N. Krachmalnicoff, S. E. Kuenstner, C.-L. Kuo, A. Kusaka, J. Lashner, A. Lee, E. Lee, D. Leon, J. S. Y. Leung, A. Lewis, Y. Li, Z. Li, M. Limon, E. Linder, C. Lopez-Caraballo, T. Louis, L. Lowry, M. Lungu, M. Madhavacheril, D. Mak, F. Maldonado, H. Mani, B. Mates, F. Matsuda, L. Maurin, P. Mauskopf, A. May, N. McCallum, C. McKenney, J. McMahon, P. D. Meerburg, J. Meyers, A. Miller, M. Mirmelstein, K. Moodley, M. Munchmeyer, C. Munson, S. Naess, F. Nati, M. Navaroli, L. Newburgh, H. N. Nguyen, M. Niemack, H. Nishino, J. Orlowski-Scherer, L. Page, B. Partridge, J. Peloton, F. Perrotta, L. Piccirillo, G. Pisano, D. Poletti, R. Puddu, G. Puglisi, C. Raum, C. L. Reichardt, M. Remazeilles, Y. Rephaeli, D. Riechers, F. Rojas, A. Roy, S. Sadeh, Y. Sakurai, M. Salatino, M. Sathyanarayana Rao, E. Schaan, M. Schmittfull, N. Sehgal, J. Seibert, U. Seljak, B. Sherwin, M. Shimon, C. Sierra, J. Sievers, P. Sikhosana, M. Silva-Feaver, S. M. Simon, A. Sinclair, P. Siritanasak, K. Smith, S. R. Smith, D. Spergel, S. T. Staggs, G. Stein, J. R. Stevens, R. Stompor, A. Suzuki, O. Tajima, S. Takakura, G. Teply, D. B. Thomas, B. Thorne, R. Thornton, H. Trac, C. Tsai, C. Tucker, J. Ullom, S. Vagnozzi, A. van Engelen, J. Van Lanen, D. D. Van Winkle, E. M. Vavagiakis, C. Vergès, M. Vissers, K. Wagoner, S. Walker, J. Ward, B. Westbrook, N. Whitehorn, J. Williams, J. Williams, E. J. Wollack, Z. Xu, B. Yu, C. Yu, F. Zago, H. Zhang, N. Zhu, and Simons Observatory Collaboration, "The Simons Observatory: science goals and forecasts," *Journal of Cosmology and Astroparticle Physics*, vol. 2019, p. 056, Feb. 2019

S. Takakura, M. A. O. Aguilar-Faùndez, Y. Akiba, K. Arnold, C. Baccigalupi, D. Barron, D. Beck, F. Bianchini, D. Boettger, J. Borrill, K. Cheung, Y. Chinone, T. Elleflot, J. Errard, G. Fabbian, C. Feng, N. Goeckner-Wald, T. Hamada, M. Hasegawa, M. Hazumi, L. Howe, D. Kaneko, N. Katayama, B. Keating, R. Keskitalo, T. Kisner, N. Krachmalnicoff, A. Kusaka, A. T. Lee, L. N. Lowry, F. T. Matsuda, A. J. May, Y. Minami, M. Navaroli, H. Nishino, L. Piccirillo, D. Poletti, G. Puglisi, C. L. Reichardt, Y. Segawa, M. Silva-Feaver, P. Siritanasak, A. Suzuki, O. Tajima, S. Takatori, D. Tanabe, G. P. Teply, and C. Tsai, "Measurements of Tropospheric Ice Clouds with a Ground-based CMB Polarization Experiment, POLARBEAR," *The Astro-physical Journal*, vol. 870, p. 102, Jan. 2019

T. Elleflot, Y. Akiba, K. Arnold, J. Avva, D. Barron, A. N. Bender, A. Cukierman, T. de Haan, M. Dobbs, J. Groh, M. Hasegawa, M. Hazumi, W. Holzapfel, L. Howe, G. Jaehnig, B. Keating, A. Kusaka, A. T. Lee, L. Lowry, J. Montgomery, H. Nishino, C. Raum, K. M. Rotermund, M. Silva-Feaver, A. Suzuki, B. Westbrook, and N. Whitehorn, "Detector and Readout Assembly and Characterization for the Simons Array," *Journal of Low Temperature Physics*, vol. 193, pp. 1094Ð1102, Dec. 2018

L. Howe, C. Tsai, L. Lowry, K. Arnold, G. Coppi, J. Groh, X. Guo, B. Keating, A. Lee, A. J.

May, L. Piccirillo, N. Stebor, and G. Teply, "Design and characterization of the POLARBEAR-2b and POLARBEAR-2c cosmic microwave background cryogenic receivers," in *Millimeter, Submillimeter, and Far-Infrared Detectors and Instrumentation for Astronomy IX* (J. Zmuidzinas and J.-R. Gao, eds.), vol. 10708 of *Society of Photo-Optical Instrumentation Engineers (SPIE) Conference Series*, p. 107083W, July 2018

S. Takakura, M. Aguilar, Y. Akiba, K. Arnold, C. Baccigalupi, D. Barron, S. Beckman, D. Boettger, J. Borrill, S. Chapman, Y. Chinone, A. Cukierman, A. Ducout, T. Elleflot, J. Errard, G. Fabbian, T. Fujino, N. Galitzki, N. Goeckner-Wald, N. W. Halverson, M. Hasegawa, K. Hattori, M. Hazumi, C. Hill, L. Howe, Y. Inoue, A. H. Jaffe, O. Jeong, D. Kaneko, N. Katayama, B. Keating, R. Keskitalo, T. Kisner, N. Krachmalnicoff, A. Kusaka, A. T. Lee, D. Leon, L. Lowry, F. Matsuda, T. Matsumura, M. Navaroli, H. Nishino, H. Paar, J. Peloton, D. Poletti, G. Puglisi, C. L. Reichardt, C. Ross, P. Siritanasak, A. Suzuki, O. Tajima, S. Takatori, and G. Teply, "Performance of a continuously rotating half-wave plate on the POLARBEAR telescope," *Journal of Cosmology and Astroparticle Physics*, vol. 2017, p. 008, May 2017

D. Poletti, G. Fabbian, M. Le Jeune, J. Peloton, K. Arnold, C. Baccigalupi, D. Barron, S. Beckman, J. Borrill, S. Chapman, Y. Chinone, A. Cukierman, A. Ducout, T. Elleflot, J. Errard, S. Feeney, N. Goeckner-Wald, J. Groh, G. Hall, M. Hasegawa, M. Hazumi, C. Hill, L. Howe, Y. Inoue, A. H. Jaffe, O. Jeong, N. Katayama, B. Keating, R. Keskitalo, T. Kisner, A. Kusaka, A. T. Lee, D. Leon, E. Linder, L. Lowry, F. Matsuda, M. Navaroli, H. Paar, G. Puglisi, C. L. Reichardt, C. Ross, P. Siritanasak, N. Stebor, B. Steinbach, R. Stompor, A. Suzuki, O. Tajima, G. Teply, and N. Whitehorn, "Making maps of cosmic microwave background polarization for B-mode studies: the POLARBEAR example," *Astronomy and Astrophysics*, vol. 600, p. A60,Apr. 2017

POLARBEAR Collaboration, P. A. R. Ade, M. Aguilar, Y. Akiba, K. Arnold, C. Baccigalupi, D. Barron,D. Beck, F. Bianchini, D. Boettger, J. Borrill, S. Chapman, Y. Chinone, K. Crowley, A. Cukierman, R. Dunner, M. Dobbs, A. Ducout, T. Elleflot, J. Errard, G. Fabbian, S. M. Feeney, C. Feng, T. Fujino, N. Galitzki, A. Gilbert, N. Goeckner-Wald, J. C. Groh, G. Hall, N. Halverson, T. Hamada, M. Hasegawa, M. Hazumi, C. A. Hill, L. Howe, Y. Inoue, G. Jaehnig, A. H. Jaffe, O. Jeong, D. Kaneko, N. Katayama, B. Keating, R. Keskitalo, T. Kisner, N. Krachmalnicoff, A. Kusaka, M. Le Jeune, A. T. Lee, E. M. Leitch, D. Leon, E. Linder, L. Lowry, F. Matsuda, T. Matsumura, Y. Minami, J. Montgomery, M. Navaroli, H. Nishino, H. Paar, J. Peloton, A. T. P. Pham, D. Poletti, G. Puglisi, C. L. Reichardt, P. L. Richards, C. Ross, Y. Segawa, B. D. Sherwin, M. Silva-Feaver, P. Siritanasak, N. Stebor, R. Stompor, A. Suzuki, O. Tajima, S. Takakura, S. Takatori, D. Tanabe, G. P. Teply, T. Tomaru, C. Tucker, N. Whitehorn, and A. Zahn, "A Measurement of the Cosmic Microwave Background B-mode Polarization Power Spectrum at Subdegree Scales from Two Years of POLARBEAR Data," *The Astrophysical Journal*, vol. 848, p. 121, Oct. 2017

N. Stebor, P. Ade, Y. Akiba, C. Aleman, K. Arnold, C. Baccigalupi, B. Barch, D. Barron, S. Beckman, A. Bender, D. Boettger, J. Borrill, S. Chapman, Y. Chinone, A. Cukierman, T. de Haan, M. Dobbs, A. Ducout, R. Dunner, T. Elleflot, J. Errard, G. Fabbian, S. Feeney, C. Feng, T. Fujino, G. Fuller, A. J. Gilbert, N. Goeckner-Wald, J. Groh, G. Hall, N. Halverson, T. Hamada,

M. Hasegawa, K. Hattori, M. Hazumi, C. Hill, W. L. Holzapfel, Y. Hori, L. Howe, Y. Inoue, F. Irie, G. Jaehnig, A. Jaffe, O. Jeong, N. Katayama, J. P. Kaufman, K. Kazemzadeh, B. G. Keating, Z. Kermish, R. Keskitalo, T. Kisner, A. Kusaka, M. Le Jeune, A. T. Lee, D. Leon, E. V. Linder, L. Lowry, F. Matsuda, T. Matsumura, N. Miller, J. Montgomery, M. Navaroli, H. Nishino, H. Paar, J. Peloton, D. Poletti, G. Puglisi, C. R. Raum, G. M. Rebeiz, C. L. Reichardt, P. L. Richards, C. Ross, K. M. Rotermund, Y. Segawa, B. D. Sherwin, I. Shirley, P. Siritanasak, L. Steinmetz, R. Stompor, A. Suzuki, O. Tajima, S. Takada, S. Takatori, G. P. Teply, A. Tikhomirov, T. Tomaru, B. Westbrook, N. Whitehorn, A. Zahn, and O. Zahn, "The Simons Array CMB polarization experiment," in *Millimeter, Submillimeter, and Far-Infrared Detectors and Instrumentation for Astronomy VIII* (W. S.Holland and J. Zmuidzinas, eds.), vol. 9914 of *Society of Photo-Optical Instrumentation Engineers (SPIE) Conference Series*, p. 99141H, July 2016

A. Suzuki, P. Ade, Y. Akiba, C. Aleman, K. Arnold, C. Baccigalupi, B. Barch, D. Barron, A. Bender, D. Boettger, J. Borrill, S. Chapman, Y. Chinone, A. Cukierman, M. Dobbs, A. Ducout, R. Dunner, T. Elleflot, J. Errard, G. Fabbian, S. Feeney, C. Feng, T. Fujino, G. Fuller, A. Gilbert, N. Goeckner-Wald, J. Groh, T. D. Haan, G. Hall, N. Halverson, T. Hamada, M. Hasegawa, K. Hattori, M. Hazumi, C. Hill, W. Holzapfel, Y. Hori, L. Howe, Y. Inoue, F. Irie, G. Jaehnig, A. Jaffe, O. Jeong, N. Katayama, J. Kaufman, K. Kazemzadeh, B. Keating, Z. Kermish, R. Keskitalo, T. Kisner, A. Kusaka, M. L. Jeune, A. Lee, D. Leon, E. Linder, L. Lowry, F. Matsuda, T. Matsumura, N. Miller, K. Mizukami, J. Montgomery, M. Navaroli, H. Nishino, J. Peloton, D. Poletti, G. Puglisi, G. Rebeiz, C. Raum, C. Reichardt, P. Richards, C. Ross, K. Rotermund, Y. Segawa, B. Sherwin, I. Shirley, P. Siritanasak, N. Stebor, R. Stompor, J. Suzuki, O. Tajima, S. Takada, S. Takakura, S. Takatori, A. Tikhomirov, T. Tomaru, B. Westbrook, N. Whitehorn, T. Yamashita, A. Zahn, and O. Zahn, "The Polarbear-2 and the Simons Array Experiments," *Journal of Low Temperature Physics*, vol. 184, pp. 805Ð810, Aug. 2016

Y. Inoue, P. Ade, Y. Akiba, C. Aleman, K. Arnold, C. Baccigalupi, B. Barch, D. Barron, A. Bender, D. Boettger, J. Borrill, S. Chapman, Y. Chinone, A. Cukierman, T. de Haan, M. A. Dobbs, A. Ducout, R. Dunner, T. Elleflot, J. Errard, G. Fabbian, S. Feeney, C. Feng, G. Fuller, A. J. Gilbert, N. Goeckner-Wald, J. Groh, G. Hall, N. Halverson, T. Hamada, M. Hasegawa, K. Hattori, M. Hazumi, C. Hill, W. L. Holzapfel, Y. Hori, L. Howe, F. Irie, G. Jaehnig, A. Jaffe, O. Jeong, N. Katayama, J. P. Kaufman, K. Kazemzadeh, B. G.Keating, Z. Kermish, R. Keskitalo, T. S. Kisner, A. Kusaka, M. Le Jeune, A. T. Lee, D. Leon, E. V. Linder, L. Lowry, F. Matsuda, T. Matsumura, N. Miller, K. Mizukami, J. Montgomery, M. Navaroli, H. Nishino, H. Paar, J. Peloton, D. Poletti, G. Puglisi, C. R. Raum, G. M. Rebeiz, C. L. Reichardt, P. L. Richards, C. Ross, K. M. Rotermund, Y. Segawa, B. D. Sherwin, I. Shirley, P. Siritanasak, N. Stebor, R. Stompor, J. Suzuki, A. Suzuki, O. Tajima, S. Takada, S. Takatori, G. P. Teply, A. Tikhomirov, T. Tomaru, N. Whitehorn, A. Zahn, and O. Zahn, "POLARBEAR-2: an instrument for CMB polarization measurements," in *Millimeter, Submillimeter, and Far-Infrared Detectors and Instrumentation for Astronomy VIII* (W. S. Hollandand J. Zmuidzinas, eds.), vol. 9914 of *Society of Photo-Optical Instrumentation Engineers (SPIE) Conference Series*, p. 99141I, July 2016

P. A. R. Ade, K. Arnold, M. Atlas, C. Baccigalupi, D. Barron, D. Boettger, J. Borrill, S. Chapman, Y. Chinone, A. Cukierman, M. Dobbs, A. Ducout, R. Dunner, T. Elleflot, J. Errard, G. Fabbian, S.

Feeney, C. Feng, A. Gilbert, N. Goeckner-Wald, J. Groh, G. Hall, N. W. Halverson, M. Hasegawa, K. Hattori, M. Hazumi, C. Hill, W. L. Holzapfel, Y. Hori, L. Howe, Y. Inoue, G. C. Jaehnig, A. H. Jaffe, O. Jeong, N. Katayama,J. P. Kaufman, B. Keating, Z. Kermish, R. Keskitalo, T. Kisner, A. Kusaka, M. Le Jeune, A. T. Lee, E. M. Leitch, D. Leon, Y. Li, E. Linder, L. Lowry, F. Matsuda, T. Matsumura, N. Miller, J. Montgomery, M. J. Myers, M. Navaroli, H. Nishino, T. Okamura, H. Paar, J. Peloton, L. Pogosian, D. Poletti, G. Puglisi, C. Raum, G. Rebeiz, C. L. Reichardt, P. L. Richards, C. Ross, K. M. Rotermund, D. E. Schenck, B. D. Sherwin, M. Shimon, I. Shirley, P. Siritanasak, G. Smecher, N. Stebor, B. Steinbach, A. Suzuki, J.-i. Suzuki, O. Tajima, S. Takakura, A. Tikhomirov, T. Tomaru, N. Whitehorn, B. Wilson, A. Yadav, A. Zahn, O. Zahn, and Polarbear Collaboration, "POLARBEAR constraints on cosmic birefringence and primordial magnetic fields," *Physical Review D*, vol. 92, p. 123509, Dec. 2015

T. Essinger-Hileman, A. Ali, M. Amiri, J. W. Appel, D. Araujo, C. L. Bennett, F. Boone, M. Chan, H.-M. Cho, D. T. Chuss, F. Colazo, E. Crowe, K. Denis, R. Dunner, J. Eimer, D. Gothe, M. Halpern, K. Harrington, G. C. Hilton, G. F. Hinshaw, C. Huang, K. Irwin, G. Jones, J. Karakla, A. J. Kogut, D. Larson, M. Limon, L. Lowry, T. Marriage, N. Mehrle, A. D. Miller, N. Miller, S. H. Moseley, G. Novak, C. Reintsema, K. Rostem, T. Stevenson, D. Towner, K. U-Yen, E. Wagner, D. Watts, E. J. Wollack, Z. Xu, and L. Zeng, "CLASS: the cosmology large angular scale surveyor," in *Millimeter, Submillimeter, and Far-Infrared Detectors and Instrumentation for Astronomy VII* (W. S. Holland and J. Zmuidzinas, eds.), vol. 9153 of *Society of Photo-Optical Instrumentation Engineers (SPIE) Conference Series*, p. 91531I, July 2014

J. W. Appel, A. Ali, M. Amiri, D. Araujo, C. L. Bennett, F. Boone, M. Chan, H.-M. Cho, D. T. Chuss, F. Colazo, E. Crowe, K. Denis, R. Dunner, J. Eimer, T. Essinger-Hileman, D. Gothe, M. Halpern, K. Harrington, G. Hilton, G. F. Hinshaw, C. Huang, K. Irwin, G. Jones, J. Karakla, A. J. Kogut, D. Larson, M. Limon, L. Lowry, T. Marriage, N. Mehrle, A. D. Miller, N. Miller, S. H. Moseley, G. Novak, C. Reintsema, K. Rostem, T. Stevenson, D. Towner, K. U-Yen, E. Wagner, D. Watts, E. Wollack, Z. Xu, and L. Zeng, "The cosmology large angular scale surveyor (CLASS): 38-GHz detector array of bolometric polarimeters," in *Millimeter, Submillimeter, and Far-Infrared Detectors and Instrumentation for Astronomy VII* (W. S. Hollandand J. Zmuidzinas, eds.), vol. 9153 of *Society of Photo-Optical Instrumentation Engineers (SPIE) Conference Series*, p. 91531J, July 2014

ABSTRACT OF THE DISSERTATION

Preparation and Deployment of the Telescopes and POLARBEAR-2b Receiver for the Simons Array Cosmic Microwave Background Polarization Experiment

by

Lindsay Ng Lowry

Doctor of Philosophy in Physics

University of California San Diego, 2021

Professor Brian Keating, Chair

The Simons Array is a polarization-sensitive cosmic microwave background (CMB) experiment located in the Atacama Desert in northern Chile. Observations of the CMB, which consists of the oldest observable light in the universe, have been invaluable for cosmological research in recent decades, producing a wealth of information regarding the universe's beginning and evolution, and providing substantial evidence in support of the Lambda-Cold Dark Matter model of cosmology. The field continues to grow as technological advances enable ever more sensitive measurements of both the intensity and polarization patterns imprinted in the CMB. The Simons Array aims to further our understanding of cosmology by measuring the polarization

pattern of the CMB at angular scales ranging from a few arcminutes to a few degrees, with a focus on the faint *B*-mode polarization signals predicted at these scales.

The Simons Array is composed of three identical telescopes, each coupled to a cryogenic receiver. The receivers are developed and characterized in laboratories before installation at the observatory site in Chile at an altitude of 5,200 m, with significant upgrades compared to POLARBEAR-1, the Simons Array's predecessor, to improve the experiment's sensitivity. In particular, the upgraded receivers employ larger focal planes with increased detector counts and sensitivity across multiple frequency bands. This dissertation describes the Simons Array experiment as a whole, with an emphasis on the telescope accessories and laboratory characterization of the POLARBEAR-2b receiver, the second receiver of the Simons Array.

Chapter 1

Introduction

1.1 The Lambda-CDM Universe

The current widely held cosmological understanding is that the universe follows a Lambda-Cold Dark Matter (Lambda-CDM or ΛCDM) model. As with other Big Bang cosmological models, the ΛCDM universe began in an extremely hot and dense state and has been expanding and cooling ever since, with the evolution of the universe following the theory of general relativity. Earlier descriptions of the universe relied entirely on known baryonic matter (protons and neutrons) and electromagnetic radiation (photons) to make up all the energy in the universe, but these descriptions were found to be insufficient as astrophysical data regarding the formation of galaxies [2], anisotropies in the cosmic microwave background [3], and the expansion rate of the current universe [4] became available. These findings illuminated the need for a cosmological model that includes not-yet-known physics to account for the additional apparent gravitational force in structures in the universe and for the accelerating expansion despite these gravitational forces opposing it. In ΛCDM, these come in the form of cold (non-relativistic) dark matter and dark energy represented by a cosmological constant, Λ. Although the specific nature of dark matter and dark energy are not yet understood [5, 6], their basic properties are incorporated into

and predicted by the ΛCDM model.

The ΛCDM model is based on six main parameters [7]: physical baryon density ($\Omega_b h^2$), physical dark matter density ($\Omega_c h^2$), age of the universe (t_0), amplitude of the initial fluctuations (Δ_R^2), scalar spectral index (n_s), and reionization optical depth (τ). Despite its simplicity, the ΛCDM model has been shown to match extremely well to a diverse set of cosmological data. Perhaps the best illustration of its success is from studies of the cosmic microwave background, the primary focus of this work.

1.2 The Cosmic Microwave Background

1.2.1 Formation and Characteristics of the CMB

The universe is 13.8 billion years old [8] and has evolved through many phases since its beginning. In very early times, the universe containing radiation, matter (dark and baryonic), and dark energy, is hot and dense and immediately begins expanding and cooling. As this happens, the energies of the particles in the universe decrease and their interactions consequently evolve.

For example, once the universe has cooled to an average particle energy of about 1 MeV, neutrinos, which are electrically neutral elementary particles that interact with other particles only through gravity and the weak force, decouple from baryonic matter as the rate of these weak interactions drops below the rate of expansion of the universe. This occurs at a time of around $t = 1$ s (where $t = 0$ represents the beginning of the universe in this model) [9]. Big Bang nucleosynthesis, the period in the early universe during which nuclei (predominantly helium-4, with small amounts of deuterium, helium-3, and lithium) formed, occurs soon after neutrino decoupling, on the order of minutes after $t = 0$ [9]. As we move much further in time, we see the formation of the first stars and galaxies after a few hundred million years [10], which then evolve further to form galactic clusters and superclusters a few billion years later and provide the basis for what we see today, at $t_0 = 13.8$ billion years, as we observe the structure of our universe. One

crucial epoch not mentioned above is that known as recombination, the time in the universe's history during which the cosmic microwave background (CMB) was formed.

Recombination (an unfortunately misleading term for the epoch, at least when considering a ΛCDM model for the universe) refers to the time when the universe has cooled enough for neutral hydrogen (a proton bound to an electron) to form without a photon immediately ionizing the atom. Before this time, free electrons are ubiquitous in the universe and constantly interact with photons, primarily through Thomson scattering. These electromagnetic interactions between photons and electrons effectively make the universe opaque at these early times, as the mean-free path of a photon is extremely short. However, once neutral hydrogen forms and removes this prevalence of free electrons, the photons are able to free-stream. This radiation, which has redshifted as the universe has expanded, now has wavelengths corresponding to the microwave regime of the electromagnetic spectrum and we can observe it from all directions, permeating our universe even today. Recombination occurred once the universe had cooled to energies of about 1 eV, at $t \approx 380{,}000$ years. This is well after neutrino decoupling and Big Bang nucleosynthesis, but much before the formation of large-scale structure through gravitational collapse.

The CMB surrounds us, and measurements of its properties can be made at every point on a sphere surrounding the earth. Spectroscopic measurements from the FIRAS instrument on the Cosmic Background Explorer (COBE) satellite which launched in 1989 show that CMB radiation matches extremely well to that of a blackbody, as expected from Big Bang cosmological models. The data show the blackbody temperature of the CMB to be 2.725 K [11], corresponding to a peak intensity at a frequency of approximately 160 GHz (a wavelength of approximately 2 mm). A frequency spectrum for a blackbody of this temperature is shown in Figure 1.1.

In addition to the CMB resembling a perfect blackbody, it has also been found to be extremely uniform across the sky. Full-sky intensity measurements from satellite experiments show the CMB temperature to be the same across the sky to better than one part in 10^4 K [1]. Notably, the uniformity of the CMB persists even across regions of the sky never expected to

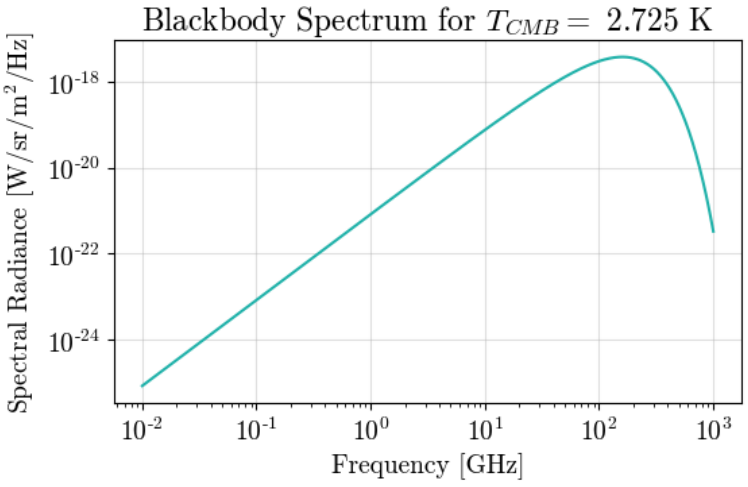

Figure 1.1: Spectrum for a perfect blackbody of temperature 2.725 K. Data from the COBE satellite indicate CMB radiation corresponds to that of a near perfect blackbody at this temperature.

have been in causal contact with each other. This is known as the horizon problem, which is the observation that since information travels at a finite speed (no faster than the speed of light), the age of the universe is not a sufficient amount of time for CMB radiation on patches of the sky separated by more than about 2° to have exchanged information by the time of recombination, and therefore no reason for us to observe these patches as having the same characteristic blackbody temperature.

The leading theory for a resolution to the horizon problem (and other early-universe quandaries) is that of inflation, which extends the ΛCDM theory of the universe to include a brief period of superluminal expansion during the first fraction of a second after the universe's beginning [12, 13]. In this paradigm, the universe begins in a state in which everything in our observable universe is in causal contact. The inflationary period, driven in most theories by a scalar field known as the inflaton [9], then expands space so rapidly as to seemingly bring different regions of the universe out of causal contact based on calculations of the regions' light cones.

The inflationary paradigm also provides a mechanism for producing the (extremely small,

but statistically significant) anisotropies that we do see in maps of the CMB [9, 14]. Quantum fluctuations in the scalar inflaton field would imprint themselves on the universe, appearing as small anisotropies in the CMB and providing the seeds for structure formation from gravitational instability [15]. These fluctuations are referred to as scalar or density perturbations to the spacetime metric.

1.2.2 Measuring the CMB Temperature Anisotropies

Since the CMB was emitted at such an early time in the universe's history, measurements of its properties, including anisotropies potentially sourced during inflation, are crucial tools in furthering our understanding of what the universe was like in early times and how it has evolved. The primary way in which the CMB has been studied is to make maps of its intensity at points across the full sky, and then to measure the statistical properties and compare them to predictions from the ΛCDM model.

CMB Temperature Maps

Maps of the CMB are made by measuring CMB properties at points on the celestial sphere. Full-sky CMB maps are generally shown as projections of this sphere in 2D in galactic coordinates, where the plane of the galaxy lies along the equator, with color maps to depict the relative value of the desired parameter across the sky. Maps of CMB intensity are referred to as temperature maps. Because CMB radiation is in the form of a blackbody, increases in intensity at a given observational frequency correspond directly to increases in temperature.

CMB temperature maps have been created since the first large scale measurements of the CMB were made with the COBE satellite [3]. Since then, two other satellites, the Wilkinson Microwave Anisotropy Probe (WMAP) [16], and the Planck satellite [1], have also produced full-sky maps of CMB temperature, each with increasing resolution and sensitivity. A full-sky temperature map made using the most recent data from Planck is shown in Figure 1.2.

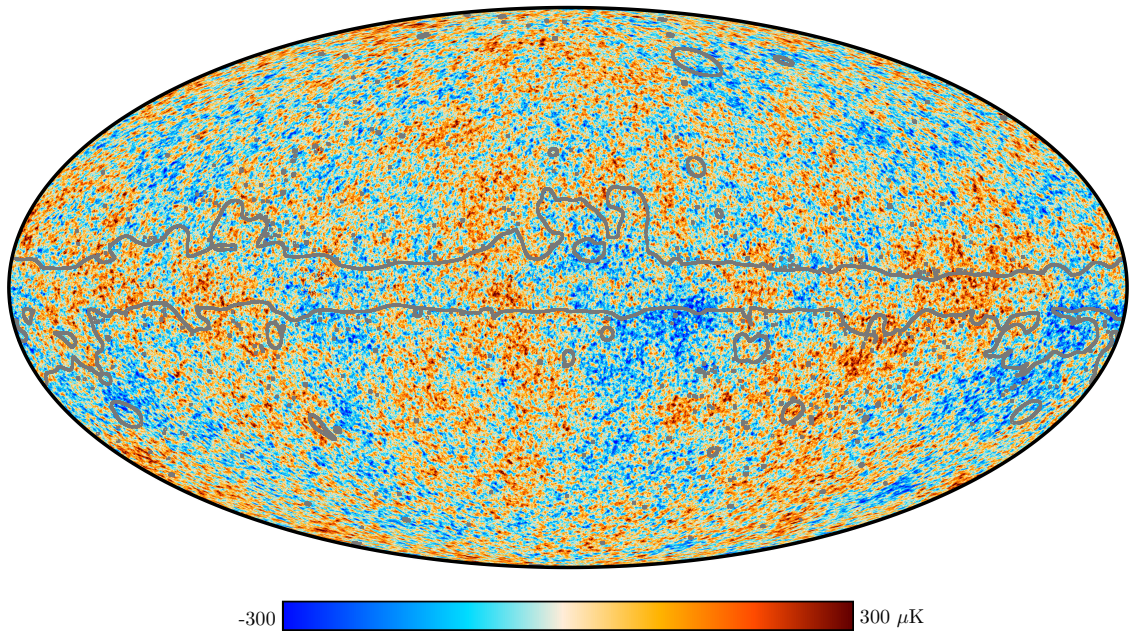

Figure 1.2: CMB full-sky temperature map with data from the Planck satellite from Planck Collaboration, 2020 [1]. Colors indicate the small fluctuations in temperature across the sky. The gray lines indicate the masked region where foreground emission, primarily from galactic sources, is more significant.

Maps are shown with the mean CMB temperature subtracted such that only the fluctuations about the mean are shown, and after removal of a dipole component introduced in the CMB as viewed from earth as a result of our galaxy's motion. Recent maps also account for and subtract out galactic emission based on models.

CMB temperature maps have also been made using data from ground-based experiments. Individual ground-based experiments are not able to observe the full sky, and therefore generally produce temperature maps of much smaller patches. As will be discussed, these maps still contribute to the analysis of the statistical properties of the CMB, and often have greater sensitivity and finer resolution than maps from satellite experiments [17].

CMB Power Spectra

In order to quantitatively analyze the statistical properties of the CMB and compare the observations to models of the universe, we transform the measured map data into power spectra which indicate the relative amounts of signal at different scales. For one-dimensional data, the corresponding power spectrum can be obtained by performing a Fourier transform on the data, decomposing it into a series of sine waves with distinct frequencies and determining the relative amplitudes. For two-dimensional data on a sphere, as in the case of CMB temperature maps, the data can be decomposed into a set of spherical harmonics as

$$T(\hat{n}) = \sum_{\ell m} a_{\ell m} Y_{\ell m}(\hat{n}), \tag{1.1}$$

where $\hat{n}$ represents the point on the sphere, $T(\hat{n})$ is the measured parameter at each point, and $a_{\ell m}$ represents the amplitude of the corresponding spherical harmonic. From this decomposition, the power spectrum is calculated as[1]

$$C_\ell = \frac{1}{2\ell+1} \sum_m a_{\ell m} a^*_{\ell m}, \tag{1.2}$$

where * indicates the complex conjugate. If the CMB is statistically isotropic, as expected based on the cosmological principle, the directional dependence encoded in the m index of the spherical harmonics should vanish, and we can evaluate properties of CMB based only on this power spectrum.

When applied to CMB temperature maps, the spherical harmonic decomposition forms a power spectrum with characteristic peaks and troughs as seen in Figure 1.3, which shows the CMB temperature power spectrum calculated using data from the Planck satellite. In this figure, the data extracted from the CMB temperature maps are in red and the blue line indicates the ΛCDM model

[1] Note that power spectra are often presented using the quantity $D_\ell = \ell(\ell+1)C_\ell/2\pi$.

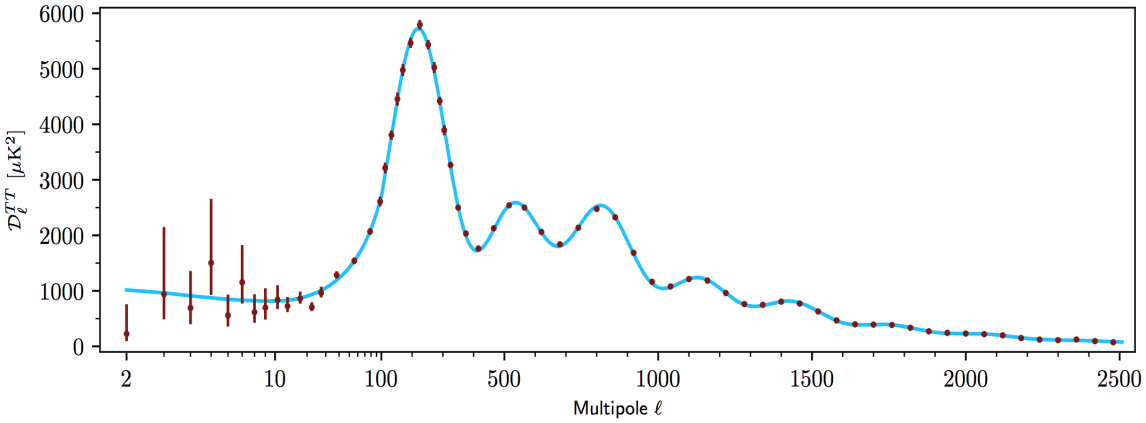

Figure 1.3: CMB temperature power spectrum from the Planck satellite from Planck Collaboration, 2020 [1]. Red points indicate the data while the blue line indicates the Planck 2018 best-fit ΛCDM model.

with best-fit parameters. The model is shown to be a very good fit to the data [1], further supporting the ΛCDM model of the universe and imposing tight constraints on the model parameters that help us to better understand the physical properties of the early universe. For example, the peaks in the spectrum correspond to oscillations in the photon-baryon fluid (known as acoustic oscillations) at frequencies that had reached maximum compression at the time of photon decoupling (last scattering). The first peak corresponds to the oscillation mode that had time to undergo exactly one compression, and later peaks corresponds to harmonics of this oscillation mode [18]. The location of this first peak in the CMB temperature power spectrum therefore depends on the time to recombination, the sound speed of the photon-baryon fluid, and the curvature of the universe. Precise measurements of the CMB power spectrum, including those represented in Figure 1.3, indicate the first peak corresponds to multipole moment $\ell \approx 200$ (angular separations on the order of one degree), consistent with a flat universe[2] [1, 19, 20]. Impacts from other cosmological parameters on the temperature power spectrum include increasing or decreasing the relative peak heights, influencing the peak spacing, and damping the power spectrum at small angular scales [9].

[2]The "flatness" problem is also something thought to be solved by the inflationary model.

1.3 Polarization of the CMB

While much can be learned about the universe from CMB temperature maps and power spectra, further information is contained in the faint polarization signal within the CMB. The polarization signal is orders of magnitude smaller than the temperature anisotropy signal, making it much more difficult to measure. However, having made increasingly more precise measurements of the temperature spectrum over the past few decades, much of the focus of the CMB community has shifted toward polarization. Some of the mechanisms for producing and examining this polarization signal in the CMB are discussed, with a focus on what is known as *B*-mode polarization.

1.3.1 Polarization of Light

Polarization of light corresponds to the orientation of a light wave's electric field. A light wave is said to be linearly polarized in a particular direction if the electric field oscillates in a single plane, and circularly or elliptically polarized if the orientation of the electric field oscillations rotates about the wave's direction of propagation. A light source emitting many photons can be fully polarized in which all photons exhibit the same polarization, unpolarized in which the number of photons of any given polarization state is equal to that of all other polarization states, or partially polarized in which there is a preferred polarization state.

Polarization can be parameterized using the Stokes parameters, I, Q, U, and V. I represents the total intensity of the light, Q and U describe the amount of linear polarization along axes rotated 45° with respect to one another, and V describes the amount of circular polarization. Elliptical polarization is represented as a combination of linear and circular polarization. The polarization fraction is calculated as

$$p = \frac{\sqrt{Q^2 + U^2 + V^2}}{I}, \tag{1.3}$$

and $0 < p < 1$ corresponds to partially polarized light.

In the case of the CMB, theory predicts a small amount of linear polarization and many current CMB experiments are designed to be sensitive to this signal[3]. As with temperature, maps can be made of CMB linear polarization by plotting the values of the Q and U Stokes parameters at every point on the sky. However, one problem with the Stokes formalism is that it is coordinate-system dependent, as Q and U must be referenced to some specified directions. Thus, statistical analysis of CMB polarization in the same way as was done for temperature requires a change of basis to one that is independent of coordinate system choice. This is typically done by converting Q and U information into information on E-modes and B-modes [22], illustrated in Figure 1.4. Once the CMB polarization is described in this new, rotationally invariant basis, power spectra of the two polarization modes can be computed and analyzed.

Describing CMB polarization patterns using E- and B-modes has the added benefit of enabling a more intuitive interpretation of the formation of polarization in the CMB. E-modes are curl-free and have even parity, while B-modes are divergence-free and have odd parity. The type of symmetry characteristic of a given polarization pattern is determined by the physical mechanism that produced it, and physical processes that produce E-modes are distinct from those that produce B-modes. The two power spectra therefore reveal different cosmological information.

1.3.2 CMB Polarization from Density Perturbations

One source of CMB polarization is the same set of metric perturbations that create the temperature anisotropies. When quantum fluctuations in the early universe create hot and cold spots in the temperature of the photons in the fluid, electrons off which the photons scatter can see a quadrupole moment with hot (higher energy) photons incident from one direction and cold

[3]The Cosmology Large Angular Scale Surveyor, a CMB polarization experiment, includes a polarization modulator which makes it sensitive to circular polarization as well and has been used to measure circularly polarized atmospheric emission [21].

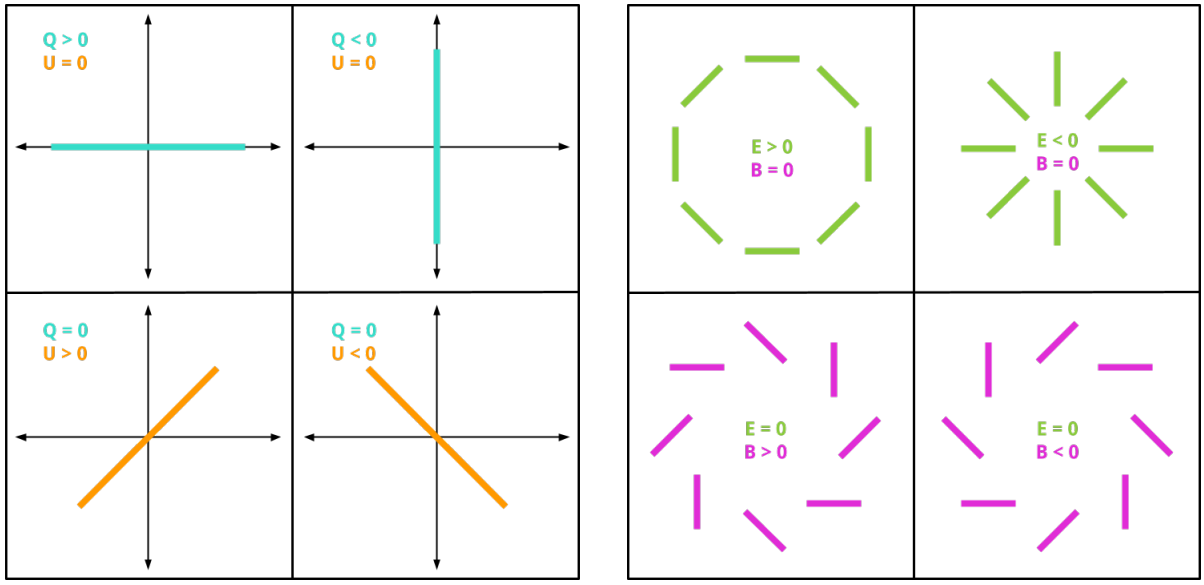

(a) Illustration of linear polarization states described by Stokes Q and U parameters.

(b) Illustration of linear polarization states described by E- and B-modes.

Figure 1.4: Illustrations of two bases with which to describe patterns of linearly polarized light. Figure (a) illustrates polarization states described by various combinations of Stokes Q and U parameters. Values of these Stokes parameters depend on the choice of coordinate system shown in black, where Stokes Q corresponds to light polarized along the coordinate system axes and Stokes U corresponds to light polarized along axes rotated by 45°. Combinations of $Q \neq 0$ and $U \neq 0$ produce linearly polarized light at different angles. Figure (b) illustrates polarization states described by combinations of E-modes and B-modes. The polarization of a single light wave cannot be represented as a combination of E- and B-modes, but maps of linear polarization states can. E-modes correspond to polarization patterns that have even parity, while B-modes correspond to polarization patterns that odd parity. A description of a polarization pattern in terms of E- and B-modes does not depend on choice of coordinate system.

(lower energy) photons incident from another. In this environment, the interacting electron will be accelerated preferentially along one axis, emitting polarized light. The scalar perturbations that produce the temperature anisotropies, however, are only able to produce the even-parity E-mode polarization pattern [22]. Thus the E-mode power spectrum, and the power spectrum correlating the temperature fluctuations to the E-mode pattern (known as the TE spectrum), are important in confirming our understanding of the temperature anisotropies with respect to the ΛCDM model and the physical mechanisms thought to produce it. Models of the temperature and E-mode power spectra arising from these types of perturbations are shown in Figure 1.5. The

E-mode signal, however, is significantly fainter than the corresponding temperature anisotropy.

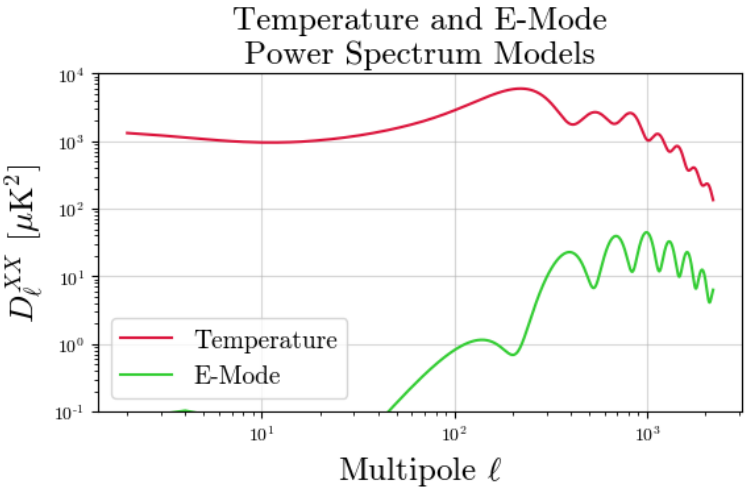

Figure 1.5: Theoretical temperature and E-mode power spectra. Acoustic peaks arising from primordial density perturbations can be seen in both spectra. The E-mode polarization signal, however, is much fainter than the corresponding temperature anisotropy. Data for the theoretical curves were simulated using the CAMB online software tool, using fiducial values for all parameters and ignoring power from gravitational lensing [23, 24].

1.3.3 CMB Polarization from Gravitational Lensing

Gravitational lensing is another mechanism by which power can appear in the E- and B-mode power spectra. Unlike density perturbations, however, gravitational lensing is not a mechanism for producing polarization in the early universe, and anisotropies from gravitational lensing are thus known as secondary anisotropies rather than primary anisotropies. Instead, lensing impacts the polarization spectra by re-mapping already polarized CMB radiation (consequently converting observed E-mode power into B-mode power, and vice versa), causing the polarized radiation to appear to earth observers as originating from one direction on the sky while the true (primordial) signal would show it coming from a slightly shifted direction, i.e.

$$X_{obs}(\hat{n}) = X_{true}(\hat{n} + \vec{d}(\hat{n})) \tag{1.4}$$

where X_{obs} is the observed parameter, X_{true} is the primordial signal, and $\vec{d}$ represents the deflection of photons originating from a given direction. This re-mapping from gravitational lensing occurs due to the presence of intervening matter between earth today and the surface of last scattering. Large scale structures composed mostly of dark matter distort the paths CMB photons as they free-stream toward earth, shifting the observed pattern relative to the true pattern and influencing the resulting power spectra. $\vec{d}(\hat{n})$ is thus related to what is known as the lensing potential, $\phi(\hat{n})$, which describes the angular distribution of this large scale structure in the universe by specifying the integrated gravitational potential along a line of sight. Gravitational lensing impacts both temperature and polarization measurements, but we focus here on its influence on polarization.

As discussed, density perturbations in the early universe produce the most prevalent polarization signal in the CMB. This is in the form of E-mode polarization at angular scales peaking around $\ell \approx 1000$ [25, 26]. The corresponding B-mode polarization signal resulting from gravitational lensing thus peaks at these same angular scales. As we will see in Section 1.3.4, our current cosmological models do not include mechanisms for producing primary B-mode polarization at angular scales this small. However, the lensing signal in the B-mode power spectrum extends to lower ℓ values as well, where modern theories do predict a very faint primordial B-mode signal. Therefore it is crucial that we are able to discern effects due to gravitational lensing from those signals of primordial origin if we want to accurately make conclusions about the early universe.

In this way, the existence of these secondary anisotropies from gravitational lensing obscures our view of the desired early universe signals. Luckily, however, there are procedures for de-lensing, or extracting the primordial signal, due to the expected isotropy and Gaussianity of the primordial perturbations. Gravitational lensing produces correlations between angular scales that would not otherwise exist, and this effect can be exploited to determine the lensing potential [27, 28]. Not only does this reconstruction of ϕ allow us to extract the primordial polarization signals, it enables better understanding of the matter distribution in the universe and can help

to constrain the sum of the neutrino masses [29]. Total neutrino mass is currently constrained from below to $\sum m_\nu > 60$ meV using neutrino oscillation experiments [30], and from above to $\sum m_\nu < 120$ meV from measurements of the CMB [1]. Further constraints from more sensitive CMB experiments may also help to inform whether neutrino mass follows a normal or inverted hierarchy.

1.3.4 CMB Polarization from Tensor Perturbations (Primordial Gravitational Waves)

So far we have only seen E-modes produced in the early universe, with B-modes only being produced from the re-mapping of E-modes at later times (after the surface of last scattering). We now discuss a mechanism for producing B-modes at early times.

In addition to the scalar perturbations impacting the spacetime metric, tensor perturbations corresponding to gravitational waves are also expected to be produced during inflation. The gravitational waves stretch spacetime in a way that is, importantly, anisotropic, creating quadrupolar variations that are capable of producing both even-parity E-mode polarization and odd-parity B-mode polarization at large angular scales ($\ell \approx 100$).

Because the ΛCDM model has no other known way of producing primordial B-mode polarization, detection of this signal would provide important evidence in support of the inflationary model (often referred to as the "smoking gun" of inflation). However, inflationary models can exist with this B-mode signal arbitrarily small, such that it is possible for the inflationary model to be correct but for our observations to never have the sensitivity needed to see this imprint on the polarization spectrum. The strength of these perturbations is parameterized with the tensor-to-scalar ratio, r, quantified as the relative strength between scalar and tensor perturbations as indicated in the name. Figure 1.6 shows theoretical B-mode power spectra assuming different values of r and indicating the impact of gravitational lensing on our ability to extract the primordial component. Current limits from CMB experiments constrain this to $r < 0.07$ using purely

B-mode data [31], which means the primordial *B*-mode signal is at least five orders of magnitude smaller than the temperature signal. Combining *B*-mode data with other CMB measurements imposes tighter limits. Current and future CMB polarization experiments are pushing to further tighten this constraint.

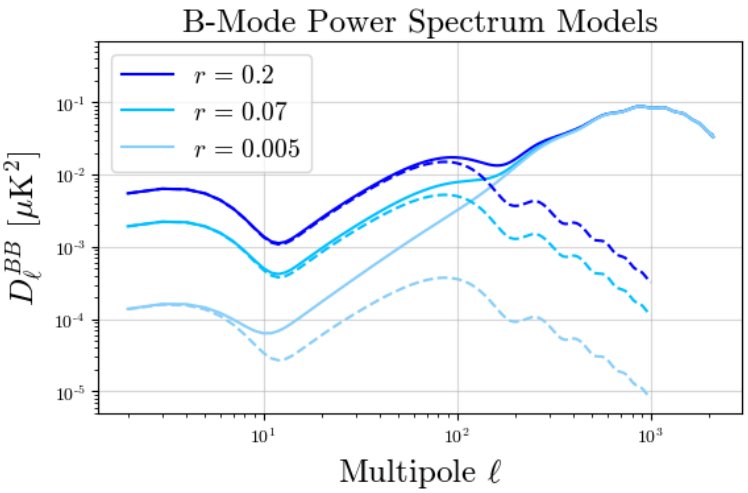

Figure 1.6: Theoretical *B*-mode power spectra assuming different values of the tensor-to-scalar ratio, *r*, indicated by the different shades of blue. The dashed lines include only power from primordial *B*-modes, while the solid lines show the total *B*-mode power (including that from gravitational lensing). The contribution from primordial *B*-modes peaks around $\ell = 100$. For $r = 0.2$, this peak is above the contribution from lensing *B*-modes. However, $r = 0.2$ has already been ruled out by CMB data. For lower values of *r*, de-lensing becomes more and more important for measuring primordial *B*-modes as the contribution from gravitational lensing of *E*-modes begins to dominate at all $\ell \lesssim 10$. Data for the theoretical curves were simulated using the CAMB online software tool, using fiducial values for all parameters other than *r* [23, 24].

1.3.5 Polarized Foregrounds

In observing the CMB, because we are looking at light that is coming from the very early universe and is therefore very far away, we need to look through the rest of the universe, including our atmosphere and galaxy, which can emit photons in our observing bands and contaminate our measurements. Many of these foreground sources only produce unpolarized light and therefore do not produce systematic effects impacting our ability to measure the polarized CMB. However,

three important sources of polarized emission must be taken into account.

One source of polarized foregrounds comes from synchrotron emission in our galaxy [32]. Synchrotron emission that is strongly polarized in the plane of motion results from the radial acceleration of relativistic charged particles about magnetic field lines [33]. Cosmic ray electrons with energies on the order of GeV interact with galactic magnetic fields with strengths of a few microgauss to produce synchrotron radiation peaking in the MHz-GHz range [34, 35].

Dust grains in the interstellar medium within our galaxy can also produce polarized emission at frequencies near the CMB peak frequency. In the presence of magnetic fields, elongated dust grains can become preferentially aligned with their spin axes parallel to the magnetic field lines, and the resulting thermal emission from these grains is polarized [36, 37]. This emission is generally in the far-infrared regime of the electromagnetic spectrum, peaking at higher frequencies than the CMB.

Finally, earth's atmosphere has also been shown to produce polarized foreground emission. Ice crystals in tropospheric clouds can be aligned to scatter thermal emission with horizontal polarization, and it has been shown that the amount of polarized contamination from the atmosphere is correlated with the existence of clouds in the sky during CMB observations [38].

Although these foreground signals add an extra uncertainty in detecting the primordial signal, observations at multiple frequencies can help mitigate these errors. Because emission from the different sources of polarized foregrounds have different frequency dependencies compared to each other and compared to the CMB, the components can be separated if data is collected over a range of frequencies. For example, synchrotron radiation tends to dominate over the CMB signal at lower frequencies and then become less important at higher frequencies, while polarized dust emission impacts the signal in an opposing way. Methods for removing foreground contamination from CMB data include the internal linear combination method [39] and template removal [40]. Polarized foreground removal, and therefore observations across several frequencies, will be crucial for next-generation CMB experiments aimed at observing the faint B-mode signal

from inflation. Atmospheric foreground emission further differs from the CMB signal in that it is determined by the telescope's pointing in azimuth and elevation rather than its pointing in right ascension and declination on the celestial sphere. Some mitigation of contamination from tropospheric clouds can also be achieved by performing in-situ measurements of clouds during normal CMB observations [38].

1.4 Current CMB Measurements

Figure 1.7 shows a compilation of recent CMB power spectra measurements from multiple experiments as published by the Planck collaboration in [1]. The top panel shows the TT, EE, and BB power spectra, the middle panel shows the TE cross-correlation spectrum, and the bottom panel shows the lensing deflection power spectrum. Best-fit ΛCDM model curves are shown as the dashed lines. The data shown represent both ground- and space-based experiments. The CMB community is large and continuing to grow, with experiments noted in the figure continuing to observe and with even more, highly sensitive experiments planned to start observations within the next several years [30, 41]. As can be seen from the data, the temperature and EE power spectra have been measured with high precision, and over a wide and densely packed range of angular scales. The BB power spectrum, on the other hand, is much less well measured due to the faintness of the associated signal. So far, detections have only been placed on the B-mode power originating from gravitational lensing of E-modes, with the first of these measurements using purely CMB data coming from the POLARBEAR team in 2014 [42]. However, only upper limits have been placed on power from primordial gravitational waves at the larger angular scales where this signal is expected. The recent B-mode results from the BICEP2/Keck Array team, combined with temperature and E-mode data from Planck, place the most stringent limit on the strength of this signal with $r < 0.044$ [43]. Current and future measurements aim to push these limits farther in hopes of constraining or finding evidence for the inflationary paradigm.

1.5 Acknowledgements

The dissertation author acknowledges ESA and the Planck Collaboration for production of Figures 1.2, 1.3, and 1.7, originally published in Planck Collaboration, 2020 [1].

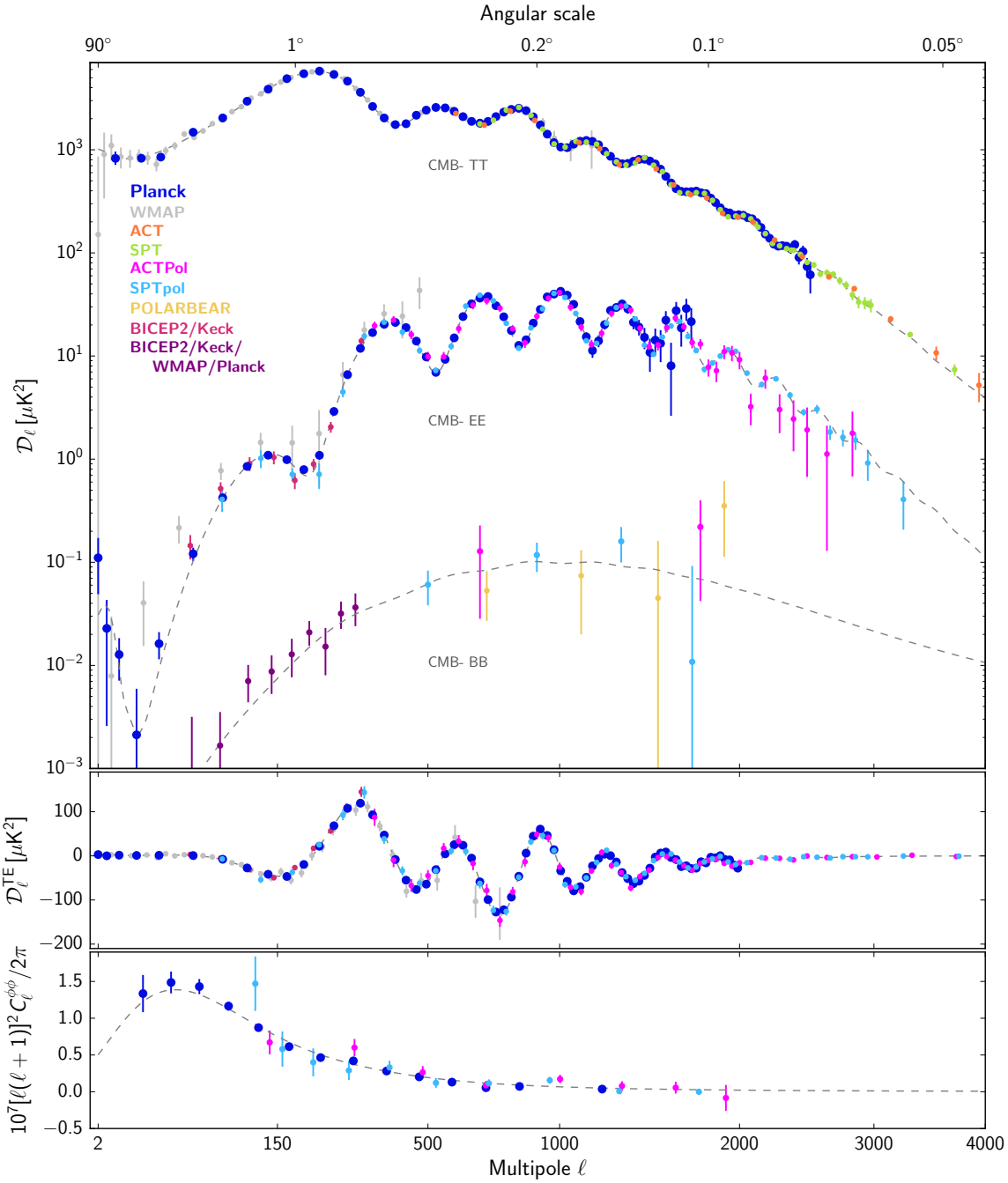

Figure 1.7: Compilation of recent CMB power spectra measurements from Planck Collaboration, 2020 [1]. The top panel shows the temperature and polarization power spectra, the middle panel shows the TE cross-correlation spectrum, and the bottom panel shows the lensing deflection power spectrum. The dashed lines in all panels represent the best-fit ΛCDM model.

Chapter 2

The Simons Array

The Simons Array (SA) is a set of three telescopes designed specifically to measure the polarized signal from the cosmic microwave background (CMB). Each telescope consists of two reflectors and holds a cryogenic receiver which houses additional reimaging optics along with detectors and readout electronics. This array of telescopes is an expansion of the POLARBEAR-1 (PB-1) experiment, which observed the CMB for five seasons beginning in 2012, leading to measurements of the CMB polarization power spectra [25, 42, 44, 45] and other cosmological measurements [46, 47, 48]. Like PB-1, SA aims to characterize the *B*-mode spectrum of the CMB at both large and small angular scales ($\ell \sim 50 - 3000$) in order to refine the information we have on gravitational lensing and put constraints on primordial *B*-modes. Both experiments are situated in the Atacama Desert of northern Chile. SA utilizes an identical telescope design to that of PB-1, but employs upgraded receivers designed to increase the experiment's sensitivity to the faint *B*-mode signal from the CMB. Upgrades include:

- an increase of approximately six in detector count per receiver (about a 20-fold increase in total experiment detector count) and correspondingly larger focal planes,
- an increase from a single observing band to multiple bands enabling improved foreground subtraction, made possible by the use of dichroic pixels, and

- the use of a continuously rotating half-wave plate located near the window of each receiver to provide modulation of the incoming radiation.

Section 2.1 describes the observatory site and the telescope design, including various telescope accessories made to support the upgraded experiment. Section 2.2 describes the cryogenic receivers of the three telescopes, named POLARBEAR-2a, POLARBEAR-2b, and POLARBEAR-2c (where the general receiver design is referred to as POLARBEAR-2 or PB-2), and their subsystems. Section 2.3 briefly describes SA's science goals.

2.1 Site and Telescopes

2.1.1 Observatory Location

The Simons Array is situated on a plateau on Cerro Toco, a mountain in the Atacama Desert located about 50 km east of the town of San Pedro de Atacama and near Chile's borders with Bolivia and Argentina. The observatory site is at an elevation of 5,200 m. Figure 2.1 shows an image of the plateau with the three SA telescopes identified.

The main motivation for choosing this site location for both PB-1 and SA comes from the site's elevation and dryness. CMB radiation peaks at a frequency of around 160 GHz, and thus CMB experiments, including SA, utilize detectors sensitive to frequencies near this value. However, when observing the CMB from the ground, molecules such as water vapor in the atmosphere can absorb radiation at CMB frequencies, making it harder to detect an already faint signal. At an elevation of 5,200 m, the air pressure is about half that at sea level and the water content is substantially further reduced, decreasing the ability for the atmosphere to interfere with the targeted signal. In addition to the elevation, the dryness of the Atacama Desert further removes water vapor from the atmosphere, allowing more CMB radiation to reach our telescopes. Figure 2.2 shows the atmospheric transmission at the SA observatory site as a function of frequency

Figure 2.1: Photo from June 2019 of the plateau of Cerro Toco, the location of the Simons Array as well as a number of other CMB experiments. The three telescopes of the Simons Array are indicated by the yellow box. The Atacama Cosmology Telescope can be seen directly behind SA, and the Cosmology Large Angular Scale Surveyor can be seen behind and to the left of SA. Photo thanks to Tom Ayotte.

for different levels of precipitable water vapor (PWV), with SA's observing bands (see Section 2.2.3) overplotted in gray dashed lines. The average PWV at our observatory site is about 1 mm [49], compared to about 25 mm globally [50], allowing significantly more CMB radiation to be detected.

Secondly, the location of Cerro Toco means that well over half the sky can be observed from the SA site. This gives us the freedom to study different regions of the sky and to access many different astrophysical sources for calibration. Importantly, the available sky area coincides with regions being studied by many other CMB and astrophysical experiments such that SA observations can be cross-correlated with data from other surveys to improve cosmological results.

Finally, as can be seen in Figure 2.1, several other CMB and astronomical observatories

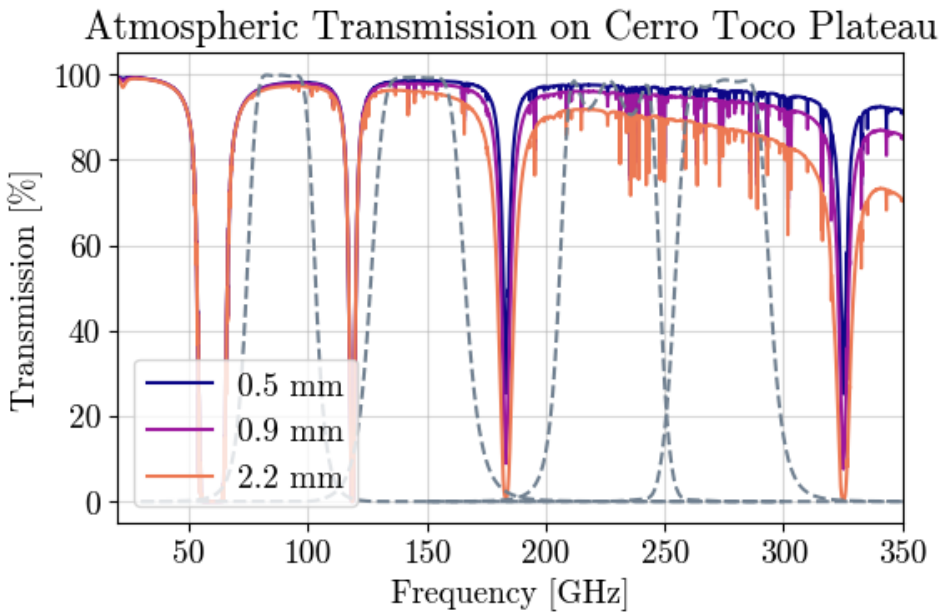

Figure 2.2: Atmospheric transmission as a function of frequency for the SA observatory site on Cerro Toco. Transmission data obtained using the *am* atmospheric model package using files created for the ACT site, which is located on the same plateau as SA [51]. The solid lines represent atmospheric transmission for three different levels of precipitable water vapor (PWV), with transmission decreasing as PWV increases. The plotted values assume a zenith angle of zero degrees (looking straight up). Gray dashed lines represent the four SA observing bands, designed to fit within the atmospheric windows.

exist on Cerro Toco and in the surrounding area. The Atacama Cosmology Telescope [52, 53], the Cosmology Large Angular Scale Surveyor [54], and soon the Simons Observatory [41], all operate from Cerro Toco, and other observatories such as the Atacama Large Millimeter/submillimeter Array [55] and the Atacama Pathfinder Experiment [56] operate from a plateau about 10 km away. The existence of these neighboring observatories allows the POLARBEAR/Simons Array team to share resources with other groups, greatly enhancing both the efficiency and safety of working on-site.

SA personnel working at the observatory site stay in the town of San Pedro de Atacama (at an elevation of about 2,400 m) and commute to the Cerro Toco plateau each workday. An office for SA also exists in San Pedro de Atacama, and a radio link sends information between the observatory "high" site and this "low" site, from which data can be transferred to a supercomputer

in the northern hemisphere for storage and analysis.

In addition to these advantages, operating SA at the chosen site comes with challenges. Despite the incredibly dry environment, weather can often cause problems with power and site access. Lightning storms can disrupt power and communication systems, and snow storms can occasionally prevent safe road access for days to weeks at at time. Care also must be taken to protect the telescope electronics from water damage after snow accumulation, as is discussed in Section 2.1.3. Furthermore, electrical power for the observatory must be generated entirely onsite and is done by a set of two diesel-engine generators. These are intended to alternate the load every several days so that maintenance can be done on the "off" generator. Keeping these generators working stably and reliably in the often harsh weather conditions has been a challenge, and the required manual maintenance in combination with occasional site access disruptions can impact telescope operation. Recent installation of a new set of generators with the ability to switch between generators without a power outage has drastically increased the robustness of site operations, but power generation remains an important concern for SA. Lastly, the high altitude and sometimes harsh weather at the observatory site can make working conditions very difficult, with SA personnel typically carrying supplemental oxygen as they work.

2.1.2 Telescopes

The term "telescope" is used here to refer to the experiment's reflecting optical components and the structures and mechanical assemblies required to hold the receivers and scan the sky for making observations. The telescope used in the PB-1 experiment was built by General Dynamics[1], with its optical system designed by Huan Tran [57]. This telescope is now named the Huan Tran Telescope, and the SA telescopes have an identical optical design. However, other parts of the telescope structure and some of the accessory hardware were updated when designing for SA in order to account for the larger and heavier PB-2 receivers and increased need for supporting

[1] https://www.gd.com/

electronics. Two new telescopes were built to hold the first two receivers, again by General Dynamics, and PB-1's Huan Tran Telescope is being modified to hold the third receiver. The two new telescopes are named the Nicholas Simons Telescope and the Paul Simons Telescope. The Paul Simons Telescope, before installation of its receiver and accessory hardware, is shown in Figure 2.3.

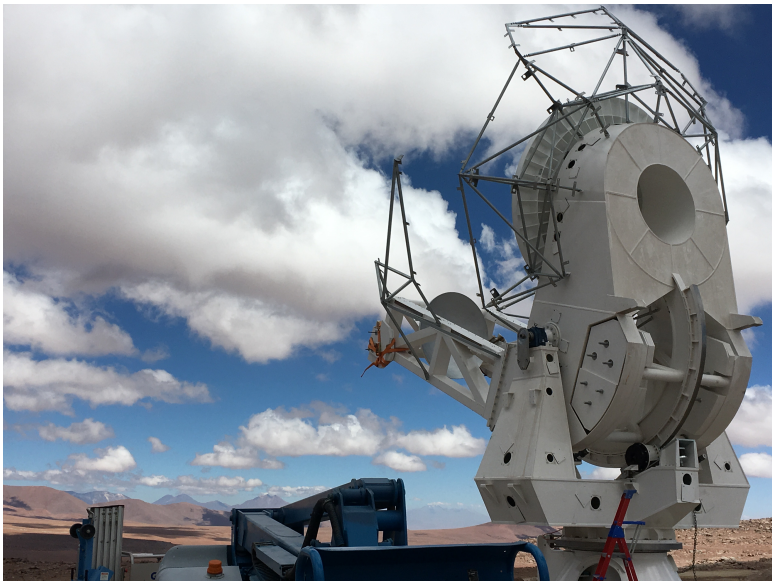

Figure 2.3: Photo of the Paul Simons Telescope from 2016, taken after installation at the SA site. The photo shows the bare telescope structure, including structural components and reflectors, before the receiver and other telescope accessories have been installed. The back of the primary reflector and the front of the smaller, secondary reflector can be seen mounted on the upper and lower booms of the telescope structure, respectively. Some of the counterweights can also be seen behind and below the primary reflector. The metal frame structure seen is used for supporting some of the optical shielding.

Telescope Optical Design

The three SA telescopes employ an off-axis Gregorian optical design, with a parabolic primary reflector and elliptical secondary reflector. The off-axis nature of the design enables the telescope to be constructed without necessitating any structural elements be placed in the optical path, creating a more well-defined beam pattern with lower contamination from sidelobes [58]. The reflectors are designed such that they satisfy the Mizuguchi-Dragone condition, with

the axes of the primary and secondary reflectors tilted with respect to one another in such a way as to minimize cross-polarization and astigmatism [59]. A ray trace showing the design of the reflectors is shown in Figure 2.4. Each reflector is machined from a monolithic piece of aluminum to a surface accuracy of 53 μm (RMS) [60]. The parabolic surface of the primary reflector is extended radially by a "ring shield" composed of eight separate panels. These additional panels serve to help ensure any spillover gets deflected to the sky, but is not considered within the main beam [61]. The primary reflector is shaped as a 2.5 m-diameter section of a paraboloid, with the ring shield extending this diameter to 3.5 m. The elliptical secondary reflector measures 1.3 m in diameter. The resultant beam measures about 3.5 arcmin for 150 GHz and 5.5 arcmin for 90 GHz (full width at half maximum) and the field of view, considering the reimaging optics described in Section 2.2.2, is circular with a diameter measuring 4.5 degrees [61]. This enables SA to efficiently observe patches of sky measuring tens to hundreds of square degrees necessary for probing *B*-modes from inflation, while also achieving sufficiently high angular resolution to probe *B*-modes from gravitational lensing.

The two reflectors are aligned with respect to each other and to the rest of the telescope structure (and thus the receiver) using photogrammetry. Photogrammetry targets are distributed across the surfaces of each reflector as well as at various points along the telescope structure. Photos are then taken from various angles that are used to reconstruct the reflector surfaces in 3D space and to fit the points to the expected parabolic and elliptical shapes. The positions and angles of the reflectors can then be manipulated using alignment screws on the backs of the reflectors such that they match the design. Photogrammetry measurements are taken iteratively after each set of adjustments until the reflectors are shown to be in the correct positions.

Telescope Operation

Motion of the SA telescopes is controlled with motors along two axes of rotation, one in azimuth and one in elevation, in order to target and scan across different patches of sky. The

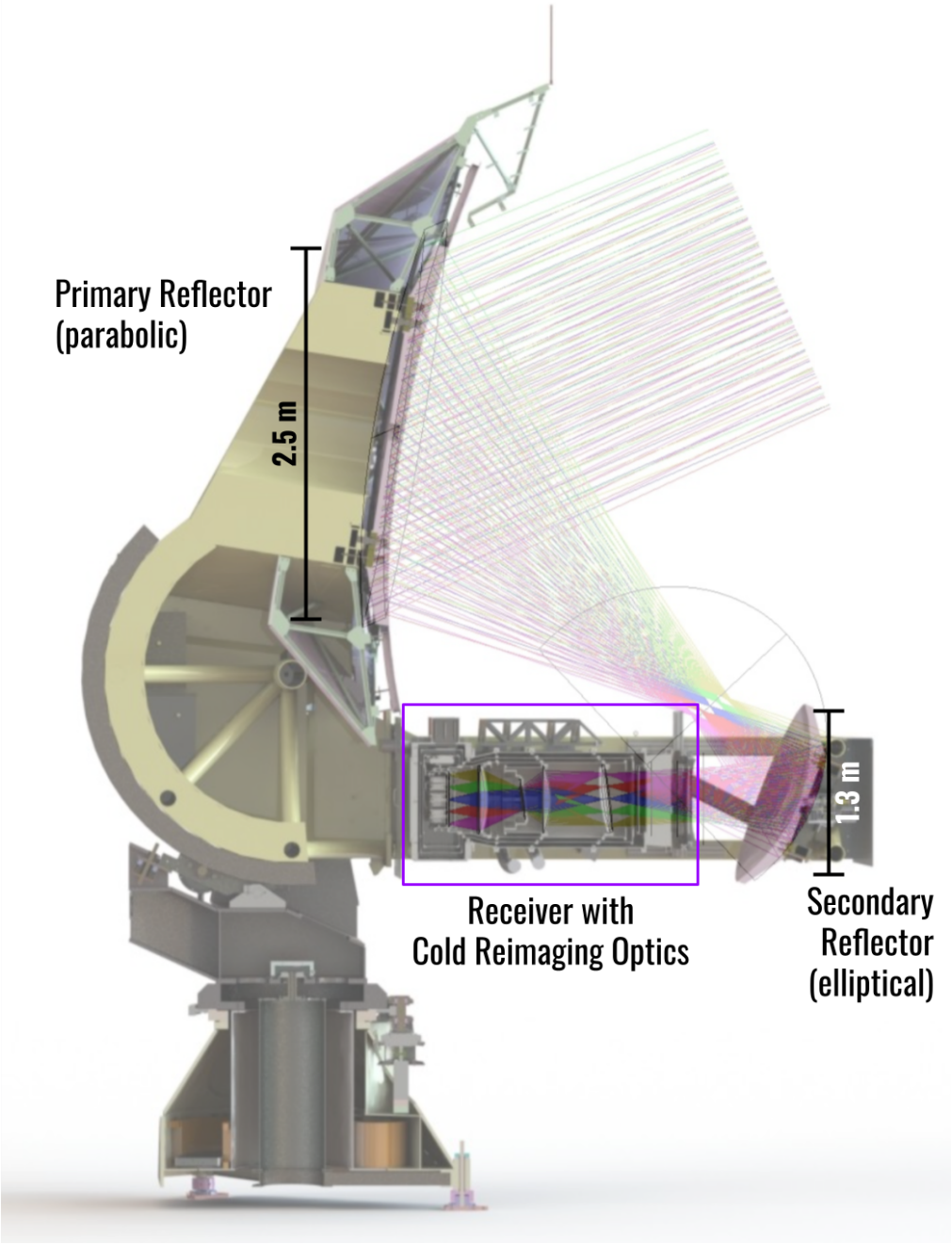

Figure 2.4: Cross sectional view of a 3D computer-aided design (CAD) model of one of the SA telescopes, with geometric ray trace illustrating the optical design superimposed. The telescope is an off-axis Gregorian design containing a 2.5 m parabolic primary reflector mounted to the telescope's upper boom and a 1.3 m elliptical secondary reflector mounted to the telescope's lower boom. The cryogenic receiver for each telescope, which contains additional optical elements and the focal plane with detectors, also gets mounted to the lower boom. Ray trace created using Zemax by Fred Matsuda.

telescopes are able to move a total of about 120 degrees in elevation and about 400 degrees in azimuth. The motors for controlling telescope motion along each axis can be operated separately or in parallel, allowing for various methods of scanning the sky for different observations. These include scans in azimuth while keeping the elevation angle constant (constant-elevation scans or CESs), scans in elevation to calibrate detectors at different locations on the focal plane using different levels of atmospheric emission, and celestial source tracking to calibrate properties such as beam shape.

SA telescopes will observe two patches of the sky as their primary CMB science targets, one above and one below the galactic plane. The patches are chosen based on current understanding of foreground sources, on the accessibility of the different sky regions at different times, and on the ability to have SA sky coverage overlap with that of other astrophysical experiments. In particular, the patch in the northern part of the sky overlaps with the observing regions of experiments such as Subaru's Hyper Suprime-Cam [62], and the patch in the southern part of the sky overlaps with the observing regions of CMB experiments BICEP/Keck Array [31] and SPT [63]. Furthermore, both SA patches are intended to overlap with the observing region of the Simons Observatory's small aperture telescopes [64]. The northern patch encompasses roughly 5% of the sky, while the southern patch encompasses roughly 8%. These CMB patches will be observed using CESs to avoid changes in atmospheric loading during a single scan. As described in Section 2.1.3, a chopped thermal source is observed at the beginning and end of each CMB observation to allow proper calibration even with time-variation in the gain of the detectors.

Observations are run using custom telescope control software that commands the telescope's position, velocity, and acceleration about its two rotational axes [60]. The observations are programmed as "schedules" that involve scanning patches of the sky along with operations to control the refrigeration system, tune detectors and readout electronics to prepare them for data acquisition, and run calibration procedures. A live monitoring system that can be accessed online is employed that tracks the status of each telescope, including parameters such as elevation and

azimuth pointing, power to various receiver electronics, and thermal/cryogenic conditions, as well as more general site conditions such as generator status and weather conditions.

Counterweights are installed behind the primary reflectors in order to balance the telescopes in a way that accounts for their motion about the elevation axis. These weights are installed in phases during telescope commissioning as the receivers and other accessories are installed in order to provide the necessary counter-torque as mass on the lower boom increases.

2.1.3 Telescope Accessories

In addition to the structure designed and assembled by GD which integrates the telescope optics, we designed and fabricated several telescope accessories serving a variety of purposes. These include a receiver enclosure, optical baffling, electronics housings, a thermal calibration source, and components at the interface between the receiver and the telescope structure. Although the PB-1 experiment required the same type of accessory hardware, the specific design of each sub-assembly was updated for SA, largely necessitated by the increased receiver and focal plane sizes. Figure 2.5 depicts the Nicholas Simons Telescope from 2021, with the vast majority of telescope accessory hardware installed. These sub-assemblies are described in detail in the following sections.

Receiver Enclosure

Once integrated with the telescope, each PB-2 receiver is situated between the telescope's secondary reflector and its elevation axis of rotation. It is mounted to the telescope's "lower boom" via an interface described later in this section. In order to protect the receiver from snow, wind, and dust at the observatory site, ensuring the optical apertures remain clear and mechanical and electrical interfaces remain robust over the lifetime of the experiment, an enclosure is installed around this lower boom area.

The enclosure is constructed from a series of 1/4 inch-thick aluminum honeycomb panels

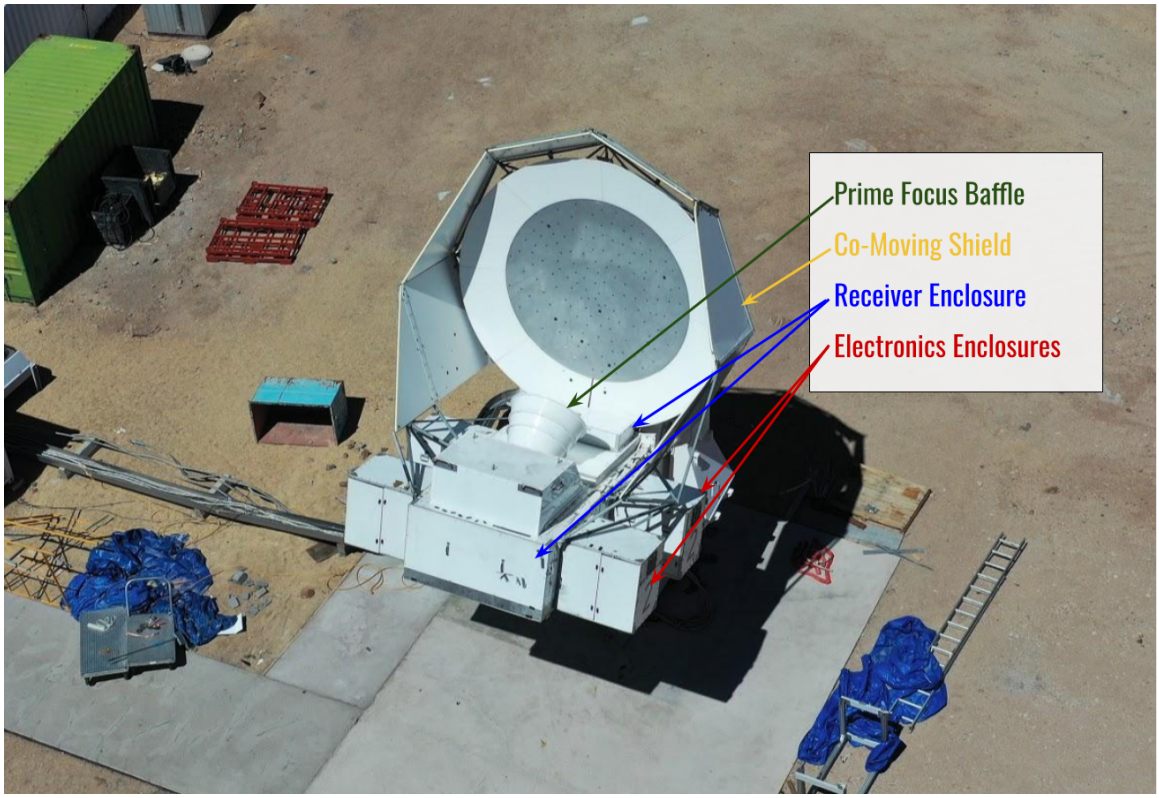

Figure 2.5: Photo of the Nicholas Simons Telescope from 2021, after the majority of telescope accessory hardware had been installed. The telescope's prime focus baffle, additional optical shielding, receiver enclosure, and electronics enclosures can be seen. Photo thanks to Nolberto Oyarce.

mounted to the telescope structure either directly or via custom machined solid aluminum mounting brackets. All panels and mounting brackets are installed with environmental gasket along the interfaces to seal the interior from water and dust. Honeycomb aluminum is used in order to provide the necessary rigidity of the structure against the often strong winds at the observatory site, while not adding excessive weight to the receiver-side of the boom that could offset the balance. The weight reduction provided by the honeycomb aluminum also allows for easier manipulation of the enclosure parts such that site personnel can open the enclosure to access the receiver for maintenance as necessary. It is required that the receiver is accessible on the telescope from the front, back, top, and bottom with as little disassembly of other components as possible. The back panels of the receiver enclosure contain holes through which telescope

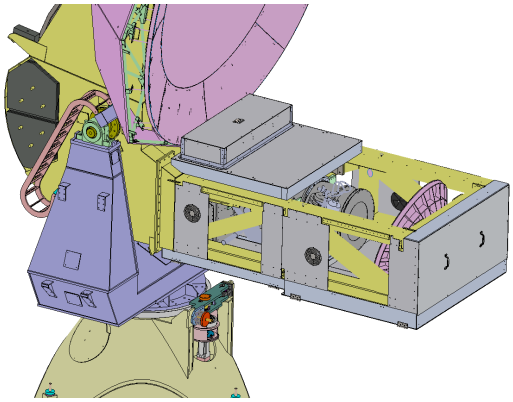

(a) 3D model of receiver enclosure for the Nicholas Simons Telescope.

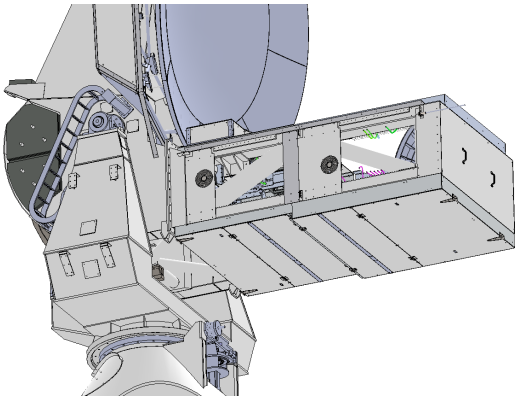

(b) 3D model of receiver enclosure for the Paul Simons Telescope.

Figure 2.6: 3D CAD models of the receiver enclosures on the first two SA telescopes, created using SolidWorks. The panels and mounting components shown in the figure in gray in the left figure (and corresponding components in the right figure) make up the receiver enclosures, with components mounted to the top, bottom, front, back, and sides of the telescope's lower boom. The receiver can be seen in the CAD model of the left figure through holes in the top and sides of the lower boom. In practice, these holes are sealed with a baffle structure and electronics housings, which are omitted from this image for clarity. The receiver enclosure designs for the two telescopes contain slight differences, though these differences are not highlighted in these images. The models are shown from different viewpoints for the two telescopes to show different aspects of the design.

cabling and hoses for the receiver's cryogenic equipment are fed.

3D models of the receiver enclosures designed for first two SA telescopes are shown in Figure 2.6. The two designs are largely the same, with some small upgrades included in that for the Paul Simons Telescope to improve accessibility based on experience working with the original[2]. In both designs, the receiver enclosure interfaces with the prime focus baffle and the electronics enclosures discussed later in this section. Installation of the receiver enclosure for the Nicholas Simons Telescope, which holds the PB-2a receiver, was completed in early 2021. A photo taken in 2017 during a test assembly of the machined parts is shown in Figure 2.7. Parts for the receiver enclosure for the Paul Simons Telescope have been machined and installation is planned following integration of the PB-2b receiver with the telescope.

[2]Essential contributions to these designs were made by Christopher Aleman and Calvin Tsai.

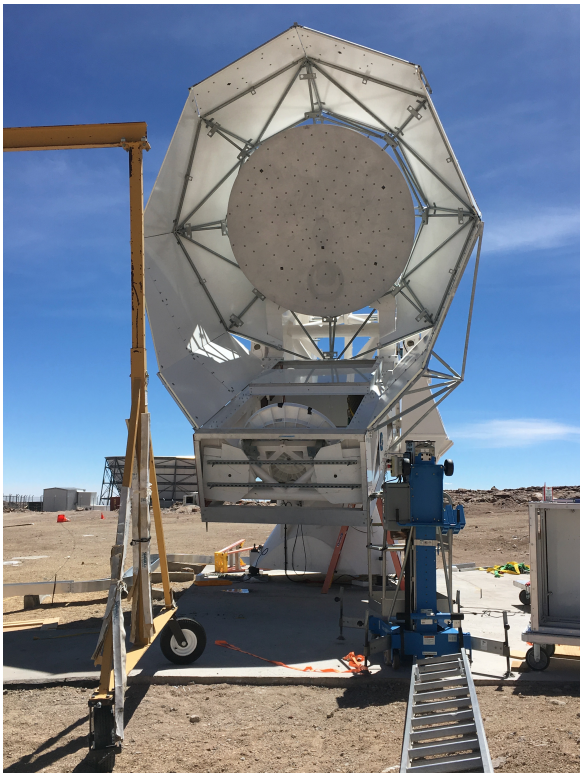

Figure 2.7: Photo of the Nicholas Simons Telescope from 2017 during a test assembly of the receiver enclosure. The receiver enclosure's solid aluminum beams along the front and bottom of the telescope's lower boom can be seen, along with some of the honeycomb aluminum panels located on the top and back. Additional paneling not seen in this photo is included in the final configuration of the receiver enclosure, shielding the receiver from environmental elements. The complete receiver enclosure assembly for the Nicholas Simons Telescope is shown in Figure 2.5.

Prime Focus Baffle and Co-Moving Shield

Optical baffling on the telescope is required to help reduce the amount of bright, stray light that enters the system. For the SA telescopes, the biggest source of this stray light is the ground, which radiates at around 300 K and is therefore several orders of magnitude brighter than the variations in radiation from the CMB that we are trying to measure. To avoid ground radiation from reaching the receiver, a baffle placed at the telescope's prime focus (between the primary and secondary reflectors) was fabricated. The design of this baffle was informed by the results of reverse-time optical simulations performed by Fred Matsuda in which isotropic radiation was

propagated from the surface of the receiver window. These simulations were performed with different apertures specified at various points between the two reflectors, with the goal of finding appropriate aperture sizes and placements to force any rays from the window to terminate either on the before the aperture or to make it all the way to the primary reflector (and thus the sky).

The optical requirements set by these simulations are shown in Figure 2.8. A set of three apertures is specified, with one placed in the plane of prime focus and two others closer to the primary reflector. The resulting mechanical design involves creating these apertures by forming a cone piece, with the wider end of the cone toward the primary reflector.

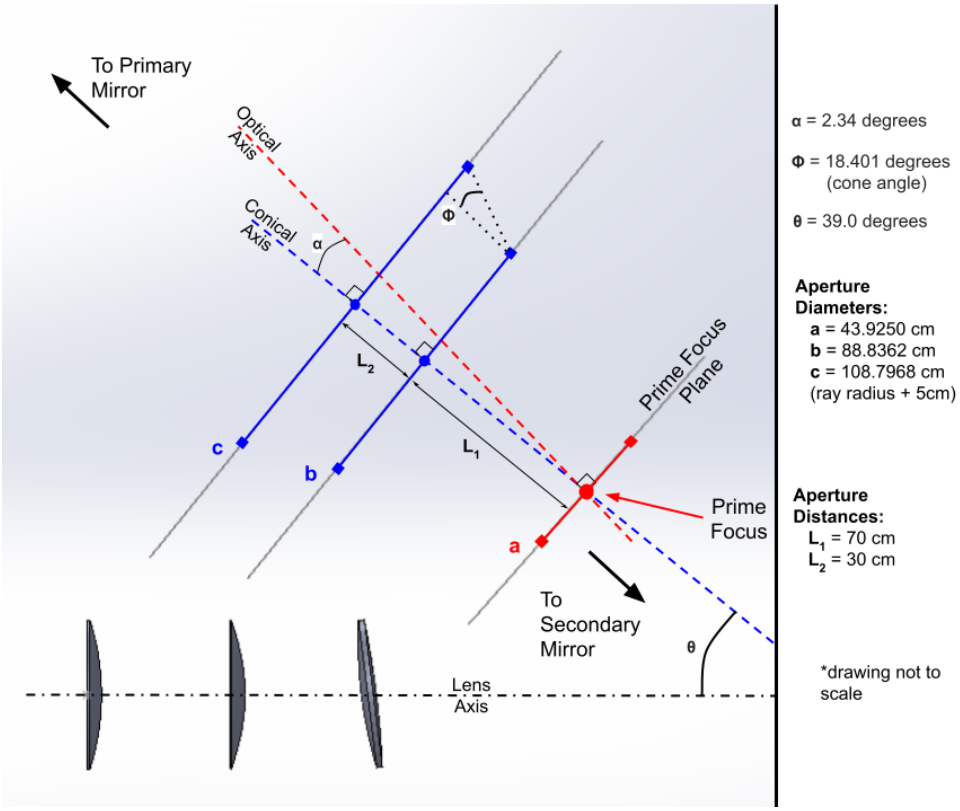

Figure 2.8: Specifications for the prime focus baffle apertures resulting from optical simulations. Apertures calculated using optical simulations are indicated by the red and blue lines terminated by squares. Aperture *a* is placed directly in the plane of prime focus and is specified as 44 cm in diameter. Apertures *b* and *c* are positioned closer to the primary reflector along the "conical axis" and are set to have diameters of 89 cm and 109 cm, respectively. The optical axis traces the chief ray from the center detector on the focal plane. An angle exists between this axis and the conical axis about which the baffle apertures are centered due to the orientation of the primary mirror.

In addition to the optical specifications, design of the prime focus baffle was required to meet mechanical constraints. The PB-2a receiver on the Nicholas Simons Telescope is built to operate with an external half-wave plate modulator that is situated between the telescope's secondary reflector and the receiver window. The baffle structure was required to account for this additional component, which motivated the use of a detachable aperture at prime focus (aperture *a* in Figure 2.8) as opposed to a simple extension of the cone. Furthermore, exact optimal positioning of the receiver on the telescope cannot be known ahead of installation due to potential discrepancies between the layout of designed and built optical and structural components while reflector alignment is performed on-site, and the inclusion of the flat half-wave plate in optical path increases this uncertainty. Therefore, the baffle was required to have ± 2 cm of adjustability in the z-direction (direction of the receiver's optical axis). Since the baffle covers an opening into the telescope's lower boom, it was also required to interface smoothly with the receiver enclosure and provide protection from weather. Finally, the baffle structure was required to be lightweight enough such that the designed counterweights could accommodate its added torque on the elevation axis motor, especially given its location relatively far from the axis of rotation.

The resulting baffle structure meeting the above requirements is shown during a test assembly in the lab at UCSD from 2016 in Figure 2.9. As with the receiver enclosure, most panels are fabricated from honeycomb aluminum to decrease the weight of the assembly. The panel that directly interfaces with the cone section of the baffle is made of solid aluminum pieces that have been made more lightweight by removing material. Before use on the telescope, all surfaces on the interior of the baffle structure were coated with microwave absorber Eccosorb HR-10[3] such that radiation reaching the receiver from these surfaces does not overwhelm the sky signal. The interior surface of the cone was also coated with this absorber, and with an added layer of 1/16 inch-thick Volara[4] closed cell polyethylene foam to protect the absorber from snow.

[3]https://www.laird.com/products/microwave-absorbers/microwave-absorbing-foams/eccosorb-hr/301060005
[4]https://masterpak-usa.com/products/volara-r-voltek

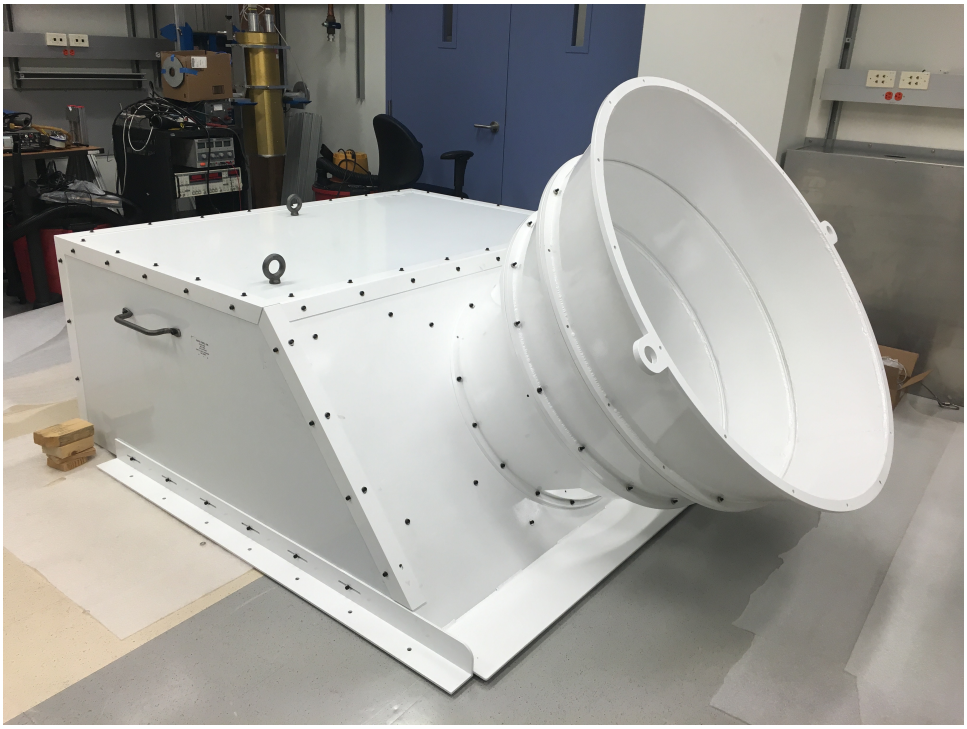

Figure 2.9: Prime focus baffle structure for the first SA telescope during a test assembly in the lab at UCSD in 2016. This test assembly was performed before any surfaces had been lined with microwave absorber. When installed on the telescope, the baffle is situated between the primary and secondary reflectors, with the wider part of the baffle's cone section pointing toward the primary reflector.

A 1 inch-thick disk of Zotefoam HD30[5], another closed cell polyethylene foam, is placed at the narrow end of the baffle's cone section to create a seal that blocks out precipitation and dust while staying transparent to microwave radiation. A grating is placed at the bottom of the cone section just before this Zotefoam piece to prevent snow accumulation inside the baffle, and mounting holes that allow for installation on the telescope are slotted such that the position of the baffle can be adjusted with respect to the receiver and reflectors. The baffle for the Nicholas Simons Telescope can be seen fully installed in Figure 2.5, and work is in progress to optimize its location. Parts for the second SA baffle have been machined, and installation on the Paul Simons Telescope will occur after the receiver has been installed. The second SA baffle is optically identical to the first, but its mechanical structure has been updated to provide more clearance in the receiver

[5]https://www.flextechfoam.com/resources/zotefoams-datasheets/

cabin[6].

The SA telescopes additionally employ a co-moving shield to further block ground radiation. This shield prevents ground radiation from diffracting around telescope apertures, potentially becoming incident on detectors. As seen in Figure 2.5, the shield is mounted entirely to the upper and lower booms of the telescope, moving with the receiver and optics as the telescope moves about both its rotational axes.

Electronics Enclosures

Though the electronics required for controlling telescope motion are located on the ground around the observatory site, many of the electronics associated with running the receiver and collecting data must be installed on the telescope structure itself and move with the receiver. This reduces the amount of wiring running through the limited space in the cable wraps inside the telescope and reduces the wiring lengths needed to read out data from the receiver. This is done for both the PB-1 and SA experiments using electronics enclosures that mount to the sides of the lower boom structure of the telescope. For the PB-1 experiment, two electronics enclosures were used, with one on each side of the lower boom. For SA, four electronics enclosures are required due to the increased number of detectors and thus increased amount of necessary readout electronics, and two are placed on either side of the lower boom as can be seen in Figure 2.5. In addition to the detector readout electronics, other auxiliary electronics for operating and monitoring the receiver and telescope, such as thermometer readout electronics, half-wave plate control, and control of calibration sources, are housed in these enclosures.

The electronics enclosures are designed to be weather-sealed to protect both the electronics they contain as well as the receiver itself, as these enclosures interface directly with the broader receiver enclosure. The mounting hardware for the racks inside the enclosures are made of insulating material so as to allow the electronics to be isolated from the rest of the telescope when

[6]Essential contributions to this updated design were made by Calvin Tsai.

necessary, and each electronics enclosure is temperature-controlled [65].

Stimulator

Each SA telescope employs a "stimulator," which is a thermal calibration source for the receiver that can be optically modulated at different frequencies by a chopper. The gain of SA detectors, or the conversion factor between the intensity of the incident radiation and the corresponding electrical signal output by the detector, can vary over time. Measuring a known thermal source before and after each sky observation helps to calibrate the detectors and decrease the systematic error associated with this variation. This calibration source is also useful in identifying readout channels and in making measurements of detector time constants. Stimulators for SA operate at a temperatures of about 700 degrees C (973 K).

The stimulator is assembled with a light pipe that directs the radiation through a small opening. The entire assembly is then positioned directly behind the secondary reflector on the telescope, which has a small hole in its center for this light pipe. The stimulator for the Nicholas Simons Telescope has been installed and has been used in measurements made by the PB-2a receiver [66]. The stimulator for the Paul Simons Telescope was constructed at UCSD and characterized during in-lab testing of the PB-2b receiver discussed in Chapter 3.

Telescope-Receiver Interface and Installation Equipment

The PB-2 receivers (described in detail in Section 2.2) are fabricated and tested independently of their corresponding telescopes. Custom hardware was designed to serve as the mechanical interface between the receiver and the telescope, referred to as the receiver mount, and additional hardware was designed to facilitate safe receiver installation. Both of these assemblies required redesign compared to those used in the PB-1 experiment due to the larger size and weight of the PB-2 receivers. The PB-1 receiver weighed approximately 750 lbs, while each PB-2 receiver weighs over 1600 lbs.

The receiver mount is required to allow the receiver to be electrically isolated from the telescope structure, allow for adjustments in the x- and z-directions (two directions perpendicular to gravity assuming the receiver is horizontal) and in the pitch of the receiver with respect to the telescope structure, and of course to safely and reliably support the weight of the receiver as the telescope moves. This is achieved using a rigid steel truss structure that mounts to the telescope's lower boom to which the receiver attaches via hinges on either side of the optical axis. The truss attaches to the telescope at four points and using a set of slide blocks that can be precisely pushed in the x- and z-directions via fine-threaded bolts to align the receiver. Adjustments can be made in the y-direction (parallel to the direction of gravity) by shimming these blocks, though adjustment in this direction is not expected to be necessary. The steel hinges attach directly to the truss and to aluminum I-beams that run along the cylindrical part of the receiver. Between the hinges and I-beams is a flat adapter plate machined of G-10 fiberglass to provide electrical isolation between the components.

There is an additional attachment point between the truss and the receiver at the front and in the center of the truss. This attachment point is not intended to support the main load of the receiver, but instead is meant to reinforce the desired pitch angle of the receiver as set by the hinges. Another G-10 fiberglass plate is used at this interface to provide electrical isolation. A photo of the PB-2a receiver mount on the Nicholas Simons Telescope is shown in Figure 2.10. The PB-2b receiver mount is identical apart from this front attachment point which includes small updates.

When the lower boom is horizontal as is necessary for receiver installation, the receiver mount attachment points are approximately 3.5 m off the ground. Thus, a custom hoisting structure was designed to enable the receivers to be lifted into positions where they could be mated to the receiver mounts. Several factors constrained the design of this assembly. First, the hoisting structure needed to support the weight of the PB-2 receivers with a large margin to ensure the safety of both the equipment and personnel. With an estimated receiver weight $>$ 1600 lbs,

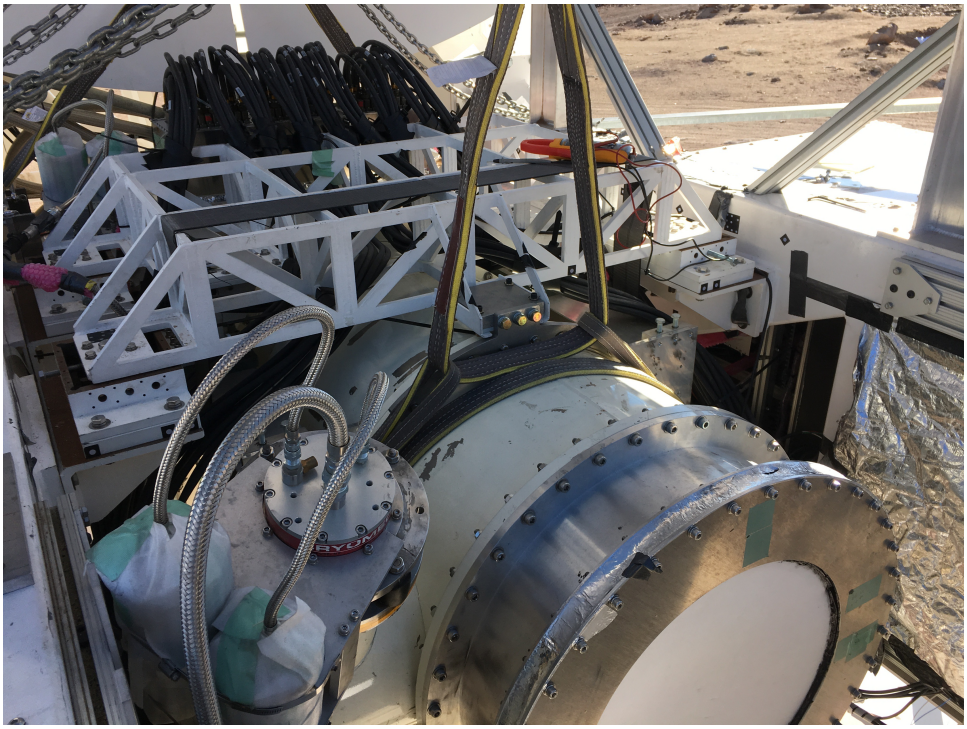

Figure 2.10: Photo of the PB-2a receiver mount installed on the Nicholas Simons Telescope from 2019. The rigging equipment seen in this photo is from installation of these parts and is not present while the telescope is operating. The steel truss structure and three of its four attachment points to the telescope can be see, along with the front attachment point between the receiver and the truss. Hinges that are obscured in this view of the telescope connect the rear part of the truss structure to the receiver via I-beams along the receiver sides.

all equipment was chosen to be rated for use with a minimum of 4000 lbs. Next, due to physical constraints of the telescope and receiver assembly procedure, the receiver must be translated in the z-direction in order to be installed on the telescope in addition to being lifted in the y-direction. Translational motion, however, is restricted by the presence of the truss. Finally, the height of the hoisting structure was restricted by the angle of the hoisting straps and the proximity to the primary reflector.

The resulting design is shown in Figure 2.11. The structure employs a total of ten I-beams, the center of which acts as a rail on which trolleys can move. The vertical support beams mount directly to the telescope's lower boom. This center trolley beam is made of steel as it supports the most weight, while the other beams are made of aluminum. Simulations in SolidWorks assuming

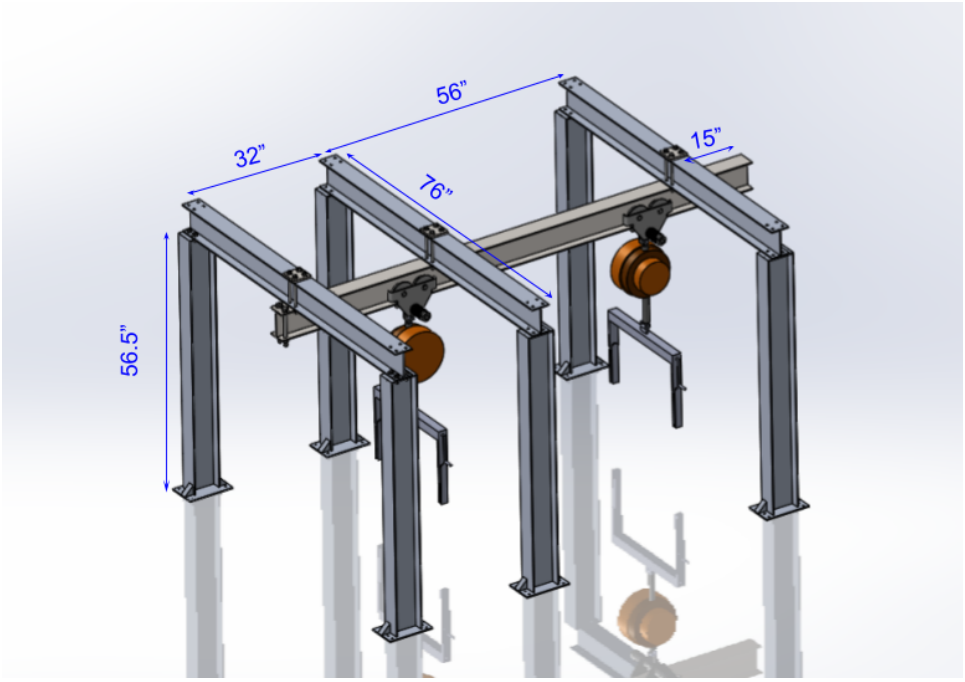

Figure 2.11: CAD model of the receiver hoisting structure, with dimensions. Not shown are four small diagonal members that were added to the design following the load test.

these materials and a total load of 2000 lbs showed a safety factor of about 14 for the center beam and of about 6 for the three beams that span the lower boom, far exceeding the requirement. Calculations concerning the strength of the vertical beams demonstrated even larger factors of safety. Trolleys, chain hoists, and load levelers (two of each) were used that are rated for use up to 4000-lbs each. Figure 2.12 shows the structure during a test assembly and load test performed at UCSD before shipping the materials to the observatory site for use. Four small diagonal members, each attaching from one of the vertical I-beams to the telescope structure, were added following the load test to improve rigidity of the overall structure. The structure was employed successfully to install the PB-2a receiver on the Nicholas Simons Telescope in 2018, and was used again in 2020 to remove and re-install the receiver for a retrofit operation. This same structure will be used to install the PB-2b receiver.

Figure 2.12: Photo of the hoisting structure during a load test performed at UCSD prior to implementation at the observatory site. The block used as the load during this test weighed about 2500 lbs, significantly more than the weight of the receiver. Though it was successful, diagonal members were added to the design following this test to improve rigidity along the axis parallel to the center trolley beam.

2.1.4 Site Layout and Operation

The SA site layout is shown in Figure 2.13. The three SA telescopes roughly form a line from north to south, with the Nicholas Simons Telescope at the north end, the Paul Simons Telescope at the south end, and the Huan Tran Telescope in the center. For the Simons Array, the PB-2a, PB-2b, and PB-2c receivers will be mounted on these telescopes, respectively. Compressors supporting the receivers' cryogenic systems, along with the electronics and computers used in telescope operations, are housed in various shipping containers around the site, with necessary hoses and wiring routed the each telescope inside cable trays. The two diesel-engine generators are housed in a larger container on the edge of the site, with hoses connecting them to a 25,000-L diesel tank.

Figure 2.13: Aerial view of the SA site. The telescopes roughly form a line in the north-south direction, with the Nicholas Simons Telescope (PB-2a receiver) on the north end, the Paul Simons Telescope (PB-2b receiver) on the south end, and the Huan Tran Telescope (originally PB-1 receiver, planned PB-2c receiver) in the center. The structure that houses the site generators is shown in the bottom right corner of the photo. Also seen in the image are the various shipping containers that house the telescope control electronics and computers, compressors for the receiver cryogenic systems, and general storage items. Photo thanks to Nolberto Oyarce.

Though not shown in Figure 2.13, the Atacama Cosmology Telescope and Cosmology Large Angular Scale Surveyor, two other CMB experiments, are located just west of the SA site. The sites for these experiments include high bay areas that have been used for assembly of the PB-2 receivers before they are installed on the telescopes.

2.2 POLARBEAR-2 Receivers

Each SA telescope houses a single PB-2-style receiver. The term "receiver" here refers to the instrument that holds the detectors and thereby receives the incident CMB radiation. All

components interior to the receiver shell are cryogenically cooled to reduce loading on the detectors due to thermal radiation.

A cross-sectional view of one of the SA receivers is shown in Figure 2.14. Each SA

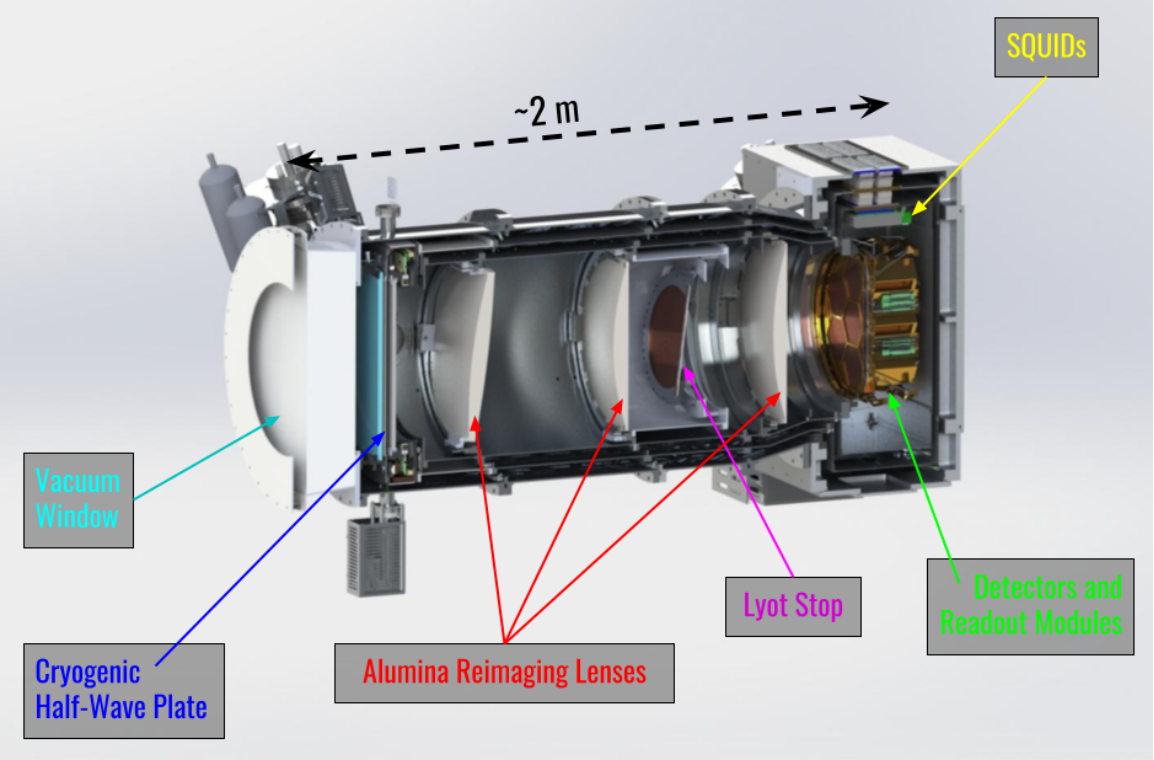

Figure 2.14: Cross-sectional view of the PB-2b receiver, generated by SolidWorks. The receiver is broken into two distinct sections, the cylindrical optics tube on the left, which contains the vacuum window, cryogenic half-wave plate (for PB-2b and PB-2c), reimaging lenses, and Lyot stop, and the rectangular backend on the right, which contains the detectors and cryogenic readout components. Each section is cryogenically cooled by a pulse-tube cryocooler not visible in this cross-sectional view. Detector and readout components in the backend are further cooled by sub-kelvin refrigeration components, also not visible. Each receiver measures about 2 m in length.

receiver is composed of two main sections: a cylindrical optics tube, which contains a vacuum window, cryogenic half-wave plate (for PB-2b and PB-2c), three reimaging lenses, and Lyot stop, and a rectangular backend, which contains the detectors and cryogenic readout components.

The three SA receivers employ the same basic design, but differ in a few key areas that will be highlighted in the following sections. Most importantly, the PB-2a and PB-2b receivers

are designed to be sensitive to radiation bands centered about 90 and 150 GHz, while the PB-2c receiver is designed for higher frequencies (in order to provide data with which to clean the CMB signal of foreground emission from galactic dust). And although all three receivers utilize a continuously rotating half-wave plate (HWP) for modulation of the incoming polarization signal, the HWP for the PB-2a receiver operates at ambient temperature and is a separate instrument, while the HWPs for the PB-2b and PB-2c receivers operate at cryogenic temperatures and are contained within the receivers themselves.

2.2.1 Cryogenics

The receivers for SA must be cryogenically cooled both to reduce the loading from thermal emission of receiver elements on the detectors and in order for the detectors and readout electronics to operate. As will be described further in Section 2.2.3, SA employs transition edge sensor detectors which operate on their superconducting transition, which for SA detectors lies near 450 mK. To meet these requirements, three cryogenic cooling systems are implemented in each PB-2 receiver.

Two pulse-tube cryocoolers (PTCs) are used to cool each PB-2 receiver to approximately 4 K, with one PTC installed in the receiver optics tube and another in the receiver backend. The PTCs used in SA are the commercially available two-stage PT415 models from Cryomech with remote motor option[7]. This is a closed-loop refrigeration system utilizing compressed helium gas, designed to have a cooling capacity of 40 W at 45 K (at its first stage) and of 1.5 W at 4.2 K (at its second stage). The receivers are assembled as a set of nested aluminum shells, as can be seen in the cross-sectional view in Figure 2.14. Multi-layer insulation (MLI) consisting of several aluminized polyester sheets exists between each of the shells to reduce the radiative loading from one shell to the next. The outermost shell utilizes thicker aluminum and provides a seal for the receiver such that its interior can be brought to near-vacuum pressures ($< 10^{-4}$ Torr)

[7] https://www.cryomech.com/products/pt415/

during operation. Evacuating the receiver is critical before cryogenically cooling as it removes mass that would require additional cooling power and prevents molecules from condensing on the equipment, which would add further thermal loading and potentially damage the receiver components. The inner two shells are constructed of thinner aluminum panels and frame pieces, with lengths of high-purity (99.9999%) aluminum serving as heat straps to ensure sufficient thermal conduction between shell pieces on the same stage. Additional heat straps of the same material connect the shells to various components inside the receiver that require cooling, such as the reimaging lenses (see Section 2.2.2). Each of these inner shells is thermally connected to one stage of the PTC, again via high-purity aluminum strips as well as gold-plated copper interfaces. The PTC first stage, which reaches a temperature of approximately 50 K, attaches to the middle receiver shells, while the PTC second stage, which reaches a temperature of approximately 4 K, attaches to the innermost receiver shells. These two shells are thus often referred to as the 50-K and 4-K shells. Because the optics tube and backend sections of each PB-2 receiver use separate PTCs, the two sections can be cryogenically characterized individually before the full receiver is integrated and tested, simplifying the integration process.

In addition to providing cooling for elements within the receiver that could produce optical loading on the detectors, the backend PTC plays the crucial role of supplying a stage at which condensation of helium-4 (He-4) can occur, which is necessary for cooling the focal plane to sub-kelvin temperatures. In each PB-2 receiver, sub-kelvin refrigerators from Chase Research Cryogenics[8] are attached to the 4-K stage in the backend [67]. The Chase refrigeration systems used in the three PB-2 receivers are helium adsorption fridges, operating by way of evaporative cooling on three distinct fridge heads. One fridge head implements He-4, while the other two use He-3. The three fridge heads reach temperatures of approximately 1 K, 350 mK, and 250 mK, respectively, with each stage providing a buffer for the subsequent cooler stage. The 250-mK refrigerator cools the stage to which the detectors directly mount, allowing them to operate stably

[8] https://www.chasecryogenics.com/

on their superconducting transition. Heat straps constructed of flexible gold-plated copper foil with rigid gold-plated copper feet on the ends provide the thermal connection between the fridge heads and the corresponding temperature stages of the focal plane structure, as discussed in Section 2.2.3.

These helium adsorption refrigerators do not provide continuous cooling, and must be "recycled" (liquifying the helium) once the helium in any one of the three fridge heads has completely evaporated and cooling has ceased (referred to as the fridge "expiring"). Though the sub-kelvin cryogenic systems for all three receivers utilize Chase helium fridges, the specifications of each individual system vary slightly based on the target "hold time" of the receiver, defined as the amount of time between the fridge heads reaching their target base temperatures and the fridges expiring. A newer version of the Chase system was chosen for PB-2b, which increases the hold time compared to the system used in PB-2a. An additional He-4 "booster" fridge with a base temperature of around 1 K is also used in PB-2b, which further increases the hold time. (Specific characterization of the PB-2b cryogenic system is discussed in Section 3.4.) Based on the performance of the PB-2b combined sub-kelvin refrigeration system, a custom fridge was designed for use in the PB-2c receiver [67].

2.2.2 Optical Elements

As shown in Figure 2.14, the main optical elements contained within the receiver are reimaging lenses, a Lyot stop, a HWP polarization modulator, and a Zotefoam window (with index of refraction near one at relevant wavelengths [68]). Optical filters are also included in the system to prevent out-of-band radiation from reaching the detectors. The details of some of these elements are described below.

Reimaging Lenses

Three reimaging lenses are utilized within each PB-2 receiver optics tube in order to create a flat and telecentric focal plane in the backend. These refractive elements in the optical path are cooled to about 4 K via the optics tube PTC as described earlier so that thermal emission from the lens masses does not overwhelm the optical loading on the detectors.

The PB-2 lenses are machined from high-purity alumina (aluminum oxide, Al_2O_3), which has an index of refraction of about 3.1 [69, 70]. This relatively high index of refraction enables the lens surfaces to have larger radii of curvature while still focusing the light reasonably fast compared to other commonly used materials in mm-wave optics such as high-density or ultra-high-molecular-weight polyethylene [70]. Larger radii of curvature are beneficial because they are easier to machine precisely and easier to coat for anti-reflection (AR) purposes. Silicon is another choice for mm-wave optics, but manufacturing of large silicon pieces with robust AR-coating techniques for silicon has only been recently developed [71].

AR-coatings for the refractive elements in the PB-2 receivers are required to reduce reflections and achieve an acceptable level of optical efficiency, and to ensure the thermal loading remains small. Because each PB-2 receiver is sensitive in two observing bands, the optical elements must employ two-layer coatings to minimize reflections over a broad range of frequencies. Different techniques are used to coat the lenses in the different receivers for SA, dependent on the available technologies at the time of fabrication and on the various radii of curvature for different lenses and receivers. Lens surfaces in the PB-2a receiver are coated either with two layers of epoxy or with mullite and Skybond [69]. Two of the three lenses for the PB-2b receiver are coated via a two-layer plasma-spray technique [72]. An epoxy-coated lens has been fabricated for the remaining PB-2b lens, though there remains a possibility to replace this with a lens coated with mullite and Duroid as the epoxy coatings are less robust to thermal cycling (see Section 3.3). Lenses for the PB-2c receiver have not yet been coated.

The optical area of each lens in the system has a diameter of 470 mm. The lens materials

have extended diameters of about 500 mm in order to include a flange used for mounting and aligning the lenses with respect to the rest of the receiver and for attaching the heat straps. This optical area is significantly larger than that of the lenses utilized in PB-1, motivated by the increased number of pixels and thus increased focal plane diameter of PB-2. The lens surfaces are conically shaped, and two of the six surfaces are flat [61]. The detector-side of each lens is placed at a distance of approximately 250 mm, 740 mm, and 1170 mm from the focal plane. All lenses are mounted directly to the 4-K shell of the optics tube via custom mounting brackets that provide the necessary freedom to align the lenses accurately and repeatably. A photo of the installation of the lens that gets mounted closest to the focal plane in the PB-2b receiver is shown in Figure 2.15.

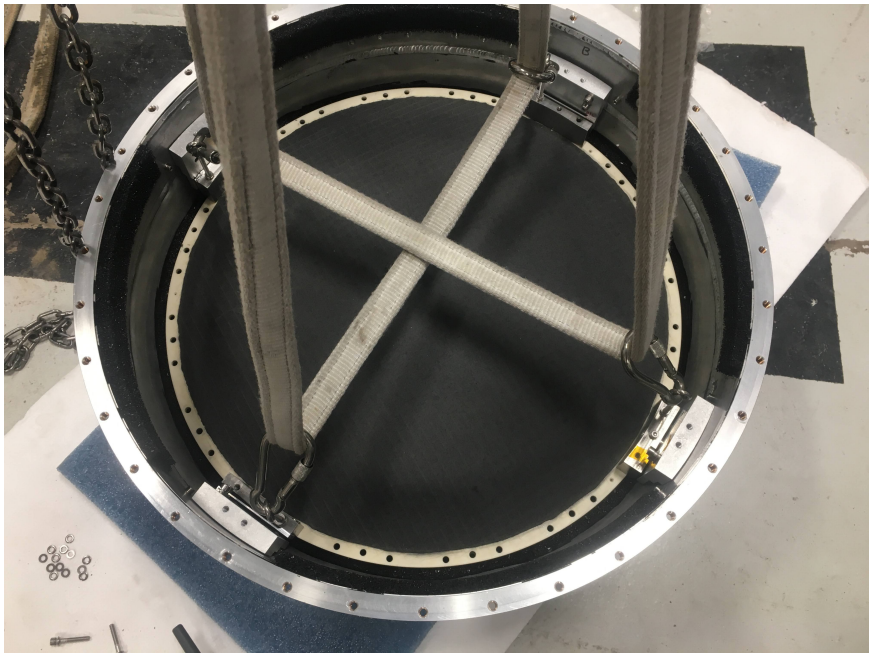

Figure 2.15: Photo of the epoxy-coated reimaging lens during installation in the PB-2b receiver. This lens gets placed nearest to the focal plane. The two other PB-2b reimaging lenses are coated for anti-reflection purposes using a different technique. Four mounting blocks along the edge of the lens attach the lens to the 4-K shell of the receiver's optics tube, a section of which is shown in the photo. Additional holes around the edge of the lens are used for installing high-purity aluminum heat straps, which thermally connect the lens to the receiver shell and thus the cold stage of the PTC. Installation of these heat straps was done after this photo was taken.

Filters

Optical filters are incorporated into the receiver system at different points along the optical path in order to block higher-frequency radiation from reaching the detectors[9]. Radio-transparent MLI (RT-MLI) [73] is located immediately after the window, with a cutoff frequency around 2000 GHz. One infrared (IR) filter, machined from alumina as is done with the lenses and AR-coated using similar techniques, exists as the receiver's first cold optical element. This filter measures 530 mm in diameter and is mounted to the middle shell of the optics tube, thus reaching a temperature near 50 K when the receiver is cooled. The filter is designed to transmit light at frequencies below 650 GHz [68].

Low-pass metal-mesh filters fabricated at Cardiff University exist at two positions in the optical path to further reduce loading, including from optical elements within the receiver [74]. Two filters are located at the Lyot stop, and another set of filters is positioned just before the focal plane, with one filter per detector wafer (seven filters total in this position). The filters placed at the Lyot stop are attached to the 4-K shell of the optics tube, while the other metal-mesh filters mount directly to the structure which holds the focal plane, thermally connected to the 350 mK fridge head. The filters are designed to have low-pass cutoff frequencies around 360, 261, and 188 GHz, in order from farthest to closest to the focal plane [68].

Polarization Modulators

One crucial optical element in each of the SA telescopes is the polarization modulator in the form of a half-wave plate (HWP). Time-varying fluctuations in the atmosphere can cause low-frequency noise in the polarization signal detected by the receiver through instrumental polarization effects [49, 75]. In order to make measurements of the faint degree-scale CMB polarization while maintaining reasonably slow telescope scan speeds (constrained both by telescope construction and by necessary mitigation of vibration-induced heating of focal plane

[9] On-chip band-defining filters are incorporated into the detector arrays.

elements) despite this time variation, continuous polarization modulation can be used in which the signal incident on the modulator is combined with a known modulation tone at a specified frequency. The signal seen by the detectors is then demodulated in analysis given the known modulation frequency in order to extract the input signal free from any instrumental effects introduced later in the optical chain. If the modulation frequency is sufficiently above the characteristic (or "knee") frequency of the noise, this noise term can be mitigated [75, 76].

In SA, this modulation is achieved through the use of a continuously rotating HWP located at the front end of each receiver, building on the successful implementation of a HWP at prime focus on the HTT with the PB-1 experiment. The principle of operation for polarization modulation via a HWP involves rotating a birefringent material (a stack of three sapphire pieces to provide modulation of a broadband signal, in the case of SA). Birefringent materials have a crystal structure such that the material's index of refraction is dependent upon the linear polarization state of the radiation, effectively producing a phase shift between two orthogonally polarized light waves as they pass through. When the material is rotated at a known, stable frequency, the polarized signal is modulated. This technique has the added benefit of allowing a single, linearly-polarized detector to measure both polarization states, removing the need to combine data from orthogonally polarized detectors within the same pixel in order to measure polarization and thus avoiding systematic errors due to mismatch between co-located detectors (such as bandpass mismatch or differential gain). Other polarization modulation techniques implemented in CMB experiments include the variable-delay polarization modulator, recently in use on the CLASS telescopes [77]. These are reflective optical elements that modulate incoming polarized radiation with the use of a polarizing grid and a flat mirror [78]. Reflective elements are often advantageous as they can be employed for a wide range of observing frequencies and do not require AR-coatings, but are more difficult to integrate on telescopes with larger optics like those in SA. PB-1 employed a continuously rotating HWP starting in 2014. Using this HWP, PB-1 was able to achieve a low-frequency noise knee frequency capable of measuring polarization signals

at low-ℓ ($\ell \sim 39$) [79].

In SA's Nicholas Simons Telescope with the PB-2a receiver, an ambient-temperature continuously rotating HWP supplies this polarization modulation and is mounted to the telescope's lower boom just in front of the receiver window (near the telescope's Gregorian focus) [80]. A cryogenic continuously rotating HWP which has the benefit of decreased optical loading on the detectors was then developed for use in the PB-2b and PB-2c receivers [81]. These HWPs are integrated with the receivers such that the sapphire stack is positioned between the alumina IR filter and the first reimaging lens in the optical path. The mechanism for rotating the sapphire stack is thermally connected to the 50-K shell of the optics tube, both cooling the sapphire and enabling the use of a superconducting magnetic bearing to provide continuous rotation.

2.2.3 Focal Plane

Each PB-2 receiver backend in SA contains a focal plane composed of 7,588 polarization-sensitive detectors. A photo of the assembled focal plane for the PB-2b receiver is shown in Figure 2.16. The detectors are fabricated on a set of seven hexagonal silicon wafers, each containing 271 pixels such that each pixel carries four optically sensitive detectors: two detectors sensitive to light in each of two frequency bands, with each sensitive to one of two orthogonal linear polarization states. Detectors in the PB-2a and PB-2b receiver focal planes are sensitive to light in frequency bands centered around 90 and 150 GHz, while the detectors in the PB-2c focal plane are sensitive to light in frequency bands centered around 220 and 270 GHz [82]. Additional "dark" detectors also exist on the focal plane that are not sensitive to optical signals and instead are used for characterization and calibration purposes. The majority of these detectors are not electrically connected to the readout electronics during normal operations.

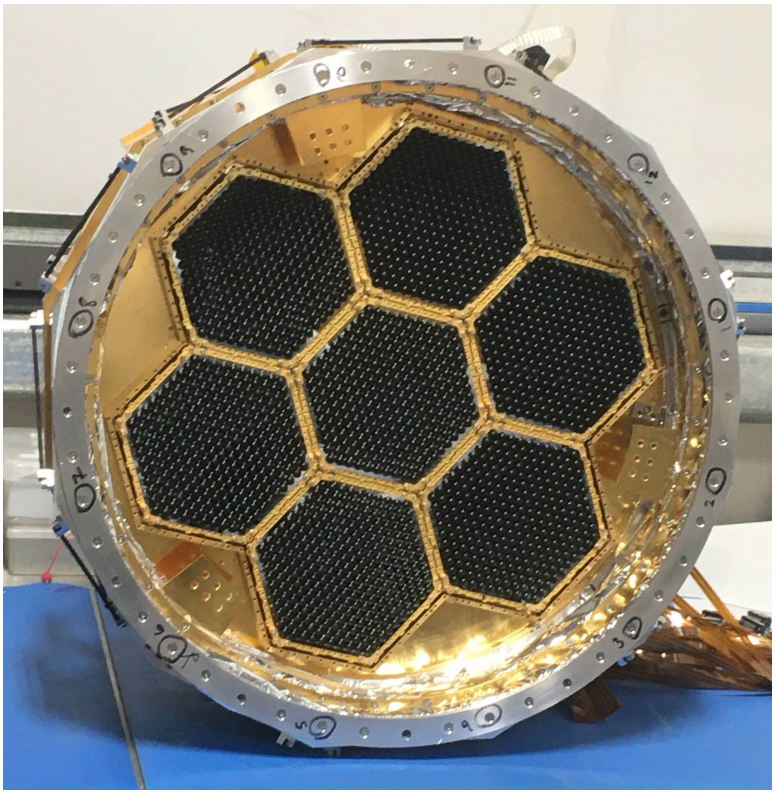

Figure 2.16: Photo of the complete focal plane in its assembly structure (focal plane tower) for the PB-2b receiver, viewed from the front or "sky" side, taken in 2021 during assembly at the SA telescope site. The focal plane is made up of seven hexagonal detector wafers, each measuring approximately 15 cm across.

Optical Coupling to Detectors

In SA, mm-wave radiation is optically coupled to the detectors via lenslet arrays. The lenslets, seen as the black components in Figure 2.16, are small, silicon lenses in the shape of extended hemispheres, each of which couples to a single pixel on the focal plane. These are fabricated in sets of 271 and assembled on silicon hexagonal arrays which directly mount to the detector arrays. Like the other optical components in the PB-2 receivers, the lenslets contain a two-layer AR-coating to maximize the optical efficiency of the system in the two observing bands. The lenslets for PB-2 have radii of 3.393 mm [83].

The first components (from the point of view of incoming radiation) of the detector arrays are sinuous antennas which lie directly below the lenslets [83]. There is one antenna per pixel.

The sinuous antenna, shown in Figure 2.17, is a broadband antenna with a log-periodic design that is capable of receiving light in both observing bands of the detector array [84].

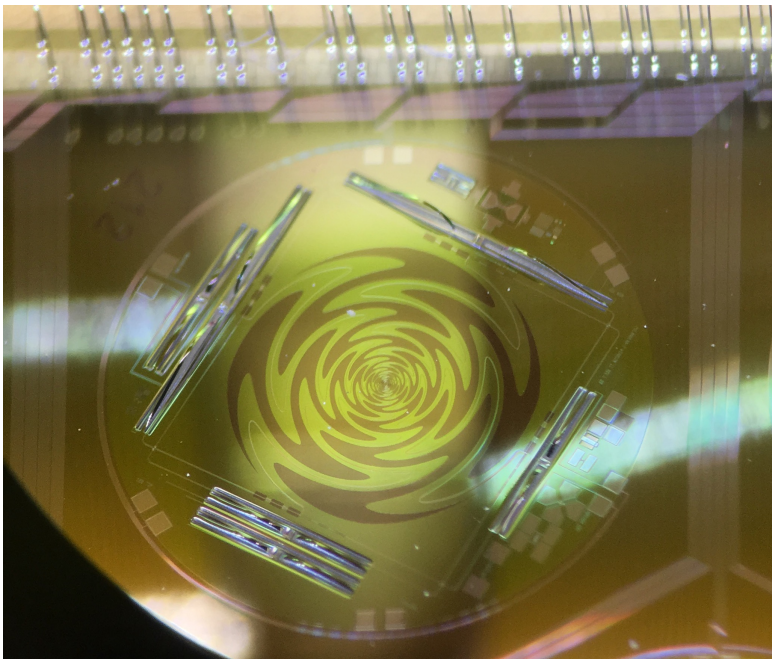

Figure 2.17: Photo of a single pixel on a PB-2 detector wafer. The spiral pattern in the center of the circular pixel is the broadband sinuous antenna. Six TES bolometers can be seen as the rectangular components surrounding the sinuous antenna. The four TESs closer to the antenna are coupled to the optical signal, with length corresponding to observing band. The two TESs farther from the antenna are dark bolometers (not coupled to the optical signal from the antenna) and are used for calibration.

Transition Edge Sensors

Detectors for SA are in the form of transition-edge sensor (TES) bolometers. Six TESs can be seen as the rectangular components surrounding the sinuous antenna in Figure 2.17 [82], and a schematic diagram of a TES is shown in Figure 2.18. In general, a bolometer consists of a thin film thermistor at temperature T that is weakly connected to a thermal bath maintained at a temperature T_{bath}, where $T_{bath} < T$. Optical power incident on the film gets absorbed and thus changes its temperature by ΔT. The power then gets dissipated to the thermal bath with a time constant that depends on the conductance of the thermal link, G, and on the heat capacity of

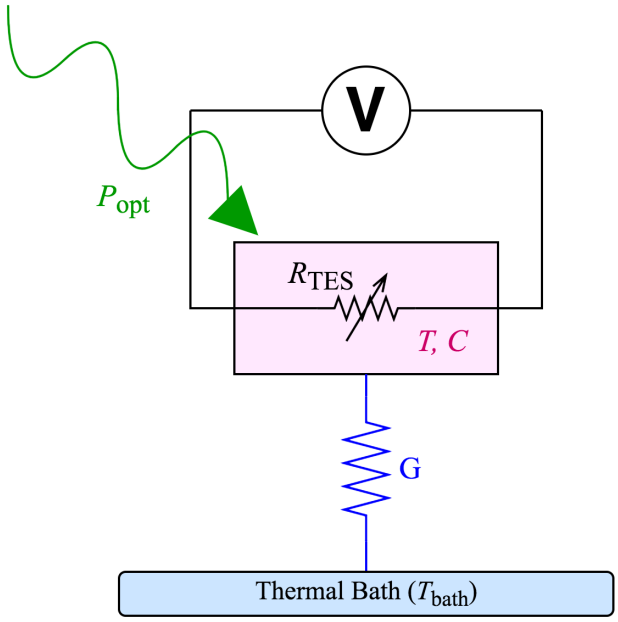

Figure 2.18: Schematic diagram of a transition-edge sensor, or TES, bolometer. A thermistor at temperature T and with heat capacity C, represented by the pink box with variable resistance R_{TES}, is weakly connected to a thermal bath at temperature T_{bath}, represented by the blue box, via a link with thermal conductance G. $T_{bath} < T_c$, the transition temperature of the TES, such that the TES can be maintained at a point along its superconducting transition via an electrical bias voltage. Incident optical power, P_{opt}, represented by the green arrow, can then be absorbed by the TES, heating it and creating a subsequent increase in R_{TES} and corresponding decrease in current through the TES which is measured. The voltage bias acts to ensure negative electro-thermal feedback such that as P_{opt} increases, the corresponding P_{elec} from the voltage bias decreases and the TES remains at its transition.

the film, C. The principle of operation of a bolometer is to measure the intensity of the incident optical power, and changes in its intensity, by measuring ΔT.

With a TES, the thermistor is made of superconducting material, and the thermal bath is maintained such that $T_{bath} < T_c$, the temperature at which the film becomes superconducting, known as the critical temperature. For these materials, there is a small temperature regime around T_c where the material is transitioning between a normal resistive state and a superconducting state. In this regime, very small changes in temperature (which, in the application of a bolometer as described above, can be caused by absorption of small amounts of optical power) correspond to

relatively large changes in resistance through the thermistor. This is illustrated in Figure 2.19, showing resistance as a function of temperature around T_c for a PB-2 TES bolometer. To produce

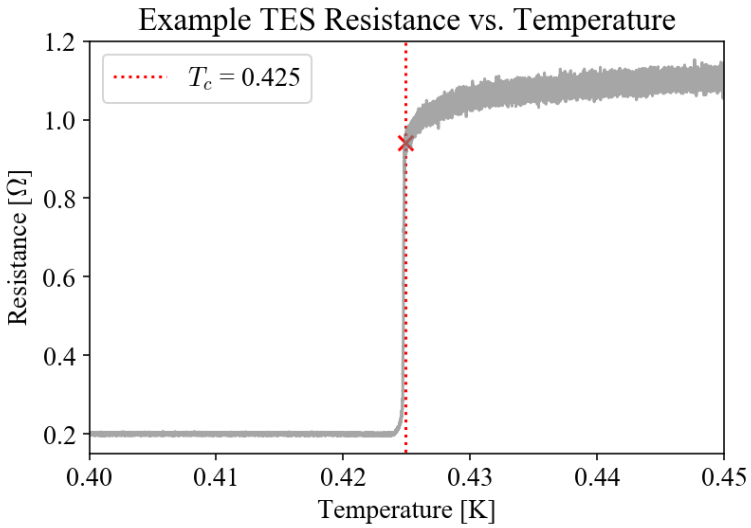

Figure 2.19: TES resistance as a function of temperature around the TES critical temperature, T_c, for an example PB-2b bolometer. At high temperatures, the TES is in its normal regime and acts as a resistor with constant resistance near 1 Ω. As the temperature is lowered, the TES transitions into its superconducting regime where the TES resistance is zero. Between these two regimes, while the TES is transitioning, its resistance drops dramatically with temperature, enabling measurements of very small changes in temperature. The TES critical temperature indicates the temperature at which this transition from the normal to the superconducting regime occurs. For PB-2, T_c is often defined as the temperature at which the TES resistance has dropped to 80% of its resistance in the normal regime, shown at 0.425 K with the red dotted line for this particular PB-2 bolometer. The measured and plotted resistance in the superconducting regime is non-zero due to stray impedance in the bias and readout circuit.

a measurable change in electrical signal across the TES as the optical power is absorbed and the thermistor's resistance changes, a initial electrical bias must be put in place. For PB-2 detectors, this bias is in the form of a voltage bias in order to create a negative electrothermal feedback loop in the system and enable it to operate stably. A bias power, P_{bias}, is applied across the TES to set the voltage bias. As optical power, P_{opt}, is incident on and absorbed by the TES, the TES's temperature and therefore resistance increase. Due to the constant voltage bias, V_{bias}, the increased resistance corresponds to a decrease in current through the TES, which corresponds to a decrease in P_{bias}. This inverse relationship between P_{opt} and P_{bias} prevents the thermistor from

experiencing increases in temperature during normal operating conditions that would otherwise drive it out of its transition [85].

The PB-2 TESs, along with the other components contained on the detector arrays, are fabricated at the University of California Berkeley Marvell Nanofabrication Laboratory [86]. The TESs corresponding to a single PB-2 pixel can be seen in Figure 2.17. These are custom-designed to have properties meeting the requirements of SA. The final design employs TESs made of aluminum manganese with a critical temperature of around 450 mK and a normal (above-T_c) resistance of 1 Ω [82]. Nominal operating power for the TESs, closely related to what is commonly referred to as saturation power, is specified for each TES dependent upon its targeted observing band [82].

The frequency band to which each TES is sensitive is defined using on-chip lumped-element filters along transmission lines running between the TES optical coupling and the TES. As noted, the TESs for the PB-2a and PB-2b receivers are designed to detect radition in bands centered at 90 and 150 GHz. Each observing band has a fractional bandwidth of approximately 30% [82].

Focal Plane Tower and Assembly

The mechanical structure that holds the focal plane is known as the focal plane tower (FPT). The FPT contains four metal stages which are thermally isolated from each via carbon fiber rods [87]. The warmest, "4-K" stage mates directly to the 4-K shell of the receiver backend at the point where it interfaces with the optics tube, while the colder stages mate to the fridge heat straps described in Section 2.2.1 and reach temperatures of approximately 1 K, 350 mK, and 250 mK. The detector arrays mate to this coldest, 250-mK stage which provides the necessary cooling of the TESs during operation. The warmer stages provide thermal intercepts for wiring from the detector arrays to reduce the loading on the coldest fridge heads. The FPT's 350-mK stage also serves the purpose of cooling and providing a mounting point for the metal mesh filters

described in Section 2.2.2. The bare mechanical structure is shown in Figure 2.20a.

Mechanical design of the FPT was motivated by thermal and spatial constraints, but also with the goal of minimizing the vibrational coupling between the receiver and the focal plane. Simulations of the structure were performed before construction to ensure avoidance of resonance frequencies that could potentially be excited by telescope motion [87].

Some of the readout electronics, as described in Section 2.2.4, are susceptible to interference from radio frequency (RF) radiation. For this reason, the 4-K cavity within the receiver backend is designed to be completely shielded from RF interference. Since the FPT is situated between the backend and the optics tube, it must provide an RF seal at this interface. Two pieces produce this RF seal. An inter-wafer RF shield is machined from a very thin piece of metal. This has hexagonal cutouts for the detector arrays and is positioned to prevent RF radiation from leaking into the backend through the gaps between arrays. The second piece consists of a "ring" of aluminized mylar to create a continuous conductive connection between the focal plane and the 4-K shell without creating excessive loading.

Assembly of the focal plane and FPT is done in steps. First, the seven detector modules (which include the detector arrays and their readout electronics as discussed in Section 2.2.4) are assembled individually and then installed into the machined hexagonal slots in the FPT's 250-mK stage. Once the detector modules are in place, the inter-wafer RF shield is added which closes the gaps between them. Braces are then installed on the back (readout side) of the modules to constrain their motion with respect to one another in order to further prevent vibrational motion of the focal plane. Wiring from the readout is then routed through custom parts connected to successively warmer stages. Finally, the MMFs and RF shield ring are installed on the front of the FPT and the fully assembled FPT is installed inside the receiver backend as a unit. Photos depicting some of the steps of this process are shown in Figure 2.20.

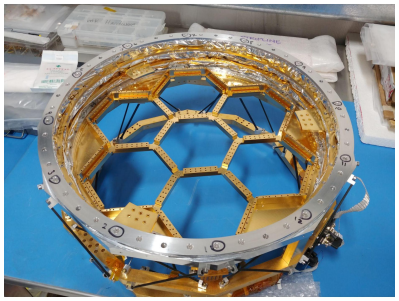

(a) Photo of the PB-2b focal plane tower, the mechanical structure that holds the detector modules.

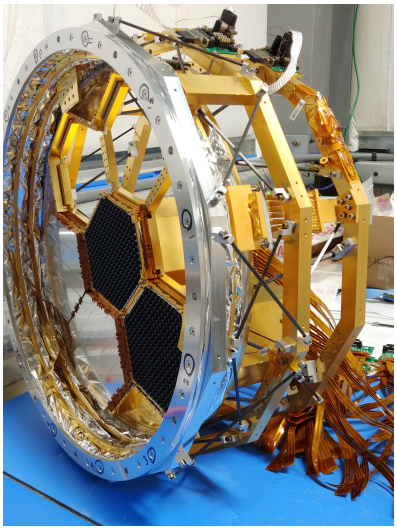

(b) Photo of the PB-2b focal plane tower after installation of four of seven detector modules.

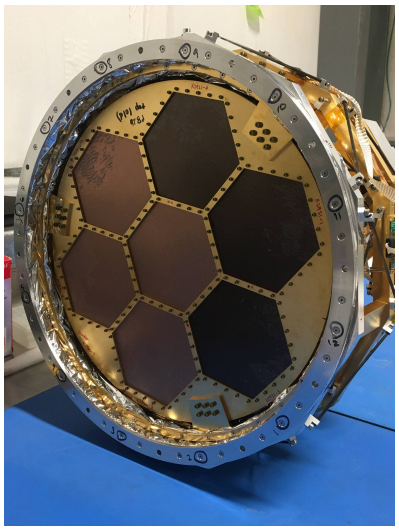

(c) Photo of the PB-2b focal plane tower after full assembly, including low-pass filters.

Figure 2.20: Photos of the focal plane tower for the PB-2b receiver at different stages of assembly. Photos were taken in 2021 during receiver assembly at the observatory site for installation on the telescope. Photo (a) shows the bare focal plane tower mechanical structure before any detector modules have been installed. Photo (b) shows the focal plane tower after installation of four out of seven detector modules. The hexagonal wafers with black lenslet couplings are visible on two wafers, while the lenslets on the other two wafers are covered by plates used for protection of the wafer modules during assembly. Photo (c) shows the focal plane tower after its full assembly. The hexagonal pieces visible in front of the detector modules are the low-pass metal-mesh filters. Photos (a) and (b) thanks to Jennifer Ito.

2.2.4 Readout System

The readout system for SA refers to the set of electronics required to operate and collect data from the detectors. This includes both cryogenic and ambient-temperature components.

With the large numbers of detectors needed for modern CMB polarization experiments, a few different types of readout schemes have been and are currently being implemented. This includes time-domain multiplexing [53, 85], digital frequency-domain multiplexing [88], and microwave-multiplexing [41]. Multiplexing refers to the method of operating and reading out several (N) detectors on a single pair of wires, which is essential for experiments with tens or even hundreds of thousands of detectors because it reduces the wiring complexity within the

receiver and reduces the thermal loading on the fridges. SA utilizes a digital frequency-domain multiplexing (DfMux) scheme, and has been part of the effort to scale this technology to higher multiplexing factors.

Digital Frequency Multiplexing

SA's DfMux readout system was developed by a team at McGill University to be used in SA and SPT-3G, and builds on the system implemented in the PB-1 and SPTpol experiments. A schematic diagram of the system implemented in the PB-2 receivers, which employs a multiplexing factor of $N = 40$, is shown in Figure 2.21. This is a significant increase over the multiplexing factor of the PB-1 readout system, which had $N = 8$. In this system, each detector, represented in

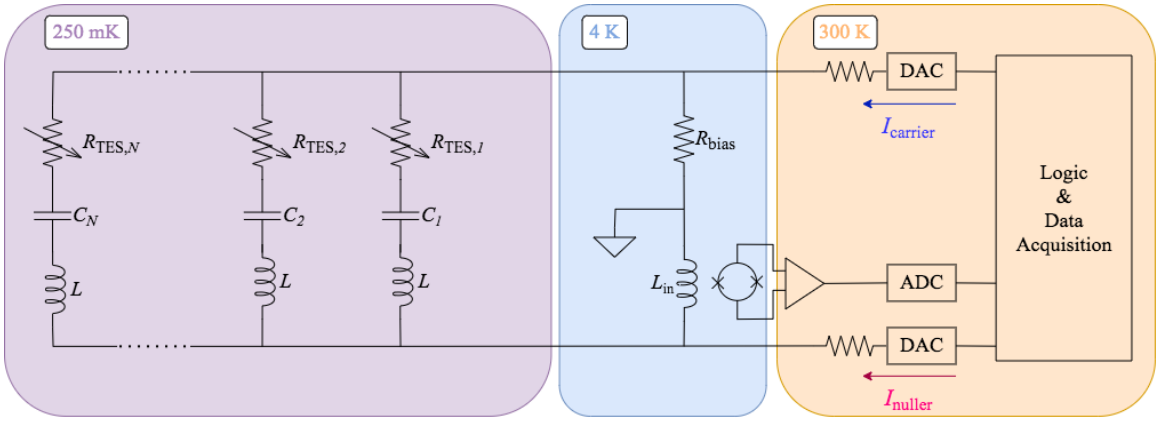

Figure 2.21: Circuit diagram schematic for the PB-2b readout system utilizing digital frequency-domain multiplexing, showing the circuit for a single readout module with multiplexing factor $N = 40$. An *LC* resonator is placed in series with each TES ($R_{TES,i}$) in the module, with each resonator in the circuit having a distinct capacitance and therefore a distinct resonant frequency within the 1.6−4.6 MHz band. The 40 *RCL* circuits are connected in parallel, and bias tones at each resonant frequency are generated by room temperature electronics. The individual tones are amplitude-modulated based on the resistance of the corresponding TES. The tones are then summed and combined with a nulling signal, and the resulting current is amplified using a SQUID array before it is returned to room temperature electronics and demodulated. Additional low-frequency feedback exists between the output of the SQUID array and its input coil but is not shown here.

the diagram as a variable resistor, $R_{TES,i}$, is connected in series to an *LC* resonator, and the 40 *RCL* circuits within a single readout module are connected in parallel. The set of *RCL* circuits

for a module is often referred to as a "comb" because of the series of peaks shown in a network analysis of the admittance of the bolometer circuit (see Figure 2.23). The resonators consist of a capacitor, C_i, and an inductor, L. All inductors have the same inductance with $L = 60\ \mu H$, but each capacitor within a readout module has a distinct capacitance, thereby creating a distinct resonant frequency for each *RCL* circuit. Capacitance values vary between 21 pF and 161 pF, resulting in resonant frequencies between 1.6 and 4.6 MHz. The spacing between resonator frequencies is such that neighboring resonators (in frequency space) are no less than 40 kHz apart, motivated by the need to keep crosstalk (the signal from one detector influencing the measured signal from another) low [89]. With this configuration, an electrical signal consisting of several voltage bias "tones" can be injected on a single wire, and each tone will be directed through the *RCL* circuit with that corresponding frequency. As a TES absorbs incident optical power, it will amplitude-modulate the current through only its circuit element. The individual tones can be summed again after the resonator elements, where the combined signal is amplified and transmitted outside the receiver. Ambient-temperature electronics are then able to demodulate the signal so that data from individual detectors can be collected and evaluated.

The 40 *LC* resonators for each readout module are made of niobium and fabricated onto a single piece of silicon which is adhered to a printed circuit board (PCB) and enclosed by an aluminum shield. 30 of these boards are mounted to the back of each detector wafer assembly and electrically connected via flexible cables, ideally enabling readout of 1,080 optical detectors, 60 dark detectors, and 60 calibration resistors (located on the *LC* PCBs) per wafer. Photos of a single *LC* PCB and of a nearly assembled detector module containing the wafer module and 30 resonator circuits is shown in Figure 2.22. (A fully assembled module would include a gold-plated copper radiation enclosure covering the mounted *LC* PCBs.) Signals to and from the cold *LC* PCBs are carried via the custom niobium-titanium low-inductance cabling shown in the figure.

Although the PCBs are designed with specific resonator frequencies in mind, exact operating frequencies for each circuit vary based on unavoidable small variations in the fabrication

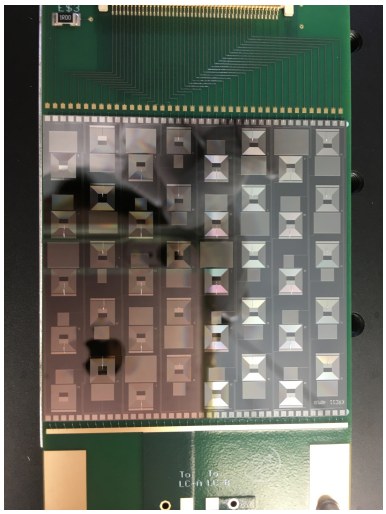

(a) Photo of an *LC* PCB with resonator chip visible.

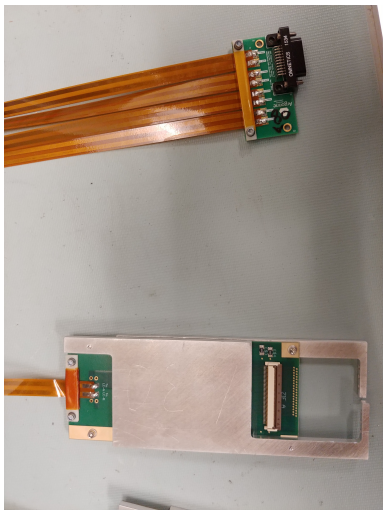

(b) Photo of an *LC* PCB with cabling and aluminum shield.

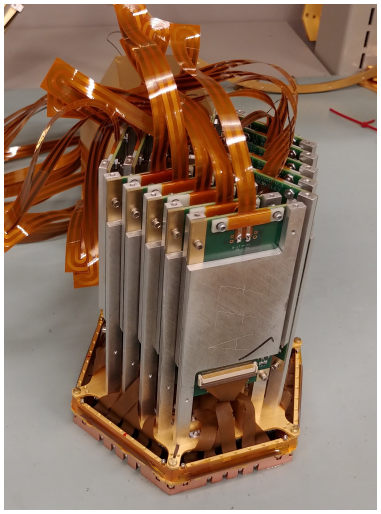

(c) Photo of a detector module after installation of *LC* PCBs.

Figure 2.22: Photos of *LC* resonator components used in the PB-2 receivers' DfMux readout system. Photo (a) shows a single chip with 40 *LC* resonators mounted onto its *LC* PCB. Photo (b) shows an assembled *LC* PCB with its aluminum shield and custom niobium-titanium cabling. The PCB seen in the photo at the other end of the cabling connects to a PCB holding SQUID amplifiers. Photo (c) shows a nearly assembled detector module. The detector and lenslet wafers are located at the bottom of the image in hexagonal packaging. The shielded *LC* PCBs mount directly to the back of this detector housing. 30 *LC* PCBs are needed per detector module. The *LC* PCBs are assembled back-to-back in sets of two. Complete assembly of a detector module includes installation of a gold-plated copper enclosure that surrounds the *LC* PCBs and serves as a radiation shield. Photos (b) and (c) thanks to Jennifer Ito.

process. For this reason, resonator frequencies for each *LC* PCB are measured after it has been installed within a detector module through a network analysis in which carrier tones in frequencies throughout the expected range of around 1.6-4.6 MHz, usually with a resolution of about 0.5 kHz, are generated and sent through the system with the TESs superconducting. A generated tone will pass through the circuit and create a signal on the output if it matches a resonator frequency, but will instead be directed to the electrical ground point through the bias resistor if it does not. An example of the result of this procedure is shown in Figure 2.23, where output signal is plotted against input tone frequency. Peaks in the data indicate resonator frequencies, and successive detector operations can be performed by generating bias tones only at these frequencies.

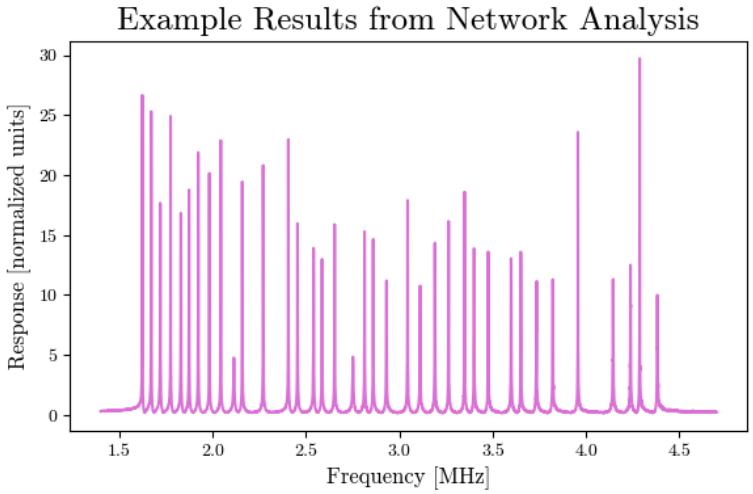

Figure 2.23: Example results from network analysis for a single set of *LC* resonators and corresponding TESs. The data is obtained by sending carrier and nuller tones in a range of frequencies through the readout system and measuring the response. The peaks correspond to resonant frequencies of the *LC* circuit. Network analyses such as this are used to determine the bias frequencies that are needed to operate and read out detectors. Due to variations in the fabrication process, these bias frequencies are not identical for all combs, and not all combs have perfect yield of detectors and resonators. 37 peaks can be seen in this network analysis, out of a maximum 40 possible.

Superconducting Quantum Interference Devices

As in other CMB experiments, including PB-1, SA utilizes superconducting quantum interference devices (SQUIDs[10]) as preamplifiers in its readout systems due to their low-impedance and low-noise properties [88, 91]. One SQUID is used per set of *LC* resonators, thereby reading out up to 40 channels. A SQUID is made of a superconducting loop containing two Josephson junctions. The junctions consist of two superconductors coupled through a weak link, generally made of non-superconducting material. Current is able to flow freely through this type of junction without resistance up to a certain threshold called the critical current, $I_{c,JJ}$, at which point a voltage will develop across the junction and increase with further increases in current. With two (identical) Josephson junctions configured in a SQUID, current passed through the SQUID is

[10]In this writing, SQUID is used to refer to a DC SQUID rather than an RF SQUID. RF SQUIDs involve a superconducting loop with a single Josephson junction, and have been used in different applications, including in the Simons Observatory's microwave multiplexing readout system [90].

split between the two junctions, and a voltage will develop across the SQUID only once the input current surpasses twice the critical current of a single junction ($I_c = 2I_{c,JJ}$).

SQUIDs are used as magnetometers because of the properties of a superconducting loop. Magnetic flux through a superconducting loop is quantized such that

$$\Phi = n\Phi_0 = n\frac{h}{2e}, \tag{2.1}$$

where Φ is the flux through the superconducting loop, n is an integer, and $\Phi_0 = h/2e$ with h being Planck's constant and e the elementary charge [92]. Thus, in the presence of a magnetic field, an additional current is induced along the SQUID loop in order to either cancel out or add to the magnetic flux to satisfy Eq. 2.1. In measuring this induced current by measuring the voltage across the SQUID, one can determine the magnetic flux of the external field.

Within the PB-2 readout system, SQUIDs serve to amplify the signal from the detectors by sending the signal through an inductor, known as the SQUID input coil and represented by L_{in} in Figure 2.21. When the signal moves through this input coil, a magnetic field is created that is proportional to the current from the detectors. The SQUID converts this to a voltage which is then passed to successive components in the readout system. Though not explicitly shown in the figure, additional low-frequency feedback between the output of the SQUID and its input coil serves to account for slow variations in the external (not produced by either the signal or the bias) magnetic field during observations [93].

Precisely measuring the current through the input coil requires tuning the SQUID into a regime where it is sensitive to the expected external magnetic flux. This tuning is achieved via two biases. A current bias, $I_{bias} > I_c$, is applied across the SQUID such that the current through each Josephson junction in the superconducting loop is above the critical current of the junctions, allowing a voltage to develop across the loop even in the absence of magnetic flux. A separate bias referred to as a flux bias, generated as a current sent through the input coil or other nearby

inductor, then creates an external magnetic flux, Φ_{bias}, through the SQUID loop. Figure 2.24 illustrates this operation, indicating the current bias, the flux bias, and the signal.

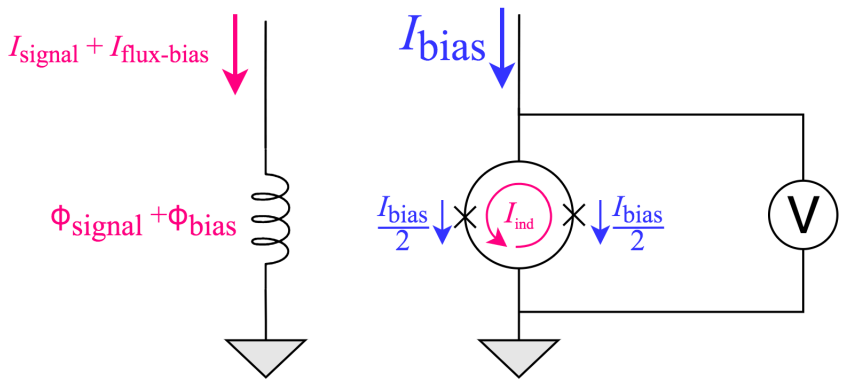

Figure 2.24: Schematic diagram of SQUID operation. The SQUID consists of a superconducting loop interrupted by two Josephson junctions, represented by $\times$ marks. A bias current, I_{bias}, represented in blue, is applied across the SQUID loop and is split between the two junctions. In the presence of a magnetic field, an additional, induced current, I_{ind}, shown in pink, develops around the SQUID loop in order to cancel out or add to the magnetic flux through the loop such that it is equal to an integer number of flux quanta. As long as the total current through the SQUID is greater than the SQUID's critical current, I_c, a voltage can be read out. Changes in this voltage correspond to changes in induced current, which correspond to changes in the external magnetic field. This allows the SQUID to precisely measure a current signal, I_{signal}, shown in pink, that is sent through a nearby inductor. The bias current and an additional flux bias, Φ_{bias} induced by $I_{flux-bias}$, also shown in pink, are chosen such that the SQUID sensitivity to changes in this current signal is optimized.

Figure 2.25a shows the results of output voltage measurements under a set of current and flux bias combinations, referred to as a voltage-flux or $V-\Phi$ curve. This is formed in practice by setting I_{bias}, sweeping through several values of Φ_{bias}, and repeating for additional I_{bias} values. The curve for each I_{bias} choice above the SQUID's critical current is periodic as Φ_{bias} is swept through several flux quanta. Peaks in the $V-\Phi$ curve indicate instances when the external flux generated by the flux bias is equal to a half-integer number of flux quanta, necessitating a large induced current around the SQUID loop. Troughs in the curve indicate instances when the external flux is equal to an integer number of flux quanta, in which case there is no induced

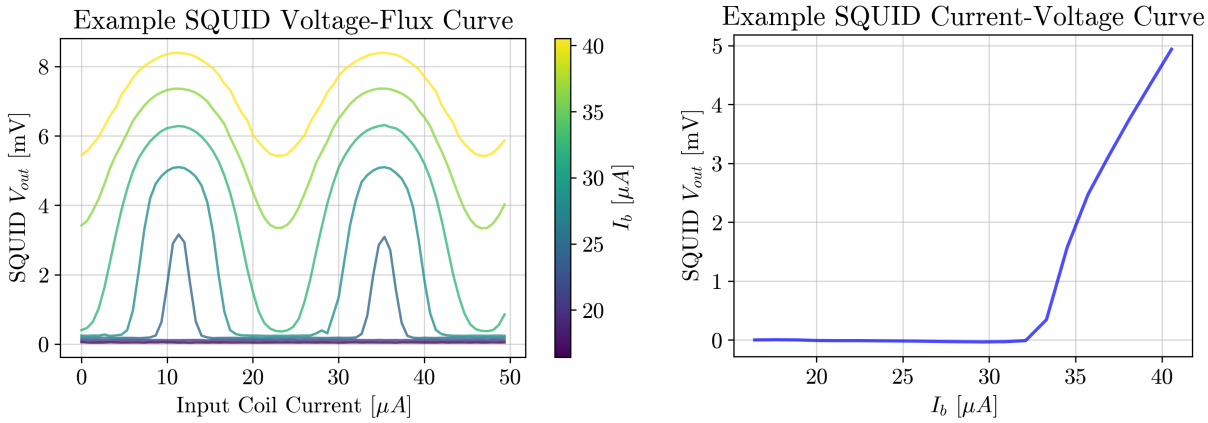

(a) Voltage vs. flux curve for a SQUID array.

(b) Corresponding current vs. voltage curve.

Figure 2.25: SQUID voltage vs. flux ($V-\Phi$) and current vs. voltage (IV) curves for a single SQUID array. Each curve in Figure (a) measures the voltage response as a function of flux bias (generated by current through the input coil) for a given bias current. The flux bias modulates the output voltage as different levels of magnetic flux induce different amounts of current through the SQUID loop. The IV curve in Figure (b) plots the minimum output voltage as a function of bias current, accounting for a linear drift. Only when the bias voltage increases above the SQUID's critical current does an output voltage develop across the SQUID.

current around the SQUID loop. Before using SQUIDs to read out detector signals, optimal bias points for each device are determined such that the SQUID lies roughly between a peak and a trough where it is most sensitive to changes in the magnetic flux and therefore to changes in current through the input coil. Figure 2.25b shows the corresponding plot of minimum output voltage (corresponding to the troughs in the $V-\Phi$ curves) as a function of bias current[11] (IV curve). As can be seen in both plots, the output voltage is zero for bias currents less than the critical current of the SQUID. Below this threshold, only in the presence of magnetic flux at near half-integer flux quanta values is the output voltage measured to be non-zero. Above this threshold, the output voltage is measured to be non-zero for all values of magnetic flux, though changes in magnetic flux still modulate the voltage.

Application of SQUIDs, particularly in SA and in many other CMB experiments, involves connecting SQUID elements into arrays in which the many SQUIDs work together as an amplifier.

[11] A linear detrend is applied to the data to account for parasitic resistance in the circuit that would otherwise show non-zero output voltage at low current bias)

This is the case for both PB-1 and SA, which utilize the SA4b and SA13a SQUID array designs from the National Institute of Standards and Technology, respectively[12]. Configuring the SQUIDs in arrays with elements both in parallel and in series enables the gain, dynamic impedance, input-referred noise, and input inductance to be tuned for specific applications [94]. The SA13a SQUID arrays used in the PB-2 receivers for SA are configured as 3 banks of SQUIDs in series $\times$ 2 banks in parallel, with each bank of SQUIDs containing 64 SQUID elements in series [94]. Details about how this SQUID array design was chosen are described in Section 3.2.

SQUID arrays are assembled onto custom SQUID PCBs in sets of eight which are installed with magnetic shields in each PB-2 receiver backend at the 4-K shell. Photos of assembled SQUID PCBs are shown in Figure 2.26. Two different versions of the SQUID PCB (versions 7 and 8) are used in SA. The main difference between the two designs is that version-7 PCBs employ a 2-point connection to the SQUID input, while version-8 PCBs employ a 4-point connection, as seen in Figure 2.26a. SQUID arrays in the PB-2a receiver are mounted on version-7 PCBs, while SQUID arrays in the PB-2b receiver are mounted primarily on version-8 PCBs. Each SQUID PCB is thermally attached to the 4-K shell via heat straps made of gold-plated copper. Edge connectors on the SQUID PCBs electrically connect the SQUID arrays to wiring that leads out of the receiver to the ambient-temperature readout components. Electrical connections between the SQUID chips and the SQUID PCBs are made through aluminum wirebonds. The custom cabling from eight *LC* resonator PCBs feeds into one connector which mates to the SQUID PCB. A total of 210 SQUID arrays, one for each *LC* PCB, are required to read out a full PB-2 focal plane. These are installed in the receiver across 28 SQUID PCBs[13].

[12] Choice of SQUID design for use in the PB-2c receiver is not yet finalized, but the SA13a design is used in PB-2a and PB-2b.

[13] Not all $28 \times 8 = 224$ available slots on the SQUID PCBs are populated with an active SQUID array; seven of the 28 PCBs only contain six active SQUID arrays. The SQUID arrays and PCBs are distributed in this way due to constraints from connections made to the *LC* PCBs and detector wafers.

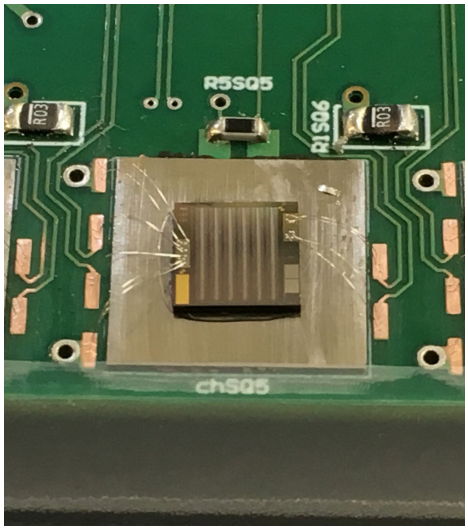

(a) Photo of a single SQUID chip populated onto a SQUID PCB, connected to the PCB via aluminum wirebonds.

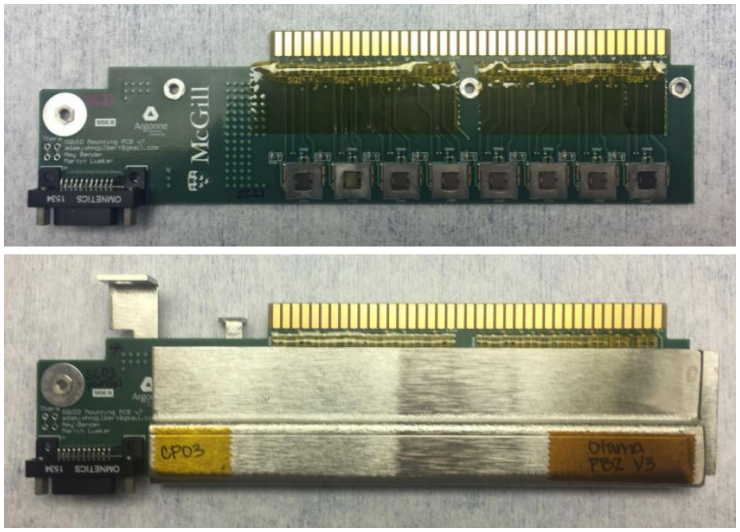

(b) Photos of a SQUID PCB fully populated with eight SQUID chips, with (bottom) and without (top) magnetic shielding installed.

Figure 2.26: Photos of SQUID PCBs populated with SQUID chips. The SQUID chips (NIST SA13a design shown) are connected to the PCBs via aluminum wirebonds. A maximum of eight SQUID chips can be populated onto a single SQUID PCB. The black connector on the left side of the SQUID PCB connects to cabling that routes to the *LC* PCBs, and the edge connector shown at the top of the SQUID PCB connects to wiring on the receiver's 4-K shell that leads to ambient-temperature electronics outside the receiver. The SQUID PCB with its magnetic shielding is shown in the bottom panel of Figure (b).

Digital Active Nulling

A significant difference between the PB-1 and SA readout system is the use of digital active nulling (DAN) with SA [93, 95]. With DAN, additional narrow-band nulling tones (I_{nuller} in Figure 2.21) are generated by the ambient-temperature readout electronics along with the carrier tones ($I_{carrier}$) at the same frequencies. The nuller tones, however, are continuously adjusted in amplitude and phase based on feedback from the SQUID, and are injected into the circuit at a point between the *RCL* comb and the SQUID input coil. The currents are not meant to flow through the resonators and TESs, but rather to combine with the carrier tones at this junction and cancel them out such that the signal through the SQUID input coil is nearly zero. The incorporation of this precise, active feedback loop means that it is easier to maintain the

SQUID operating point within its linear regime even when the signal from many TESs may be changing. This eliminates the need for a shunt-feedback circuit to around the SQUID [88] implemented in the PB-1 readout system, which limited the bandwidth of the readout system and thus the achievable multiplexing factor. Utilization of DAN directly enables the use of the 1.6-4.6 MHz band for readout, corresponding to SA's increased multiplexing factor and ability to readout significantly more detectors than PB-1. The DfMux system for SA is designed for a multiplexing factor of 40, but other systems that implementing the same readout technology have achieved multiplexing factors up to 68 and higher [96].

Ambient-Temperature Electronics and System Summary

The ambient-temperature electronics for the PB-2 DfMux system comprise three components: a SQUID controller board, a mezzanine, and a motherboard. Each SQUID controller board controls four SQUID arrays, so two of these boards are needed for each SQUID PCB. The SQUID controller boards connect directly to connectors on the outside of the PB-2 receiver vacuum shell so that the (still small) signals output by the SQUID arrays and transmitted outside the receiver can be immediately amplified [97]. An aluminum structure with conductive gasket is placed around the set of SQUID controller boards on the receiver to create an RF shield around these electronics. These boards also provide the biases needed to tune the SQUID arrays. On the other hand, the mezzanines and motherboards live in the electronics enclosures described in Section 2.1.3. Each mezzanine corresponds to one SQUID controller board, and each motherboard connects to two mezzanines. The mezzanines hold the electronics primarily responsible for generating the carrier and nuller tones and for synthesizing the output signals [93, 97]. The motherboards carry a field-programmable gate array and are responsible for digital signal processing and data streaming [97]. A list of the detector and readout components, and the number of each type required for reading out a full PB-2 focal plane, are indicated in Table 2.1.

Table 2.1: List of readout components required for a single PB-2 receiver. Components are listed by location in the readout circuit, which also corresponds to the temperature stage at which they are located. Both cryogenic and ambient-temperature components are included.

Readout Component	Number Required	Temperature Stage
Detector wafers	7	250 mK
LC PCBs	210	250 mK
SQUID arrays	210	4 K
SQUID PCBs	28	4 K
SQUID controller boards	56	300 K
Mezzanines	56	300 K
Motherboards	28	300 K

2.3 Science Goals

The Simons Array's primary science goals focus on further characterization of the CMB's *B*-mode power spectrum. The first of these goals is to put constraints on the predicted *B*-mode signal from inflationary gravitational waves. As noted in Section 1.3.4, this signal is expected to peak at angular scales of $\ell \approx 100$, corresponding to roughly degree-sized features. The second is to use polarization measurements to reconstruct the lensing potential. The signal from gravitational lensing, described in Section 1.3.3, peaks at angular scales of $\ell \approx 1000$, corresponding to features roughly a few arcminutes in size. Measurement of the lensing power spectrum not only will provide data with which SA and other CMB experiments can de-lens the total *B*-mode signal, thus improving constraints on inflation, but will also be used to put constraints on the total neutrino mass. SA's ability to make polarization measurements at angular scales between $\ell = 50$ and $\ell = 3000$ is designed specifically for these two goals. Additionally, SA will be able to use *E*-mode measurements to constrain N_{eff} (related to the energy density of light, weakly-coupled particles) [98] and n_s (the spectral index of scalar fluctuations), and will probe physics beyond ΛCDM and inflation such as cosmic birefringence and primordial magnetic fields using the *EB* cross spectra (expected to be zero in standard cosmological models) [48, 99].

To forecast the level of constraining power an experiment's data will have on these types of

cosmological parameters, models are often used that take into account the experiment's instrument sensitivity, fraction of the sky to be observed, and observing time and efficiency. These types of sensitivity calculators can also be used to inform instrument design and technological choices to ensure the experiment's technical design will allow it to meet its science goals. One sensitivity calculator, BoloCalc [75, 100], was designed for use with the Simons Observatory. Though it was developed after much of SA's technical design had been finalized, BoloCalc has been used within SA for sensitivity forecasting.

Instrument sensitivity is calculated by examining the noise contributions from different parts of the system. These noise contributions are often quoted in the form of a noise-equivalent power (NEP), which corresponds to the power a signal would need to have to reach a signal-to-noise of one in a one-Hertz output bandwidth, or, equivalently, after measuring for 0.5 seconds. For CMB experiments like SA, the total NEP for a detector has contributions from photon noise, thermal carrier noise in the TESs, and readout noise[14]:

$$\mathrm{NEP}_{det} = \sqrt{\mathrm{NEP}_{\gamma}^2 + \mathrm{NEP}_{G}^2 + \mathrm{NEP}_{readout}^2}. \tag{2.2}$$

These contributions are added in quadrature, as shown, assuming they are white (equal intensity at all frequencies) and uncorrelated, and have units of [power]/$\sqrt{[\text{frequency}]}$. Photon noise ($\mathrm{NEP}_{\gamma}$) arises from the fundamental fluctuations in photon arrival time and is related to the optical power on incident on the bolometers. Thermal carrier noise (NEP_{G}) comes from fluctuations in the heat flow between the TES thermistor and the thermal bath to which it is connected via a link with thermal conductance G. Readout noise ($\mathrm{NEP}_{readout}$) contains contributions from several sources in the readout system, including the SQUID arrays. The readout noise contribution is generally characterized as a noise-equivalent current ($\mathrm{NEI}_{readout}$) as referred to the input to the SQUID amplifier, which has units of [current]/$\sqrt{[\text{frequency}]}$. In order to convert this to an NEP

[14] Johnson also exists due to thermal fluctuations in the bolometer, but for modern CMB experiments the contribution from Johnson noise is often negligible compared to other noise sources and thus is left out in this discussion.

on the bolometer, it must be divided by TES responsivity (sensitivity to changes in optical power, dI_{TES}/dP_{opt}).

For CMB experiments, it is then useful to convert the NEP into a noise-equivalent CMB temperature (NET) with units of [temperature]$\sqrt{[\text{time}]}$. Similar to NEP, NET is defined as the fluctuation in CMB temperature that would create a signal-to-noise ratio of one after one second of integration time. This conversion must account for the change in power seen at the bolometer for a given change in CMB temperature on the sky (dP/dT_{CMB}), and is given by

$$\text{NET}_{det} = \frac{\text{NEP}_{det}}{\sqrt{2}\frac{dP}{dT_{CMB}}}. \tag{2.3}$$

The factor of $\sqrt{2}$ arises because we are defining NET by an integration time of one second rather than a bandwidth of one Hertz. Because CMB experiments employ arrays of detectors whose data are combined when making maps of the sky, the sensitivity is improved and we can define an array NET as [100]

$$\text{NET}_{arr} = \frac{\text{NET}_{det}}{\sqrt{YN_{det}}}\Gamma \tag{2.4}$$

where N_{det} is the total number of detectors, Y is the fractional detector yield, and Γ represents the degree to which noise is correlated between different detectors. Thus, experiment sensitivity increases as the square root of the number of operational detectors, motivating the large increase in detector count from PB-1 to SA, and in other current CMB experiments.

Finally, the noise in the resulting CMB maps can be calculated from a given NET_{arr} by accounting for the size of the observed sky patch and the observing time. This measure, known as map depth, determines how precisely an experiment can measure the CMB, and therefore how well it can constrain different parameters. Increasing the observing time and decreasing the sky coverage improve map depth.

SA is planned to operated for five years, with different receivers coming online at different times, and to observe the patches of the sky described in Section 2.1.2. Estimates of SA sensitivity

indicate its ability to place upper bounds on the tensor-to-scalar ratio and the sum of the neutrino masses of $r \leq 0.02$ and $\sum m_\nu \leq 40$ meV[15]. On-sky measurements with the PB-2a and PB-2b receivers in the coming months (see Chapter 4) will provide better estimates of NET_{arr} values to better understand SA's expected constraining power.

2.4 Acknowledgements

Figure 2.21 with its caption is an updated reprint of a figure published in J. Ito, L. N. Lowry, T. Elleflot, K. T. Crowley, L. Howe, P. Siritanasak, T. Adkins, K. Arnold, C. Baccigalupi, D. Barron, B. Bixler, Y. Chinone, J. Groh, M. Hazumi, C. A. Hill, O. Jeong, B. Keating, A. Kusaka, A. T. Lee, K. Mitchell, M. Navaroli, A. T. P. Pham, C. Raum, C. L. Reichardt, T. J. Sasse, J. Seibert, A. Suzuki, S. Takakura, G. P. Teply, C. Tsai, and B. Westbrook, "Detector and readout characterization for POLARBEAR-2b," in *Millimeter, Submillimeter, and Far-Infrared Detectors and Instrumentation for Astronomy X* (J. Zmuidzinas and J.-R. Gao, eds.), vol. 11453, pp. 286 - 301, International Society for Optics and Photonics, SPIE, 2020. The dissertation author was second author on and made essential contributions to this work.

The dissertation author thanks Jennifer Ito for providing the data shown in Figure 2.19 and the analysis code used to present it.

[15] This projected constraint on $\sum m_\nu$ assumes SA data is combined with BAO measurements from DESI [101]. This number is notably lower than the upper bound of 60 meV set by oscillation experiments as noted earlier, indicating that a detection of neutrino mass by cosmological measurements is possible in the near future.

Chapter 3

Lab Characterization of the PB-2b Receiver

The PB-2b receiver went through a series of measurements at UCSD during various points in its development prior to assembly in the field in preparation for later installation on the Paul Simons Telescope. These measurements of both the individual subsystems and the integrated receiver serve to certify that chosen components will work reliably under normal observing conditions in Chile and that they have expected properties that meet design requirements. Particularly with regard to cryogenic components, replacement in the field is time-consuming and costly, and risks further damage. We thus want to be confident all components for use in the field are working as expected in the lab before the receiver gets integrated with the telescope. For experiments like the Simons Array, where control of systematic effects is crucial in achieving the sensitivity needed for making meaningful measurements of the CMB's faint polarization signal, these laboratory measurements also provide the opportunity to understand procedures for performing precise on-sky characterization of various system properties which are used as inputs in the analysis in order to accurately account for instrumental effects.

Section 3.1 discusses measurements of PB-2b detector properties prior to deployment of

the receiver. Section 3.2 details measurements of the readout system, with a particular emphasis on the SQUID array amplifiers. Sections 3.3 and 3.4 briefly describe in-lab characterization of the receiver's optical and cryogenic systems.

3.1 Detectors

Detectors for use in the PB-2b receiver in the field were tested in the lab in multiple stages before being shipped to Chile. These tests include probing the electrical connections following fabrication, small-scale initial measurements of sample pixels, full-scale testing in a "dark" environment (no optical power incident on the detectors), and optical measurements in the integrated receiver. Not all detector wafers undergo laboratory testing at every stage, but because the seven PB-2b detector wafers are all fabricated using the same process we expect similar performance and have been able to confidently choose wafers that we expect will work well in the field based on the laboratory data taken.

3.1.1 Detector Properties

The primary properties used to characterize PB-2b detectors in the laboratory are normal resistance (R_n), turnaround power (P_{turn}), lowest operating fractional resistance, and critical temperature. These properties can all be measured under dark conditions. R_n refers to the resistance of the TES when it is operating at a temperature above that at which it transitions to its superconducting state. In this regime, the TESs act as typical resistors. PB-2b TESs are fabricated with a target of $R_n = 1.2 \pm 0.3\ \Omega$ [82]. P_{turn} refers to the power at which $dI/dV = 0$. P_{turn} is used as a proxy for optimal operating power of each TES, which is an important parameter for biasing detectors for observations in the field. The target P_{turn} value is dependent on the observing band to which a given TES is sensitive because the expected levels of incident optical power on the detectors under typical observing conditions depends on this choice. For PB-2b

detectors sensitive to the 90 GHz band, the target P_{turn} range is $7.8 - 10.0$ pW, while for detectors sensitive to the 150 GHz band the target range is $18.9 - 26.7$ pW [82]. Lowest achieved fractional resistance refers to how far into the transition (decreasing the TESs resistance) the TESs can be biased and still operate stably. As the resistance of the TES decreases, parasitic resistances elsewhere in the circuit begin to have a larger effect on the system and it reaches a point at which the TES no longer becomes stable and abruptly moves to a fully superconducting state (known as "latching"). The lower the fractional resistance (operating resistance compared to R_n) at which latching occurs, the more freedom there is to tune to TESs to regimes with high responsivity. Finally, T_c refers to the temperature at which the TES transitions from normal to superconducting. The target range for T_c is $420 - 470$ mK [82].

Some optical properties can also be measured in the lab prior to use in the field. This includes measurements of optical detector time constants, τ, which characterize the finite response times of the TESs. Given constraints from the readout circuit and the expected rotation frequency of the cryogenic half-wave plate, the target range for PB-2b detector time constants is $1 - 5$ ms [102]. Optical measurements can also be made to determine the polarization angle of the detectors, each of which, for PB-2, is sensitive incident radiation with a specific linear polarization. The detector wafers are fabricated with two types of pixels that differ based on polarization angle, and within each pixel are detectors sensitive to orthogonal polarization angles. Thus, across a single wafer there exist detectors sensitive to four linear polarization states, spaced 45° apart. Furthermore, for each pixel type sensitive to a given polarization angle, there is a corresponding pixel type that is its mirror image in order to account for the effect of polarization wobble in sinuous antennas. Finally, optical spectroscopic measurements can be performed in order to measure the bandpass of each detector (the range of frequencies to which it is sensitive). PB-2b detectors have target band centers at 89.5 ± 4.5 GHz and 147.5 ± 7.4 GHz and fractional bandwidths of about 30% [82].

3.1.2 PB-2b Detector Testing and Results

Detector wafers for PB-2 receivers are fabricated alongside single-pixel witness samples. Following fabrication, each wafer is first probed to identify and record any open electrical connections. The samples are then measured in smaller cryogenic testbeds to verify general functionality and properties. These preliminary measurements generally include R_n, P_{turn}, and T_c, and sometimes also include spectral measurements of the detectors' bandpasses. If these measurements indicate reasonable performance, the wafer is assembled in its mechanical mount and fitted with a lenslet array and readout electronics, creating the detector module. An assembled module can then be tested using the pyDfmux software (described in Section 3.2.1) either alone or in parallel with others in larger cryogenic testbeds, including the PB-2 receivers. Detector modules are tested under dark conditions (either in an optically closed testbed or with custom covers directly in front of the lenslets) before undergoing any potential optical tests.

The main test of PB-2b detector modules intended for use in the field occurred at UCSD in 2019 using the PB-2b receiver. During this cooldown, a full set of seven detector modules was installed in the receiver. Four of the seven modules were installed with covers to allow for dark characterization, while the remaining three modules were open to optical signals[1]. Five of the seven detector modules were eventually selected for use in the field, while the remaining two modules did not meet requirements. The two additional detector modules selected for use in the field with PB-2b were thus characterized separately in other testbeds.

Measurements from this set of tests performed on the PB-2b detector modules are published in Ito, et al., 2020 [102]. This includes measurements of the dark detector properties (R_n, P_{turn}, lowest operating fractional resistance, and T_c), along with optical time constant and polarization measurements on a subset of the detectors exposed to to optical signals. The results, summarized in Table 3.1, demonstrate values within the indicated target ranges for all parameters

[1]The three optical detector modules were installed with neutral-density filters made of machinable microwave absorber MF-110 to attenuate optical signals from the laboratory environment, which are much larger than the CMB signals for which the detectors are optimized.

Table 3.1: Summary of results from tests from PB-2b's final in-lab cooldown showing measured properties of detector modules selected for deployment. Detailed distributions are shown in Ito, et al., 2020 [102]. Mean values for all properties listed fall within the target design ranges for PB-2b detectors. Lowest operating fractional resistance is not included in this table as a mean value was not published, but results indicate values suitable for reaching target time constants.

	Mean Value
Normal Resistance (R_n)	0.99 Ω
Turnaround Power (P_{turn}) - 90 GHz Band	9.5 pW
Turnaround Power (P_{turn}) - 150 GHz Band	21.7 pW
Critical Temperature	451 mK
Optical Time Constant (τ) at $R_{TES} = 0.7R_n$	3.4 ms

listed.

Laboratory measurements of bandpasses using a Fourier-transform spectrometer (FTS) had been planned, but due to time constraints large-scale spectral measurements of PB-2b detectors were not performed prior to integration of the receiver at the observatory site. Data from witness sample measurements provide sufficient indication that the spectral properties are as designed. Large-scale spectral measurements of the PB-2b detectors will be delayed until the receiver is operating in the field, at which time a custom FTS will be used to collect the data that can be applied to analysis of CMB data. The FTS is one that was built to specifically couple to the SA telescopes, and was previously used to measure the spectral properties of detectors in the PB-1 receiver [103].

With this set of tests showing good agreement between designed and measured values for detector properties, along with the successful operation of similar detector modules in the PB-2a receiver in the field, we are confident the seven detector modules chosen for deployment with the PB-2b receiver will perform well.

3.2 Readout and SQUIDs

As described in Section 2.2.4, the readout system for the Simons Array receivers utilizes digital frequency-domain multiplexing (DfMux) and consists of both cryogenic and ambient-temperature components. The components of the DfMux system contribute to the overall noise level of the experiment, and imperfections during component fabrication, handling, and operation can decrease to the experiment's detector yield. Both of these factors can decrease PB-2b's sensitivity to the CMB. Thus, careful attention to our choice of readout technology, as well as screening and quality control of individual readout components, are important parts of laboratory receiver measurements before fielding a successful experiment.

Noise contributions from the readout system can be characterized as a noise-equivalent current, $\mathrm{NEI}_{readout}$, measured in $\mathrm{pA}/\sqrt{\mathrm{Hz}}$ and referred to the input of the SQUID array. Minimizing noise from the readout system is a key challenge for modern CMB experiments. Warm amplifier noise, carrier and nuller DAC noise, fundamental SQUID noise, and warm and cold resistor Johnson noise all contribute to $\mathrm{NEI}_{readout}$ [88]. Targets for readout noise are set by comparing these noise contributions to photon and bolometer noise (see Section 2.3) and requiring that the readout noise be as small as possible compared to these more fundamental noise sources in the overall system noise. For PB-2 receivers, an estimate for the minimum expected photon + bolometer noise-equivalent current is about 20 $\mathrm{pA}/\sqrt{\mathrm{Hz}}$[2]. We require the readout to perform such that it is not the dominant noise source ($\mathrm{NEI}_{readout} < 20\mathrm{pA}/\sqrt{\mathrm{Hz}}$), and target values lower than this so that readout noise is significantly sub-dominant. Because $\mathrm{NEI}_{readout}$ refers to a noise current at the SQUID input coil, the importance of readout noise produced in sources after the SQUID array in the readout circuit is affected by the properties of the SQUID array itself, and SQUID devices must additionally be screened to account for their impact on this conversion factor.

[2]This estimate is calculated using values for optical power and bolometer resistance that would produce the lowest expected photon + bolometer noise. This conservatively low minimum photon + bolometer noise is thus used to set a maximum allowable readout noise.

Along with readout components adding to system noise, failure of these components leads directly to loss of data and therefore a reduction in sensitivity. Yield hits from minor flaws in the readout system such as broken wire bonds on a single LC resonator result in the loss of single detectors, but, due to the nature of multiplexing, damage to other single pieces of readout electronics can result in the loss of several detectors and significant impacts to system sensitivity. With PB-2's multiplexing factor of 40, though the receiver employs over 7,500 optical detectors, failure of any single component that interacts with the summed signal amounts to a yield hit of about 0.5%. It is therefore critically important that we thoroughly test each of the readout components and ensure they are capable of robust, stable operation before deploying the PB-2b receiver.

This section will describe selection and characterization of components in PB-2b's readout system, with an emphasis on the SQUID array amplifiers. These not only contribute their own amplifier noise to the system and are components where single device failure affects multiple detectors, but are also of particular importance in the readout system because properties of the SQUID array impact the conversion factor between noise produced in sources post-SQUID array in the readout circuit and the signal through the SQUID input coil. The dynamic range of the SQUID arrays also impacts our ability to operate our detectors. Therefore, multiple SQUID array designs were considered and tested before SQUID devices were selected for deployment with PB-2b.

3.2.1 SQUID Properties and Measurement Techniques

A variety of SQUID properties can be measured during in-lab characterization of the PB-2b receiver. These properties, along with some of the measurement tools and techniques, are described below.

pyDfmux

A software library known as pyDfmux is used to operate the SA readout system by controlling the ambient-temperature electronics. This library contains algorithms for a number of operations, including generating carrier and nuller tones at specific frequencies and amplitudes, biasing bolometers, biasing SQUID arrays, measuring SQUID array properties, and reading out bolometer signals. It also includes a set of transfer functions necessary for converting "counts" in the analog-to-digital and digital-to-analog converters to physical units through electronic components in the readout system [97]. The pyDfmux framework is what is used in making all measurements described in this section, and is what will be used to operate the PB-2b detector and readout system in the field.

Heating SQUIDs

Before any tests of the readout system, the SQUID arrays are heated to above their superconducting transition temperature ($\sim$ 9 K) using resistors on the SQUID PCB and are then allowed to cool back down to their operating temperature ($\sim$ 4 K). This is done to remove any trapped flux through the individual SQUID loops that would cause the full array to lose sensitivity to signals through the input coil [104, 105]. This process is done using a pyDfmux algorithm which takes approximately 20 minutes to complete. SQUID arrays should not need to be heated more than once for a given cryogenic cycle unless the receiver is undergoing extreme tests, but the arrays are often heated immediately before any SQUID-specific tests in order to ensure an accurate measurement.

Voltage-Flux Curves

As described in Section 2.2.4, by sweeping through a range of current and flux biases one can map out a voltage-flux, or $V - \Phi$, curve for a SQUID. A set of $V - \Phi$ curves can be measured for a desired set of bias points using a pyDfmux algorithm that controls the SQUID controller

boards to set the biases and measure the output voltage at each point.

Ideally a SQUID $V - \Phi$ curve, for current biases above the SQUID's critical current, will show a smooth, nearly sinusoidal, periodic pattern with a period equal to one flux quantum [91]. Some features can arise on top of this sine-like curve (in particular a "kink" on the falling edges of the curves) that are well understood and produced by other electronic components in the system [106]. However, other features have been seen for which the production mechanism is not fully understood. These features can make reliably and repeatably tuning the SQUID arrays to a stable operating point difficult, especially when trying to do so efficiently with an automated algorithm. For this reason, SQUID $V - \Phi$ curves are checked in laboratory tests prior to use in the field to ensure no unwanted features will hinder operation.

Maximum peak-to-peak voltage, V_{pp}, is a measure of the full height of the $V - \Phi$ curve for the current bias choice which maximizes this property. V_{pp} can be measured with a $V - \Phi$ curve, and is sometimes used as a proxy for transimpedance, described below, as the two properties are generally correlated.

Transimpedance

One of the most important properties of a SQUID array amplifier is its transimpedance, Z_t, defined as

$$Z_t = \frac{\partial V_{out}}{\partial I_{in}}, \tag{3.1}$$

where V_{out} is the measured voltage across the SQUID and I_{in} is the signal current through the input coil. The SQUID amplifier converts current to voltage, and the transimpedance represents the gain of this amplifier. Higher transimpedance amplifies the signal and thereby reduces the impact of noise sources post-SQUID in the readout system compared to the signal. Transimpedance corresponds to the slope of the $V - \Phi$ curve at a given current and flux bias, and the pyDfmux SQUID tuning algorithm chooses current and flux biases to nearly maximize transimpedance. For PB-2, we require SQUID arrays used in the field to demonstrate $Z_t > 350\ \Omega$ after normal tuning

to ensure the desired signal is amplified sufficiently as to not be overwhelmed by noise sources later in the readout system.

Dynamic Impedance

Dynamic impedance, Z_{dyn}, also referred to as output impedance, is defined as

$$Z_{dyn} = \frac{\partial V_{out}}{\partial I_{bias}}, \tag{3.2}$$

where V_{out} again is the measured voltage across the SQUID and I_{bias} is the bias current through the SQUID. Higher dynamic impedance values can add noise to the system by converting current noise through the SQUID Josephson junctions to a voltage noise at the output. For an optimal transimpedance, the SQUIDs can be tuned to an operating point with either high or low dynamic impedance. Unfortunately, the regime in which low dynamic impedance is achieved is prone to kinks in the $V-\Phi$ curve discussed earlier, and stable operation at this point is not possible in the current readout configuration [96]. We therefore assume operation at the high-Z_{dyn} bias point and require $Z_{dyn} < 900\ \Omega$ here. Note that work is being done to find solutions that would allow operation at the low-Z_{dyn} bias point by implementing a low-pass filter in the system that would prevent resonances from influencing the $V-\Phi$ curves.

Linearity

Measurements of SQUID linearity, or linear dynamic range, can be performed by increasing the amplitude of nuller tones sent through the SQUID arrays' input coils and measuring the change in transimpedance as the operation point moves along the $V-\Phi$ curve. As the operation point nears a peak or trough in the curve, the slope, and therefore the transimpedance, changes. A wider range of amplitudes for which the transimpedance remains near its maximum value is preferable as this indicates a wider range of signals over which the SQUID arrays act stably and

with high gain. Though no specific requirements for linearity were in place for PB-2b SQUID arrays, this parameter was considered when comparing different SQUID designs.

Noise from Zero-Amplitude Network Analysis

One way of measuring the readout noise is by performing a network analysis with the amplitude of the tones set to zero. As described in Section 2.2.4, during a network analysis carrier and/or nuller tones are injected into the system over a range of frequencies and the demodulator channels read out the signal at each. This procedure is normally used as a means of identifying the resonator frequencies in the *RCL* circuit, but the same algorithm can also be used to measure noise when the amplitude is set to zero, effectively removing the injected signal and instead allowing the demodulator channels to read out only the noise. The measurement can be performed with the focal plane above or below the transition temperature of the detectors.

To quantify and compare results from this type of network analysis, we generally measure a noise level at 6,000 frequencies over a range of frequencies slightly larger than the readout band, and then take the median of these values to represent the noise level of a particular module or SQUID array. We require a median noise lower than 20 pA/$\sqrt{\text{Hz}}$ for PB-2b SQUID arrays.

Amplitude-Dependent Noise

Another noise measurement was made to evaluate the SQUID array's ability to support a full comb (up to 40 channels) of current without significant noise increases. In this measurement, the bolometer stage is heated above the transition temperature of the TESs and a voltage bias is set at the corresponding resonant frequencies ("overbiased" state of the bolometers). The amplitude of the carrier tones is then increased gradually, with bolometer noise measured at each amplitude for each carrier frequency. Tests of this type for the PB-2b readout system include amplitudes from 0.0001 to 0.05 as measured in normalized units from the ambient-temperature readout electronics. It is important that this measurement be performed on SQUID arrays connected to

resonator combs with high yield, as yield hits will cause lower currents through the SQUID array than would be expected in the field.

Results from operation of PB-2a in the field indicate typical overbias amplitudes of around 0.035. However, absolute noise values from this measurement cannot be directly linked to noise when operating detectors using the same overbias amplitude in the field because the detectors will be in a different state (overbiased as opposed to in the transition with optical power), which affects the actual current amplitude through the system. We instead focus the amplitude-dependent noise results discussed later in this section on the degree to which this amplitude dependence exists rather than on the specific noise values achieved at a given amplitude.

Input Inductance

The inductance of the SQUID input coil, L_{in}, is set during fabrication of the SQUID chips and is not expected to vary significantly among SQUIDs of the same design. Design values of L_{in} was a critical factor in selecting SQUID arrays for PB-2 as is discussed in Section 3.2.2. Effective input coil inductance, which accounts for any stray inductance in the wiring of the readout circuit, can also be estimated by looking at changes in noise as a function of frequency.

3.2.2 Selection of PB-2b SQUID Design

After a series of measurements with different SQUID array designs, the SA13a design from the National Institute of Standards and Technology (NIST) [94] was chosen for use in PB-2b. This is the same type of SQUID array as is in use in the PB-2a receiver. Other candidates considered include the SA4b design also from NIST [94] and the E2 and F2 designs from STAR Cryoelectronics[3,4].

[3] https://starcryo.com/

[4] The STAR Cryoelectronics SQUID array designs were not considered for PB-2a due to PB-2a's deployment timeline.

SQUID Input Inductance Consideration

NIST SA4b SQUID arrays were originally intended to be used in the Simons Array following their successful use in the PB-1 receiver. The critical difference between this design and the SA13a or STAR Cryoelectronics designs is the inductance of the SQUID input coil which is designed to be $\mathcal{O}(100)$ nH for SA4b SQUID arrays and $\mathcal{O}(10)$ nH for the other SQUID arrays [107]. This difference was found to be important considering the active nulling involved in the PB-2 readout system due to an effect referred to as "current sharing" [87]. With PB-2's use of digital active nulling (DAN) as described in Section 2.2.4, in the ideal case a nuller signal is created that perfectly cancels the signal from the carrier tones and neither the carrier nor the nuller signal is affected by the impedance of the SQUID input coil. However, DAN uses feedback from the signal at the ADC and therefore also attempts to null any noise that gets injected into the system from sources after the SQUID input coil. Since these nulling signals are not canceled by the carrier tones, they see two paths to ground - one through the SQUID input coil and one through the resonator comb and bias resistor - as shown in Figure 3.1. With $Z_{SQ} > 0$, the current through the SQUID is less than the uncanceled nuller current because some of this current finds an easier path to ground through the resonator comb. The system then needs to generate a larger nuller signal to combat the injected noise signal, and the overall system noise increases. This effect is greater at higher frequencies because inductor impedance scales with frequency. The reduced input coil inductance and therefore reduced Z_{SQ} associated with the SA13a and STAR Cryoelectronics SQUID array designs lessens the overall impact of current sharing, and for this reason it was clear the SA4b SQUID arrays would not be suitable for any PB-2 receiver.

Overview of Low-Inductance SQUID Designs

After identifying the need for low-inductance input coils, two SQUID array designs were primarily considered for use in PB-2b: NIST's SA13a design and STAR Cryoelectronics' E2

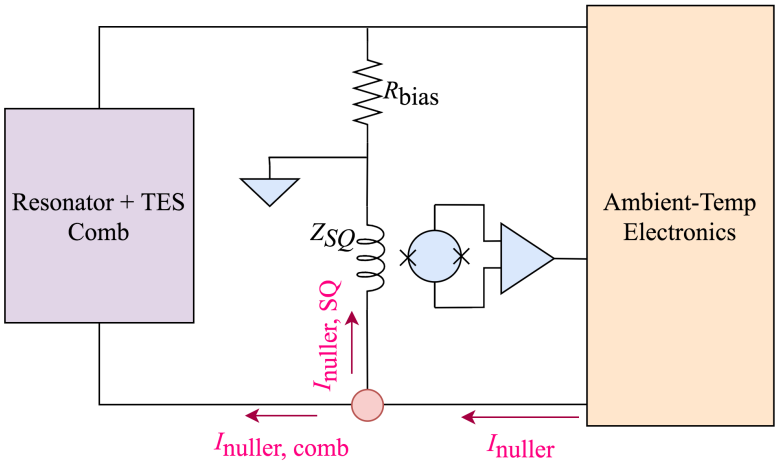

Figure 3.1: Simplified diagram of the PB-2 DfMux readout circuit illustrating current sharing. The full circuit diagram is shown in Figure 2.21. Particularly when there is noise injected into the system in components situated post-SQUID array, I_{nuller} can include signals that are not canceled by the carrier current that is driven through the *RCL* circuit represented by the purple box. These uncanceled nuller tones see two paths to ground from the junction represented by the red dot - one (desired) path through the SQUID input coil, and one through the *RCL* circuit and the bias resistor. SQUID arrays with lower input coil inductance create a lower impedance through this first path, resulting in less unwanted nuller current through the resonator comb and less overall noise in the system.

design[5]. Table 3.2 gives a summary of a comparison between these two SQUID array designs based on design values and laboratory measurements. These measurements and results are discussed in detail in the following sections.

Input Inductance, Transimpedance, Dynamic Impedance, and Linearity

The design values for the different input coil inductances for the different SQUID array designs are listed in Table 3.3 [107]. Additionally, noise measurements at a range of frequencies within the readout bandwidth were performed on a small set of SA13a and STAR Cryoelectronics SQUID arrays ($\mathcal{O}(10)$ each) to determine the effective input coil inductance, which includes stray inductance from the circuit wiring. These measurements show the E2 SQUID arrays having

[5]STAR Cryoelectronics' F2 design was also briefly investigated, but was removed from consideration after a set of small-scale measurements with around 20 SQUID arrays indicated a slightly better performance of the E2 arrays.

Table 3.2: Summary comparing STAR Cryoelectronics E2 and NIST SA13a SQUID designs based on several SQUID parameters. Columns 2 and 3 indicate quantitative results when applicable, while column 4 contains conclusions. Italicized values indicate design values, while all other values are measured mean values from large-scale laboratory tests unless otherwise specified.

SQUID Parameter	**Star Cryo. E2**	**NIST SA13a**	**Conclusions**
Input Inductance (L_{in})	*11 nH*	*50 nH*	Sufficiently low L_{in} for both designs. **Slight preference for E2** design due to lower value.
Transimpedance (Z_t)	820 Ω	690 Ω	Sufficiently high Z_t for both designs. **Slight preference for E2 design** due to lower value.
Dynamic Impedance (Z_{dyn})	$\sim$ 580 Ω	740 Ω	Majority with sufficiently low Z_{dyn} for both designs, but with a few outliers. **Slight preference for E2 design** due to lower value.
Linearity	-	-	Sufficiently good linearity for both (based on small-scale testing). **Slight preference for E2 design** due to larger linear dynamic range.
Efficiency / Reliability of Tuning	-	-	Unacceptable tuning efficiency and reliability for E2 design due to high occurrence rate of problematic $V-\Phi$ behavior. **Strong preference for SA13a design** due to better $V-\Phi$ behavior and demonstrated reliability of tuning in PB-2a.
Noise	8.4 pA/$\sqrt{\text{Hz}}$ (median value from zero-amp network analysis)	5.5 pA/$\sqrt{\text{Hz}}$ (median value from zero-amp network analysis)	Sufficiently low noise achieved with both designs as measured by zero-amplitude network analyses. More high-noise outliers seen for SA13a design. Noise increases with carrier tone amplitude seen for both SQUID designs. **Slight preference for SA13a design** due to slightly lower occurrence rate of poorly understood amplitude-dependent noise and lower median noise from zero-amplitude network analysis.

a lower effective input coil inductance compared to the SA13a SQUID arrays by about 30 nH [107].

Table 3.3: SQUID array input coil inductance design values for the NIST SA4b, NIST SA13a, and STAR Cryoelectronics E2 and F2 designs. Measurements have been made of $L_{in,effective}$ for the SA13a and E2 designs [107], which includes contributions from the wirebonds and other wiring to the SQUID array, but design values are listed here to give a better comparison to the SA4b design and because the stray inductance values should be consistent across SQUID designs so long as the same readout hardware and wiring technique is used.

	L_{in} [nH]
NIST SA4b	300
NIST SA13a	50
STAR Cryoelectronics (E2 & F2)	11

The lower input coil inductance of the STAR Cryoelectronics SQUID arrays makes them a better candidate for use in PB-2b, but both designs sufficiently suppress the noise enhancement from current sharing compared to the SA4b design.

Figure 3.2 shows histograms of the tuned transimpedances achieved by a nearly full set of E2 SQUID arrays and of SA13a SQUID arrays. Data from the E2 SQUID arrays were obtained during an in-lab cooldown of the PB-2b receiver during which a full set of detectors and readout electronics were in use. Data from the SA13a SQUID arrays were obtained during in-field measurements in the PB-2a receiver from an arbitrarily selected day of observation. The two designs perform similarly, with both distributions showing mean values well over the requirement of $Z_t > 350\ \Omega$. Though the E2 distribution contains some SQUID arrays below this threshold while the SA13a distribution does not, this is a result of the different conditions under which the SQUID arrays were selected. The SA13a arrays shown here were rigorously screened for use in the field with PB-2a and only selected if they had been previously shown to meet transimpedance requirements. Since the E2 data comes from a laboratory test, fewer restrictions were imposed upon the SQUID arrays during the selection process. On the other hand, the E2 data also show a greater number of SQUID arrays with transimpedance greater than that achieved by any of the

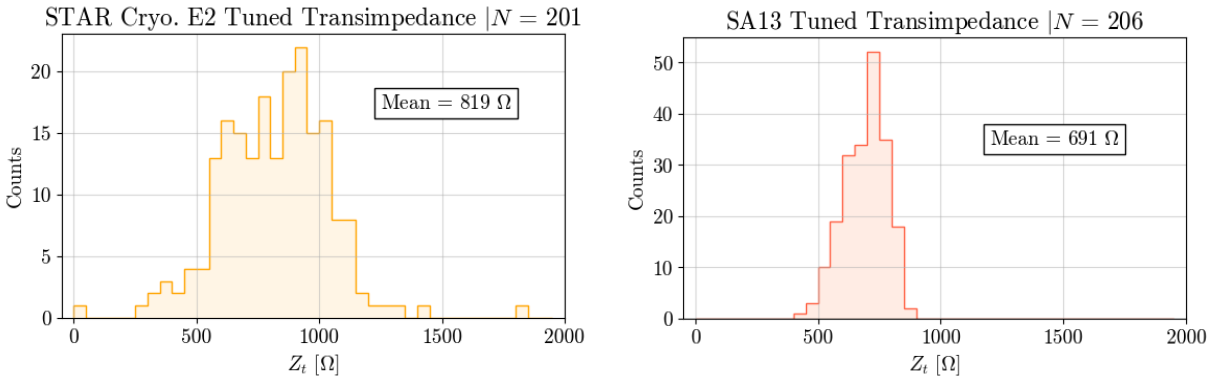

(a) Histogram of transimpedance values from STAR Cryoelectronics E2 SQUID arrays.

(b) Histogram of transimpedance values from NIST SA13a SQUID arrays.

Figure 3.2: Histograms showing the measured transimpedance of STAR Cryoelectronics E2 SQUID arrays compared to NIST SA13a SQUID arrays. Both distributions indicate SQUID arrays that meet the requirement of $Z_t > 350$ Ω. The wider distribution of E2 SQUID arrays on the low-Z_t side is mainly a result of selection effects as described in the text. The wider distribution of E2 SQUID arryas on the high-Z_t side indicate a preference for the E2 design over the SA13a design in this regard.

SA13a arrays. Because of this, the data show a very slight preference for E2 SQUID arrays, but indicate that both designs meet the transimpedance required for use in the field.

Figure 3.3 shows histograms of the dynamic impedances achieved by a full set of SA13a SQUID arrays and of E2 SQUID arrays. Data used in the histograms were obtained during the same two measurement periods described above for the transimpedance data. The two SQUID designs have similar dynamic impedance values. Both datasets show a few outlier SQUID arrays with Z_{dyn} above the threshold of 900 Ω. Again there is a slight preference for the STAR Cryoelectronics E2 design due to its slightly lower mean Z_{dyn} value, but the data indicate both designs meet requirements.

Measurements of each SQUID design's linear dynamic range were also performed on the smaller set of SQUID arrays tested for L_{in} measurements. Detailed techniques and measurement results are reported in [107], with results showing a slight preference for the STAR Cryoelectronics E2 SQUID arrays.

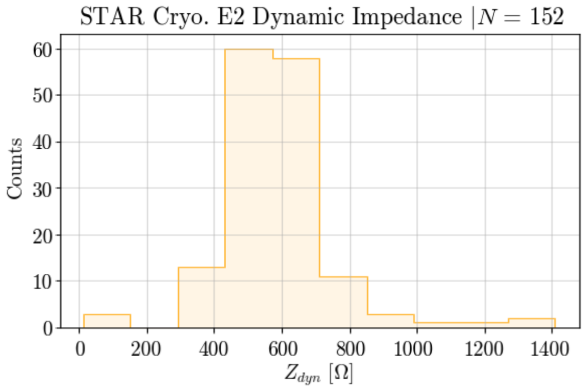

(a) Histogram of dynamic impedance values from STAR Cryoelectronics E2 SQUID arrays.

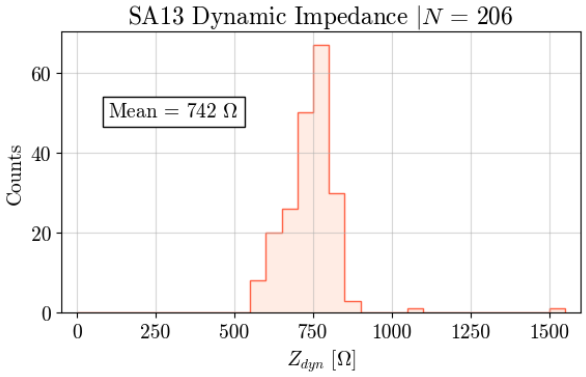

(b) Histogram of dynamic impedance values from NIST SA13a SQUID arrays.

Figure 3.3: Histograms showing the measured dynamic impedance of STAR Cryoelectronics E2 SQUID arrays compared to NIST SA13a SQUID arrays. The distributions for the two designs are similar, with most SQUID arrays achieving Z_{dyn} values between 400 and 900 Ω, meeting the requirement. Both sets show a few outlier SQUID arrays with high Z_{dyn}.

Full-Scale Operation/Reliability and Noise Measurements

STAR Cryoelectronics E2 SQUID Arrays

A full-scale test of the PB-2b readout system using STAR Cryoelectronics E2 SQUID arrays was performed in 2019 at UCSD during a cooldown of the PB-2b receiver. Testing of E2 SQUID arrays prior to this cooldown had been done on a smaller scale as mentioned above (see Howe, 2019 [107]), and on a larger scale but without the SQUID arrays connected to resonators and detectors, but this cooldown was the first full test of system operation. The cooldown in which this full-scale readout test was performed was the last in-lab cooldown of the PB-2b receiver, which also included tests of the detectors and of the cryogenic HWP system, as discussed elsewhere in this chapter.

During this cooldown, 29 SQUID PCBs containing a total of 230 E2 SQUID arrays (one SQUID PCB was populated with only six SQUID arrays rather than eight) were installed in the PB-2b receiver, 28 of which were connected to detector modules. All SQUID PCBs were thermally connected to the PB-2b backend's 4-K shell via gold-plated copper heat straps. This setup corresponds to the deployment-style receiver configuration that will be implemented when

observing in the field. A full set of ambient-temperature electronics were connected to the SQUID PCBs on the outside of the receiver such that all SQUID arrays could be operated in parallel and their properties measured under field-like conditions. About ten SQUID arrays were not able to be operated during this cooldown due to networking issues with the ambient-temperature electronics, but characterization data for the remaining SQUID arrays were obtained.

One primary test of the SQUID arrays that was performed under these field-like conditions was to take densely sampled voltage-flux ($V-\Phi$) curves using the pyDfmux algorithm described earlier. Looking at the $V-\Phi$ curves helped us to evaluate our ability to reliably and repeatably tune the SQUID arrays to stable operating points, as unwanted features or kinks apparent in a $V-\Phi$ curve can cause the SQUID to have a lower transimpedance and a smaller linear dynamic range.

$V-\Phi$ curves for the operable SQUID arrays were obtained several times over the course of the cooldown and visually inspected for unwanted features, appropriate tuning points, and repeatability. In the final dataset of this cooldown in which densely sampled $V-\Phi$ curves were measured for 214 SQUID arrays, 33% of SQUID arrays were flagged during visual inspection for displaying unwanted features. For comparison, unwanted $V-\Phi$ behavior was not seen to be an issue worth quantifying in earlier, smaller-scale tests of the E2 SQUID arrays. The flagged $V-\Phi$ curves were categorized based on the type of unwanted features they exhibited, though the curves within each category varied in prominence of the unwanted feature(s). The four categories were (1) falling-edge kinks (25 SQUID arrays, 12%), (2) rising-edge kinks (2 SQUID arrays, 1%), (3) double shoulder (37 SQUID arrays, 17%), and (4) broad peaks (7 SQUID arrays, 3%). Examples of each are shown in Figures 3.4, 3.5, 3.6, and 3.7.

Some of the unwanted features in their $V-\Phi$ curves showed some correlation with position on the SQUID PCB and attachment to resonators and detectors. As seen in Figure 2.26b, each SQUID PCB contains up to eight SQUID arrays, and thus each SQUID array is placed in one of eight possible positions. Position 1 refers to that closest to the connector which leads to the

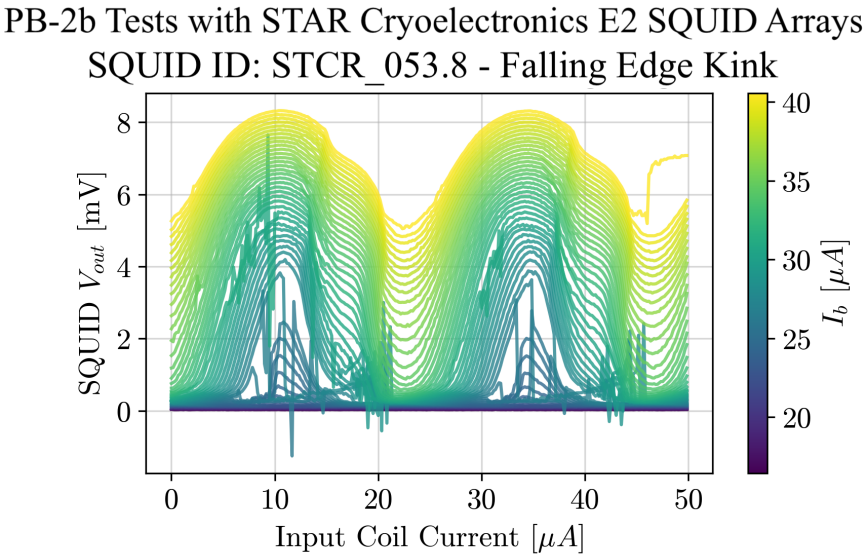

Figure 3.4: Example of a $V - \Phi$ curve from STAR Cryoelectronics E2 SQUID array STCR_053.8 during full-scale tests, flagged for having a kink on the falling edge. 24 other $V - \Phi$ curves were flagged for similar behavior after visual inspection.

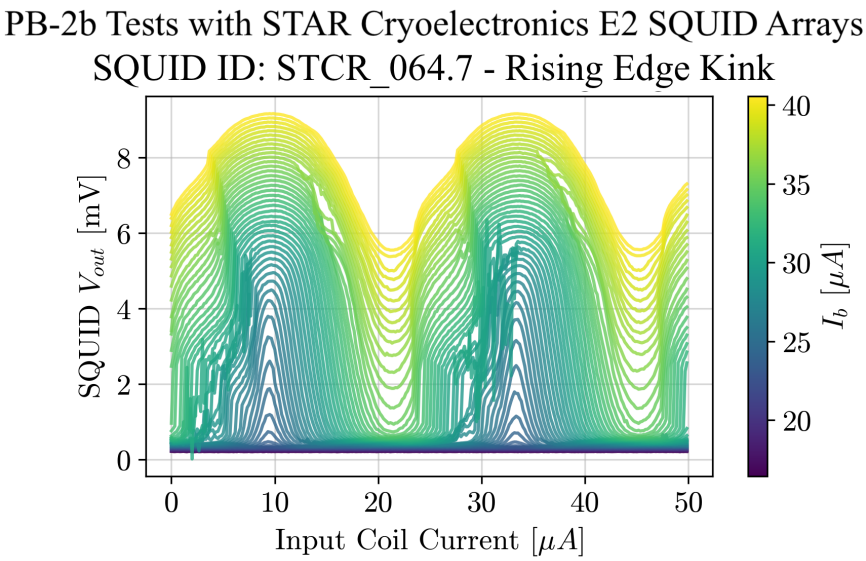

Figure 3.5: Example of a $V - \Phi$ curve from STAR Cryoelectronics E2 SQUID array STCR_064.7 during full-scale tests, flagged for having a kink on the rising edge. One other $V - \Phi$ curve was flagged for similar behavior after visual inspection.

wiring for the resonators and detectors, and position 8 refers to that farthest from the connector. All $V - \Phi$ curves exhibiting falling-edge kinks were seen on SQUID arrays in positions 5-8 on the SQUID PCB, and half were in position 8. This position dependence follows logically given

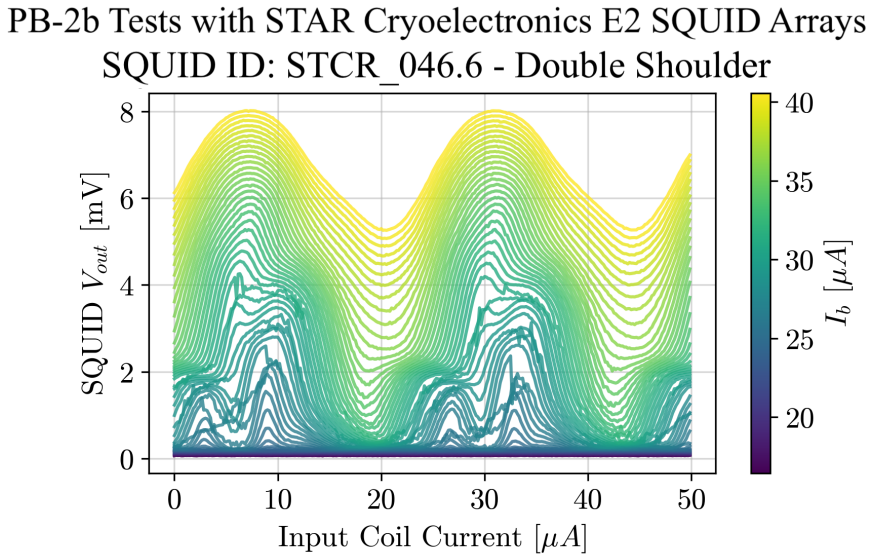

Figure 3.6: Example of a $V - \Phi$ curve from STAR Cryoelectronics E2 SQUID array STCR_046.6 during full-scale tests, flagged for having a double shoulder. 36 other $V - \Phi$ curves were flagged for similar behavior after visual inspection.

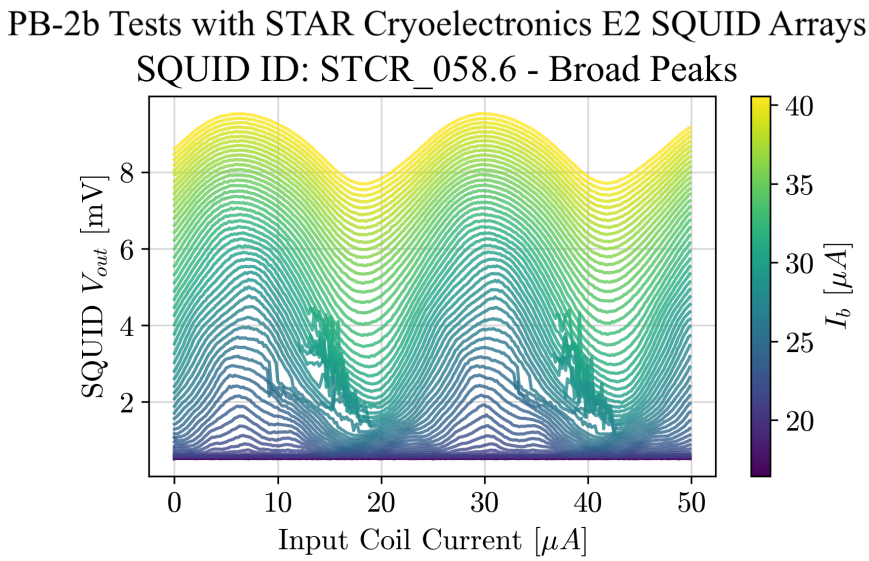

Figure 3.7: Example of a $V - \Phi$ curve from STAR Cryoelectronics E2 SQUID array STCR_058.6 during full-scale tests, flagged for having broad peaks. Six other $V - \Phi$ curves were flagged for similar behavior after visual inspection.

distortions known to occur when parasitic capacitance is present in the SQUID circuit [106] and given the longer PCB traces leading to positions 5-8. Conversely, the double-shoulder features for which we do not understand the production mechanism were not seen to depend on the SQUID

array's position on the PCB. Additionally, though the sample size was small, only one of 14 SQUID arrays not connected to detectors and resonators displayed features in its $V-\Phi$ curve, explaining why the pervasiveness of this effect was not seen in earlier large-scale measurements. More testing with different configurations would be required to understand how the rest of the readout circuit is interacting with the SQUID arrays to influence this behavior. Attempts were made to improve SQUID array performance by eliminating or minimizing all unintentional paths to electrical/Earth ground, but these changes did not significantly impact the percentage of SQUID arrays suffering from these effects.

Though all categories of $V-\Phi$ curves can cause difficulties with tuning, some can be accounted for with careful configuring. With feedback from the DAN system, the PB-2 SQUID arrays should remain near their tuning point when in use, so it is only strictly necessary to have a stable operating point on one side of the $V-\Phi$ curve. For reasons related to the slow feedback loop, PB-2 SQUID arrays must be biased on the falling edge of a $V-\Phi$ curve, so SQUID arrays exhibiting rising-edge kinks can generally still be used. Likewise, SQUID arrays exhibiting falling-edge kinks can theoretically be used if the SQUID output is connected in its reverse configuration, effectively moving the kink to the opposite side. "Double-shoulder" SQUID arrays, on the other hand, show disruptions on both sides of the curve, often making stable operation impossible. In some instances a stable operating point can be identified if a higher current bias is used that moves the operating point away from regimes in which features are present, but this often comes at the cost of transimpedance. Likewise, SQUID arrays with "broad peaks" in their $V-\Phi$ curves often show degraded transimpedance.

Although many of these SQUID arrays can in principle be tuned to stable operating points, use of SQUID arrays exhibiting these types of features in the field can be problematic for three reasons. Firstly, as noted above, finding stable operating points can often require sub-optimal tuning at a point with lower transimpedance. This means readout noise produced in sources post-SQUID in the readout chain will have a larger impact on the bolometer signals. With the

requirement of $Z_t > 350\ \Omega$ and given the achievable transimpedance values of E2 SQUID arrays shown in Figure 3.2a, for many SQUID arrays there is room for transimpedance degradation without dipping below this threshold, but not for all.

Secondly, the reliability and efficiency of finding stable operating points for the SQUID arrays must be considered for operation in the field. For example, it is important to note that the data shown in Figure 3.2a, where the STAR Cryoelectronics E2 SQUID arrays are demonstrated to be capable of achieving high tuned transimpedance values, were obtained after hand-tuning of the SQUID arrays based on careful examination of their $V - \Phi$ curves to manually identify stable operating points – a procedure that is not sustainable or efficient for continuous observations in the field.

Finally, the high percentage of SQUID arrays exhibiting some form of this behavior combined with a lack of understanding about the mechanisms causing it is reason for concern. Slight variations in the $V - \Phi$ behavior were seen across multiple measurements (within the same cooldown/test configuration). Without clear, reliable repeatability during lab tests, and without a clear correlation that explains the behavior, there is definite risk associated with operating these SQUID arrays in the field, and the possibility cannot be ruled out that an even higher percentage of SQUID arrays would exhibit similar behavior when subjected to the conditions in the field compared to those in the lab.

Full-scale tests of amplitude dependent noise were also performed during this cooldown. As mentioned, these tests are performed by injecting carrier tones of increasing amplitudes into the system and measuring the noise at each. An example of results from this measurement for a single SQUID array and set of resonators is shown in Figure 3.8. The results are shown only for I-phase (in-phase) noise, but similar, often more extreme trends are also shown in the Q-phase (quadrature) data [108]. The Q-phase data are omitted here because Q-phase data are not typically used in PB-2 science analysis. Noise increases are seen with respect to both bias frequency and carrier tone amplitude. The plots shown in Figure 3.8 are fairly representative of the sample of

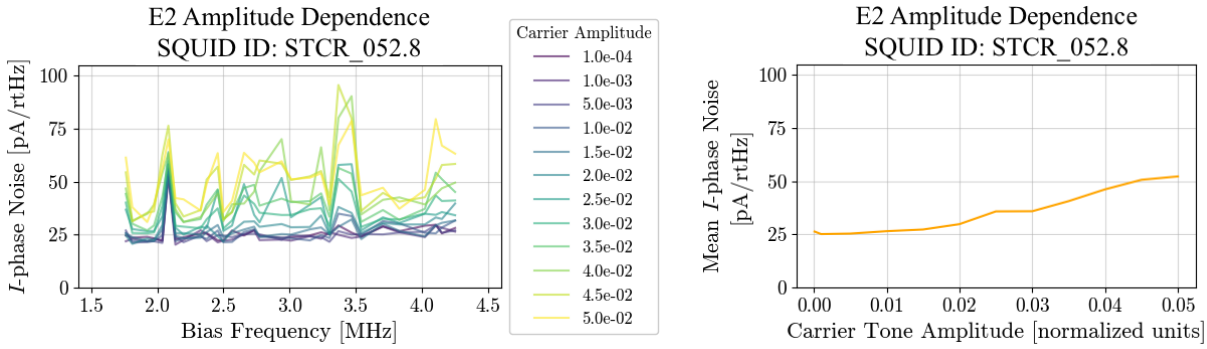

(a) Noise vs. bias frequency for a set of carrier tone amplitudes during an amplitude-dependent noise measurement on a single E2 SQUID array, STCR_052.8.

(b) Corresponding noise vs. carrier tone amplitude averaged over all bias frequencies during an amplitude-dependent noise measurement.

Figure 3.8: Example of the results of an amplitude-dependent noise measurement on a STAR Cryoelectronics E2 SQUID array, STCR_052.8. The left plot shows the noise as a function of bias (resonator) frequency, where each colored line corresponds to a different amplitude of carrier tones injected into the system. The right plot shows the same data but averaged over bias frequency, with mean noise plotted as a function of carrier tone amplitude. A general increase in noise is seen with increasing carrier tone amplitude for this SQUID array. The degree to which the noise increases with carrier tone amplitude varies by SQUID array, with some SQUID arrays exhibiting a much weaker change in noise as carrier tone amplitude changes, and some a much stronger change.

E2 SQUID arrays tested, though the degree to which the noise increases with both carrier tone amplitude and bias frequency varies. Noise increases with respect to bias frequency are generally subtle and are thought to result from increases in parasitic impedance of inductive elements in the circuit. Noise increases with respect to carrier tone amplitude, however, are expected to correspond to the SQUID array's ability to handle increases in current through the input coil, and were seen in several SQUID arrays during this cooldown to be significant.

Figure 3.9 shows histograms of the results for one set of amplitude-dependent noise measurements performed on 180 sets of resonators late in the cooldown, after work had been done to optimize the grounding configuration of the readout electronics and the receiver. Each "count" plotted in the histograms corresponds to a single readout *channel* (single resonator in a comb), rather than to an entire readout module or SQUID array. Thus, data from a single SQUID array are represented by about 40 channels or counts. At low carrier tone amplitude, a large

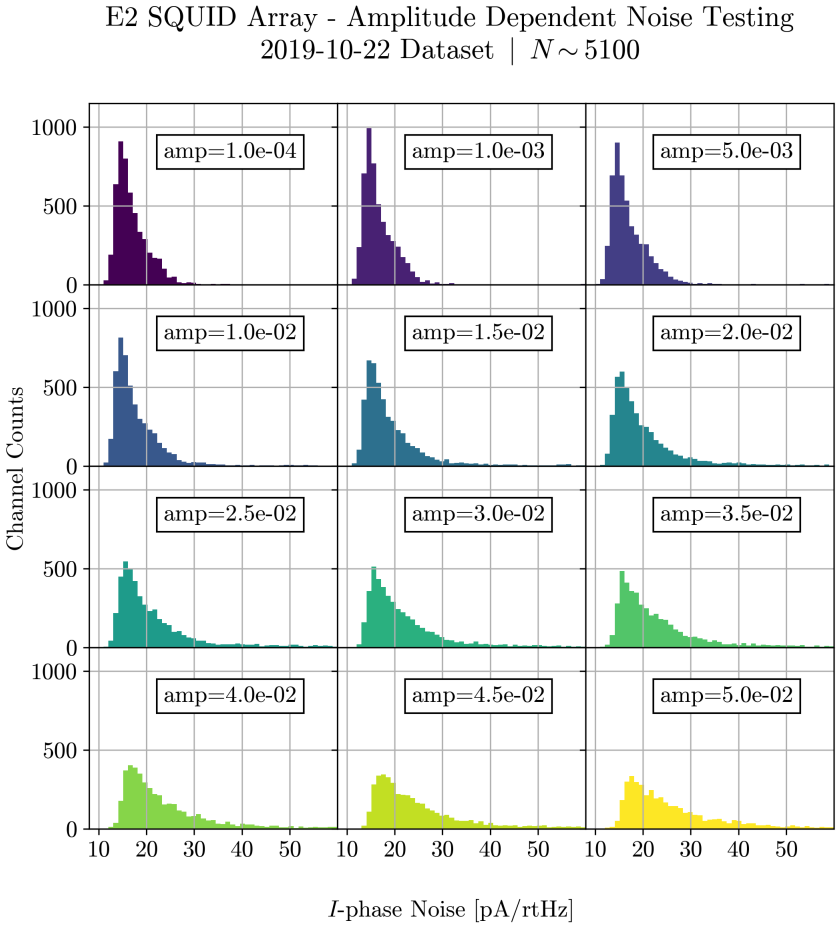

Figure 3.9: Results of amplitude-dependent noise measurements taken on a set of 180 E2 SQUID arrays. Each plot depicts a histogram of the I-phase noise values measured for the active channels when a carrier tone of a given amplitude was passed through the resonator circuit. A total of about 5100 channels were measured during this test, with the exact number of active channels at each carrier tone amplitude varying. As carrier tone amplitude is increased, overall noise levels of the system increase and the histograms flatten. The mean and median noise values for the lowest carrier tone amplitude, 1.0×10^{-4}, are 17.2 and 16.1 pA/$\sqrt{\text{Hz}}$, respectively, while the mean and median noise values for the highest carrier tone amplitude, 5.0×10^{-2}, are 79.2 and 25.7 pA/$\sqrt{\text{Hz}}$, respectively. The histograms only show data up to 60 pA/$\sqrt{\text{Hz}}$, but many channels, especially at higher carrier tone amplitudes, had noise values much higher than this. Carrier tone amplitude are quoted in normalized units from the ambient-temperature readout electronics.

majority, 82%, of channels show noise levels below 20 pA/$\sqrt{\text{Hz}}$. However, once the carrier tone amplitude has been increased to 1.0×10^{-2} (in normalized units from the ambient-temperature readout electronics), the percentage drops to 74%, and again to 28% once the amplitude reaches

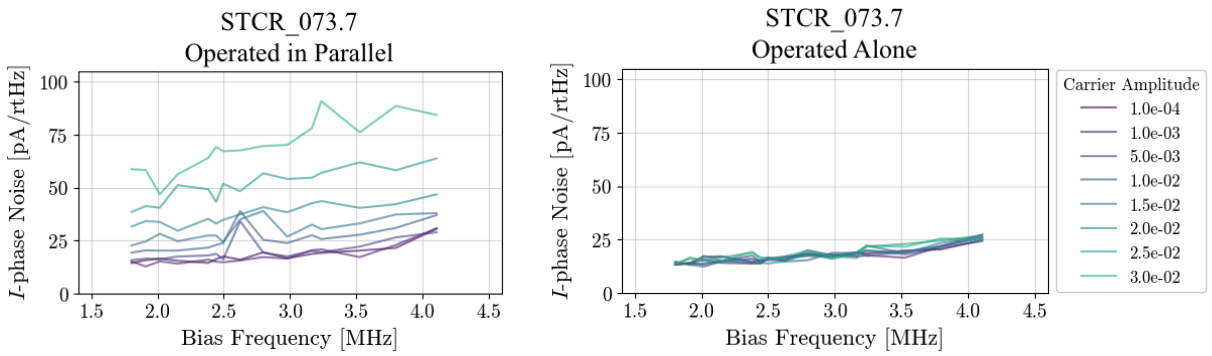

(a) Amplitude-dependent noise measurement results for E2 SQUID array STCR_073.7 during a test in which a nearly full set of SQUID arrays were operated in parallel.

(b) Amplitude-dependent noise measurement results for E2 SQUID array STCR_073.7 during a test in which this SQUID array was operated by itself (no measurements running in parallel).

Figure 3.10: Noise vs. frequency data for E2 SQUID array STCR_073.7 during two tests of amplitude-dependent noise, one in which the SQUID array was operated in parallel with others (left) and on in which it was operated by itself (right). Different colored lines correspond to different carrier tone amplitudes. The noise increase as a function of carrier tone amplitude seen in the plot on the left completely disappears when the SQUID is operated alone, indicating that contamination from other readout circuits may have a large impact on the amplitude dependence.

5.0×10^{-2}, the highest measured during this test.

Attempts were made to reduce overall amplitude-dependent noise in the system by investigating the impact of operating channels on different SQUID arrays in parallel. In a dedicated test of one SQUID array, STCR_073.7, the results of which are shown in Figure 3.10, nearly all amplitude-dependence was removed once the SQUID array was measured with channels on all other SQUID arrays turned off. However, this SQUID array also underwent a significant degradation of transimpedance over the course of the multi-SQUID array measurement, while its transimpedance remained stable during the single-SQUID array test, so the root cause of the amplitude-dependent noise remains unclear. Additional amplitude-dependent noise tests of single SQUID arrays indicated various levels of improvement. However, none provided a robust explanation or solution, and the specific methods used for acquiring the improved data are not realistic to apply to field operations. Further investigation at a larger scale would be needed to understand the effectiveness of these techniques and if they can be implemented in a way that

could be used during regular observations in the field.

Amplitude-dependent noise measurements were also made over larger sets of SQUID arrays but with certain "bad" channels turned off to see if doing so would allow other channels to show improved performance. The data shown in Figure 3.9 were measured on channels on 180 SQUID arrays[6] (rather than on the full set needed to read out all detectors, which is 210). "Bad" channels that were turned off during this measurement were chosen as those on SQUID arrays seen to be outliers based on noise performance from other metrics (such as median noise from zero-amplitude network analyses, as described below). Histograms from a measurement during which all available channels were operating is shown in Figure 3.11. Comparing these data to those shown in Figure 3.9, a slightly lower percentage of channels (70%) show noise less than 20 pA/$\sqrt{\text{Hz}}$ at a carrier tone amplitude of 1.0×10^{-2} (and similarly shifted for other carrier tone amplitudes). However, the difference is in part just from removing the "bad" channels rather than from improvement on the measured channels, and the difference is not large enough to provide a reliable solution to this problem in the field.

Lastly, a phase rotation was applied to the I- and Q-noise data to test whether or not it was possible to shift to a coordinate system (I' and Q') in which all of the amplitude dependence exists only in the Q' component of the signal [87, 108]. This was shown to be somewhat effective in earlier small-scale measurements with STAR Cryoelectronics E2 SQUID arrays [107]. Results of applying this phase rotation to the large-scale data are shown in Figure 3.12, and some statistics of the data comparing the noise at the lowest and highest carrier tone amplitudes before and after applying this phase rotation are summarized in Table 3.4. As can be seen in the data, application of a phase rotation is effective at reducing the overall I-phase noise levels at both high and low amplitudes. However, the amplitude-dependent nature of this noise remains even after applying a phase rotation as we still observe a dramatic increase in mean and median noise levels with increases in carrier tone amplitude.

[6] Although the algorithm was run for a total of 180 SQUID arrays, the number of SQUID arrays for which results were obtained may be smaller than this.

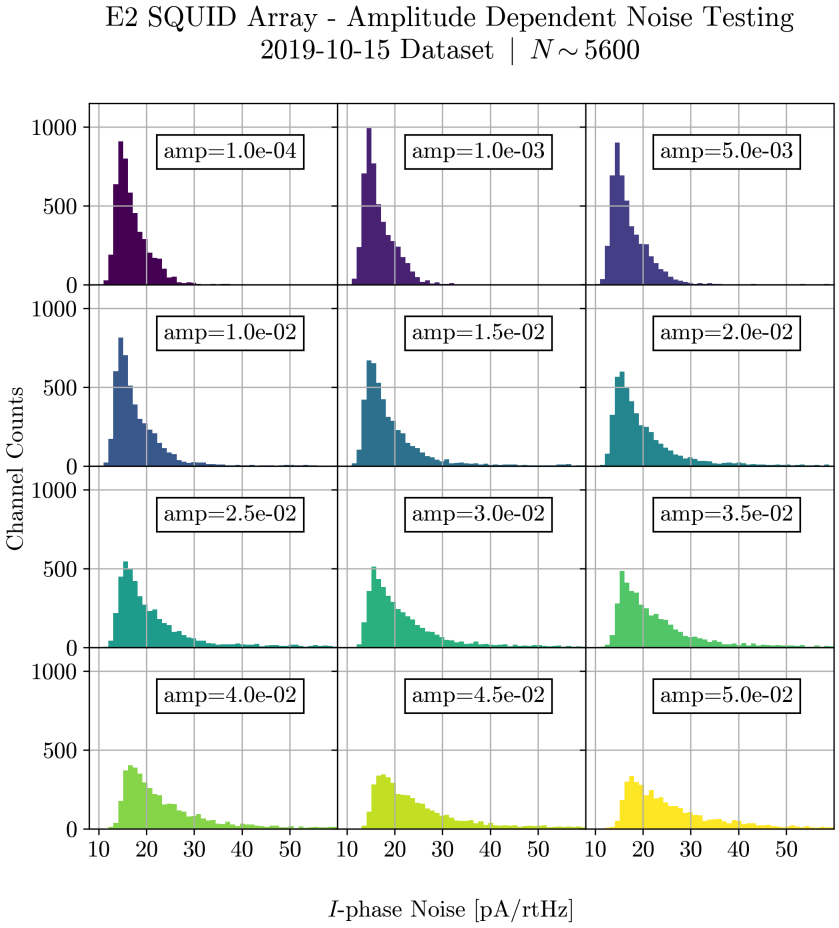

Figure 3.11: Results of amplitude-dependent noise measurements taken on a set of 206 E2 SQUID arrays. This measurement differs from that shown in Figure 3.9 in that it includes a nearly full set of SQUID arrays, rather than intentionally turning off SQUID arrays that had previously exhibited high noise. The goal was to determine if turning off "bad" SQUID arrays would allow others to achieve improved noise levels. The mean and median noise values for the lowest carrier tone amplitude, 1.0×10^{-4}, are 17.5 and 16.4 pA/$\sqrt{\text{Hz}}$, respectively, while the mean and median noise values for the highest carrier tone amplitude, 5.0×10^{-2}, are 81.4 and 27.9 pA/$\sqrt{\text{Hz}}$, respectively. These values are slightly higher than those achieved when the "bad" SQUID arrays are turned off, as expected, but the overall difference in performance is not large enough to solve the problem of amplitude dependence.

Although the histograms in Figures 3.9, 3.11, 3.12 depict the most straightforward way of representing the data collected in this measurement, a better indicator of SQUID array performance is to plot channel noise as a function of total current through a full comb of resonators and TESs (corresponding to a single SQUID array) as opposed to as a function of individual

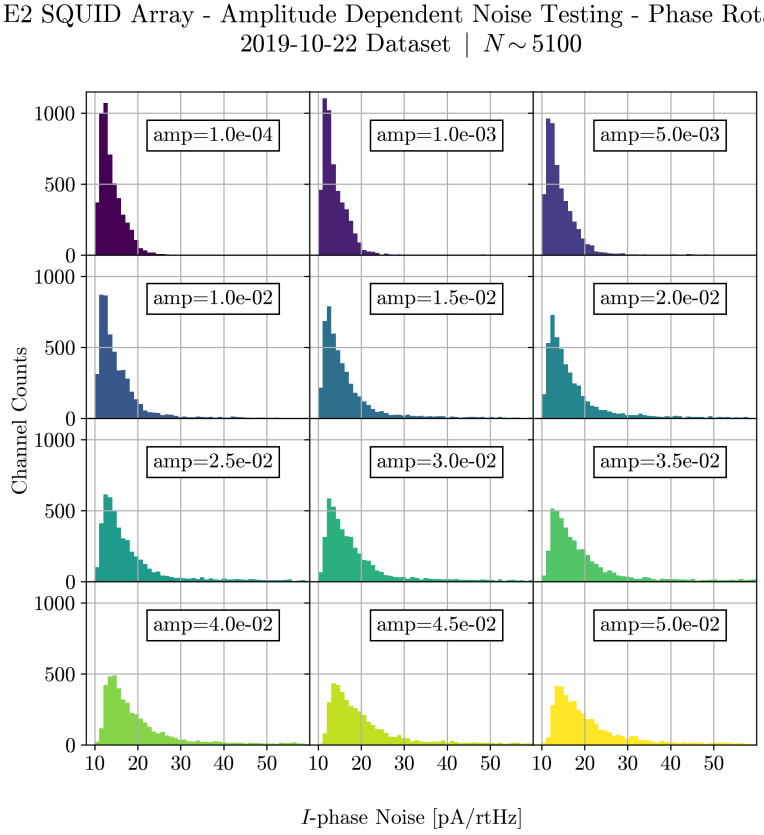

Figure 3.12: Results of applying a phase rotation to the data shown in Figure 3.9 (taken on a set of 180 E2 SQUID arrays) in order to minimize the I-phase noise. Although this technique is effective in reducing the overall noise levels at all carrier tone amplitudes, it is clear that I-phase noise in the rotated coordinate system still suffers from an amplitude dependence, with noise levels increasing with carrier tone amplitude. Statistics on this data with and without applying the phase rotation are indicated in Table 3.4.

carrier tone amplitude. These two values are not directly comparable when comparing different SQUID arrays involved in the measurement because channel yield varies for each readout module, and thus the number of bias tones associated with each SQUID array varies. Although ideally the DAN feedback causes the corresponding current through the SQUID array input coil to be zero regardless of carrier tone amplitude and number of carrier tones (because the corresponding nuller tones will cancel them), this is not necessarily the case in practice due to noise sources such as crosstalk (signal from tones on neighboring resonator combs contaminating the signal through the measured module). In general, it is believed that the current load on the SQUID array scales with

Table 3.4: Statistics corresponding to amplitude-dependent noise data collected for 180 E2 SQUID arrays before and after applying a phase rotation to reduce the I-phase noise. Statistics shown correspond to the 2019-10-22 dataset shown in Figures 3.9 and 3.12 (before and after phase rotation, respectively). "Low Amplitude" and "High Amplitude" correspond to carrier tone amplitudes of 1.0×10^{-4} and 5.0×10^{-2} in normalized units, the lowest and highest amplitudes measured, respectively. "Low Noise" indicates channels with median noise < 20 pA/$\sqrt{\text{Hz}}$. Applying the phase rotation reduces the overall noise levels and increases the percentage of channels with low noise, but does not remove the amplitude dependence of the noise. Even after applying the phase rotation, significant increases are seen in both the mean and median noise levels as carrier tone amplitude is increased.

		Before Phase Rotation	**After Phase Rotation**
Median Noise $\left[\text{pA}/\sqrt{\text{Hz}}\right]$	Low Amplitude	16.1	13.1
	High Amplitude	25.7	19.9
	% Change	60%	52%
Mean Noise $\left[\text{pA}/\sqrt{\text{Hz}}\right]$	Low Amplitude	17.2	14.0
	High Amplitude	79.2	53.7
	% Change	360%	280%
% Low Noise	Low Amplitude	82%	96%
	High Amplitude	28%	51%

the current through the corresponding comb, though the proportionality is not precisely known. Because of this, we use total current through the resonator combs as a proxy for current load on the SQUID array. We group the data for each histogram based on this quantity which is found by summing the currents through each resonator/TES on a given comb for a given carrier tone amplitude. Figure 3.13 shows this depiction, using the same data plotted in Figure 3.9.

Using data from dark detector measurements, we roughly estimate the current through an individual TES to be about 4.8 μA when observing the CMB in the field. We then estimate the total RMS current through the comb as

$$I_{tot} = \frac{I_{TES}}{\sqrt{2}} \times \sqrt{N} \approx 21 \ \mu\text{A}, \tag{3.3}$$

assuming the resonator comb has 100% yield ($N = 40$). We therefore can conservatively evaluate the expected amplitude-dependent noise performance of the STAR Cryoelectronics E2 SQUID

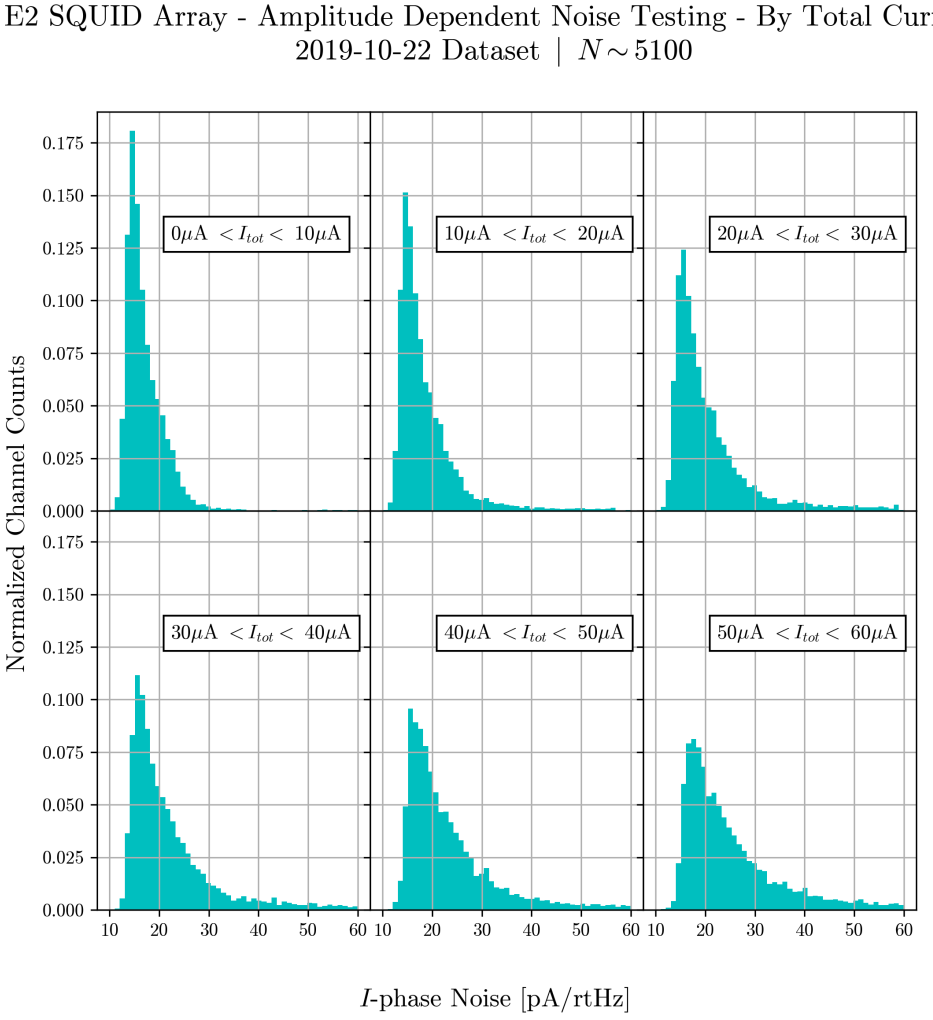

Figure 3.13: Results of amplitude-dependent noise measurements taken on a set of 180 E2 SQUID arrays (same dataset as shown in Figure 3.9) organized by total current through the resonator comb (I_{tot}). Each plot depicts a histogram of the I-phase noise values measured for the active channels when the total (RMS) current through the resonator comb was within the specified range. The y-axis indicates normalized channel counts rather than absolute channel counts because the total number of channels measured for each current range varies significantly (due to differences in channel yield on different combs). Like with carrier tone amplitude, as total current through the resonator comb increases, overall noise levels of the system increase and the histograms flatten. The mean noise values for the most relevant current ranges, $10\mu A < I_{tot} < 20\mu A$ and $20\mu A < I_{tot} < 30\mu A$, are 26.0 and 37.5 pA/$\sqrt{\text{Hz}}$, respectively. The median noise values for these current ranges are 16.9 and 18.6 pA/$\sqrt{\text{Hz}}$, respectively. The histograms only show data up to 60 pA/$\sqrt{\text{Hz}}$, but many channels, especially at higher current ranges, had noise values much higher than this.

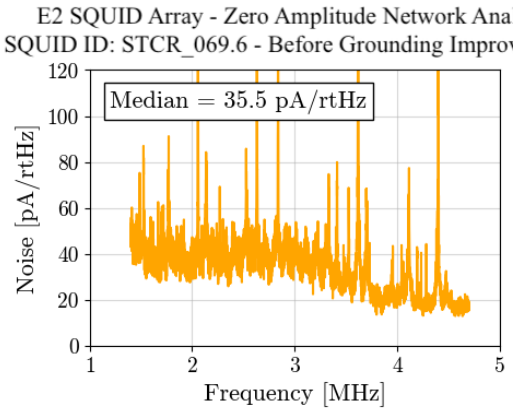

(a) Noise vs. frequency for zero-amplitude network analysis noise measurement on E2 SQUID array STCR_069.6 using data taken before grounding improvements were made to the system. Results indicate noise levels that do not meet the requirement, with a median noise level of 35.5 pA/$\sqrt{\text{Hz}}$.

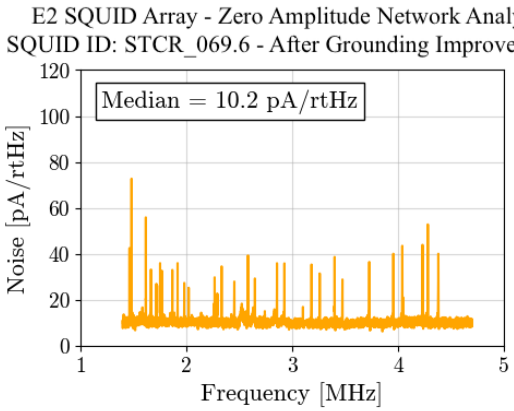

(b) Noise vs. frequency for zero-amplitude network analysis noise measurement on E2 SQUID array STCR_069.6 using data taken after grounding improvements were made to the system. Results indicate noise levels that meet the requirement, with a median noise level of 10.2 pA/$\sqrt{\text{Hz}}$.

Figure 3.14: Zero-amplitude network analysis example plots for a single E2 SQUID array during full-scale tests in the PB-2b receiver performed while the focal plane was cooled below the transition temperature of the detectors. The plot on the left shows data taken before improvements had been made to the grounding of the ambient-temperature readout electronics, while the plot on the right shows data taken after. The reduction of overall noise levels between the two datasets indicates that readout noise levels for E2 SQUID arrays depend heavily on the grounding scheme of the readout electronics. Both datasets exhibit narrow-band features which are thought to arise from environmental pickup but are unlikely to influence the overall readout noise level significantly.

arrays in the field by examining the top-center and top-right panels of Figure 3.13, which show channel noise levels for SQUID arrays operating with $10-20$ μA and $20-30$ μA of current through their corresponding resonator combs, respectively. In these two regimes, 71% and 58% of channels exhibit noise levels below 20 pA/$\sqrt{\text{Hz}}$, leaving a significant number of E2 SQUID arrays linked to high noise at full scale.

Finally, noise measurements from zero-amplitude network analyses were performed on the full set of E2 SQUID arrays during this cooldown. Examples of data from a single SQUID array measured at different times during the cooldown are shown in Figure 3.14, with noise plotted against frequency. The two datasets were measured two weeks apart, with the most crucial change between the two measurements being the ground connection for some of the SQUID

controller boards. The left (earlier) plot shows data from a SQUID array with a median noise level of 35.5 pA/$\sqrt{\text{Hz}}$ and elevated noise levels across a wide region of the readout band. The right (later) plot shows data from the same SQUID array, now with a median noise level of 10.2 pA/$\sqrt{\text{Hz}}$ and only narrow-band features present. Both wide-band and narrow-band features are indicative of environmental pickup within the electronics. Narrow-band features should not influence the overall readout noise level significantly so long as they do not over lap directly with the resonator frequencies, which is unlikely. For this reason, we take the median of the data from this measurement to represent the noise associated with a given SQUID array. Wide-band features, however, along with elevated noise floors, can span multiple resonator frequencies and therefore can impact overall readout noise. This measurement illustrates the need to implement proper grounding in order to minimize environmental pickup.

Overall results for 206 SQUID arrays (nearly full set) are shown in Figure 3.15, where the median noise level associated with each SQUID array is plotted. With the grounding iterations, the noise levels in all SQUID arrays was reduced to less than 20 pA/$\sqrt{\text{Hz}}$, as required.

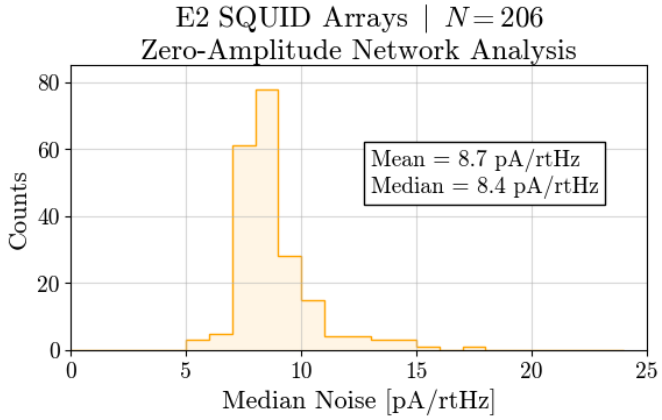

Figure 3.15: Histogram of median noise levels of a nearly full set of E2 SQUID arrays measured during zero-amplitude network analyses. Data shown were taken after improvements to the grounding configuration of the ambient-temperature electronics had been implemented, decreasing the noise levels on some SQUID arrays. During this test, all measured SQUID arrays achieved noise levels below 20 pA/$\sqrt{\text{Hz}}$, as desired, with a mean of 8.7 pA/$\sqrt{\text{Hz}}$ and a median of 8.4 pA/$\sqrt{\text{Hz}}$.

It is important to note, however, that both the zero-amplitude network analysis data and the amplitude-dependent noise data were measured after careful assessment of the SQUID arrays' $V-\Phi$ curves to identify acceptable tuning points. If the $V-\Phi$ curves were to change significantly, they could require manual re-optimization of the tuning points to achieve acceptably low noise, a procedure which, as stated, is not feasible regularly in the field.

The problems identified with full-scale operation of E2 SQUID arrays during the cooldown described in this section are linked but not entirely correlated. As with the $V-\Phi$ curves, some trends were seen between noise (both from zero-amplitude network analyses and from amplitude-dependent tests) and position on the SQUID PCB, with SQUID arrays farther from the connection point to resonator combs more often exhibiting high noise.

NIST SA13a SQUID Arrays

Development of the readout system for PB-2b benefited from experience with the PB-2a receiver. Though no full-scale tests were performed with NIST SA13a SQUID arrays in laboratory measurements of the PB-2b receiver, this type of SQUID design was implemented in PB-2a and has been used in both laboratory and field measurements with a fully populated focal plane and readout system. Though there exist differences between the two receivers, the PB-2a and PB-2b readout systems are nearly identical[7], and thus data taken in PB-2a was able to help inform the choice of SQUID design for PB-2b. However, fewer SQUID-specific measurements have been run in the PB-2a receiver because the collaboration's focus has been on full-receiver characterization and calibration. Since installation of the PB-2a in the field, the NIST SA13a SQUID arrays in PB-2a have fortunately not played a limiting role in receiver operation and observations, reducing the need for this type of data.

Densely sampled $V-\Phi$ curves for a nearly full set of SA13a SQUID arrays in the PB-2a

[7]The readout system initially deployed with the PB-2a receiver differed from that in PB-2b receiver due to its use of aluminum *LC* resonators. However, these were replaced in 2020 with niobium LC resonators, matching those in PB-2b.

receiver were measured shortly after the receiver was installed in the field. An example of one of these measurements is shown in Figure 3.16. The $V-\Phi$ curve shown in Figure 3.16

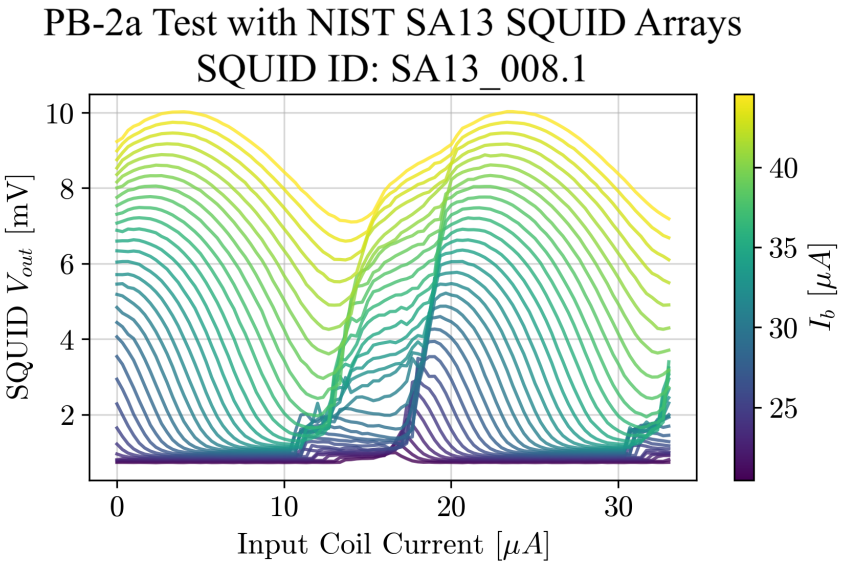

Figure 3.16: Example of a $V-\Phi$ curve from a NIST SA13a SQUID array taken in the PB-2a receiver in the field in 2019. The curve for this particular SQUID array is representative of the larger set of $V-\Phi$ curves measured across the receiver. Although there is a clear distortion on the rising edge of the curve, this type of feature is not expected to hinder our ability to operate the SQUID arrays sufficiently as SQUID tuning points are chosen to be on the opposite side.

is representative of the larger set of 207 $V-\Phi$ curves recorded across the receiver during this measurement. There is a clear distortion on the rising edge of the curve, as was seen for many other SQUID arrays. These types of features actually correspond to the "falling-edge kinks" described in relation to E2 SQUID array testing due to the flipped orientation of the SQUID connection on the PCB, and are not unexpected as they had been seen in laboratory measurements and are likely due to parasitic capacitance in the circuit [106]. The flipped nature of the SQUID connection was implemented intentionally in order to prevent these features from hindering our ability to operate the SQUID arrays as SQUID tuning points are chosen to be on the opposite side.

From visual inspection, other types of features were seen on only about 6% of $V-\Phi$ curves, and the features seen are relatively mild. Additionally, unlike the trends seen with the E2 SQUID arrays, no significant dependence on the SQUID array's position on the SQUID PCB has

been observed with the SA13a SQUID arrays in PB-2a.

The smooth $V - \Phi$ behavior of these SQUID arrays directly impacts our ability to tune them reliably and efficiently in preparation for data taking with bolometers in the field. Since its installation in the field, SQUID tuning has not caused any problems for PB-2a, with high and often perfect tuning yield on SQUIDs attached to active resonator combs.

Amplitude-dependent noise data for the set of SA13a SQUID arrays in the PB-2a receiver are shown in Figures 3.17 and 3.18. These figures show histograms of median channel noise for each carrier tone amplitude. Figure 3.17 shows the original data, while Figure 3.18 shows data from the same measurement after applying a phase rotation as was done for the E2 SQUID array data. Statistics from this dataset before and after applying the phase rotation are summarized in Table 3.5.

Table 3.5: Statistics corresponding to amplitude-dependent noise data collected for 137 SA13a SQUID arrays before and after applying a phase rotation to reduce the I-phase noise. Statistics shown correspond to the 2021-05-17 dataset shown in Figures 3.17 and 3.18 (before and after phase rotation, respectively) collected using SA13a SQUID arrays operating in the PB-2a receiver in the field. "Low Amplitude" and "High Amplitude" correspond to carrier tone amplitudes of 1.0×10^{-4} and 5.0×10^{-2} in normalized units, the lowest and highest amplitudes measured, respectively. "Low Noise" indicates channels with median noise < 20 pA/$\sqrt{\text{Hz}}$. Applying the phase rotation reduces the overall noise levels and increases the percentage of channels with low noise. Though the phase rotation does not remove the amplitude dependence of the noise entirely, the data show this technique to have a larger impact on SA13a SQUID arrays than on E2 SQUID arrays in this regard. Corresponding data for E2 SQUID arrays can be found in Table 3.4 for comparison.

		Before Phase Rotation	**After Phase Rotation**
Median Noise $\left[\text{pA}/\sqrt{\text{Hz}}\right]$	Low Amplitude	16.6	13.6
	High Amplitude	20.8	15.9
	% Change	25%	17%
Mean Noise $\left[\text{pA}/\sqrt{\text{Hz}}\right]$	Low Amplitude	18.2	14.9
	High Amplitude	60.4	39.1
	% Change	230%	160%
% Low Noise	Low Amplitude	73%	88%
	High Amplitude	47%	68%

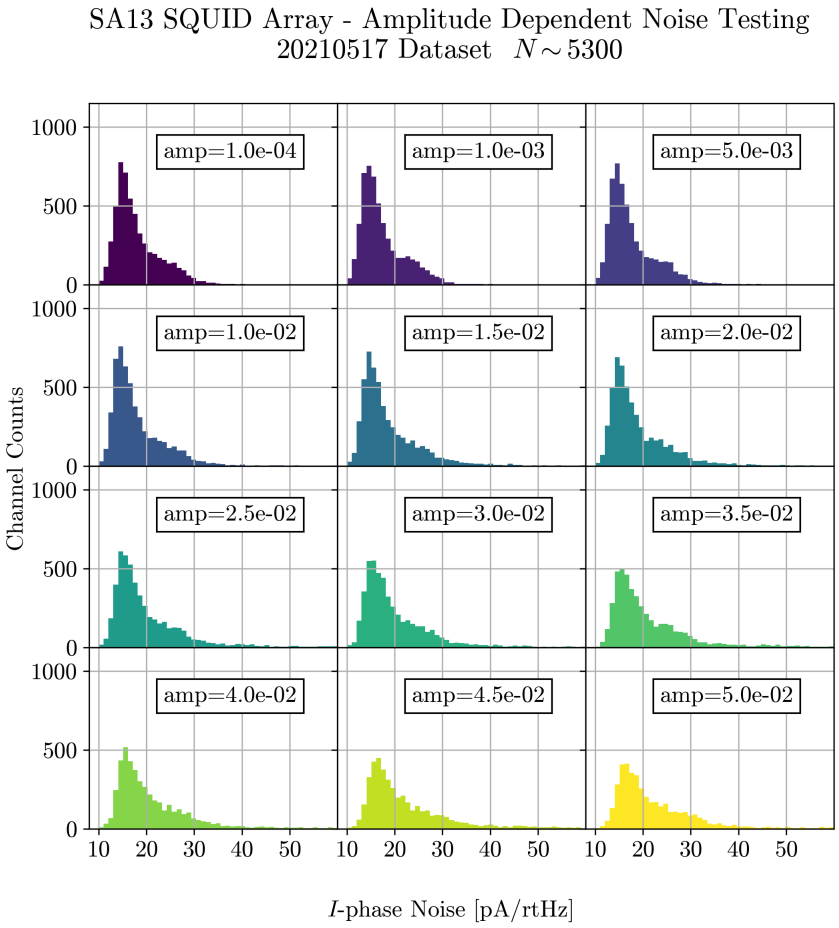

Figure 3.17: Results of amplitude-dependent noise measurements taken on a set of 137 SA13a SQUID arrays in the PB-2a receiver while operating in the field. Each plot depicts a histogram of the I-phase noise values measured for the active channels when a carrier tone of a given amplitude was passed through the resonator circuit. A total of about 5300 channels were measured during this test, with the exact number of active channels at each carrier tone amplitude varying. Corresponding data for E2 SQUID arrays can be found in Figure 3.9 for comparison. As with the E2 SQUID arrays, overall noise levels are seen to increase as carrier tone amplitude is increased, though the correlation is slightly less pronounced. Some statistics for this dataset are shown in Table 3.5. The histograms only show data up to 60 pA/$\sqrt{\text{Hz}}$, but many channels, especially at higher carrier tone amplitudes, had noise values much higher than this. Carrier tone amplitudes are quoted in normalized units from the ambient-temperature readout electronics.

As was seen for the E2 SQUID arrays, there is a clear correlation between I-phase noise levels and carrier tone amplitude, with noise increasing as amplitude is increased. However, this dependence is less dramatic for the SA13a SQUID arrays compared to the E2 SQUID arrays, and

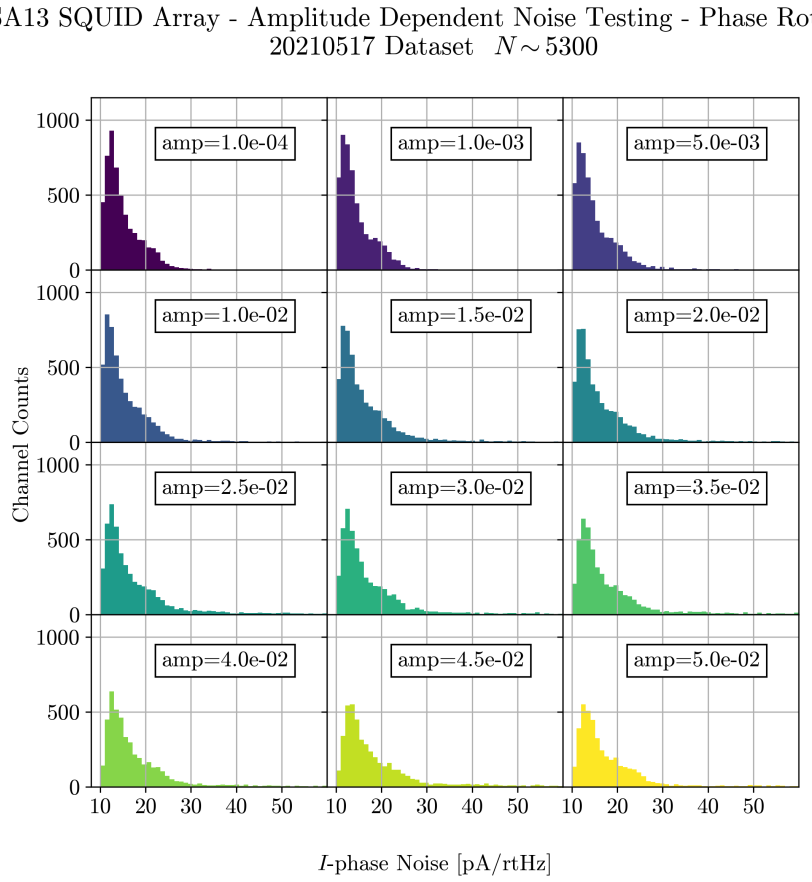

Figure 3.18: Results of applying a phase rotation to the data shown in Figure 3.17 (taken on a set of 137 SA13a SQUID arrays while operating in the field) in order to minimize the I-phase noise. Corresponding data for E2 SQUID arrays can be found in Figure 3.12 for comparison. As with the E2 SQUID arrays, applying the phase rotation reduces the overall noise levels at all carrier tone amplitudes but a dependence on carrier tone amplitude persists, though this dependence is reduced. Statistics on this data with and without applying the phase rotation are indicated in Table 3.5.

the implementation of a phase rotation further reduces this dependence for the SA13a SQUID arrays. While a weaker dependence on carrier tone amplitude is beneficial for operating SQUID arrays in the field reliably under varying conditions, the SA13a SQUID arrays also show slightly higher noise values at low carrier tone amplitude compared to the E2 SQUID arrays.

Preliminary noise measurements from zero-amplitude network analyses have also been made for SA13a SQUIDs in the PB-2a receiver in the field. Figure 3.19 shows a histogram of

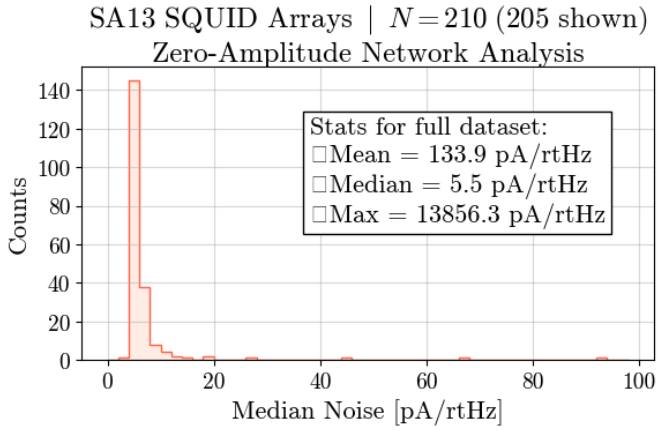

Figure 3.19: Histogram of median noise from zero-amplitude network analyses performed on a full set of SA13a SQUID arrays during operation in the field in the PB-2a receiver. Though data was collected for the full set of 210 SQUID arrays, the data plotted correspond only to the 205 SQUID arrays with noise levels below 100 pA/$\sqrt{\text{Hz}}$, for clarity. However, the statistics listed are calculated using the full set of data. A large majority of SA13a SQUID arrays (96%) achieve noise levels below 20 pA/$\sqrt{\text{Hz}}$, indicating that this SQUID design is capable of meeting the requirement. However, a few outliers show higher noise.

median noise values taken from a measurement performed in 2019.

96% of SQUID arrays achieve noise levels below 20 pA/$\sqrt{\text{Hz}}$, meeting the requirement. The median value for the full set is 5.5 pA/$\sqrt{\text{Hz}}$, well below this threshold. However, nine SQUID arrays were measured with noise levels above this value, two of which showed extremely high noise ($>$ 10000 pA/$\sqrt{\text{Hz}}$) and severely impacted the mean value of the full dataset. Figure 3.19 only plots data up to 100 pA/$\sqrt{\text{Hz}}$, but the statistics listed take the full set of data into account.

Without additional iterations on this measurement which have not been a priority compared to other commissioning tasks in the field, it is unclear whether the outliers are caused by problems in the SQUID or by other factors in the readout system. The overall set of data from PB-2a, however, indicates that SA13a SQUID arrays are capable of performing with low noise in the field.

One important note about the SA13a SQUID arrays operating in the PB-2a receiver is that all of these SQUID arrays underwent screening in the laboratory before being chosen for use in the field. At minimum, this screening involved tuning with the pyDfmux algorithm with

the SQUID arrays operated in a PB-2 receiver, with or without being connected to resonators and detectors, to ensure transimpedance levels meeting the 350 Ω requirement. The full-scale measurements presented in this section of the E2 SQUID arrays also came after screening, but the criteria for these SQUID arrays were less stringent because the SQUID arrays were to be used in a laboratory test and because the data from the screening runs were less reliable.

Decision to Use NIST SA13a SQUID Arrays

In all, the STAR Cryoelectronics E2 SQUID arrays demonstrated promising characteristics during small-scale tests, and a majority have been shown to achieve required performance in large-scale tests with careful attention to tuning parameters and grounding schemes. Unfortunately, a lack of demonstrated ease and reliability of tuning, combined with a stronger dependence of noise on carrier tone amplitude that is not yet understood, would make full-scale operation in the field risky without further testing thought to be incompatible with PB-2b's commissioning schedule.

On the other hand, though the NIST SA13a SQUID arrays show slightly worse (but still sufficient) performance with regard to quantitative parameters like transimpedance, they have been shown to perform very reliably at full-scale. For this reason, NIST SA13a SQUID arrays were chosen for use in the PB-2b receiver in the field[8]. STAR Cryoelectronics SQUID arrays remain a promising possibility for use in future experiments and are being further characterized and tested in other systems within the CMB community [109]. Section 3.2.3 details laboratory measurements performed on the set of NIST SA13a SQUID arrays intended for use in the field.

3.2.3 Characterization of PB-2b Deployment SQUIDs (SA13s)

The SA13a SQUID arrays deployed with PB-2b were fabricated at NIST in late 2019 and are identical in design to those operating in the PB-2a receiver. A total of 360 SQUID arrays were

[8]Earlier publications indicate a choice of STAR Cryoelectronics E2 SQUID arrays for PB-2b. This was the project's plan following small-scale testing, but results from large-scale testing prompted re-evaluation, and ultimately a reversal of this decision.

fabricated across two silicon wafers (evenly distributed) for potential use in the PB-2b receiver, where a minimum of 210 SQUID arrays is needed to read out all detectors. The wafers are shown in Figure 3.20.

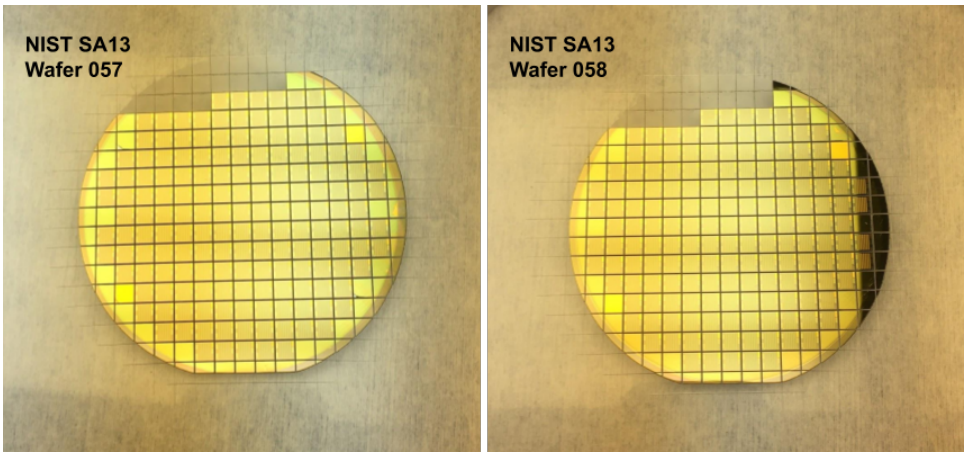

Figure 3.20: Photos of the two fabricated wafers of NIST SA13a SQUID arrays for use in PB-2b, W057 and W058. Photos were taken after eight SQUID arrays had been removed from each wafer to be used for initial screening.

Eight SQUID arrays from each fabricated wafer were tested at UC Berkeley in a small test cryostat upon arrival of the wafers. The purpose of this immediate small-scale test was to verify basic operability of these SQUID arrays before investing time and resources into large-scale testing, given the tight deployment schedule at the time. Results from this initial test are shown in Figure 3.21.

The results demonstrated expected SQUID functionality with sufficiently high transimpedance values, indicating no overall problems with fabrication. This gave us confidence to move forward with large-scale screening of devices for use in the field.

Screening of the remaining SQUID arrays occurred in the PB-2c receiver backend, also at UC Berkeley. This is thought to be a suitable environment for PB-2b SQUID array screening as the PB-2c backend is nearly identical to that of PB-2b apart from the details of the sub-kelvin refrigeration components, which are not expected to impact SQUID performance. A total of 256 SQUID devices were screened across two cooldowns of this receiver. In the first cooldown,

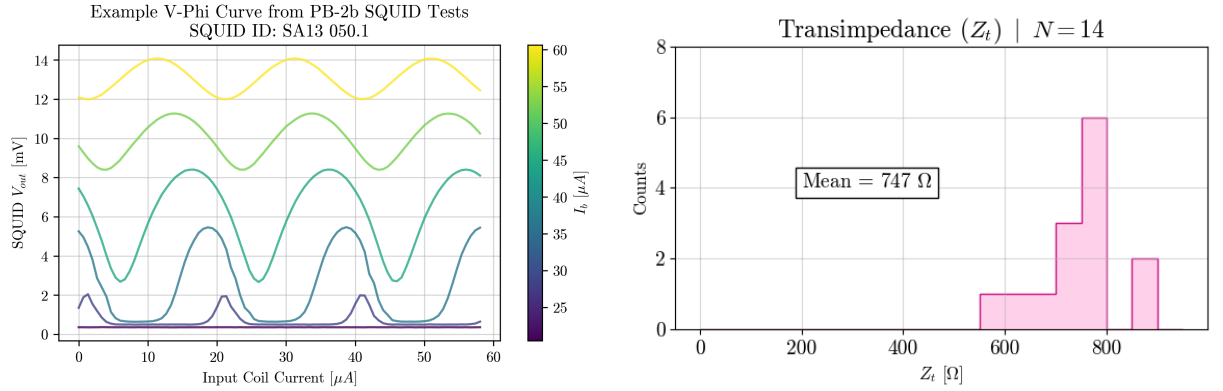

(a) Voltage vs. flux curve for one of the SQUID arrays tested during initial screening of SA13a SQUID arrays for the PB-2b receiver.

(b) Overall results for the achieved transimpedance for the 14 SA13a SQUID arrays measured during this test.

Figure 3.21: Results from initial screening of NIST SA13a SQUID arrays intended for use in PB-2b. Eight SQUID arrays from each fabricated wafer were assembled across two SQUID PCBs and tested at UC Berkeley. Two of the 16 SQUID arrays, one from each wafer, could not be operated during this test for reasons thought to be unrelated to the SQUID chip and are not included in these results. The left plot shows a set of voltage vs. flux curves for one of the SQUID arrays tested. The voltage behavior at different current and flux biases matches expectations for NIST SA13a SQUID arrays from previous measurements using the PB-2a devices. The histogram on the right depicts the overall results of achieved transimpedance for the 14 SQUID arrays. The results were sufficient such that we felt confident moving forward with large-scale testing of these wafers.

208 SA13a SQUID devices were populated onto 26 version-8 SQUID PCBs. In the second, 48 SQUID devices were populated onto four version-7 SQUID PCBs and two version-8 SQUID PCBs. 24 of the 26 SQUID PCBs from the first cooldown remained in the receiver for the second, some with slight changes in their electrical configurations, in order to test for repeatability. The two PCB versions differ mainly in the connection made between the PCB and the SQUID input coil as described in 2.2.4, but both designs are expected to be suitable for use in the PB-2b receiver and this choice should not impact results from screening[9].

A voltage vs. flux ($V - \Phi$) curve for one of the SQUIDs tested during these runs in shown in Figure 3.22. The plot on the left shows data from the first cooldown and the plot on the right

[9]SQUID arrays in the PB-2a receiver are all populated on version-7 SQUID PCBs, which have been working well.

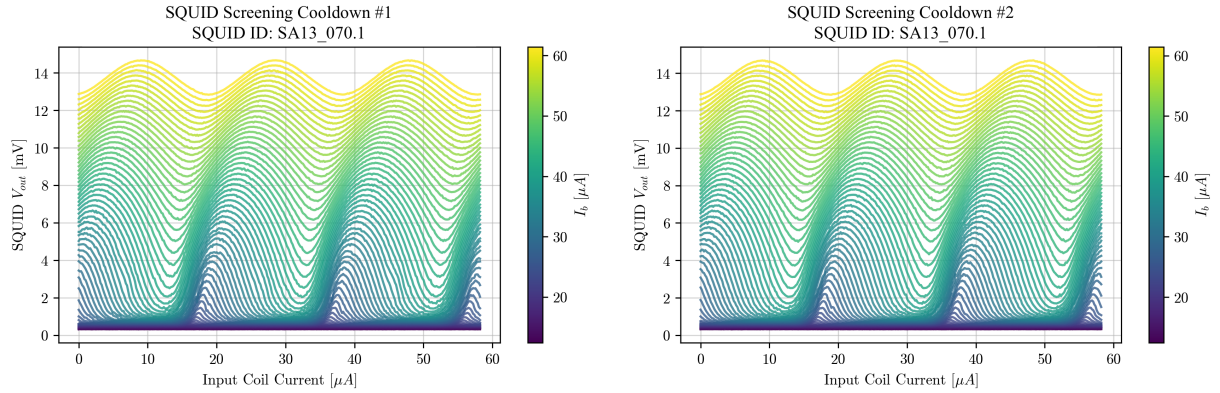

(a) Data from first PB-2b SA13a SQUID screening cooldown.

(b) Data from second PB-2b SA13a SQUID screening cooldown.

Figure 3.22: Voltage vs. flux ($V - \Phi$) curves for SQUID array SA13_070.1 during testing in both screening cooldowns inside the PB-2c receiver backend. SA13_070.1, like the majority of SQUID arrays screened during these cooldowns, was tested without its output connected to resonators and detectors. The curves shown are representative of the larger set of SQUID arrays that were tested during these screening cooldowns, and match with expectations given measurements made with SA13a SQUID arrays used in the PB-2a receiver. The left plot shows data from the first cooldown and the right shows data from the second. The results show consistency between these two separate cooldowns, providing further evidence that these SQUID arrays will operate reliably in the field.

shows data from the second. The data measured in the two separate cooldowns are extremely similar, showing nearly identical SQUID array behavior and providing evidence that these SQUID arrays will operate reliably in the PB-2b receiver in the field. Furthermore, these $V - \Phi$ curves are representative of the overall set of SQUID arrays tested and match with expectations formed from measurements of other SA13 SQUID arrays.

Overall results of SQUID properties measured in the two cooldowns are shown in Figure 3.23. Data for 231 of the 256 SQUID arrays were obtained after running the SQUID tuning algorithm. No data were obtained for the remaining 25 SQUID arrays due to an inability to tune the arrays, either due to open electrical connections or unknown issues either with the SQUID chip or another piece of hardware. In all, distributions were found with means of 582 Ω, 5 mV, and 675 Ω for transimpedance, peak-to-peak voltage, and dynamic impedance, respectively, in agreement with expectations based on data from the PB-2a receiver. Furthermore, noise measurements with

these SQUID arrays were performed, the results of which are discussed below and depicted in Figure 3.24.

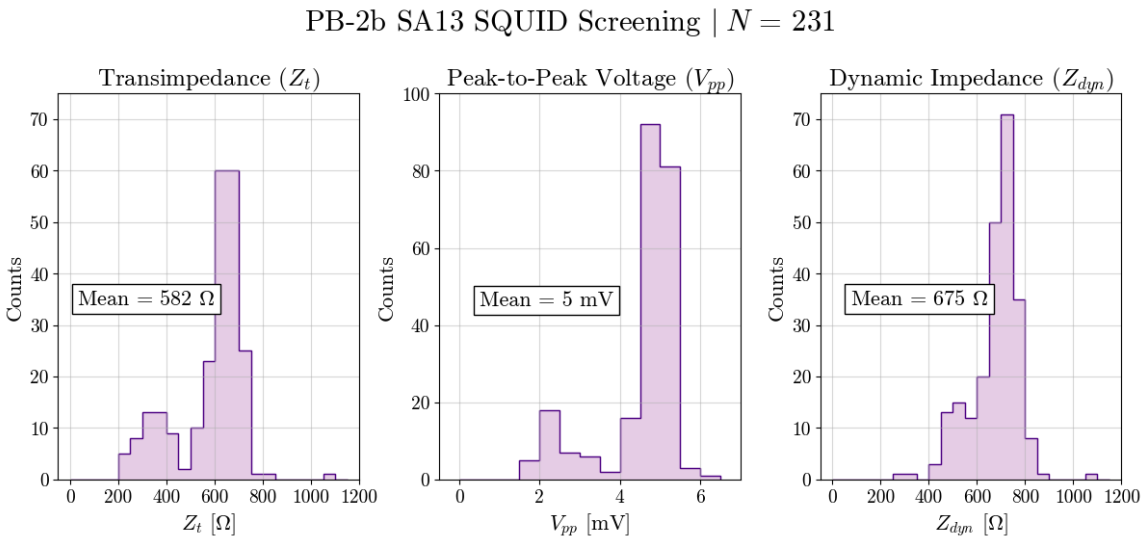

Figure 3.23: Histograms of measured SQUID properties for the 231 SA13a SQUID arrays that were tested in the PB-2c receiver backend. There were 25 additional SA13a SQUID arrays included in these cooldowns for which we were not able to measure data. The distributions for transimpedance (Z_t) and peak-to-peak voltage (V_{pp}) contain two peaks, with the larger peaks centered around 650 Ω and 5 mV, respectively. A set of six SQUID PCBs were found to contain only SQUID arrays whose measured Z_t and V_{pp} values fell in the smaller, lower-valued peaks of the distributions, indicating a problem with other components of the electronics system rather than with the SQUID arrays themselves. Nevertheless, SQUID arrays on these cards were not selected for deployment. The distribution for dynamic impedance (Z_{dyn}) is more uniform, with a mean value of 675 Ω.

During these screening cooldowns, the SQUID PCBs were installed in the PB-2c backend similarly to how they will be installed in the PB-2b receiver, but with two notable differences. Firstly, during these test runs the majority of SA13a SQUID arrays were tested with open input coils rather than being electrically connected in a deployment-like configuration. Only two SQUID PCBs during each cooldown contained SQUID arrays whose input coils were connected to resonators and detectors. Secondly, PB-2b employs SQUID cooling brackets made of gold-plated copper [65]. These brackets provide a thermal link between the SQUID PCBs and the 4-K shell of the receiver backend, but also serve as an important ground path for the SQUID

chips. In the test cooldowns in the PB-2c backend, only the SQUID PCBs connected to resonators and detectors were installed with these deployment-style SQUID cooling brackets. These two changes to the readout circuit for certain SQUID arrays resulted in a clear correlation between the properties of a given SQUID chip and its position on the SQUID PCB. For SQUID PCBs that were not connected to detectors and did not have deployment-style cooling brackets, the corresponding SQUID arrays located farthest from the intended connection point to resonators and detectors (position 8) exhibited a clear degradation in transimpedance and noise properties, as illustrated by the yellow points in Figure 3.24. Comparatively, SQUID arrays in other positions on the SQUID PCBs, as well as SQUID arrays in position 8 on SQUID PCBs that were connected to detectors and resonators, achieved high transimpedance and low noise, as shown by the cyan points and black stars, respectively[10]. Because the correlation between performance and deployment-style connections is so definitive, we do not expect this type of SQUID array position dependence to arise when operating PB-2b in the field. In addition to this trend with SQUID position for some SQUID PCBs, we also observed six SQUID PCBs for which all SQUID arrays exhibited uncharacteristically low transimpedance and peak-to-peak voltage values compared to other SA13 SQUID arrays both from this batch and from previous fabricated wafers. Data from these SQUID arrays are represented by the red "Low-V_{pp} SQUID PCB" points in Figure 3.24. Because the set of SQUID arrays showing this poor performance was entirely correlated with SQUID PCB and thus other pieces of readout hardware, we did not take these results to be indicative of a larger issue with the SQUID array fabrication. However, the root cause of the problem seen with the performance of SQUID arrays on these PCBs remains unknown.

In order to ensure reliable and repeatable operation of PB-2b in the field with suitably low readout noise, selection criteria for PB-2b SQUID arrays were put in place and SQUID

[10]There is one yellow data point at high Z_t and relatively low noise compared to the other "Position 8 - No Detectors" SQUID arrays. However, this SQUID array was tested with a diode thermometer attached to its SQUID PCB, which may have been providing a comparable ground path to one that is normally provided by a SQUID cooling bracket. This additional connection may explain the relatively good performance of this SQUID array despite its position on the SQUID PCB and its lack of connection to detectors and resonators.

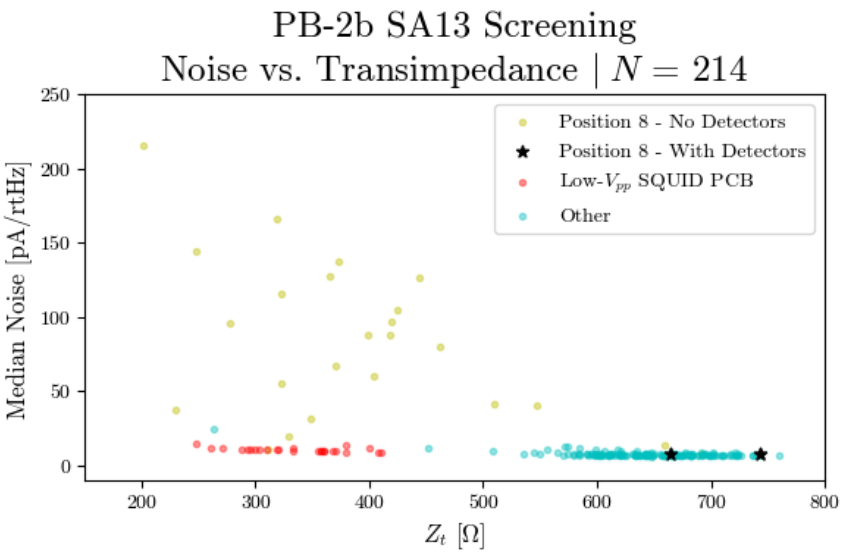

Figure 3.24: Measured transimpedance vs. median noise from zero-amplitude network analysis for 214 SA13a SQUID arrays tested in the PB-2c receiver backend for screening. Data for an additional three SA13 SQUID arrays was obtained during these cooldowns but are omitted from this plot for clarity because the points lie outside the axis limits (one SQUID array in the "Position 8 - No Detectors" category with very high noise, and two SQUID arrays in the "Other" category with very high transimpedance). The data points are colored to highlight the differences across four categories of SQUID arrays. The yellow points represent SQUID arrays that were installed in the eighth position on the SQUID PCB, farthest from the connector which generally leads to detectors and resonators but which was left open for this test. The black stars represent two SQUID arrays also in this eighth position on the SQUID PCB, but ones that were connected to detectors and resonators during this test. Though the sample size is small, it is clear that this degraded performance for position-8 SQUID arrays shows up only when the SQUID array is not connected in its deployment-style configuration, giving us confidence that even SQUID arrays deployed in the field in position 8 will work well to read out detectors. The red points represent SQUID arrays that were contained on a subset of six SQUID PCBs whose SQUID arrays exhibited unusually poor performance. As seen in the plot, because this poor performance was so highly correlated to SQUID PCB, it is unlikely the problem is in the SQUID arrays themselves or is indicative of a problem with the fabrication batch. Neither these SQUID arrays nor these SQUID PCBs will be used in the field. The cyan points represent all other SQUID arrays that were tested during these screening cooldowns, which are seen in general to have high transimpedance and low noise, as desired.

arrays were selected based on their performance in the screening runs described above. SQUID arrays were chosen only if they showed $Z_t > 350\ \Omega$, $Z_{dyn} < 900\ \Omega$, and median noise from zero-amplitude network analysis measurements $< 20\ \mathrm{pA}/\sqrt{\mathrm{Hz}}$. We also required the SQUID array to have been successfully tuned using the standard pyDfmux tuning algorithm and that

its $V - \Phi$ curve was shown to be free of any major features. Exceptions were made for the Z_t and noise requirements only for SQUIDs that were screened in position 8 on the SQUID PCB and that satisfied all other criteria (21 SQUID arrays fell into this category). In addition, the 16 SQUID arrays that were included in the initial smaller-scale tests did not undergo Z_{dyn} or noise measurements, and these criteria were ignored when evaluating this set of SQUID arrays.

Of the 272 SQUID arrays tested between these three runs, 215 satisfied these criteria. The total number needed to read out the full PB-2b focal plane is 210, leaving 5 SQUID arrays to be used as spares. One additional SQUID array fell short of the noise requirement slightly but met all other criteria and was selected as an additional spare. Histograms of Z_t, Z_{dyn}, median noise from zero-amplitude network analysis measurements, and V_{pp} are shown in Figure 3.25.

In all, 240 SQUID arrays were prepared across five version-7 SQUID PCBs and 25 version-8 SQUID PCBs for deployment with the PB-2b receiver. 210 of the screened and selected SQUID arrays were populated across 28 SQUID PCBs in positions such that they will be connected to resonators and detectors when the PB-2b receiver is operating in the field. The remaining 6 screened SQUID arrays, along with 24 additional unscreened SQUID arrays, were populated into the remaining PCB positions to be used either as spares or for calibration and troubleshooting in the field[11].

3.2.4 Other Readout Components

Other components of the readout system were also tested before deploying the PB-2b receiver. On the side of the cryogenic readout components, the *LC* resonators intended for use in PB-2b are made of niobium and differ in material compared to those originally deployed with PB-2a and PB-1, which were made of aluminum[12]. The higher superconducting temperature

[11] Not counting a handful of SQUID arrays that failed to meet screening requirements seemingly due to issues with the SQUID PCB or other hardware in the readout chain, 96% of SQUID arrays fabricated on these NIST wafers satisfied our requirements, giving us confidence that the unscreened SQUID arrays will work well if needed.

[12] Though PB-2a was originally deployed with aluminum *LC* resonators, these were replaced in 2020 with niobium resonators like those used in PB-2b.

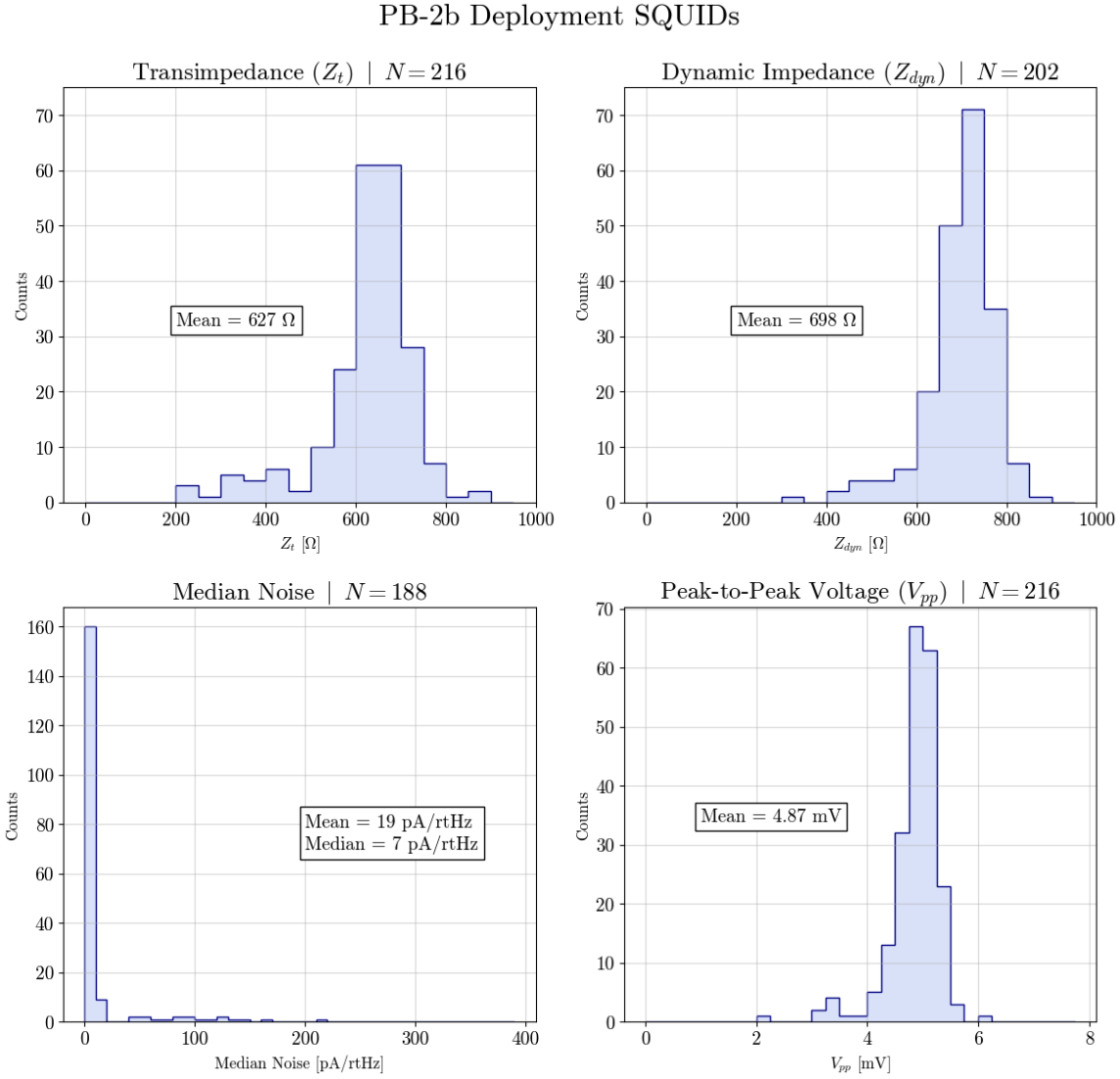

Figure 3.25: Histograms of measured transimpedance (Z_t), dynamic impedance (Z_{dyn}), median noise from zero-amplitude network analysis, and peak-to-peak voltage (V_{pp}) for the SA13a SQUID arrays that underwent in-lab testing and were selected for use with the PB-2b receiver in the field. Choice of field-use SQUID arrays was based on selection criteria described in the text. Peak-to-peak voltage is not included as a selection criterion, but a histogram is included for completeness. 216 SA13a SQUID arrays fall into this category, 210 of which will be connected to resonators and detectors as PB-2b operates in the field. The remaining 6 SQUID arrays, along with 24 additional but untested SQUID arrays, have been designated for use as spares. A small subset of these deployment SQUID arrays were not tested for dynamic impedance and/or median noise, as indicated by the sample number (N) values at the top of each plot.

of niobium makes this a better choice, but the fabrication and assembly processes needed to be developed to ensure robustness of the connections to prevent substantial yield hits. Once

these processes were established, *LC* PCBs were checked during test cooldowns of the system to confirm high channel yield on each. Additionally, during integrated testing of the PB-2b receiver it was found that the glue used to adhere the resonator chips on to the PCBs had not been applied in the same manner on each PCB, causing some chips to crack or slide after undergoing cryogenic cycling. These types of failures result in large detector yield hits, and to mitigate this problem every *LC* resonator chip was inspected after the last laboratory test before being shipped for use in the field. Finally, one of the most physically fragile parts of the readout system is the soldered connection between the custom cabling that connects the *LC* PCBs to the SQUID PCBs (seen in Figure 2.22), which requires the use of ultrasonic solder. Like a crack in an *LC* resonator chip, failure of a single one of these connection points results in a loss of 38 detector channels. To ensure robustness, the solder joints are stressed immediately following assembly before being installed in the receiver [65].

In addition to mitigation efforts to reduce yield hits from any single readout component, each full connection through the custom cabling, through the *LC* resonator chip and PCB, through the set of detectors, and back through the custom cabling is probed at every step during the installation process as the receiver is assembled so that we can be aware of and repair any broken connections that arise.

Careful testing of all the readout components that reside inside the receiver is crucial before assembly in the field as these components cannot be replaced without substantial loss of observation time and risk to other components. This is not the case for the ambient-temperature readout components, which can be accessed much more easily. However, these were used in laboratory measurements in a deployment-like configuration to ensure the receiver readout could be tested in as close to field-like conditions as possible. A replica of one of the electronics enclosures described in Section 2.1.3 was created for use in the lab, which is where the readout motherboards and mezzanines were mounted during integrated receiver measurements. Additionally, scripts written using the pyDfmux software along with custom breakout connectors were created to

perform quality control checks on the ambient-temperature electronics separately from the rest of the readout system. These were used on readout components during laboratory testing, but are also intended for use in the field if needed.

3.3 Receiver Optical Components

The PB-2b receiver's optical components are also characterized prior to deployment in the field. These components include the vacuum window, the filters, the alumina lenses, and the cryogenic half-wave plate (CHWP). Details of some of the AR-coating techniques and optical measurements made by the POLARBEAR/Simons Array team will be published in an upcoming paper that is currently under preparation [110].

The PB-2b window is made from Zotefoam and is 200-mm in thickness. The window material is the same as that used in both the PB-1 and PB-2a receivers, and thus no additional optical characterization was performed for PB-2b. However, the window assembly was tested prior to use in the field to ensure it is capable of holding vacuum. The window was successfully able to hold vacuum in a laboratory test performed over six days, indicating it is ready for use in the field where the pressure differential from the interior to the exterior of the receiver is substantially lower due to the altitude.

The low-pass metal mesh filters that exist in the receiver at the Lyot stop in the optics tube and just in front of each detector wafer undergo ambient-temperature spectroscopy measurements at Cardiff University where they are fabricated prior to use in the PB-2b receiver. These measurements serve to verify the cutoff frequencies of the filters are as designed to ensure out-of-band radiation is appropriately attenuated so as to not overwhelm the sub-Kelvin thermal stages. The alumina filter located just behind the receiver window is also optically tested prior to receiver deployment to the field. For PB-2b, the AR-coating for this filter is made of mullite and Duroid 5880LZ [75]. Reflectivity of the AR-coated filter across a range of frequencies is measured

and data are compared to models based on measurements of the filter and coating thicknesses. Laboratory measurements of all filters for PB-2b were shown to match expectations from models and previous measurements of similar materials in the PB-2a receiver.

The custom reimaging lenses are machined of alumina such that the optical surfaces are of the correct shape as defined in the optical model. Following machining, each surface of the lens is measured using a coordinate-measuring machine (CMM) to ensure the machined surface matches the design. Additionally, samples of the lens material are tested using an FTS to confirm expected indices of refraction.

Once the lens surfaces and indices of refraction have been verified, two layers of AR-coatings must be added to maximize the CMB signal that is able to reach the detectors within the two observing bands. Due to constraints on the accessibility of different technologies that were exacerbated by the COVID-19 pandemic, two different AR-coating methods are employed on lenses for the PB-2b receiver. For the two lenses closer to the Zotefoam window in PB-2b, a plasma-spray technique is used to apply both layers of AR-coating. This technique involves spraying the desired surfaces with heated mixtures of ceramic materials using different plasma energies, and allows the dielectric constant of the coating to be tuned [72]. For the remaining lens, the coating is made of two layers of epoxy with different indices of refraction [75]. Each epoxy layer is carefully applied to the surface via a mold and then machined down to a uniform desired thickness. The epoxy layers are then diced in a grid pattern to prevent the coatings from detaching from the lens surface as a result of differential thermal contraction of the different materials upon cooling in the receiver. Photos of the three AR-coated PB-2b reimaging lenses are shown in Figure 3.26. However, the epoxy technique appears less robust following multiple cryogenic cycles, especially around the edges of the lens. Because of this, there remains a possibility to replace the epoxy-coated lens with one coated using the mullite and Duroid technique mentioned above. Coated lens samples undergo a final optical test to determine the level of transmission within PB-2b's observing bands.

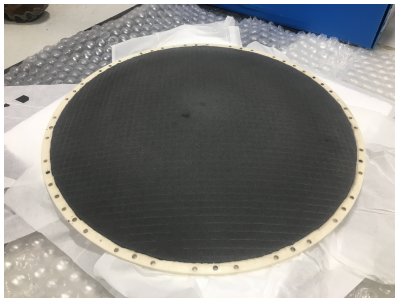

(a) PB-2b collimator lens, for installation closest to the focal plane.

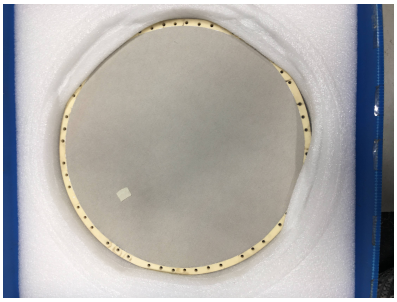

(b) PB-2b aperture lens, for installation in the middle of the optics tube.

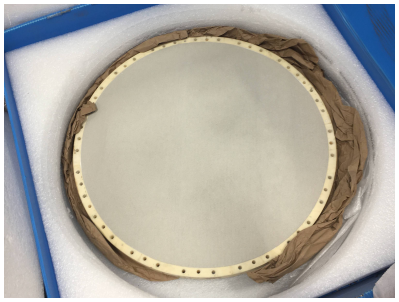

(c) PB-2b field lens, for installation closest to the receiver window.

Figure 3.26: Photos of the three AR-coated reimaging lenses for the PB-2b receiver, prior to installation in the receiver during assembly at the site. The AR-coating on the collimator lens (seen in Figure (a)) is a two-layer epoxy coating, while the aperture and field lenses (seen in Figures (b) and (c)) are coated using a plasma-spray technique. The darker spots near the center of the collimator lens are areas where the epoxy is slightly under-cured, but this is not expected to be a problem for lens performance. However, the epoxy coating is expected to be less robust to multiple cryogenic cycles, and there remains a possibility to replace this lens in the future.

The CHWP is located at the front of the PB-2b receiver, just after the window and the alumina filter. It is composed of three pieces of sapphire, which is a birefringent material that provides the polarization modulation when rotated. The pieces are stacked together using epoxy such that the crystal axis of the middle piece is at an angle with respect to the outer pieces, allowing the HWP to modulate broadband radiation [111]. The individual pieces of sapphire are measured to identify the orientation of each crystal axis prior to stacking, and the alignment of the pieces relative to one another is checked after assembly.

For PB-2b, AR-coatings for the sapphire stack are in the form of thin sheets of alumina that are coated separately and then adhered to the sapphire on either side. The full assembly is then tested for transmission as a function of HWP angle to confirm modulation and measure efficiency.

In addition to optical tests of the sapphire assembly, the rotation mechanism for the CHWP was thoroughly tested. The mechanism was first developed in a dedicated cryogenic testbed at University of California Berkeley, and then integrated with the PB-2b receiver during its final

in-lab cooldown. The test included all mechanical parts of the CHWP, but employed a single piece of sapphire in order to allow work machining and coating the deployment piece to continue in parallel. Detailed results from tests of operational performance and data quality, including angle encoder performance and measurements of magnetic interference, are presented in Hill, et al., 2020 [81]. The results demonstrate satisfaction of all system requirements for PB-2b. Following this success, work is being done to implement similar systems in other CMB experiments [81].

Finally, although the final AR-coated lenses, filter, and CHWP sapphire stack were not installed during PB-2b's in-lab cooldowns, these pieces or representative samples were cooled in separate testbeds in order to verify their robustness to cryogenic cycling.

3.4 Cryogenic System

Tests of the PB-2b cryogenic system occurred in phases as the receiver was built. These tests are crucial to the success of the experiment in the field and are used to ensure:

- all stages reach sufficiently low base temperatures (lowest stable temperature) for operating detectors, operating SQUID arrays, and cooling optical components,
- the procedures for controlling the fridge in order to perform fridge cycles and operate detectors are understood,
- the fridge hold time (time between the fridge stages reaching their lowest temperature and the helium expiring) is sufficient for science observations, and
- all receiver components, in particular the optical components and AR-coatings, can withstand cryogenic cycling.

The first phase of cryogenic characterization involved only the receiver backend, with additional panels in place to seal the area at which the optics tube would normally attach. During

this testing period, the PB-2b backend underwent several cooldowns during which the initial time needed to cool was measured, fridge cycle operations were understood and fridge cycle time measured, and load curves (base temperature and hold time as a function of loading) were recorded for the various PTC and sub-kelvin refrigeration stages. Several thermometers and heaters were placed in different locations within the receiver backend during these tests in order to fully characterize the thermal environment under different loading conditions, including characterizing thermal gradients across each stage. Load curves of PB-2b's Chase helium fridge alone during this phase of testing motivated the development of the secondary sub-kelvin booster fridge to provide extra cooling power and extend the hold time. Detailed measurement descriptions and results indicating suitable performance are presented in Howe, et al., 2018 [67].

Work was done to characterize the cryogenic performance of the receiver optics tube on its own, similar to backend characterization (but with no sub-kelvin refrigeration). However, all tests of this type indicated unacceptable levels of loading on the thermal stages, with base temperatures higher than expected from calculations and from experience with the PB-2a receiver optics tube. It was determined that this excess loading was likely the result of insufficient insulation between the 300-K and 50-K shells, and cryogenic testing of the full receiver moved forward assuming additional insulating material would be added at the necessary interfaces [107].

The next phase of cryogenic validation thus involved integration of the full PB-2b receiver (backend and optics tube). These tests occurred over two cooldowns − one under dark conditions where metal blankoff plates were attached to the end of the optics tube in place of the CHWP and window, and one fully optical. Setup details and results for the dark test and the first optical test are shown in Howe, 2019 [107]. The final in-lab cooldown of the PB-2b receiver (the same cooldown as was referenced in Sections 3.1 and 3.2) included a nearly deployment-like configuration[13], providing the most comprehensive test of cryogenic performance. A photo of

[13]The one crucial difference between this cooldown and the receiver's configuration in the field is the use of optical components without AR-coatings. The omission of these coatings causes a larger percentage of radiation to get "trapped" inside the receiver's 4-K cavity, heating up the optics and thereby further loading the detector stage.

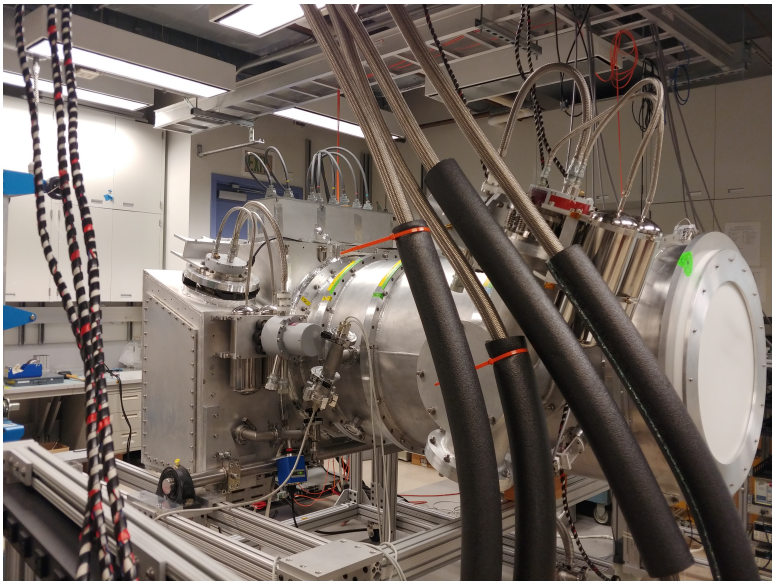

Figure 3.27: Photo of the PB-2b receiver just prior to its final in-lab cooldown during which tests of all the subsystems were performed. The PTCs which provide cooling for the 4-K and 50-K stages inside the receiver for both the backend and the optics tube can be seen on the right side of the receiver. Photo thanks to Jennifer Ito.

the receiver just prior to this cooldown is shown in Figure 3.27. Table 3.6 indicates the base temperatures measured by thermometers situated at several locations within the receiver. Cycling the fridge during this test generally took about 7 hours. A dedicated test of hold time was also performed which indicated a maximum hold time of 48 hours. These measurements demonstrate sufficiently low temperatures for operating the receiver and indicate our ability to schedule operations with a duty cycle of two days.

This final in-lab cooldown of the PB-2b receiver also included testing the impact of vibration on the cryogenic performance. In this test, the receiver was driven at a range of frequencies for several seconds at a time while recording the temperatures of various stages inside the receiver. Increases in the temperatures of sub-kelvin components could be seen corresponding to the vibration. This has the potential to be a problem when the receiver operates on the telescope, as telescope motion may cause vibrational heating, but with the data collected it is unclear how severe the effect will be. This will be examined during initial calibration checks in the field, and

Table 3.6: Summary of base temperatures achieved at various locations within the PB-2b receiver during its final in-lab cooldown. This cooldown included a nearly deployment-like configuration, providing the most comprehensive test of cryogenic performance.

Thermometer Location	**Base Temperature**
Backend PTC First Stage Head	40 K
Backend PTC Second Stage Head	3.2 mK
Backend 4-K Shell	3.9 K
SQUID Card	3.9 K
Booster Fridge Head	910 mK
Chase Fridge Coldest Head	250 mK
MMF Stage	450 mK
Bolometer Stage	250 mK
Optics Tube PTC First Stage Head	40 K
Optics Tube PTC Second Stage Head	3.5 K
CHWP Baseplate	50 K
Optics Tube 4-K Shell	4.5 K
Aperture Lens (Closest to Focal Plane)	6 K

mitigation steps such as setting up a feedback loop to actively control and stabilize the fridge head temperature are being developed and will be implemented if necessary.

3.5 Acknowledgements

Chapter 3 includes material published in J. Ito, L. N. Lowry, T. Elleflot, K. T. Crowley, L. Howe, P. Siritanasak, T. Adkins, K. Arnold, C. Baccigalupi, D. Barron, B. Bixler, Y. Chinone, J. Groh, M. Hazumi, C. A. Hill, O. Jeong, B. Keating, A. Kusaka, A. T. Lee, K. Mitchell, M. Navaroli, A. T. P. Pham, C. Raum, C. L. Reichardt, T. J. Sasse, J. Seibert, A. Suzuki, S. Takakura, G. P. Teply, C. Tsai, and B. Westbrook, "Detector and readout characterization for POLARBEAR-2b," in *Millimeter, Submillimeter, and Far-Infrared Detectors and Instrumentation for Astronomy X* (J. Zmuidzinas and J.-R. Gao, eds.), vol. 11453, pp. 286 - 301, International Society for Optics and Photonics, SPIE, 2020. The dissertation author was second author on and made essential

contributions to this work.

The dissertation author thanks Darcy Barron, Kevin T. Crowley, Tucker Elleflot, Logan Howe, Jennifer Ito, and Praween Siritanasak for their contributions to the material presented in this chapter. These contributions include but are not limited to data-taking and writing scripts used in the analysis and presentation of results. The dissertation author additionally thanks all those who were involved in preparing the PB-2b receiver for the cooldowns during which many of the presented measurements were taken.

Chapter 4

Conclusion

We still have so much to learn from the CMB, and the community continues to expand and grow with both the Simons Array and several other current and future experiments. Technological advancements have been made throughout the history of CMB observations which make these experiments possible, and many share similar technologies, including SQUID arrays. For example, receivers for the current BICEP Array experiment at the South Pole utilize time-domain multiplexing readout schemes with series SQUID arrays [112]. Likewise, CMB-Stage 4, a future experiment designed to incorporate telescopes at both the South Pole and in the Atacama Desert, will use time-domain multiplexing readout with DC SQUID arrays [113]. The Simons Observatory, a experiment in the Atacama Desert for which receiver characterization is currently underway, will utilize RF SQUIDs in its microwave multiplexing readout scheme [114]. Work is simultaneously being done to understand our ability to utilize SQUID arrays positioned at colder stages in the receiver which could help to decrease parasitic impedances in the readout circuit in future CMB experiments [115], as well as to better understand how to efficiently use the newer low-inductance SQUID arrays such as those considered for SA.

Recent progress with the Simons Array includes the construction of the two new telescopes at the observatory site in Chile in 2016 alongside the original Huan Tran Telescope, at which time

the receivers were under development in laboratories in Japan and the United States. Laboratory characterization of SA's first two receivers is complete, while SA's third receiver, PB-2c, remains under development in the lab in order to prioritize the commissioning of PB-2a and PB-2b.

SA's first receiver, PB-2a, was installed on the Nicholas Simons Telescope at the SA observatory site in late 2018, achieving first light in early 2019. Initial calibration measurements were taken, but complications with the cryogenic and readout systems of the receiver made progress to science-level observations difficult in the first two years. In late 2020, the PB-2a receiver was removed from the telescope and its cryogenic and readout systems updated based on instrument performance data that had been collected. The updated PB-2a receiver was reinstalled on the telescope in December 2020, and commissioning is underway with both calibration and CMB data collected regularly.

The PB-2b receiver described in detail in Chapter 3 was shipped to the SA observatory site in early 2020 for assembly and installation on the Paul Simons Telescope. Unfortunately, assembly at the site was halted in March 2020 almost immediately after it had begun due to the COVID-19 pandemic which required our team to evacuate the country. Availability of required personnel, along with safety concerns over the number of people working at once, prevented further progress on PB-2b until after work on PB-2a had been completed. Thankfully, receiver assembly work was able to safely continue in March 2021 and is expected to be completed in Q3 of 2021. Once the receiver is installed on the telescope, calibration will begin to ensure all subsystems are operating as expected and can be run reliably and repeatably. The characterization performed in the laboratory prior to receiver shipment in 2020 gives us confidence the instrument will perform as expected, and we look forward to analyzing the CMB observations from this telescope over the next several years.

With both the Simons Array and innovative new projects like those mentioned above coming online over the next decade, the field of CMB science is at a very inspiring point. Experiment sensitivity to the sum of the neutrino masses is approaching the lower bound made by

laboratory experiments, such that a detection which will shed light on these fundamental particles is possible in the near future. Sensitivity to the B-mode signal from gravitational waves will also see dramatic improvements, with CMB-S4 in particular expecting to place an upper limit on the tensor-to-scalar ratio r of 0.001 at 95% confidence level (in the absence of a detection) [30]. With this level of sensitivity, we can expect either to see evidence for this gravitational wave signal from inflation or to be able to rule out many classes of inflationary models. These advancements and others, combined with the huge collaborative efforts from scientists in this field as experiment size and complexity grow, will undoubtedly lead to exciting new knowledge about the history of our universe.

Bibliography

[1] Planck Collaboration, N. Aghanim, Y. Akrami, F. Arroja, M. Ashdown, J. Aumont, C. Baccigalupi, M. Ballardini, A. J. Banday, R. B. Barreiro, N. Bartolo, S. Basak, R. Battye, K. Benabed, J. P. Bernard, M. Bersanelli, P. Bielewicz, J. J. Bock, J. R. Bond, J. Borrill, F. R. Bouchet, F. Boulanger, M. Bucher, C. Burigana, R. C. Butler, E. Calabrese, J. F. Cardoso, J. Carron, B. Casaponsa, A. Challinor, H. C. Chiang, L. P. L. Colombo, C. Combet, D. Contreras, B. P. Crill, F. Cuttaia, P. de Bernardis, G. de Zotti, J. Delabrouille, J. M. Delouis, F. X. Désert, E. Di Valentino, C. Dickinson, J. M. Diego, S. Donzelli, O. Doré, M. Douspis, A. Ducout, X. Dupac, G. Efstathiou, F. Elsner, T. A. Enßlin, H. K. Eriksen, E. Falgarone, Y. Fantaye, J. Fergusson, R. Fernandez-Cobos, F. Finelli, F. Forastieri, M. Frailis, E. Franceschi, A. Frolov, S. Galeotta, S. Galli, K. Ganga, R. T. Génova-Santos, M. Gerbino, T. Ghosh, J. González-Nuevo, K. M. Górski, S. Gratton, A. Gruppuso, J. E. Gudmundsson, J. Hamann, W. Handley, F. K. Hansen, G. Helou, D. Herranz, S. R. Hildebrandt, E. Hivon, Z. Huang, A. H. Jaffe, W. C. Jones, A. Karakci, E. Keihänen, R. Keskitalo, K. Kiiveri, J. Kim, T. S. Kisner, L. Knox, N. Krachmalnicoff, M. Kunz, H. Kurki-Suonio, G. Lagache, J. M. Lamarre, M. Langer, A. Lasenby, M. Lattanzi, C. R. Lawrence, M. Le Jeune, J. P. Leahy, J. Lesgourgues, F. Levrier, A. Lewis, M. Liguori, P. B. Lilje, M. Lilley, V. Lindholm, M. López-Caniego, P. M. Lubin, Y. Z. Ma, J. F. Macías-Pérez, G. Maggio, D. Maino, N. Mandolesi, A. Mangilli, A. Marcos-Caballero, M. Maris, P. G. Martin, M. Martinelli, E. Martínez-González, S. Matarrese, N. Mauri, J. D. McEwen, P. D. Meerburg, P. R. Meinhold, A. Melchiorri, A. Mennella, M. Migliaccio, M. Millea, S. Mitra, M. A. Miville-Deschênes, D. Molinari, A. Moneti, L. Montier, G. Morgante, A. Moss, S. Mottet, M. Münchmeyer, P. Natoli, H. U. Nørgaard-Nielsen, C. A. Oxborrow, L. Pagano, D. Paoletti, B. Partridge, G. Patanchon, T. J. Pearson, M. Peel, H. V. Peiris, F. Perrotta, V. Pettorino, F. Piacentini, L. Polastri, G. Polenta, J. L. Puget, J. P. Rachen, M. Reinecke, M. Remazeilles, C. Renault, A. Renzi, G. Rocha, C. Rosset, G. Roudier, J. A. Rubiño-Martín, B. Ruiz-Granados, L. Salvati, M. Sandri, M. Savelainen, D. Scott, E. P. S. Shellard, M. Shiraishi, C. Sirignano, G. Sirri, L. D. Spencer, R. Sunyaev, A. S. Suur-Uski, J. A. Tauber, D. Tavagnacco, M. Tenti, L. Terenzi, L. Toffolatti, M. Tomasi, T. Trombetti, J. Valiviita, B. Van Tent, L. Vibert, P. Vielva, F. Villa, N. Vittorio, B. D. Wandelt, I. K. Wehus, M. White, S. D. M. White, A. Zacchei, and A. Zonca, "Planck 2018 results. I. Overview and the cosmological legacy of Planck," *Astronomy and Astrophysics*, vol. 641, p. A1, Sept. 2020.

[2] V. C. Rubin and J. Ford, W. Kent, "Rotation of the Andromeda Nebula from a Spectroscopic Survey of Emission Regions," *Astrophysical Journal*, vol. 159, p. 379, Feb. 1970.

[3] C. L. Bennett, A. J. Banday, K. M. Gorski, G. Hinshaw, P. Jackson, P. Keegstra, A. Kogut, G. F. Smoot, D. T. Wilkinson, and E. L. Wright, "Four-Year COBE DMR Cosmic Microwave Background Observations: Maps and Basic Results," *Astrophysical Journal, Letters*, vol. 464, p. L1, June 1996.

[4] A. G. Riess, A. V. Filippenko, P. Challis, A. Clocchiatti, A. Diercks, P. M. Garnavich, R. L. Gilliland, C. J. Hogan, S. Jha, R. P. Kirshner, B. Leibundgut, M. M. Phillips, D. Reiss, B. P. Schmidt, R. A. Schommer, R. C. Smith, J. Spyromilio, C. Stubbs, N. B. Suntzeff, and J. Tonry, "Observational Evidence from Supernovae for an Accelerating Universe and a Cosmological Constant," *Astronomical Journal*, vol. 116, pp. 1009–1038, Sept. 1998.

[5] B.-L. Young, "A survey of dark matter and related topics in cosmology," *Frontiers of Physics*, vol. 12, p. 121201, Apr. 2017.

[6] D. Huterer and D. L. Shafer, "Dark energy two decades after: observables, probes, consistency tests," *Reports on Progress in Physics*, vol. 81, p. 016901, Jan. 2018.

[7] D. N. Spergel, "The dark side of cosmology: Dark matter and dark energy," *Science*, vol. 347, pp. 1100–1102, Mar. 2015.

[8] Planck Collaboration, N. Aghanim, Y. Akrami, M. Ashdown, J. Aumont, C. Baccigalupi, M. Ballardini, A. J. Banday, R. B. Barreiro, N. Bartolo, S. Basak, R. Battye, K. Benabed, J. P. Bernard, M. Bersanelli, P. Bielewicz, J. J. Bock, J. R. Bond, J. Borrill, F. R. Bouchet, F. Boulanger, M. Bucher, C. Burigana, R. C. Butler, E. Calabrese, J. F. Cardoso, J. Carron, A. Challinor, H. C. Chiang, J. Chluba, L. P. L. Colombo, C. Combet, D. Contreras, B. P. Crill, F. Cuttaia, P. de Bernardis, G. de Zotti, J. Delabrouille, J. M. Delouis, E. Di Valentino, J. M. Diego, O. Doré, M. Douspis, A. Ducout, X. Dupac, S. Dusini, G. Efstathiou, F. Elsner, T. A. Enßlin, H. K. Eriksen, Y. Fantaye, M. Farhang, J. Fergusson, R. Fernandez-Cobos, F. Finelli, F. Forastieri, M. Frailis, A. A. Fraisse, E. Franceschi, A. Frolov, S. Galeotta, S. Galli, K. Ganga, R. T. Génova-Santos, M. Gerbino, T. Ghosh, J. González-Nuevo, K. M. Górski, S. Gratton, A. Gruppuso, J. E. Gudmundsson, J. Hamann, W. Handley, F. K. Hansen, D. Herranz, S. R. Hildebrandt, E. Hivon, Z. Huang, A. H. Jaffe, W. C. Jones, A. Karakci, E. Keihänen, R. Keskitalo, K. Kiiveri, J. Kim, T. S. Kisner, L. Knox, N. Krachmalnicoff, M. Kunz, H. Kurki-Suonio, G. Lagache, J. M. Lamarre, A. Lasenby, M. Lattanzi, C. R. Lawrence, M. Le Jeune, P. Lemos, J. Lesgourgues, F. Levrier, A. Lewis, M. Liguori, P. B. Lilje, M. Lilley, V. Lindholm, M. López-Caniego, P. M. Lubin, Y. Z. Ma, J. F. Macías-Pérez, G. Maggio, D. Maino, N. Mandolesi, A. Mangilli, A. Marcos-Caballero, M. Maris, P. G. Martin, M. Martinelli, E. Martínez-González, S. Matarrese, N. Mauri, J. D. McEwen, P. R. Meinhold, A. Melchiorri, A. Mennella, M. Migliaccio, M. Millea, S. Mitra, M. A. Miville-Deschênes, D. Molinari, L. Montier, G. Morgante, A. Moss, P. Natoli, H. U. Nørgaard-Nielsen, L. Pagano, D. Paoletti, B. Partridge, G. Patanchon, H. V. Peiris, F. Perrotta, V. Pettorino, F. Piacentini, L. Polastri, G. Polenta, J. L. Puget,

J. P. Rachen, M. Reinecke, M. Remazeilles, A. Renzi, G. Rocha, C. Rosset, G. Roudier, J. A. Rubiño-Martín, B. Ruiz-Granados, L. Salvati, M. Sandri, M. Savelainen, D. Scott, E. P. S. Shellard, C. Sirignano, G. Sirri, L. D. Spencer, R. Sunyaev, A. S. Suur-Uski, J. A. Tauber, D. Tavagnacco, M. Tenti, L. Toffolatti, M. Tomasi, T. Trombetti, L. Valenziano, J. Valiviita, B. Van Tent, L. Vibert, P. Vielva, F. Villa, N. Vittorio, B. D. Wandelt, I. K. Wehus, M. White, S. D. M. White, A. Zacchei, and A. Zonca, "Planck 2018 results. VI. Cosmological parameters," *Astronomy and Astrophysics*, vol. 641, p. A6, Sept. 2020.

[9] S. Dodelson, *Modern cosmology*. 2003.

[10] J. D. Bowman, A. E. E. Rogers, R. A. Monsalve, T. J. Mozdzen, and N. Mahesh, "An absorption profile centred at 78 megahertz in the sky-averaged spectrum," *Nature*, vol. 555, pp. 67–70, Mar. 2018.

[11] D. J. Fixsen, "The Temperature of the Cosmic Microwave Background," *Astrophysical Journal*, vol. 707, pp. 916–920, Dec. 2009.

[12] A. H. Guth, "Inflationary universe: A possible solution to the horizon and flatness problems," *Physical Review D*, vol. 23, pp. 347–356, Jan. 1981.

[13] A. D. Linde, "A new inflationary universe scenario: A possible solution of the horizon, flatness, homogeneity, isotropy and primordial monopole problems," *Physics Letters B*, vol. 108, pp. 389–393, Feb. 1982.

[14] A. H. Guth and S. Y. Pi, "Fluctuations in the New Inflationary Universe," *Physical Review Letters*, vol. 49, pp. 1110–1113, Oct. 1982.

[15] B. Ryden, *Introduction to cosmology*. 2003.

[16] C. L. Bennett, D. Larson, J. L. Weiland, N. Jarosik, G. Hinshaw, N. Odegard, K. M. Smith, R. S. Hill, B. Gold, M. Halpern, E. Komatsu, M. R. Nolta, L. Page, D. N. Spergel, E. Wollack, J. Dunkley, A. Kogut, M. Limon, S. S. Meyer, G. S. Tucker, and E. L. Wright, "Nine-year Wilkinson Microwave Anisotropy Probe (WMAP) Observations: Final Maps and Results," *Astrophysical Journal, Supplement*, vol. 208, p. 20, Oct. 2013.

[17] S. Das, T. Louis, M. R. Nolta, G. E. Addison, E. S. Battistelli, J. R. Bond, E. Calabrese, D. Crichton, M. J. Devlin, S. Dicker, J. Dunkley, R. Dünner, J. W. Fowler, M. Gralla, A. Hajian, M. Halpern, M. Hasselfield, M. Hilton, A. D. Hincks, R. Hlozek, K. M. Huffenberger, J. P. Hughes, K. D. Irwin, A. Kosowsky, R. H. Lupton, T. A. Marriage, D. Marsden, F. Menanteau, K. Moodley, M. D. Niemack, L. A. Page, B. Partridge, E. D. Reese, B. L. Schmitt, N. Sehgal, B. D. Sherwin, J. L. Sievers, D. N. Spergel, S. T. Staggs, D. S. Swetz, E. R. Switzer, R. Thornton, H. Trac, and E. Wollack, "The Atacama Cosmology Telescope: temperature and gravitational lensing power spectrum measurements from three seasons of data," *Journal of Cosmology and Astroparticle Physics*, vol. 2014, p. 014, Apr. 2014.

[18] W. Hu, "Intermediate guide to the acoustic peaks and polarization." Available at http://background.uchicago.edu/~whu/intermediate/intermediate.html (2021/05/22), 2001. [Online].

[19] P. de Bernardis, P. A. R. Ade, J. J. Bock, J. R. Bond, J. Borrill, A. Boscaleri, K. Coble, B. P. Crill, G. De Gasperis, P. C. Farese, P. G. Ferreira, K. Ganga, M. Giacometti, E. Hivon, V. V. Hristov, A. Iacoangeli, A. H. Jaffe, A. E. Lange, L. Martinis, S. Masi, P. V. Mason, P. D. Mauskopf, A. Melchiorri, L. Miglio, T. Montroy, C. B. Netterfield, E. Pascale, F. Piacentini, D. Pogosyan, S. Prunet, S. Rao, G. Romeo, J. E. Ruhl, F. Scaramuzzi, D. Sforna, and N. Vittorio, "A flat Universe from high-resolution maps of the cosmic microwave background radiation," *Nature*, vol. 404, pp. 955–959, Apr. 2000.

[20] S. Hanany, P. Ade, A. Balbi, J. Bock, J. Borrill, A. Boscaleri, P. de Bernardis, P. G. Ferreira, V. V. Hristov, A. H. Jaffe, A. E. Lange, A. T. Lee, P. D. Mauskopf, C. B. Netterfield, S. Oh, E. Pascale, B. Rabii, P. L. Richards, G. F. Smoot, R. Stompor, C. D. Winant, and J. H. P. Wu, "MAXIMA-1: A Measurement of the Cosmic Microwave Background Anisotropy on Angular Scales of 10'-5°," *Astrophysical Journal, Letters*, vol. 545, pp. L5–L9, Dec. 2000.

[21] I. L. Padilla, J. R. Eimer, Y. Li, G. E. Addison, A. Ali, J. W. Appel, C. L. Bennett, R. Bustos, M. K. Brewer, M. Chan, D. T. Chuss, J. Cleary, J. Couto, S. Dahal, K. Denis, R. Dünner, T. Essinger-Hileman, P. Fluxá, D. Gothe, S. K. Haridas, K. Harrington, J. Iuliano, J. Karakla, T. A. Marriage, N. J. Miller, C. Núñez, L. Parker, M. A. Petroff, R. Reeves, K. Rostem, R. W. Stevens, D. A. Nunes Valle, D. J. Watts, J. L. Weiland, E. J. Wollack, and Z. Xu, "Two-year Cosmology Large Angular Scale Surveyor (CLASS) Observations: A Measurement of Circular Polarization at 40 GHz," *Astrophysical Journal*, vol. 889, p. 105, Feb. 2020.

[22] M. Zaldarriaga and U. Seljak, "All-sky analysis of polarization in the microwave background," *Physical Review D*, vol. 55, pp. 1830–1840, Feb. 1997.

[23] A. Lewis, A. Challinor, and A. Lasenby, "Efficient computation of CMB anisotropies in closed FRW models," *Astrophysical Journal*, vol. 538, pp. 473–476, 2000.

[24] "CAMB web interface." Available at https://lambda.gsfc.nasa.gov/toolbox/tb_camb_form.cfm (2021/05/22), 2019. [Online].

[25] S. Adachi, M. A. O. Aguilar Faúndez, K. Arnold, C. Baccigalupi, D. Barron, D. Beck, F. Bianchini, S. Chapman, K. Cheung, Y. Chinone, K. Crowley, M. Dobbs, H. El Bouhargani, T. Elleflot, J. Errard, G. Fabbian, C. Feng, T. Fujino, N. Galitzki, N. Goeckner-Wald, J. Groh, G. Hall, M. Hasegawa, M. Hazumi, H. Hirose, A. H. Jaffe, O. Jeong, D. Kaneko, N. Katayama, B. Keating, S. Kikuchi, T. Kisner, A. Kusaka, A. T. Lee, D. Leon, E. Linder, L. N. Lowry, F. Matsuda, T. Matsumura, Y. Minami, M. Navaroli, H. Nishino, A. T. P. Pham, D. Poletti, C. L. Reichardt, Y. Segawa, P. Siritanasak, O. Tajima, S. Takakura, S. Takatori, D. Tanabe, G. P. Teply, C. Tsai, C. Vergès, B. Westbrook, Y. Zhou, and Polarbear Collaboration, "A Measurement of the CMB E-mode Angular Power Spectrum at Subdegree Scales from 670 Square Degrees of POLARBEAR Data," *Astrophysical Journal*, vol. 904, p. 65, Nov. 2020.

[26] Planck Collaboration, N. Aghanim, Y. Akrami, M. Ashdown, J. Aumont, C. Baccigalupi, M. Ballardini, A. J. Banday, R. B. Barreiro, N. Bartolo, S. Basak, K. Benabed, J. P. Bernard, M. Bersanelli, P. Bielewicz, J. J. Bock, J. R. Bond, J. Borrill, F. R. Bouchet, F. Boulanger, M. Bucher, C. Burigana, R. C. Butler, E. Calabrese, J. F. Cardoso, J. Carron, B. Casaponsa, A. Challinor, H. C. Chiang, L. P. L. Colombo, C. Combet, B. P. Crill, F. Cuttaia, P. de Bernardis, A. de Rosa, G. de Zotti, J. Delabrouille, J. M. Delouis, E. Di Valentino, J. M. Diego, O. Doré, M. Douspis, A. Ducout, X. Dupac, S. Dusini, G. Efstathiou, F. Elsner, T. A. Enßlin, H. K. Eriksen, Y. Fantaye, R. Fernandez-Cobos, F. Finelli, M. Frailis, A. A. Fraisse, E. Franceschi, A. Frolov, S. Galeotta, S. Galli, K. Ganga, R. T. Génova-Santos, M. Gerbino, T. Ghosh, Y. Giraud-Héraud, J. González-Nuevo, K. M. Górski, S. Gratton, A. Gruppuso, J. E. Gudmundsson, J. Hamann, W. Handley, F. K. Hansen, D. Herranz, E. Hivon, Z. Huang, A. H. Jaffe, W. C. Jones, E. Keihänen, R. Keskitalo, K. Kiiveri, J. Kim, T. S. Kisner, N. Krachmalnicoff, M. Kunz, H. Kurki-Suonio, G. Lagache, J. M. Lamarre, A. Lasenby, M. Lattanzi, C. R. Lawrence, M. Le Jeune, F. Levrier, A. Lewis, M. Liguori, P. B. Lilje, M. Lilley, V. Lindholm, M. López-Caniego, P. M. Lubin, Y. Z. Ma, J. F. Macías-Pérez, G. Maggio, D. Maino, N. Mandolesi, A. Mangilli, A. Marcos-Caballero, M. Maris, P. G. Martin, E. Martínez-González, S. Matarrese, N. Mauri, J. D. McEwen, P. R. Meinhold, A. Melchiorri, A. Mennella, M. Migliaccio, M. Millea, M. A. Miville-Deschênes, D. Molinari, A. Moneti, L. Montier, G. Morgante, A. Moss, P. Natoli, H. U. Nørgaard-Nielsen, L. Pagano, D. Paoletti, B. Partridge, G. Patanchon, H. V. Peiris, F. Perrotta, V. Pettorino, F. Piacentini, G. Polenta, J. L. Puget, J. P. Rachen, M. Reinecke, M. Remazeilles, A. Renzi, G. Rocha, C. Rosset, G. Roudier, J. A. Rubiño-Martín, B. Ruiz-Granados, L. Salvati, M. Sandri, M. Savelainen, D. Scott, E. P. S. Shellard, C. Sirignano, G. Sirri, L. D. Spencer, R. Sunyaev, A. S. Suur-Uski, J. A. Tauber, D. Tavagnacco, M. Tenti, L. Toffolatti, M. Tomasi, T. Trombetti, J. Valiviita, B. Van Tent, P. Vielva, F. Villa, N. Vittorio, B. D. Wandelt, I. K. Wehus, A. Zacchei, and A. Zonca, "Planck 2018 results. V. CMB power spectra and likelihoods," *Astronomy and Astrophysics*, vol. 641, p. A5, Sept. 2020.

[27] C. Feng, *Detecting gravitational lensing from the Cosmic Microwave Background*. PhD thesis, UC San Diego, 2014. ProQuest ID: FENG_ucsd_0033D_14409. Merritt ID: ark:/20775/bb9182754d. Retrieved from https://escholarship.org/uc/item/54f002bg.

[28] D. A. Leon, *Using Cosmological Observations to Search for New Physics and Study the Structure of the Universe*. PhD thesis, UC San Diego, 2020. ProQuest ID: Leon_ucsd_0033D_19375. Merritt ID: ark:/13030/m5vq89vb. Retrieved from https://escholarship.org/uc/item/2vw9d0fq.

[29] M. Kaplinghat, L. Knox, and Y.-S. Song, "Determining Neutrino Mass from the Cosmic Microwave Background Alone," *Physical Review Letters*, vol. 91, p. 241301, Dec. 2003.

[30] K. Abazajian, G. Addison, P. Adshead, Z. Ahmed, S. W. Allen, D. Alonso, M. Alvarez, A. Anderson, K. S. Arnold, C. Baccigalupi, K. Bailey, D. Barkats, D. Barron, P. S. Barry, J. G. Bartlett, R. Basu Thakur, N. Battaglia, E. Baxter, R. Bean, C. Bebek, A. N. Bender,

B. A. Benson, E. Berger, S. Bhimani, C. A. Bischoff, L. Bleem, S. Bocquet, K. Boddy, M. Bonato, J. R. Bond, J. Borrill, F. R. Bouchet, M. L. Brown, S. Bryan, B. Burkhart, V. Buza, K. Byrum, E. Calabrese, V. Calafut, R. Caldwell, J. E. Carlstrom, J. Carron, T. Cecil, A. Challinor, C. L. Chang, Y. Chinone, H.-M. S. Cho, A. Cooray, T. M. Crawford, A. Crites, A. Cukierman, F.-Y. Cyr-Racine, T. de Haan, G. de Zotti, J. Delabrouille, M. Demarteau, M. Devlin, E. Di Valentino, M. Dobbs, S. Duff, A. Duivenvoorden, C. Dvorkin, W. Edwards, J. Eimer, J. Errard, T. Essinger-Hileman, G. Fabbian, C. Feng, S. Ferraro, J. P. Filippini, R. Flauger, B. Flaugher, A. A. Fraisse, A. Frolov, N. Galitzki, S. Galli, K. Ganga, M. Gerbino, M. Gilchriese, V. Gluscevic, D. Green, D. Grin, E. Grohs, R. Gualtieri, V. Guarino, J. E. Gudmundsson, S. Habib, G. Haller, M. Halpern, N. W. Halverson, S. Hanany, K. Harrington, M. Hasegawa, M. Hasselfield, M. Hazumi, K. Heitmann, S. Henderson, J. W. Henning, J. C. Hill, R. Hlozek, G. Holder, W. Holzapfel, J. Hubmayr, K. M. Huffenberger, M. Huffer, H. Hui, K. Irwin, B. R. Johnson, D. Johnstone, W. C. Jones, K. Karkare, N. Katayama, J. Kerby, S. Kernovsky, R. Keskitalo, T. Kisner, L. Knox, A. Kosowsky, J. Kovac, E. D. Kovetz, S. Kuhlmann, C.-l. Kuo, N. Kurita, A. Kusaka, A. Lahteenmaki, C. R. Lawrence, A. T. Lee, A. Lewis, D. Li, E. Linder, M. Loverde, A. Lowitz, M. S. Madhavacheril, A. Mantz, F. Matsuda, P. Mauskopf, J. McMahon, M. McQuinn, P. D. Meerburg, J.-B. Melin, J. Meyers, M. Millea, J. Mohr, L. Moncelsi, T. Mroczkowski, S. Mukherjee, M. Münchmeyer, D. Nagai, J. Nagy, T. Namikawa, F. Nati, T. Natoli, M. Negrello, L. Newburgh, M. D. Niemack, H. Nishino, M. Nordby, V. Novosad, P. O'Connor, G. Obied, S. Padin, S. Pandey, B. Partridge, E. Pierpaoli, L. Pogosian, C. Pryke, G. Puglisi, B. Racine, S. Raghunathan, A. Rahlin, S. Rajagopalan, M. Raveri, M. Reichanadter, C. L. Reichardt, M. Remazeilles, G. Rocha, N. A. Roe, A. Roy, J. Ruhl, M. Salatino, B. Saliwanchik, E. Schaan, A. Schillaci, M. M. Schmittfull, D. Scott, N. Sehgal, S. Shandera, C. Sheehy, B. D. Sherwin, E. Shirokoff, S. M. Simon, A. Slosar, R. Somerville, D. Spergel, S. T. Staggs, A. Stark, R. Stompor, K. T. Story, C. Stoughton, A. Suzuki, O. Tajima, G. P. Teply, K. Thompson, P. Timbie, M. Tomasi, J. I. Treu, M. Tristram, G. Tucker, C. Umiltà, A. van Engelen, J. D. Vieira, A. G. Vieregg, M. Vogelsberger, G. Wang, S. Watson, M. White, N. Whitehorn, E. J. Wollack, W. L. Kimmy Wu, Z. Xu, S. Yasini, J. Yeck, K. W. Yoon, E. Young, and A. Zonca, "CMB-S4 Science Case, Reference Design, and Project Plan," *arXiv e-prints*, p. arXiv:1907.04473, July 2019.

[31] BICEP2 Collaboration, Keck Array Collaboration, P. A. R. Ade, Z. Ahmed, R. W. Aikin, K. D. Alexander, D. Barkats, S. J. Benton, C. A. Bischoff, J. J. Bock, R. Bowens-Rubin, J. A. Brevik, I. Buder, E. Bullock, V. Buza, J. Connors, J. Cornelison, B. P. Crill, M. Crumrine, M. Dierickx, L. Duband, C. Dvorkin, J. P. Filippini, S. Fliescher, J. Grayson, G. Hall, M. Halpern, S. Harrison, S. R. Hildebrandt, G. C. Hilton, H. Hui, K. D. Irwin, J. Kang, K. S. Karkare, E. Karpel, J. P. Kaufman, B. G. Keating, S. Kefeli, S. A. Kernasovskiy, J. M. Kovac, C. L. Kuo, N. A. Larsen, K. Lau, E. M. Leitch, M. Lueker, K. G. Megerian, L. Moncelsi, T. Namikawa, C. B. Netterfield, H. T. Nguyen, R. O'Brient, R. W. Ogburn, S. Palladino, C. Pryke, B. Racine, S. Richter, A. Schillaci, R. Schwarz, C. D. Sheehy, A. Soliman, T. St. Germaine, Z. K. Staniszewski, B. Steinbach, R. V. Sudiwala, G. P. Teply, K. L. Thompson, J. E. Tolan, C. Tucker, A. D. Turner, C. Umiltà, A. G. Vieregg,

A. Wandui, A. C. Weber, D. V. Wiebe, J. Willmert, C. L. Wong, W. L. K. Wu, H. Yang, K. W. Yoon, and C. Zhang, "Constraints on Primordial Gravitational Waves Using Planck, WMAP, and New BICEP2/Keck Observations through the 2015 Season," *Physical Review Letters*, vol. 121, p. 221301, Nov. 2018.

[32] Planck Collaboration, Y. Akrami, M. Ashdown, J. Aumont, C. Baccigalupi, M. Ballardini, A. J. Banday, R. B. Barreiro, N. Bartolo, S. Basak, K. Benabed, M. Bersanelli, P. Bielewicz, J. R. Bond, J. Borrill, F. R. Bouchet, F. Boulanger, M. Bucher, C. Burigana, E. Calabrese, J. F. Cardoso, J. Carron, B. Casaponsa, A. Challinor, L. P. L. Colombo, C. Combet, B. P. Crill, F. Cuttaia, P. de Bernardis, A. de Rosa, G. de Zotti, J. Delabrouille, J. M. Delouis, E. Di Valentino, C. Dickinson, J. M. Diego, S. Donzelli, O. Doré, A. Ducout, X. Dupac, G. Efstathiou, F. Elsner, T. A. Enßlin, H. K. Eriksen, E. Falgarone, R. Fernandez-Cobos, F. Finelli, F. Forastieri, M. Frailis, A. A. Fraisse, E. Franceschi, A. Frolov, S. Galeotta, S. Galli, K. Ganga, R. T. Génova-Santos, M. Gerbino, T. Ghosh, J. González-Nuevo, K. M. Górski, S. Gratton, A. Gruppuso, J. E. Gudmundsson, W. Handley, F. K. Hansen, G. Helou, D. Herranz, S. R. Hildebrandt, Z. Huang, A. H. Jaffe, A. Karakci, E. Keihänen, R. Keskitalo, K. Kiiveri, J. Kim, T. S. Kisner, N. Krachmalnicoff, M. Kunz, H. Kurki-Suonio, G. Lagache, J. M. Lamarre, A. Lasenby, M. Lattanzi, C. R. Lawrence, M. Le Jeune, F. Levrier, M. Liguori, P. B. Lilje, V. Lindholm, M. López-Caniego, P. M. Lubin, Y. Z. Ma, J. F. Macías-Pérez, G. Maggio, D. Maino, N. Mandolesi, A. Mangilli, A. Marcos-Caballero, M. Maris, P. G. Martin, E. Martínez-González, S. Matarrese, N. Mauri, J. D. McEwen, P. R. Meinhold, A. Melchiorri, A. Mennella, M. Migliaccio, M. A. Miville-Deschênes, D. Molinari, A. Moneti, L. Montier, G. Morgante, P. Natoli, F. Oppizzi, L. Pagano, D. Paoletti, B. Partridge, M. Peel, V. Pettorino, F. Piacentini, G. Polenta, J. L. Puget, J. P. Rachen, M. Reinecke, M. Remazeilles, A. Renzi, G. Rocha, G. Roudier, J. A. Rubiño-Martín, B. Ruiz-Granados, L. Salvati, M. Sandri, M. Savelainen, D. Scott, D. S. Seljebotn, C. Sirignano, L. D. Spencer, A. S. Suur-Uski, J. A. Tauber, D. Tavagnacco, M. Tenti, H. Thommesen, L. Toffolatti, M. Tomasi, T. Trombetti, J. Valiviita, B. Van Tent, P. Vielva, F. Villa, N. Vittorio, B. D. Wandelt, I. K. Wehus, A. Zacchei, and A. Zonca, "Planck 2018 results. IV. Diffuse component separation," *Astronomy and Astrophysics*, vol. 641, p. A4, Sept. 2020.

[33] G. B. Rybicki and A. P. Lightman, *Radiative Processes in Astrophysics*. 1986.

[34] G. Di Bernardo, D. Grasso, C. Evoli, and D. Gaggero, "Diffuse synchrotron emission from galactic cosmic ray electrons," *ASTRA Proceedings*, vol. 2, pp. 21–26, Sept. 2015.

[35] A. W. Strong, E. Orlando, and T. R. Jaffe, "The interstellar cosmic-ray electron spectrum from synchrotron radiation and direct measurements," *Astronomy and Astrophysics*, vol. 534, p. A54, Oct. 2011.

[36] W. Stein, "Infrared Radiation from Interstellar Grains," *Astrophysical Journal*, vol. 144, p. 318, Apr. 1966.

[37] R. H. Hildebrand, "Magnetic fields and stardust," *Quarterly Journal of the RAS*, vol. 29, pp. 327–351, Sept. 1988.

[38] S. Takakura, M. A. O. Aguilar-Faúndez, Y. Akiba, K. Arnold, C. Baccigalupi, D. Barron, D. Beck, F. Bianchini, D. Boettger, J. Borrill, K. Cheung, Y. Chinone, T. Elleflot, J. Errard, G. Fabbian, C. Feng, N. Goeckner-Wald, T. Hamada, M. Hasegawa, M. Hazumi, L. Howe, D. Kaneko, N. Katayama, B. Keating, R. Keskitalo, T. Kisner, N. Krachmalnicoff, A. Kusaka, A. T. Lee, L. N. Lowry, F. T. Matsuda, A. J. May, Y. Minami, M. Navaroli, H. Nishino, L. Piccirillo, D. Poletti, G. Puglisi, C. L. Reichardt, Y. Segawa, M. Silva-Feaver, P. Siritanasak, A. Suzuki, O. Tajima, S. Takatori, D. Tanabe, G. P. Teply, and C. Tsai, "Measurements of Tropospheric Ice Clouds with a Ground-based CMB Polarization Experiment, POLARBEAR," *Astrophysical Journal*, vol. 870, p. 102, Jan. 2019.

[39] C. L. Bennett, R. S. Hill, G. Hinshaw, M. R. Nolta, N. Odegard, L. Page, D. N. Spergel, J. L. Weiland, E. L. Wright, M. Halpern, N. Jarosik, A. Kogut, M. Limon, S. S. Meyer, G. S. Tucker, and E. Wollack, "First-Year Wilkinson Microwave Anisotropy Probe (WMAP) Observations: Foreground Emission," *Astrophysical Journal, Supplement*, vol. 148, pp. 97–117, Sept. 2003.

[40] Planck Collaboration, P. A. R. Ade, N. Aghanim, C. Armitage-Caplan, M. Arnaud, M. Ashdown, F. Atrio-Barandela, J. Aumont, C. Baccigalupi, A. J. Banday, R. B. Barreiro, J. G. Bartlett, E. Battaner, K. Benabed, A. Benoît, A. Benoit-Lévy, J. P. Bernard, M. Bersanelli, P. Bielewicz, J. Bobin, J. J. Bock, A. Bonaldi, L. Bonavera, J. R. Bond, J. Borrill, F. R. Bouchet, F. Boulanger, M. Bridges, M. Bucher, C. Burigana, R. C. Butler, J. F. Cardoso, G. Castex, A. Catalano, A. Challinor, A. Chamballu, R. R. Chary, X. Chen, H. C. Chiang, L. Y. Chiang, P. R. Christensen, S. Church, D. L. Clements, S. Colombi, L. P. L. Colombo, F. Couchot, A. Coulais, B. P. Crill, M. Cruz, A. Curto, F. Cuttaia, L. Danese, R. D. Davies, R. J. Davis, P. de Bernardis, A. de Rosa, G. de Zotti, J. Delabrouille, J. M. Delouis, F. X. Désert, C. Dickinson, J. M. Diego, G. Dobler, H. Dole, S. Donzelli, O. Doré, M. Douspis, J. Dunkley, X. Dupac, G. Efstathiou, T. A. Enßlin, H. K. Eriksen, E. Falgarone, F. Finelli, O. Forni, M. Frailis, A. A. Fraisse, E. Franceschi, S. Galeotta, K. Ganga, M. Giard, G. Giardino, Y. Giraud-Héraud, J. González-Nuevo, K. M. Górski, S. Gratton, A. Gregorio, A. Gruppuso, F. K. Hansen, D. Hanson, D. L. Harrison, G. Helou, S. Henrot-Versillé, C. Hernández-Monteagudo, D. Herranz, S. R. Hildebrandt, E. Hivon, M. Hobson, W. A. Holmes, A. Hornstrup, W. Hovest, G. Huey, K. M. Huffenberger, A. H. Jaffe, T. R. Jaffe, J. Jewell, W. C. Jones, M. Juvela, E. Keihänen, R. Keskitalo, T. S. Kisner, R. Kneissl, J. Knoche, L. Knox, M. Kunz, H. Kurki-Suonio, G. Lagache, A. Lähteenmäki, J. M. Lamarre, A. Lasenby, R. J. Laureijs, C. R. Lawrence, M. Le Jeune, S. Leach, J. P. Leahy, R. Leonardi, J. Lesgourgues, M. Liguori, P. B. Lilje, M. Linden-Vørnle, M. López-Caniego, P. M. Lubin, J. F. Macías-Pérez, B. Maffei, D. Maino, N. Mandolesi, A. Marcos-Caballero, M. Maris, D. J. Marshall, P. G. Martin, E. Martínez-González, S. Masi, M. Massardi, S. Matarrese, F. Matthai, P. Mazzotta, P. R. Meinhold, A. Melchiorri, L. Mendes, A. Mennella, M. Migliaccio, K. Mikkelsen, S. Mitra, M. A. Miville-Deschênes, D. Molinari, A. Moneti, L. Montier, G. Morgante, D. Mortlock, A. Moss, D. Munshi, J. A. Murphy,

P. Naselsky, F. Nati, P. Natoli, C. B. Netterfield, H. U. Nørgaard-Nielsen, F. Noviello, D. Novikov, I. Novikov, I. J. O'Dwyer, S. Osborne, C. A. Oxborrow, F. Paci, L. Pagano, F. Pajot, R. Paladini, D. Paoletti, B. Partridge, F. Pasian, G. Patanchon, T. J. Pearson, O. Perdereau, L. Perotto, F. Perrotta, V. Pettorino, F. Piacentini, M. Piat, E. Pierpaoli, D. Pietrobon, S. Plaszczynski, P. Platania, E. Pointecouteau, G. Polenta, N. Ponthieu, L. Popa, T. Poutanen, G. W. Pratt, G. Prézeau, S. Prunet, J. L. Puget, J. P. Rachen, W. T. Reach, R. Rebolo, M. Reinecke, M. Remazeilles, C. Renault, A. Renzi, S. Ricciardi, T. Riller, I. Ristorcelli, G. Rocha, M. Roman, C. Rosset, G. Roudier, M. Rowan-Robinson, J. A. Rubiño-Martín, B. Rusholme, E. Salerno, M. Sandri, D. Santos, G. Savini, F. Schiavon, D. Scott, M. D. Seiffert, E. P. S. Shellard, L. D. Spencer, J. L. Starck, R. Stompor, R. Sudiwala, R. Sunyaev, F. Sureau, D. Sutton, A. S. Suur-Uski, J. F. Sygnet, J. A. Tauber, D. Tavagnacco, L. Terenzi, L. Toffolatti, M. Tomasi, M. Tristram, M. Tucci, J. Tuovinen, M. Türler, G. Umana, L. Valenziano, J. Valiviita, B. Van Tent, J. Varis, M. Viel, P. Vielva, F. Villa, N. Vittorio, L. A. Wade, B. D. Wandelt, I. K. Wehus, A. Wilkinson, J. Q. Xia, D. Yvon, A. Zacchei, and A. Zonca, "Planck 2013 results. XII. Diffuse component separation," *Astronomy and Astrophysics*, vol. 571, p. A12, Nov. 2014.

[41] A. Lee, M. H. Abitbol, S. Adachi, P. Ade, J. Aguirre, Z. Ahmed, S. Aiola, A. Ali, D. Alonso, M. A. Alvarez, K. Arnold, P. Ashton, Z. Atkins, J. Austermann, H. Awan, C. Baccigalupi, T. Baildon, A. Baleato Lizancos, D. Barron, N. Battaglia, R. Battye, E. Baxter, A. Bazarko, J. A. Beall, R. Bean, D. Beck, S. Beckman, B. Beringue, T. Bhandarkar, S. Bhimani, F. Bianchini, S. Boada, D. Boettger, B. Bolliet, J. R. Bond, J. Borrill, M. L. Brown, S. M. Bruno, S. Bryan, E. Calabrese, V. Calafut, P. Calisse, J. Carron, F. M. Carl, J. Cayuso, A. Challinor, G. Chesmore, Y. Chinone, J. Chluba, H.-M. S. Cho, S. Choi, S. Clark, P. Clarke, C. Contaldi, G. Coppi, N. F. Cothard, K. Coughlin, W. Coulton, D. Crichton, K. D. Crowley, K. T. Crowley, A. Cukierman, J. M. D'Ewart, R. Dünner, T. de Haan, M. Devlin, S. Dicker, B. Dober, C. J. Duell, S. Duff, A. Duivenvoorden, J. Dunkley, H. El Bouhargani, J. Errard, G. Fabbian, S. Feeney, J. Fergusson, S. Ferraro, P. Fluxa, K. Freese, J. C. Frisch, A. Frolov, G. Fuller, N. Galitzki, P. A. Gallardo, J. T. Galvez Ghersi, J. Gao, E. Gawiser, M. Gerbino, V. Gluscevic, N. Goeckner-Wald, J. Golec, S. Gordon, M. Gralla, D. Green, A. Grigorian, J. Groh, C. Groppi, Y. Guan, J. E. Gudmundsson, M. Halpern, D. Han, P. Hargrave, K. Harrington, M. Hasegawa, M. Hasselfield, M. Hattori, V. Haynes, M. Hazumi, E. Healy, S. W. Henderson, B. Hensley, C. Hervias-Caimapo, C. A. Hill, J. C. Hill, G. Hilton, M. Hilton, A. D. Hincks, G. Hinshaw, R. Hložek, S. Ho, S.-P. P. Ho, T. D. Hoang, J. Hoh, S. C. Hotinli, Z. Huang, J. Hubmayr, K. Huffenberger, J. P. Hughes, A. Ijjas, M. Ikape, K. Irwin, A. H. Jaffe, B. Jain, O. Jeong, M. Johnson, D. Kaneko, E. D. Karpel, N. Katayama, B. Keating, R. Keskitalo, T. Kisner, K. Kiuchi, J. Klein, K. Knowles, A. Kofman, B. Koopman, A. Kosowsky, N. Krachmalnicoff, A. Kusaka, P. La Plante, J. Lashner, A. Lee, E. Lee, A. Lewis, Y. Li, Z. Li, M. Limon, E. Linder, J. Liu, C. Lopez-Caraballo, T. Louis, M. Lungu, M. Madhavacheril, D. Mak, F. Maldonado, H. Mani, B. Mates, F. Matsuda, L. Maurin, P. Mauskopf, A. May, N. McCallum, H. McCarrick, C. McKenney, J. McMahon, P. D. Meerburg, J. Mertens, J. Meyers, A. Miller, M. Mirmelstein, K. Moodley, J. Moore, M. Munchmeyer, C. Munson, M. Murata, S. Naess,

T. Namikawa, F. Nati, M. Navaroli, L. Newburgh, H. N. Nguyen, A. Nicola, M. Niemack, H. Nishino, Y. Nishinomiya, J. Orlowski-Scherer, L. Pagano, B. Partridge, F. Perrotta, P. Phakathi, L. Piccirillo, E. Pierpaoli, G. Pisano, D. Poletti, R. Puddu, G. Puglisi, C. Raum, C. L. Reichardt, M. Remazeilles, Y. Rephaeli, D. Riechers, F. Rojas, A. Rotti, A. Roy, S. Sadeh, Y. Sakurai, M. Salatino, M. Sathyanarayana Rao, L. Saunders, E. Schaan, M. Schmittfull, N. Sehgal, J. Seibert, U. Seljak, P. Shellard, B. Sherwin, M. Shimon, C. Sierra, J. Sievers, C. Sifon, P. Sikhosana, M. Silva-Feaver, S. M. Simon, A. Sinclair, K. Smith, W. Sohn, R. Sonka, D. Spergel, J. Spisak, S. T. Staggs, G. Stein, J. R. Stevens, R. Stompor, A. Suzuki, O. Tajima, S. Takakura, G. Teply, D. B. Thomas, B. Thorne, R. Thornton, H. Trac, J. Treu, C. Tsai, C. Tucker, J. Ullom, S. Vagnozzi, A. van Engelen, J. Van Lanen, D. D. Van Winkle, E. M. Vavagiakis, C. Vergès, M. Vissers, K. Wagoner, S. Walker, Y. Wang, J. Ward, B. Westbrook, N. Whitehorn, J. Williams, J. Williams, E. Wollack, Z. Xu, S. Yasini, E. Young, B. Yu, C. Yu, F. Zago, M. Zannoni, H. Zhang, K. Zheng, N. Zhu, and A. Zonca, "The Simons Observatory," in *Bulletin of the American Astronomical Society*, vol. 51, p. 147, Sept. 2019.

[42] Polarbear Collaboration, P. A. R. Ade, Y. Akiba, A. E. Anthony, K. Arnold, M. Atlas, D. Barron, D. Boettger, J. Borrill, S. Chapman, Y. Chinone, M. Dobbs, T. Elleflot, J. Errard, G. Fabbian, C. Feng, D. Flanigan, A. Gilbert, W. Grainger, N. W. Halverson, M. Hasegawa, K. Hattori, M. Hazumi, W. L. Holzapfel, Y. Hori, J. Howard, P. Hyland, Y. Inoue, G. C. Jaehnig, A. H. Jaffe, B. Keating, Z. Kermish, R. Keskitalo, T. Kisner, M. Le Jeune, A. T. Lee, E. M. Leitch, E. Linder, M. Lungu, F. Matsuda, T. Matsumura, X. Meng, N. J. Miller, H. Morii, S. Moyerman, M. J. Myers, M. Navaroli, H. Nishino, A. Orlando, H. Paar, J. Peloton, D. Poletti, E. Quealy, G. Rebeiz, C. L. Reichardt, P. L. Richards, C. Ross, I. Schanning, D. E. Schenck, B. D. Sherwin, A. Shimizu, C. Shimmin, M. Shimon, P. Siritanasak, G. Smecher, H. Spieler, N. Stebor, B. Steinbach, R. Stompor, A. Suzuki, S. Takakura, T. Tomaru, B. Wilson, A. Yadav, and O. Zahn, "A Measurement of the Cosmic Microwave Background B-mode Polarization Power Spectrum at Sub-degree Scales with POLARBEAR," *Astrophysical Journal*, vol. 794, p. 171, Oct. 2014.

[43] M. Tristram, A. J. Banday, K. M. Górski, R. Keskitalo, C. R. Lawrence, K. J. Andersen, R. B. Barreiro, J. Borrill, H. K. Eriksen, R. Fernandez-Cobos, T. S. Kisner, E. Martínez-González, B. Partridge, D. Scott, T. L. Svalheim, H. Thommesen, and I. K. Wehus, "Planck constraints on the tensor-to-scalar ratio," *Astronomy and Astrophysics*, vol. 647, p. A128, Mar. 2021.

[44] POLARBEAR Collaboration, P. A. R. Ade, M. Aguilar, Y. Akiba, K. Arnold, C. Baccigalupi, D. Barron, D. Beck, F. Bianchini, D. Boettger, J. Borrill, S. Chapman, Y. Chinone, K. Crowley, A. Cukierman, R. Dünner, M. Dobbs, A. Ducout, T. Elleflot, J. Errard, G. Fabbian, S. M. Feeney, C. Feng, T. Fujino, N. Galitzki, A. Gilbert, N. Goeckner-Wald, J. C. Groh, G. Hall, N. Halverson, T. Hamada, M. Hasegawa, M. Hazumi, C. A. Hill, L. Howe, Y. Inoue, G. Jaehnig, A. H. Jaffe, O. Jeong, D. Kaneko, N. Katayama, B. Keating, R. Keskitalo, T. Kisner, N. Krachmalnicoff, A. Kusaka, M. Le Jeune, A. T. Lee, E. M. Leitch, D. Leon, E. Linder, L. Lowry, F. Matsuda, T. Matsumura, Y. Minami, J. Montgomery,

M. Navaroli, H. Nishino, H. Paar, J. Peloton, A. T. P. Pham, D. Poletti, G. Puglisi, C. L. Reichardt, P. L. Richards, C. Ross, Y. Segawa, B. D. Sherwin, M. Silva-Feaver, P. Siritanasak, N. Stebor, R. Stompor, A. Suzuki, O. Tajima, S. Takakura, S. Takatori, D. Tanabe, G. P. Teply, T. Tomaru, C. Tucker, N. Whitehorn, and A. Zahn, "A Measurement of the Cosmic Microwave Background B-mode Polarization Power Spectrum at Subdegree Scales from Two Years of polarbear Data," *Astrophysical Journal*, vol. 848, p. 121, Oct. 2017.

[45] Polarbear Collaboration, S. Adachi, M. A. O. Aguilar Faúndez, K. Arnold, C. Baccigalupi, D. Barron, D. Beck, S. Beckman, F. Bianchini, D. Boettger, J. Borrill, J. Carron, S. Chapman, K. Cheung, Y. Chinone, K. Crowley, A. Cukierman, M. Dobbs, H. El Bouhargani, T. Elleflot, J. Errard, G. Fabbian, C. Feng, T. Fujino, N. Galitzki, N. Goeckner-Wald, J. Groh, G. Hall, N. Halverson, T. Hamada, M. Hasegawa, M. Hazumi, C. A. Hill, L. Howe, Y. Inoue, G. Jaehnig, O. Jeong, D. Kaneko, N. Katayama, B. Keating, R. Keskitalo, S. Kikuchi, T. Kisner, N. Krachmalnicoff, A. Kusaka, A. T. Lee, D. Leon, E. Linder, L. N. Lowry, A. Mangu, F. Matsuda, Y. Minami, M. Navaroli, H. Nishino, A. T. P. Pham, D. Poletti, G. Puglisi, C. L. Reichardt, Y. Segawa, M. Silva-Feaver, P. Siritanasak, N. Stebor, R. Stompor, A. Suzuki, O. Tajima, S. Takakura, S. Takatori, D. Tanabe, G. P. Teply, C. Tsai, C. Verges, B. Westbrook, and Y. Zhou, "A Measurement of the Degree-scale CMB B-mode Angular Power Spectrum with POLARBEAR," *Astrophysical Journal*, vol. 897, p. 55, July 2020.

[46] M. A. Faúndez, K. Arnold, C. Baccigalupi, D. Barron, D. Beck, S. Beckman, F. Bianchini, J. Carron, K. Cheung, Y. Chinone, H. E. Bouhargani, T. Elleflot, J. Errard, G. Fabbian, C. Feng, T. Fujino, N. Goeckner-Wald, T. Hamada, M. Hasegawa, M. Hazumi, C. A. Hill, H. Hirose, O. Jeong, N. Katayama, B. Keating, S. Kikuchi, A. Kusaka, A. T. Lee, D. Leon, E. Linder, L. N. Lowry, F. Matsuda, T. Matsumura, Y. Minami, M. Navaroli, H. Nishino, A. T. P. Pham, D. Poletti, G. Puglisi, C. L. Reichardt, Y. Segawa, B. D. Sherwin, M. Silva-Feaver, P. Siritanasak, R. Stompor, A. Suzuki, O. Tajima, S. Takatori, D. Tanabe, G. P. Teply, C. Tsai, and Polarbear Collaboration, "Measurement of the Cosmic Microwave Background Polarization Lensing Power Spectrum from Two Years of POLARBEAR Data," *Astrophysical Journal*, vol. 893, p. 85, Apr. 2020.

[47] S. Adachi, M. A. O. Aguilar Faúndez, Y. Akiba, A. Ali, K. Arnold, C. Baccigalupi, D. Barron, D. Beck, F. Bianchini, J. Borrill, J. Carron, K. Cheung, Y. Chinone, K. Crowley, H. El Bouhargani, T. Elleflot, J. Errard, G. Fabbian, C. Feng, T. Fujino, N. Goeckner-Wald, M. Hasegawa, M. Hazumi, C. A. Hill, L. Howe, N. Katayama, B. Keating, S. Kikuchi, A. Kusaka, A. T. Lee, D. Leon, E. Linder, L. N. Lowry, F. Matsuda, T. Matsumura, Y. Minami, T. Namikawa, M. Navaroli, H. Nishino, J. Peloton, A. T. P. Pham, D. Poletti, G. Puglisi, C. L. Reichardt, Y. Segawa, B. D. Sherwin, M. Silva-Feaver, P. Siritanasak, R. Stompor, O. Tajima, S. Takatori, D. Tanabe, G. P. Teply, C. Vergès, and Polarbear Collaboration, "Internal Delensing of Cosmic Microwave Background Polarization B -Modes with the POLARBEAR Experiment," *Physical Review Letters*, vol. 124, p. 131301, Apr. 2020.

[48] P. A. R. Ade, K. Arnold, M. Atlas, C. Baccigalupi, D. Barron, D. Boettger, J. Borrill, S. Chapman, Y. Chinone, A. Cukierman, M. Dobbs, A. Ducout, R. Dunner, T. Elleflot, J. Errard, G. Fabbian, S. Feeney, C. Feng, A. Gilbert, N. Goeckner-Wald, J. Groh, G. Hall, N. W. Halverson, M. Hasegawa, K. Hattori, M. Hazumi, C. Hill, W. L. Holzapfel, Y. Hori, L. Howe, Y. Inoue, G. C. Jaehnig, A. H. Jaffe, O. Jeong, N. Katayama, J. P. Kaufman, B. Keating, Z. Kermish, R. Keskitalo, T. Kisner, A. Kusaka, M. Le Jeune, A. T. Lee, E. M. Leitch, D. Leon, Y. Li, E. Linder, L. Lowry, F. Matsuda, T. Matsumura, N. Miller, J. Montgomery, M. J. Myers, M. Navaroli, H. Nishino, T. Okamura, H. Paar, J. Peloton, L. Pogosian, D. Poletti, G. Puglisi, C. Raum, G. Rebeiz, C. L. Reichardt, P. L. Richards, C. Ross, K. M. Rotermund, D. E. Schenck, B. D. Sherwin, M. Shimon, I. Shirley, P. Siritanasak, G. Smecher, N. Stebor, B. Steinbach, A. Suzuki, J.-i. Suzuki, O. Tajima, S. Takakura, A. Tikhomirov, T. Tomaru, N. Whitehorn, B. Wilson, A. Yadav, A. Zahn, O. Zahn, and Polarbear Collaboration, "POLARBEAR constraints on cosmic birefringence and primordial magnetic fields," *Physical Review D*, vol. 92, p. 123509, Dec. 2015.

[49] J. Errard, P. A. R. Ade, Y. Akiba, K. Arnold, M. Atlas, C. Baccigalupi, D. Barron, D. Boettger, J. Borrill, S. Chapman, Y. Chinone, A. Cukierman, J. Delabrouille, M. Dobbs, A. Ducout, T. Elleflot, G. Fabbian, C. Feng, S. Feeney, A. Gilbert, N. Goeckner-Wald, N. W. Halverson, M. Hasegawa, K. Hattori, M. Hazumi, C. Hill, W. L. Holzapfel, Y. Hori, Y. Inoue, G. C. Jaehnig, A. H. Jaffe, O. Jeong, N. Katayama, J. Kaufman, B. Keating, Z. Kermish, R. Keskitalo, T. Kisner, M. Le Jeune, A. T. Lee, E. M. Leitch, D. Leon, E. Linder, F. Matsuda, T. Matsumura, N. J. Miller, M. J. Myers, M. Navaroli, H. Nishino, T. Okamura, H. Paar, J. Peloton, D. Poletti, G. Puglisi, G. Rebeiz, C. L. Reichardt, P. L. Richards, C. Ross, K. M. Rotermund, D. E. Schenck, B. D. Sherwin, P. Siritanasak, G. Smecher, N. Stebor, B. Steinbach, R. Stompor, A. Suzuki, O. Tajima, S. Takakura, A. Tikhomirov, T. Tomaru, N. Whitehorn, B. Wilson, A. Yadav, and O. Zahn, "Modeling Atmospheric Emission for CMB Ground-based Observations," *Astrophysical Journal*, vol. 809, p. 63, Aug. 2015.

[50] J. Means, *GPS precipitable water measurements used in the analysis of California and Nevada climate*. PhD thesis, UC San Diego, 2011. ProQuest ID: Means_ucsd_0033D_11892. Merritt ID: ark:/20775/bb0069512j. Retrieved from https://escholarship.org/uc/item/5pq778q7.

[51] S. Paine, "The am atmospheric model," Sept. 2019.

[52] D. S. Swetz, P. A. R. Ade, M. Amiri, J. W. Appel, E. S. Battistelli, B. Burger, J. Chervenak, M. J. Devlin, S. R. Dicker, W. B. Doriese, R. Dünner, T. Essinger-Hileman, R. P. Fisher, J. W. Fowler, M. Halpern, M. Hasselfield, G. C. Hilton, A. D. Hincks, K. D. Irwin, N. Jarosik, M. Kaul, J. Klein, J. M. Lau, M. Limon, T. A. Marriage, D. Marsden, K. Martocci, P. Mauskopf, H. Moseley, C. B. Netterfield, M. D. Niemack, M. R. Nolta, L. A. Page, L. Parker, S. T. Staggs, O. Stryzak, E. R. Switzer, R. Thornton, C. Tucker, E. Wollack, and Y. Zhao, "Overview of the Atacama Cosmology Telescope: Receiver, Instrumentation, and Telescope Systems," *Astrophysical Journal, Supplement*, vol. 194, p. 41, June 2011.

[53] R. J. Thornton, P. A. R. Ade, S. Aiola, F. E. Angilè, M. Amiri, J. A. Beall, D. T. Becker, H. M. Cho, S. K. Choi, P. Corlies, K. P. Coughlin, R. Datta, M. J. Devlin, S. R. Dicker, R. Dünner, J. W. Fowler, A. E. Fox, P. A. Gallardo, J. Gao, E. Grace, M. Halpern, M. Hasselfield, S. W. Henderson, G. C. Hilton, A. D. Hincks, S. P. Ho, J. Hubmayr, K. D. Irwin, J. Klein, B. Koopman, D. Li, T. Louis, M. Lungu, L. Maurin, J. McMahon, C. D. Munson, S. Naess, F. Nati, L. Newburgh, J. Nibarger, M. D. Niemack, P. Niraula, M. R. Nolta, L. A. Page, C. G. Pappas, A. Schillaci, B. L. Schmitt, N. Sehgal, J. L. Sievers, S. M. Simon, S. T. Staggs, C. Tucker, M. Uehara, J. van Lanen, J. T. Ward, and E. J. Wollack, "The Atacama Cosmology Telescope: The Polarization-sensitive ACTPol Instrument," *Astrophysical Journal, Supplement*, vol. 227, p. 21, Dec. 2016.

[54] K. Harrington, T. Marriage, A. Ali, J. W. Appel, C. L. Bennett, F. Boone, M. Brewer, M. Chan, D. T. Chuss, F. Colazo, S. Dahal, K. Denis, R. Dünner, J. Eimer, T. Essinger-Hileman, P. Fluxa, M. Halpern, G. Hilton, G. F. Hinshaw, J. Hubmayr, J. Iuliano, J. Karakla, J. McMahon, N. T. Miller, S. H. Moseley, G. Palma, L. Parker, M. Petroff, B. Pradenas, K. Rostem, M. Sagliocca, D. Valle, D. Watts, E. Wollack, Z. Xu, and L. Zeng, "The Cosmology Large Angular Scale Surveyor," in *Millimeter, Submillimeter, and Far-Infrared Detectors and Instrumentation for Astronomy VIII* (W. S. Holland and J. Zmuidzinas, eds.), vol. 9914 of *Society of Photo-Optical Instrumentation Engineers (SPIE) Conference Series*, p. 99141K, July 2016.

[55] A. Wootten and A. R. Thompson, "The Atacama Large Millimeter/Submillimeter Array," *IEEE Proceedings*, vol. 97, pp. 1463–1471, Aug. 2009.

[56] R. Güsten, L. Å. Nyman, P. Schilke, K. Menten, C. Cesarsky, and R. Booth, "The Atacama Pathfinder EXperiment (APEX) - a new submillimeter facility for southern skies -," *Astronomy and Astrophysics*, vol. 454, pp. L13–L16, Aug. 2006.

[57] Z. D. Kermish, P. Ade, A. Anthony, K. Arnold, D. Barron, D. Boettger, J. Borrill, S. Chapman, Y. Chinone, M. A. Dobbs, J. Errard, G. Fabbian, D. Flanigan, G. Fuller, A. Ghribi, W. Grainger, N. Halverson, M. Hasegawa, K. Hattori, M. Hazumi, W. L. Holzapfel, J. Howard, P. Hyland, A. Jaffe, B. Keating, T. Kisner, A. T. Lee, M. Le Jeune, E. Linder, M. Lungu, F. Matsuda, T. Matsumura, X. Meng, N. J. Miller, H. Morii, S. Moyerman, M. J. Myers, H. Nishino, H. Paar, E. Quealy, C. L. Reichardt, P. L. Richards, C. Ross, A. Shimizu, M. Shimon, C. Shimmin, M. Sholl, P. Siritanasak, H. Spieler, N. Stebor, B. Steinbach, R. Stompor, A. Suzuki, T. Tomaru, C. Tucker, and O. Zahn, "The POLARBEAR experiment," in *Millimeter, Submillimeter, and Far-Infrared Detectors and Instrumentation for Astronomy VI* (W. S. Holland and J. Zmuidzinas, eds.), vol. 8452 of *Society of Photo-Optical Instrumentation Engineers (SPIE) Conference Series*, p. 84521C, Sept. 2012.

[58] H. T. Tran, "Polarization comparison between on-axis and off-axis dual reflector telescopes: Zemax and grasp8 simulations," *New Astronomy Review*, vol. 47, pp. 1091–1096, Dec. 2003.

[59] C. Dragone, "A first-order treatment of aberrations in Cassegrainian and Gregorian antennas," *IEEE Transactions on Antennas and Propagation*, vol. 30, pp. 331–339, May 1982.

[60] D. Boettger, *CMB Polarization Measurements with the Polarbear Experiment*. PhD thesis, UC San Diego, 2014. ProQuest ID: Boettger_ucsd_0033D_13974. Merritt ID: ark:/20775/bb77149051. Retrieved from https://escholarship.org/uc/item/8vg397xn.

[61] F. T. Matsuda, *Cosmic Microwave Background Polarization Science and Optical Design of the POLARBEAR and Simons Array Experiments*. PhD thesis, UC San Diego, 2017. ProQuest ID: Matsuda_ucsd_0033D_16495. Merritt ID: ark:/13030/m57d7pmp. Retrieved from https://escholarship.org/uc/item/4340f15m.

[62] T. Namikawa, Y. Chinone, H. Miyatake, M. Oguri, R. Takahashi, A. Kusaka, N. Katayama, S. Adachi, M. Aguilar, H. Aihara, A. Ali, R. Armstrong, K. Arnold, C. Baccigalupi, D. Barron, D. Beck, S. Beckman, F. Bianchini, D. Boettger, J. Borrill, K. Cheung, L. Corbett, K. T. Crowley, H. El Bouhargani, T. Elleflot, J. Errard, G. Fabbian, C. Feng, N. Galitzki, N. Goeckner-Wald, J. Groh, T. Hamada, M. Hasegawa, M. Hazumi, C. A. Hill, L. Howe, O. Jeong, D. Kaneko, B. Keating, A. T. Lee, D. Leon, E. Linder, L. N. Lowry, A. Mangu, F. Matsuda, Y. Minami, S. Miyazaki, H. Murayama, M. Navaroli, H. Nishino, A. J. Nishizawa, A. T. P. Pham, D. Poletti, G. Puglisi, C. L. Reichardt, B. D. Sherwin, M. Silva-Feaver, P. Siritanasak, J. S. Speagle, R. Stompor, A. Suzuki, P. J. Tait, O. Tajima, M. Takada, S. Takakura, S. Takatori, D. Tanabe, M. Tanaka, G. P. Teply, C. Tsai, C. Vergés, B. Westbrook, Y. Zhou, POLARBEAR COLLABORATION, and SUBARU HSC SSP Collaboration, "Evidence for the Cross-correlation between Cosmic Microwave Background Polarization Lensing from Polarbear and Cosmic Shear from Subaru Hyper Suprime-Cam," *Astrophysical Journal*, vol. 882, p. 62, Sept. 2019.

[63] B. A. Benson, P. A. R. Ade, Z. Ahmed, S. W. Allen, K. Arnold, J. E. Austermann, A. N. Bender, L. E. Bleem, J. E. Carlstrom, C. L. Chang, H. M. Cho, J. F. Cliche, T. M. Crawford, A. Cukierman, T. de Haan, M. A. Dobbs, D. Dutcher, W. Everett, A. Gilbert, N. W. Halverson, D. Hanson, N. L. Harrington, K. Hattori, J. W. Henning, G. C. Hilton, G. P. Holder, W. L. Holzapfel, K. D. Irwin, R. Keisler, L. Knox, D. Kubik, C. L. Kuo, A. T. Lee, E. M. Leitch, D. Li, M. McDonald, S. S. Meyer, J. Montgomery, M. Myers, T. Natoli, H. Nguyen, V. Novosad, S. Padin, Z. Pan, J. Pearson, C. Reichardt, J. E. Ruhl, B. R. Saliwanchik, G. Simard, G. Smecher, J. T. Sayre, E. Shirokoff, A. A. Stark, K. Story, A. Suzuki, K. L. Thompson, C. Tucker, K. Vanderlinde, J. D. Vieira, A. Vikhlinin, G. Wang, V. Yefremenko, and K. W. Yoon, "SPT-3G: a next-generation cosmic microwave background polarization experiment on the South Pole telescope," in *Millimeter, Submillimeter, and Far-Infrared Detectors and Instrumentation for Astronomy VII* (W. S. Holland and J. Zmuidzinas, eds.), vol. 9153 of *Society of Photo-Optical Instrumentation Engineers (SPIE) Conference Series*, p. 91531P, July 2014.

[64] P. Ade, J. Aguirre, Z. Ahmed, S. Aiola, A. Ali, D. Alonso, M. A. Alvarez, K. Arnold, P. Ashton, J. Austermann, H. Awan, C. Baccigalupi, T. Baildon, D. Barron, N. Battaglia,

R. Battye, E. Baxter, A. Bazarko, J. A. Beall, R. Bean, D. Beck, S. Beckman, B. Beringue, F. Bianchini, S. Boada, D. Boettger, J. R. Bond, J. Borrill, M. L. Brown, S. M. Bruno, S. Bryan, E. Calabrese, V. Calafut, P. Calisse, J. Carron, A. Challinor, G. Chesmore, Y. Chinone, J. Chluba, H.-M. S. Cho, S. Choi, G. Coppi, N. F. Cothard, K. Coughlin, D. Crichton, K. D. Crowley, K. T. Crowley, A. Cukierman, J. M. D'Ewart, R. Dünner, T. de Haan, M. Devlin, S. Dicker, J. Didier, M. Dobbs, B. Dober, C. J. Duell, S. Duff, A. Duivenvoorden, J. Dunkley, J. Dusatko, J. Errard, G. Fabbian, S. Feeney, S. Ferraro, P. Fluxà, K. Freese, J. C. Frisch, A. Frolov, G. Fuller, B. Fuzia, N. Galitzki, P. A. Gallardo, J. Tomas Galvez Ghersi, J. Gao, E. Gawiser, M. Gerbino, V. Gluscevic, N. Goeckner-Wald, J. Golec, S. Gordon, M. Gralla, D. Green, A. Grigorian, J. Groh, C. Groppi, Y. Guan, J. E. Gudmundsson, D. Han, P. Hargrave, M. Hasegawa, M. Hasselfield, M. Hattori, V. Haynes, M. Hazumi, Y. He, E. Healy, S. W. Henderson, C. Hervias-Caimapo, C. A. Hill, J. C. Hill, G. Hilton, M. Hilton, A. D. Hincks, G. Hinshaw, R. Hložek, S. Ho, S.-P. P. Ho, L. Howe, Z. Huang, J. Hubmayr, K. Huffenberger, J. P. Hughes, A. Ijjas, M. Ikape, K. Irwin, A. H. Jaffe, B. Jain, O. Jeong, D. Kaneko, E. D. Karpel, N. Katayama, B. Keating, S. S. Kernasovskiy, R. Keskitalo, T. Kisner, K. Kiuchi, J. Klein, K. Knowles, B. Koopman, A. Kosowsky, N. Krachmalnicoff, S. E. Kuenstner, C.-L. Kuo, A. Kusaka, J. Lashner, A. Lee, E. Lee, D. Leon, J. S. Y. Leung, A. Lewis, Y. Li, Z. Li, M. Limon, E. Linder, C. Lopez-Caraballo, T. Louis, L. Lowry, M. Lungu, M. Madhavacheril, D. Mak, F. Maldonado, H. Mani, B. Mates, F. Matsuda, L. Maurin, P. Mauskopf, A. May, N. McCallum, C. McKenney, J. McMahon, P. D. Meerburg, J. Meyers, A. Miller, M. Mirmelstein, K. Moodley, M. Munchmeyer, C. Munson, S. Naess, F. Nati, M. Navaroli, L. Newburgh, H. N. Nguyen, M. Niemack, H. Nishino, J. Orlowski-Scherer, L. Page, B. Partridge, J. Peloton, F. Perrotta, L. Piccirillo, G. Pisano, D. Poletti, R. Puddu, G. Puglisi, C. Raum, C. L. Reichardt, M. Remazeilles, Y. Rephaeli, D. Riechers, F. Rojas, A. Roy, S. Sadeh, Y. Sakurai, M. Salatino, M. Sathyanarayana Rao, E. Schaan, M. Schmittfull, N. Sehgal, J. Seibert, U. Seljak, B. Sherwin, M. Shimon, C. Sierra, J. Sievers, P. Sikhosana, M. Silva-Feaver, S. M. Simon, A. Sinclair, P. Siritanasak, K. Smith, S. R. Smith, D. Spergel, S. T. Staggs, G. Stein, J. R. Stevens, R. Stompor, A. Suzuki, O. Tajima, S. Takakura, G. Teply, D. B. Thomas, B. Thorne, R. Thornton, H. Trac, C. Tsai, C. Tucker, J. Ullom, S. Vagnozzi, A. van Engelen, J. Van Lanen, D. D. Van Winkle, E. M. Vavagiakis, C. Vergès, M. Vissers, K. Wagoner, S. Walker, J. Ward, B. Westbrook, N. Whitehorn, J. Williams, J. Williams, E. J. Wollack, Z. Xu, B. Yu, C. Yu, F. Zago, H. Zhang, N. Zhu, and Simons Observatory Collaboration, "The Simons Observatory: science goals and forecasts," *Journal of Cosmology and Astroparticle Physics*, vol. 2019, p. 056, Feb. 2019.

[65] T. Elleflot, *Measuring the Polarization of the Cosmic Microwave Background with POLARBEAR-1 and Developing the Next-Generation Experiment POLARBEAR-2*. PhD thesis, UC San Diego, 2019. ProQuest ID: Elleflot_ucsd_0033D_18982. Merritt ID: ark:/13030/m5xq2bx0. Retrieved from https://escholarship.org/uc/item/56x406bc.

[66] D. Kaneko, S. Adachi, P. A. R. Ade, M. Aguilar Faúndez, Y. Akiba, K. Arnold, C. Baccigalupi, D. Barron, D. Beck, S. Beckman, F. Bianchini, D. Boettger, J. Borrill, J. Carron, S. Chapman, K. Cheung, Y. Chinone, K. Crowley, A. Cukierman, M. Dobbs, R. Dżnner,

H. El-Bouhargani, T. Elleflot, J. Errard, G. Fabbian, S. M. Feeney, C. Feng, T. Fujino, N. Galitzki, A. Gilbert, N. Goeckner-Wald, J. Groh, G. Hall, N. W. Halverson, T. Hamada, M. Hasegawa, M. Hazumi, C. A. Hill, L. Howe, Y. Inoue, G. Jaehnig, O. Jeong, N. Katayama, B. Keating, R. Keskitalo, S. Kikuchi, T. Kisner, N. Krachmalnicoff, A. Kusaka, A. T. Lee, D. Leon, E. Linder, L. N. Lowry, A. Mangu, F. Matsuda, Y. Minami, M. Navaroli, H. Nishino, J. Peloton, A. T. P. Pham, D. Poletti, G. Puglisi, C. L. Reichardt, C. Ross, Y. Segawa, M. Silva-Feaver, P. Siritanasak, N. Stebor, R. Stompor, A. Suzuki, O. Tajima, S. Takakura, S. Takatori, D. Tanabe, G. P. Teply, T. Tomaru, C. Tsai, C. Verges, B. Westbrook, and Y. Zhou, "Deployment of Polarbear-2A," *Journal of Low Temperature Physics*, vol. 199, pp. 1137–1147, Mar. 2020.

[67] L. Howe, C. Tsai, L. Lowry, K. Arnold, G. Coppi, J. Groh, X. Guo, B. Keating, A. Lee, A. J. May, L. Piccirillo, N. Stebor, and G. Teply, "Design and characterization of the POLARBEAR-2b and POLARBEAR-2c cosmic microwave background cryogenic receivers," in *Millimeter, Submillimeter, and Far-Infrared Detectors and Instrumentation for Astronomy IX* (J. Zmuidzinas and J.-R. Gao, eds.), vol. 10708 of *Society of Photo-Optical Instrumentation Engineers (SPIE) Conference Series*, p. 107083W, July 2018.

[68] Y. Inoue, P. Ade, Y. Akiba, C. Aleman, K. Arnold, C. Baccigalupi, B. Barch, D. Barron, A. Bender, D. Boettger, J. Borrill, S. Chapman, Y. Chinone, A. Cukierman, T. de Haan, M. A. Dobbs, A. Ducout, R. Dünner, T. Elleflot, J. Errard, G. Fabbian, S. Feeney, C. Feng, G. Fuller, A. J. Gilbert, N. Goeckner-Wald, J. Groh, G. Hall, N. Halverson, T. Hamada, M. Hasegawa, K. Hattori, M. Hazumi, C. Hill, W. L. Holzapfel, Y. Hori, L. Howe, F. Irie, G. Jaehnig, A. Jaffe, O. Jeong, N. Katayama, J. P. Kaufman, K. Kazemzadeh, B. G. Keating, Z. Kermish, R. Keskitalo, T. S. Kisner, A. Kusaka, M. Le Jeune, A. T. Lee, D. Leon, E. V. Linder, L. Lowry, F. Matsuda, T. Matsumura, N. Miller, K. Mizukami, J. Montgomery, M. Navaroli, H. Nishino, H. Paar, J. Peloton, D. Poletti, G. Puglisi, C. R. Raum, G. M. Rebeiz, C. L. Reichardt, P. L. Richards, C. Ross, K. M. Rotermund, Y. Segawa, B. D. Sherwin, I. Shirley, P. Siritanasak, N. Stebor, R. Stompor, J. Suzuki, A. Suzuki, O. Tajima, S. Takada, S. Takatori, G. P. Teply, A. Tikhomirov, T. Tomaru, N. Whitehorn, A. Zahn, and O. Zahn, "POLARBEAR-2: an instrument for CMB polarization measurements," in *Millimeter, Submillimeter, and Far-Infrared Detectors and Instrumentation for Astronomy VIII* (W. S. Holland and J. Zmuidzinas, eds.), vol. 9914 of *Society of Photo-Optical Instrumentation Engineers (SPIE) Conference Series*, p. 99141I, July 2016.

[69] Y. Inoue, *Development of POLARBEAR-2 receiver system for cosmic microwave background polarization experiment*. PhD thesis, Graduate University for Advanced Studies, 2016.

[70] J. Lamb, "Miscellaneous data on materials for millimetre and submillimetre optics," *International Journal of Infrared and Millimeter Waves*, vol. 17, pp. 1997–2034, 12 1996.

[71] J. E. Golec, J. J. McMahon, A. Ali, S. Dicker, N. Galitzki, K. Harrington, B. Westbrook, E. J. Wollack, Z. Xu, and N. Zhu, "Design and fabrication of metamaterial anti-reflection coatings for the Simons Observatory," in *Advances in Optical and Mechanical Technologies*

for Telescopes and Instrumentation IV (R. Navarro and R. Geyl, eds.), vol. 11451, pp. 1182 – 1189, International Society for Optics and Photonics, SPIE, 2020.

[72] O. Jeong, A. Lee, C. Raum, and A. Suzuki, "Broadband Plasma-Sprayed Anti-reflection Coating for Millimeter-Wave Astrophysics Experiments," *Journal of Low Temperature Physics*, vol. 184, pp. 621–626, Aug. 2016.

[73] J. Choi, H. Ishitsuka, S. Mima, S. Oguri, K. Takahashi, and O. Tajima, "Radio-transparent multi-layer insulation for radiowave receivers," *Review of Scientific Instruments*, vol. 84, pp. 114502–114502–6, Nov. 2013.

[74] P. A. R. Ade, G. Pisano, C. Tucker, and S. Weaver, "A review of metal mesh filters," in *Millimeter and Submillimeter Detectors and Instrumentation for Astronomy III* (J. Zmuidzinas, W. S. Holland, S. Withington, and W. D. Duncan, eds.), vol. 6275, pp. 248 – 262, International Society for Optics and Photonics, SPIE, 2006.

[75] C. A. Hill, *Sensitivity Simulations and Half-wave Plate Polarization Modulators for Cosmic Microwave Background Observatories*. PhD thesis, UC Berkeley, 2020. ProQuest ID: Hill_berkeley_0028E_20162. Merritt ID: ark:/13030/m5j15tmk. Retrieved from https://escholarship.org/uc/item/7vk6t7hb.

[76] A. Kusaka, T. Essinger-Hileman, J. W. Appel, P. Gallardo, K. D. Irwin, N. Jarosik, M. R. Nolta, L. A. Page, L. P. Parker, S. Raghunathan, J. L. Sievers, S. M. Simon, S. T. Staggs, and K. Visnjic, "Modulation of cosmic microwave background polarization with a warm rapidly rotating half-wave plate on the atacama b-mode search instrument," *Review of Scientific Instruments*, vol. 85, no. 2, p. 024501, 2014.

[77] K. Harrington, J. Eimer, D. T. Chuss, M. Petroff, J. Cleary, M. DeGeorge, T. W. Grunberg, A. Ali, J. W. Appel, C. L. Bennett, M. Brewer, R. Bustos, M. Chan, J. Couto, S. Dahal, K. Denis, R. Dünner, T. Essinger-Hileman, P. Fluxa, M. Halpern, G. Hilton, G. F. Hinshaw, J. Hubmayr, J. Iuliano, J. Karakla, T. Marriage, J. McMahon, N. J. Miller, C. Nuñez, I. L. Padilla, G. Palma, L. Parker, B. Pradenas Marquez, R. Reeves, C. Reintsema, K. Rostem, D. Augusto Nunes Valle, T. Van Engelhoven, B. Wang, Q. Wang, D. Watts, J. Weiland, E. Wollack, Z. Xu, Z. Yan, and L. Zeng, "Variable-delay polarization modulators for the CLASS telescopes," in *Millimeter, Submillimeter, and Far-Infrared Detectors and Instrumentation for Astronomy IX* (J. Zmuidzinas and J.-R. Gao, eds.), vol. 10708 of *Society of Photo-Optical Instrumentation Engineers (SPIE) Conference Series*, p. 107082M, July 2018.

[78] D. T. Chuss, E. J. Wollack, R. Henry, H. Hui, A. J. Juarez, M. Krejny, S. H. Moseley, and G. Novak, "Properties of a variable-delay polarization modulator," *Applied Optics*, vol. 51, p. 197, Jan. 2012.

[79] S. Takakura, M. Aguilar, Y. Akiba, K. Arnold, C. Baccigalupi, D. Barron, S. Beckman, D. Boettger, J. Borrill, S. Chapman, Y. Chinone, A. Cukierman, A. Ducout, T. Elleflot, J. Errard, G. Fabbian, T. Fujino, N. Galitzki, N. Goeckner-Wald, N. W. Halverson, M. Hasegawa,

K. Hattori, M. Hazumi, C. Hill, L. Howe, Y. Inoue, A. H. Jaffe, O. Jeong, D. Kaneko, N. Katayama, B. Keating, R. Keskitalo, T. Kisner, N. Krachmalnicoff, A. Kusaka, A. T. Lee, D. Leon, L. Lowry, F. Matsuda, T. Matsumura, M. Navaroli, H. Nishino, H. Paar, J. Peloton, D. Poletti, G. Puglisi, C. L. Reichardt, C. Ross, P. Siritanasak, A. Suzuki, O. Tajima, S. Takatori, and G. Teply, "Performance of a continuously rotating half-wave plate on the POLARBEAR telescope," *Journal of Cosmology and Astroparticle Physics*, vol. 2017, p. 008, May 2017.

[80] C. A. Hill, S. Beckman, Y. Chinone, N. Goeckner-Wald, M. Hazumi, B. Keating, A. Kusaka, A. T. Lee, F. Matsuda, R. Plambeck, A. Suzuki, and S. Takakura, "Design and development of an ambient-temperature continuously-rotating achromatic half-wave plate for CMB polarization modulation on the POLARBEAR-2 experiment," in *Millimeter, Submillimeter, and Far-Infrared Detectors and Instrumentation for Astronomy VIII* (W. S. Holland and J. Zmuidzinas, eds.), vol. 9914 of *Society of Photo-Optical Instrumentation Engineers (SPIE) Conference Series*, p. 99142U, July 2016.

[81] C. A. Hill, A. Kusaka, P. Ashton, P. Barton, T. Adkins, K. Arnold, B. Bixler, S. Ganjam, A. T. Lee, F. Matsuda, T. Matsumura, Y. Sakurai, R. Tat, and Y. Zhou, "A cryogenic continuously rotating half-wave plate mechanism for the POLARBEAR-2b cosmic microwave background receiver," *Review of Scientific Instruments*, vol. 91, p. 124503, Dec. 2020.

[82] B. Westbrook, P. A. R. Ade, M. Aguilar, Y. Akiba, K. Arnold, C. Baccigalupi, D. Barron, D. Beck, S. Beckman, A. N. Bender, F. Bianchini, D. Boettger, J. Borrill, S. Chapman, Y. Chinone, G. Coppi, K. Crowley, A. Cukierman, T. de Haan, R. Dünner, M. Dobbs, T. Elleflot, J. Errard, G. Fabbian, S. M. Feeney, C. Feng, G. Fuller, N. Galitzki, A. Gilbert, N. Goeckner-Wald, J. Groh, N. W. Halverson, T. Hamada, M. Hasegawa, M. Hazumi, C. A. Hill, W. Holzapfel, L. Howe, Y. Inoue, G. Jaehnig, A. Jaffe, O. Jeong, D. Kaneko, N. Katayama, B. Keating, R. Keskitalo, T. Kisner, N. Krachmalnicoff, A. Kusaka, M. Le Jeune, A. T. Lee, D. Leon, E. Linder, L. Lowry, A. Madurowicz, D. Mak, F. Matsuda, A. May, N. J. Miller, Y. Minami, J. Montgomery, M. Navaroli, H. Nishino, J. Peloton, A. Pham, L. Piccirillo, D. Plambeck, D. Poletti, G. Puglisi, C. Raum, G. Rebeiz, C. L. Reichardt, P. L. Richards, H. Roberts, C. Ross, K. M. Rotermund, Y. Segawa, B. Sherwin, M. Silva-Feaver, P. Siritanasak, R. Stompor, A. Suzuki, O. Tajima, S. Takakura, S. Takatori, D. Tanabe, R. Tat, G. P. Teply, A. Tikhomirov, T. Tomaru, C. Tsai, N. Whitehorn, and A. Zahn, "The POLARBEAR-2 and Simons Array Focal Plane Fabrication Status," *Journal of Low Temperature Physics*, vol. 193, pp. 758–770, Dec. 2018.

[83] P. Siritanasak, *Precise Measurement of B-mode polarization signal from the cosmic microwave background with Polarbear and the Simons Array*. PhD thesis, UC San Diego, 2018. ProQuest ID: Siritanasak_ucsd_0033D_17146. Merritt ID: ark:/13030/m5f52kkj. Retrieved from https://escholarship.org/uc/item/22f88813.

[84] R. H. DuHamel, "Dual polarized sinuous antennas," Apr. 1987. US Patent 4,658,262.

[85] K. D. Irwin and G. C. Hilton, *Transition-Edge Sensors*, vol. 99, p. 63. 2005.

[86] B. Westbrook, A. Cukierman, A. Lee, A. Suzuki, C. Raum, and W. Holzapfel, "Development of the Next Generation of Multi-chroic Antenna-Coupled Transition Edge Sensor Detectors for CMB Polarimetry," *Journal of Low Temperature Physics*, vol. 184, pp. 74–81, July 2016.

[87] J. C. Groh, *Design and Deployment of the Simons Array Cosmic Microwave Background Polarization Instrument*. PhD thesis, UC Berkeley, 2020.

[88] M. A. Dobbs, M. Lueker, K. A. Aird, A. N. Bender, B. A. Benson, L. E. Bleem, J. E. Carlstrom, C. L. Chang, H. M. Cho, J. Clarke, T. M. Crawford, A. T. Crites, D. I. Flanigan, T. de Haan, E. M. George, N. W. Halverson, W. L. Holzapfel, J. D. Hrubes, B. R. Johnson, J. Joseph, R. Keisler, J. Kennedy, Z. Kermish, T. M. Lanting, A. T. Lee, E. M. Leitch, D. Luong-Van, J. J. McMahon, J. Mehl, S. S. Meyer, T. E. Montroy, S. Padin, T. Plagge, C. Pryke, P. L. Richards, J. E. Ruhl, K. K. Schaffer, D. Schwan, E. Shirokoff, H. G. Spieler, Z. Staniszewski, A. A. Stark, K. Vanderlinde, J. D. Vieira, C. Vu, B. Westbrook, and R. Williamson, "Frequency multiplexed superconducting quantum interference device readout of large bolometer arrays for cosmic microwave background measurements," *Review of Scientific Instruments*, vol. 83, pp. 073113–073113–24, July 2012.

[89] D. Barron, K. Mitchell, J. Groh, K. Arnold, T. Elleflot, L. Howe, J. Ito, A. T. Lee, L. N. Lowry, A. Anderson, J. Avva, T. Adkins, C. Baccigalupi, K. Cheung, Y. Chinone, O. Jeong, N. Katayama, B. Keating, J. Montgomery, H. Nishino, C. Raum, P. Siritanasak, A. Suzuki, S. Takatori, C. Tsai, B. Westbrook, and Y. Zhou, "Integrated electrical properties of the frequency multiplexed cryogenic readout system for polarbear/simons array," *IEEE Transactions on Applied Superconductivity*, vol. 31, no. 5, pp. 1–5, 2021.

[90] K. Kiuchi, S. Adachi, A. M. Ali, K. Arnold, P. Ashton, J. E. Austermann, A. Bazako, J. A. Beall, Y. Chinone, G. Coppi, K. D. Crowley, K. T. Crowley, S. Dicker, B. Dober, S. M. Duff, G. Fabbian, N. Galitzki, J. E. Golec, J. E. Gudmundsson, K. Harrington, M. Hasegawa, M. Hattori, C. A. Hill, S.-P. P. Ho, J. Hubmayr, B. R. Johnson, D. Kaneko, N. Katayama, B. Keating, A. Kusaka, J. Lashner, A. T. Lee, F. Matsuda, H. McCarrick, M. Murata, F. Nati, Y. Nishinomiya, L. Page, M. S. Rao, C. L. Reichardt, K. Sakaguri, Y. Sakurai, J. Sibert, J. Spisak, O. Tajima, G. P. Teply, T. Terasaki, T. Tsan, S. Walker, E. J. Wollack, Z. Xu, K. Yamada, M. Zannoni, and N. Zhu, "Simons Observatory Small Aperture Telescope overview," in *Ground-based and Airborne Telescopes VIII* (H. K. Marshall, J. Spyromilio, and T. Usuda, eds.), vol. 11445, pp. 1372 – 1379, International Society for Optics and Photonics, SPIE, 2020.

[91] A. I. Braginski and J. Clarke, *Introduction*, ch. 1, pp. 1–28. John Wiley & Sons, Ltd, 2004.

[92] B. Chesca, R. Kleiner, and D. Koelle, *SQUID Theory*, ch. 2, pp. 29–92. John Wiley & Sons, Ltd, 2004.

[93] A. N. Bender, J.-F. Cliche, T. de Haan, M. A. Dobbs, A. J. Gilbert, J. Montgomery, N. Rowlands, G. M. Smecher, K. Smith, and A. Wilson, "Digital frequency domain multiplexing

readout electronics for the next generation of millimeter telescopes," in *Millimeter, Submillimeter, and Far-Infrared Detectors and Instrumentation for Astronomy VII* (W. S. Holland and J. Zmuidzinas, eds.), vol. 9153 of *Society of Photo-Optical Instrumentation Engineers (SPIE) Conference Series*, p. 91531A, July 2014.

[94] M. Silva-Feaver, K. Arnold, D. Barron, E. V. Denison, M. Dobbs, J. Groh, G. Hilton, J. Hubmayr, K. Irwin, A. Lee, and L. R. Vale, "Comparison of NIST SA13a and SA4b SQUID Array Amplifiers," *Journal of Low Temperature Physics*, vol. 193, pp. 600–610, Nov. 2018.

[95] T. de Haan, G. Smecher, and M. Dobbs, "Improved performance of TES bolometers using digital feedback," in *Millimeter, Submillimeter, and Far-Infrared Detectors and Instrumentation for Astronomy VI* (W. S. Holland and J. Zmuidzinas, eds.), vol. 8452 of *Society of Photo-Optical Instrumentation Engineers (SPIE) Conference Series*, p. 84520E, Sept. 2012.

[96] J. Montgomery, *Digital Frequency Domain Multiplexing readout: Design and performance of the SPT-3G instrument and LiteBIRD satellite readout*. PhD thesis, McGill University, Montreal, Quebec, Canada, 11 2020.

[97] J. Montgomery, "Development of multiplexed bolometer readout electronics for mm-wave space astronomy," Master's thesis, McGill University, 2015.

[98] K. N. Abazajian, P. Adshead, Z. Ahmed, S. W. Allen, D. Alonso, K. S. Arnold, C. Baccigalupi, J. G. Bartlett, N. Battaglia, B. A. Benson, C. A. Bischoff, J. Borrill, V. Buza, E. Calabrese, R. Caldwell, J. E. Carlstrom, C. L. Chang, T. M. Crawford, F.-Y. Cyr-Racine, F. De Bernardis, T. de Haan, S. di Serego Alighieri, J. Dunkley, C. Dvorkin, J. Errard, G. Fabbian, S. Feeney, S. Ferraro, J. P. Filippini, R. Flauger, G. M. Fuller, V. Gluscevic, D. Green, D. Grin, E. Grohs, J. W. Henning, J. C. Hill, R. Hlozek, G. Holder, W. Holzapfel, W. Hu, K. M. Huffenberger, R. Keskitalo, L. Knox, A. Kosowsky, J. Kovac, E. D. Kovetz, C.-L. Kuo, A. Kusaka, M. Le Jeune, A. T. Lee, M. Lilley, M. Loverde, M. S. Madhavacheril, A. Mantz, D. J. E. Marsh, J. McMahon, P. D. Meerburg, J. Meyers, A. D. Miller, J. B. Munoz, H. N. Nguyen, M. D. Niemack, M. Peloso, J. Peloton, L. Pogosian, C. Pryke, M. Raveri, C. L. Reichardt, G. Rocha, A. Rotti, E. Schaan, M. M. Schmittfull, D. Scott, N. Sehgal, S. Shandera, B. D. Sherwin, T. L. Smith, L. Sorbo, G. D. Starkman, K. T. Story, A. van Engelen, J. D. Vieira, S. Watson, N. Whitehorn, and W. L. Kimmy Wu, "CMB-S4 Science Book, First Edition," *arXiv e-prints*, p. arXiv:1610.02743, Oct. 2016.

[99] M. F. Navaroli, *Precise Astronomical Polarization Angle Calibration and its Impact on Studying Lorentz and Parity Violation in the Cosmic Microwave Background*. PhD thesis, UC San Diego, 2020. ProQuest ID: Navaroli_ucsd_0033D_19583. Merritt ID: ark:/13030/m5k98hbg. Retrieved from https://escholarship.org/uc/item/1380c9mn.

[100] C. A. Hill, S. M. M. Bruno, S. M. Simon, A. Ali, K. S. Arnold, P. C. Ashton, D. Barron, S. Bryan, Y. Chinone, G. Coppi, K. T. Crowley, A. Cukierman, S. Dicker, J. Dunkley,

G. Fabbian, N. Galitzki, P. A. Gallardo, J. E. Gudmundsson, J. Hubmayr, B. Keating, A. Kusaka, A. T. Lee, F. Matsuda, P. D. Mauskopf, J. McMahon, M. D. Niemack, G. Puglisi, M. Sathyanarayana Rao, M. Salatino, C. Sierra, S. Staggs, A. Suzuki, G. Teply, J. N. Ullom, B. Westbrook, Z. Xu, and N. Zhu, "BoloCalc: a sensitivity calculator for the design of Simons Observatory," in *Millimeter, Submillimeter, and Far-Infrared Detectors and Instrumentation for Astronomy IX* (J. Zmuidzinas and J.-R. Gao, eds.), vol. 10708 of *Society of Photo-Optical Instrumentation Engineers (SPIE) Conference Series*, p. 1070842, July 2018.

[101] P. Martini, S. Bailey, R. W. Besuner, D. Brooks, P. Doel, J. Edelstein, D. Eisenstein, B. Flaugher, G. Gutierrez, S. E. Harris, K. Honscheid, P. Jelinsky, R. Joyce, S. Kent, M. Levi, F. Prada, C. Poppett, D. Rabinowitz, C. Rockosi, L. Cardiel Sas, D. J. Schlegel, M. Schubnell, R. Sharples, J. H. Silber, D. Sprayberry, and R. Wechsler, "Overview of the Dark Energy Spectroscopic Instrument," in *Ground-based and Airborne Instrumentation for Astronomy VII* (C. J. Evans, L. Simard, and H. Takami, eds.), vol. 10702 of *Society of Photo-Optical Instrumentation Engineers (SPIE) Conference Series*, p. 107021F, July 2018.

[102] J. Ito, L. N. Lowry, T. Elleflot, K. T. Crowley, L. Howe, P. Siritanasak, T. Adkins, K. Arnold, C. Baccigalupi, D. Barron, B. Bixler, Y. Chinone, J. Groh, M. Hazumi, C. A. Hill, O. Jeong, B. Keating, A. Kusaka, A. T. Lee, K. Mitchell, M. Navaroli, A. T. P. Pham, C. Raum, C. L. Reichardt, T. J. Sasse, J. Seibert, A. Suzuki, S. Takakura, G. P. Teply, C. Tsai, and B. Westbrook, "Detector and readout characterization for POLARBEAR-2b," in *Millimeter, Submillimeter, and Far-Infrared Detectors and Instrumentation for Astronomy X* (J. Zmuidzinas and J.-R. Gao, eds.), vol. 11453, pp. 286 – 301, International Society for Optics and Photonics, SPIE, 2020.

[103] F. Matsuda, L. Lowry, A. Suzuki, M. Aguilar Fáundez, K. Arnold, D. Barron, F. Bianchini, K. Cheung, Y. Chinone, T. Elleflot, G. Fabbian, N. Goeckner-Wald, M. Hasegawa, D. Kaneko, N. Katayama, B. Keating, A. T. Lee, M. Navaroli, H. Nishino, H. Paar, G. Puglisi, P. L. Richards, J. Seibert, P. Siritanasak, O. Tajima, S. Takatori, C. Tsai, and B. Westbrook, "The POLARBEAR Fourier transform spectrometer calibrator and spectroscopic characterization of the POLARBEAR instrument," *Review of Scientific Instruments*, vol. 90, p. 115115, Nov. 2019.

[104] R. W. Simon, M. J. Burns, M. S. Colelough, G. Zaharchuk, and R. Cantor, *Mr. SQUID User's Guide*. STAR Cryoelectronics, LLC.

[105] S. Schöne, M. Mück, G. Thummes, and C. Heiden, "Investigation of the response of superconducting quantum interference devices to temperature variation," *Review of Scientific Instruments*, vol. 68, no. 1, pp. 85–88, 1997.

[106] K. Enpuku and T. Minotani, "Distortion of voltage vs flux relation of dc squid coupled to multiturn input coil due to input coil resonance combined with capacitive-feedback effect," *Applied Superconductivity*, vol. 5, no. 7, pp. 419–424, 1997.

[107] L. Howe, *The POLARBEAR-2 Cryogenic Receiver for Cosmic Microwave Background Polarization Science*. PhD thesis, UC San Diego, 2019. ProQuest ID: Howe_ucsd_0033D_18298. Merritt ID: ark:/13030/m5n0664t. Retrieved from https://escholarship.org/uc/item/5897v3wz.

[108] J. Groh, K. Arnold, J. Avva, D. Barron, K. T. Crowley, M. Dobbs, T. de Haan, W. Holzapfel, A. Lee, L. N. Lowry, J. Montgomery, M. Silva-Feaver, A. Suzuki, and N. Whitehorn, "Anomalous frequency noise from the megahertz channelizing resonators in frequency-division multiplexed transition edge sensor readout," *IEEE Transactions on Applied Superconductivity*, vol. 31, no. 5, pp. 1–5, 2021.

[109] T. Elleflot, A. Suzuki, C. Bebek, K. Crowley, T. de Haan, J. Groh, J. Joseph, A. Lee, and J. Montgomery, "Progress on frequency domain multiplexed readout of TES bolometers with sub-kelvin SQUID operation," in *Millimeter, Submillimeter, and Far-Infrared Detectors and Instrumentation for Astronomy X* (J. Zmuidzinas and J.-R. Gao, eds.), vol. 11453, International Society for Optics and Photonics, SPIE, 2020.

[110] M. Hasegawa *In preparation*.

[111] S. Pancharatnam, "Achromatic combinations of birefringent plates," *Proceedings of the Indian Academy of Sciences - Section A*, vol. 41, pp. 137–141, 1955.

[112] L. Moncelsi, P. A. R. Ade, Z. Ahmed, M. Amiri, D. Barkats, R. Basu Thakur, C. A. Bischoff, J. J. Bock, V. Buza, J. R. Cheshire, J. Connors, J. Cornelison, M. Crumrine, A. J. Cukierman, E. V. Denison, M. Dierickx, L. Duband, M. Eiben, S. Fatigoni, J. P. Filippini, N. Goeckner-Wald, D. Goldfinger, J. A. Grayson, P. Grimes, G. Hall, M. Halpern, S. A. Harrison, S. Henderson, S. R. Hildebrandt, G. C. Hilton, J. Hubmayr, H. Hui, K. D. Irwin, J. H. Kang, K. S. Karkare, S. Kefeli, J. M. Kovac, C. L. Kuo, K. Lau, E. M. Leitch, K. G. Megerian, L. Minutolo, Y. Nakato, T. Namikawa, H. T. Nguyen, R. O'brient, S. Palladino, N. Precup, T. Prouve, C. Pryke, B. Racine, C. D. Reintsema, A. Schillaci, B. L. Schmitt, A. Soliman, T. St. Germaine, B. Steinbach, R. V. Sudiwala, K. L. Thompson, C. Tucker, A. D. Turner, C. Umiltà, A. G. Vieregg, A. Wandui, A. C. Weber, D. V. Wiebe, J. Willmert, W. L. K. Wu, E. Yang, K. W. Yoon, E. Young, C. Yu, L. Zeng, C. Zhang, and S. Zhang, "Receiver development for BICEP Array, a next-generation CMB polarimeter at the South Pole," in *Society of Photo-Optical Instrumentation Engineers (SPIE) Conference Series*, vol. 11453 of *Society of Photo-Optical Instrumentation Engineers (SPIE) Conference Series*, p. 1145314, Dec. 2020.

[113] M. H. Abitbol, Z. Ahmed, D. Barron, R. Basu Thakur, A. N. Bender, B. A. Benson, C. A. Bischoff, S. A. Bryan, J. E. Carlstrom, C. L. Chang, D. T. Chuss, K. T. Crowley, A. Cukierman, T. de Haan, M. Dobbs, T. Essinger-Hileman, J. P. Filippini, K. Ganga, J. E. Gudmundsson, N. W. Halverson, S. Hanany, S. W. Henderson, C. A. Hill, S.-P. P. Ho, J. Hubmayr, K. Irwin, O. Jeong, B. R. Johnson, S. A. Kernasovskiy, J. M. Kovac, A. Kusaka, A. T. Lee, S. Maria, P. Mauskopf, J. J. McMahon, L. Moncelsi, A. W. Nadolski, J. M. Nagy, M. D. Niemack, R. C. O'Brient, S. Padin, S. C. Parshley, C. Pryke, N. A.

Roe, K. Rostem, J. Ruhl, S. M. Simon, S. T. Staggs, A. Suzuki, E. R. Switzer, O. Tajima, K. L. Thompson, P. Timbie, G. S. Tucker, J. D. Vieira, A. G. Vieregg, B. Westbrook, E. J. Wollack, K. W. Yoon, K. S. Young, and E. Y. Young, "CMB-S4 Technology Book, First Edition," *arXiv e-prints*, p. arXiv:1706.02464, June 2017.

[114] H. McCarrick, E. Healy, Z. Ahmed, K. Arnold, Z. Atkins, J. E. Austermann, T. Bhandarkar, J. A. Beall, S. M. Bruno, S. K. Choi, J. Connors, N. F. Cothard, K. D. Crowley, S. Dicker, B. Dober, C. J. Duell, S. M. Duff, D. Dutcher, J. C. Frisch, N. Galitzki, M. B. Gralla, J. E. Gudmundsson, S. W. Henderson, G. C. Hilton, S.-P. P. Ho, Z. B. Huber, J. Hubmayr, J. Iuliano, B. R. Johnson, A. M. Kofman, A. Kusaka, J. Lashner, A. T. Lee, Y. Li, M. J. Link, T. J. Lucas, M. Lungu, J. A. B. Mates, J. J. McMahon, M. D. Niemack, J. Orlowski-Scherer, J. Seibert, M. Silva-Feaver, S. M. Simon, S. Staggs, A. Suzuki, T. Terasaki, J. N. Ullom, E. M. Vavagiakis, L. R. Vale, J. Van Lanen, M. R. Vissers, Y. Wang, E. J. Wollack, Z. Xu, E. Young, C. Yu, K. Zheng, and N. Zhu, "The Simons Observatory microwave SQUID multiplexing detector module design," *arXiv e-prints*, p. arXiv:2106.14797, June 2021.

[115] T. de Haan, A. Suzuki, S. T. P. Boyd, R. H. Cantor, A. Coerver, M. A. Dobbs, R. Hennings-Yeomans, W. L. Holzapfel, A. T. Lee, G. I. Noble, G. Smecher, and J. Zhou, "Recent Advances in Frequency-Multiplexed TES Readout: Vastly Reduced Parasitics and an Increase in Multiplexing Factor with Sub-Kelvin SQUIDs," *Journal of Low Temperature Physics*, vol. 199, pp. 754–761, Feb. 2020.